eman ta zabal zazu

Universidad del País Vasco
Euskal Herriko Unibertsitatea

DEPARTMENT OF MATHEMATICS

DOCTOR OF PHILOSOPHY

THESIS

ADVANCED MATHEMATICAL MODELLING OF PANCREATIC β-CELLS

Thesis Advisors

Luca Gerardo-Giorda
Basque Center for Applied Mathematics, Spain

Richard Bertram
Florida State University, the United States

Student

Isabella Marinelli
Basque Center for Applied Mathematics, Spain

ACADEMIC YEAR 2019-2020

Ph. D. Thesis

Advanced Mathematical Modelling of Pancreatic β-Cells

Isabella Marinelli

Supervisors Luca Gerardo-Giorda
Richard Bertram

This research was carried out at the Basque Center for Applied Mathematics (BCAM) within the Mathematical Modelling in Biosciences (MMB) group and was supported by the Basque Government through the BERC 2014-2017 and BERC 2018-2021 programs, by the Spanish Ministry of Economics and Competitiveness MINECO through the BCAM Severo Ochoa excellence accreditation SEV-2013-0323 and grant MTM2015-69992-R (BELEMET) and by the Spanish State Research Agency through BCAM Severo Ochoa excellence accreditation SEV-2017-0718 and through project RTI2018-093416-B-I00 funded by (AEI/FEDER, UE) and acronym “MULTIQUANT”. The support of MINECO and BERC Grants is acknowledged for the four months visit at the Florida State University, Florida, US.

To my family and friends,
For always being there for me

Acknowledgement

This thesis represents the conclusion of a four-year journey that has been a truly life-changing experience for me. It would not have been possible without the support and guidance that I received from many people. It is to them that I owe my deepest gratitude.

First and foremost, my sincere thanks must go to my advisors Dr. Richard Bertram and Dr. Luca Gerardo-Giorda for the guidance, advice, enthusiasm, and motivation they have provided throughout my Ph.D. I am eternally grateful to them, and to them, I owe everything I know.
I would like to thank Dr. Arthur Sherman, Dr. Leslie Satin, Dr. Patrick Fletcher, and Dr. Theodore Vo for their assistance and their constant feedback. This thesis would not have been possible without their support.
Special thanks must go also to Dr. Luis Antonio Castaño González and Dr. Maria Sonia Gaztambide Sáenz for they introduced me to the intriguing world of pancreatic β-cells.
I deeply thank my colleagues of the Mathematical Modelling in Biosciences Group for their encouragement and insightful comments.

Last but not least, I am grateful to my family and friends spread all around the world. Un immenso grazie a papà, mamma, sorella e nonni, ovunque siano. Voi siete le fondamenta che mi hanno sostenuto e sempre mi sosterranno in futuro. La certezza della vostra presenza e il calore del vostro ricordo non mi hanno permesso di mollare mai.
Grazie ai miei amici più cari. Eleonora, Silvia (Carnevale), Roberta, grazie per tutti questi anni di amicizia. In un modo o nell'altro, nonostante la distanza, siete sempre state presenti nei momenti cruciali della mia vita, condividendo risate e lacrime. Un ringraziamento particolare a Nicole. Sei stata un'amica, una guida, un supervisor, una sorella, un basketball coach, e molto di più. Mi sei stata vicino in alcuni dei momenti più bui della mia vita, e mi hai aiutato a superarli. Grazie dal profondo del cuore. Martina, grazie per la tua preziosa amicizia. Abbiamo condiviso così tanto in pochi anni che ci conosciamo, dimostrando che il tempo non conta quando si incontrano persone meravigliose come te. Andrea, grazie per essere stato il miglior compagno d'ufficio che si possa avere e un carissimo amico con cui condividere tanti

momenti (e tanta burocrazia). Grazie a Silvia (Vitali) per il pizzico di “Sivianess” (= iperattività mista a pazzia e saggezza) che mi hai dato in questi anni, e che ha reso molti momenti indimenticabili. Un grazie speciale ad Alessio. Tra alti e bassi, sei una delle costanti della mia vita senza il cui supporto non sarei qui ora. Non penso che queste poche parole siano sufficienti per ringraziarti veramente per tutto quello che hai fatto per me, ma spero si avvicinino.
Un agradecimiento especial a Javi (Canto) y Dani. Gracias por vuestra amistad y ánimo, por compartir conmigo muchos momentos inolvidables en estos años. Y sobre todo, gracias por haberme enseñado tantas cosas sobre la cultura vasca. Eskerrik asko! Gracias a Javi (Martínez) y a todos los compañeros de“caffè y comidas” por haber hecho de estos momentos algo que he esperado con impaciencia.
Daniel, you have been a dear flatmate and an even dearer friend. You are a piece of my life in Bilbao that I will cherish forever (although neither of us will be there). Mauricio, Marco, Diana, Havva, and Sandeep, I want to thank you for your friendship and all the great moments we spent together. Gracias a Miguel, que has sido no solo un manager formidable, sino una áncora en BCAM en momentos insoportables. Grazie anche a Vittoria e Giulio per il tempo passato insieme, sopratutto in questi ultimi mesi.
Quiero agradecer también a mí sensei, sempai y kohai de kendo. En muchísimo momentos, el dojo ha sido mí propia oasis mental. ARIGATOU GOZAIMASU! En particular, muchas gracias al Young Team. Peio, Aintzane, Gaizka, nuca olvidaré de los momentos maravillosos (y las comidas!) que hemos pasado juntos. Los estimaré por toda mi vida.
A special thanks go to Theo. I thanked you as a collaborator above, I am thanking you as a friend here. You have been such a great friend during my time in Tallahassee and even after that. I am glad I got to meet you and Karen. The “coffee club” will rule forever! Many thanks to Richard and Wendy for being my “foster” family during my time in the US. You have helped, supported, and thought me so much that I don’t know how to pay you back. You will always be in heart wherever I will go. Finally, I want to thank my friends at the IMB building. Yeuran, Angie, Josh, and Susan, thank you for the wonderful time in Tallahassee. I’m going to miss you very much!

During these years I had to honour to meet amazing people whose encouragement and endless support made all this possible. While I mentioned a few above, I am sure that I forgot many others. My sincere apologies for this.

Abstract

Insulin-secreting pancreatic β-cells are responsible for maintaining the whole body glucose homeostasis. Dysfunction or loss of β-cell mass results in impaired insulin secretion and, in some cases, diabetes. Many of the factors that influence β-cell function or the insulin exocytosis, however, are not fully understood. To support the investigation, mathematical models have been developed and used to design experiments.

In this dissertation, we present the Integrated Oscillator Model (IOM) that is one of the mathematical models used for the investigation of the mechanism behind bursting activity that underlies intracellular Ca^{2+} oscillations and pulsatile insulin secretion. The IOM describes the interaction of the cellular electrical activity and intracellular Ca^{2+} with glucose metabolism via numerous feedforward and feedback pathways. These interactions, in turn, produce metabolic oscillations with a sawtooth or pulsatile time course, reflecting different oscillation mechanisms. We determine conditions favourable to each type of oscillations, and show that the model accounts for key experimental findings of β-cell activity.

We propose several extensions of the model to include all the main elements involved in the insulin secretion. The latest and most sophisticated model describes the complex metabolism in the mitochondria and the several biological processes in the insulin exocytosis cascade. The model, also, captures the changes in the β-cell activity and the resulting amount of secreted insulin in response to different concentrations of glucose in the blood. The model predictions, in agreement with findings reported in the experimental literature, show an increase of insulin secretion when the glucose level is high and a basal-low insulin concentration when the glucose level decreases.

Finally, we use the new model to simulate the interaction among β-cells (through gap junction) within the same islet. The simulations show that the electrical coupling is sufficient to synchronize the β-cells within an islet. We also show that the amplitude of the oscillations in the insulin secretion rate is bigger when the β-cells synchronize. This suggests a more efficient secretion of insulin in the bloodstream when the cells burst in unison, as it has been observed experimentally.

Sinopsis

Las células β pancreáticas secretoras de insulina son responsables de mantener la homeostasis de la glucosa en todo el organismo. Una disfunción o pérdida del conjunto de células β provoca una secreción de insulina deficiente y, en algunos casos, diabetes. Muchos de los factores que afectan a la función de las células β o la exocitosis de la insulina, sin embargo, no se entiende por completo. Para apoyar la investigación, se han desarrollado y utilizado modelos matemáticos para diseñar experimentos.

En esta tesis presentamos el Integrated Oscillator Model (IOM), que es uno de los modelos matemáticos utilizados para la investigación de los mecanismos detrás de la ráfagas de actividad (*bursts*) que subyace bajo las oscilaciones de Ca^{2+} intracelular y la secreción pulsátil de insulina. El IOM describe la interacción de la actividad eléctrica celular y del Ca^{2+} intracelular con el metabolismo de la glucosa mediante numerosas rutas de realimentación prospectiva y retroalimentación. Estas interacciones, a su vez, producen oscilaciones metabólicas con un curso del tiempo pulsátil o en zigzag, que reflejan distintos mecanismos de oscilación. Determinamos condiciones favorables para cada tipo de oscilación y demostramos que el modelo representa hallazgos experimentales fundamentales de la actividad de las células β.

Proponemos varias extensiones del modelo para incluir todos los elementos principales implicados en la secreción de insulina. El modelo más reciente y sofisticado describe el complejo metabolismo en la mitocondria y los varios procesos biológicos en la cascada de la exocitosis de la insulina. El modelo, además, captura los cambios en la actividad de las células β y la cantidad resultante de insulina secretada en respuesta a distintas concentraciones de glucosa en la sangre. Las predicciones del modelo, de acuerdo con hallazgos recogidos en la literatura experimental, indican un aumento de la secreción de insulina cuando el nivel de glucosa es alto y una baja concentración de insulina basal cuando el nivel de glucosa disminuye.

Por último, utilizamos el nuevo modelo para simular la interacción entre células β (mediante conexión comunicante) dentro de un mismo islote. Las simulaciones indican que el acoplamiento eléctrico es suficiente para sincronizar las células β dentro de un islote. También demostramos que la amplitud de las oscilaciones en la

velocidad de secreción de la insulina es mayor cuando las células β se sincronizan. Esto sugiere una secreción más eficaz de insulina al torrente sanguíneo cuando las células estallan al unísono, ya que se ha observado a nivel experimental.

Laburpena

Intsulina jariatzaileak diren β-zelula pankreatikoen lana gorputzaren glukosa-homeostasia mantentzean datza. Zelula hauen disfuntzioak edota galerak intsulina-jarioaren txikitzea dakar, eta batzuetan diabetesa ere eragin dezake. Hala ere, β-zelulen funtzionamenduan eta intsulinaren exozitosian eragiten duten faktore asko ez dira oraindik guztiz ondo ezagutzen. Hauek ikertzen eta esperimentuak diseinatzen laguntzen duten hainbat eredu matematiko daude.

Tesi honetan, aipatutako ereduetako bat aurkeztuko dugu, Integrated Oscillator Model (IOM) delakoa, alegia. Intsulina-jario taupakariaren eta zelula barneko Ca^{2+}-aren oszilazioaren azpian dauden aktibitate-boladen mekanismoa aztertzeko erabiltzen da. Eredu honek zelulen aktibitate elektrikoaren, zelula barneko Ca^{2+}-aren eta glukosaren metabolismoaren arteko elkarrekintza deskribatzen du, horretarako hainbat *feedforward* eta *feedback* bide erabiliz. Gainera, elkarrekintza honek portaera taupakaria daukaten oszilazio metabolikoak eragiten ditu, oszilazio mekanismo desberdinak erakutsiz. Oszilazio mota bakoitzaren aldeko baldintzak zehaztuko ditugu, eta erakutsiko dugu ereduak esperimentuetan beha daitezkeen β-zelulen aktibitatearen ezaugarriak ondo jasotzen dituela.

Eredu hau orokortzea proposatuko dugu, horretarako intsulinaren jarioan eragina duten elementu nagusiak kontuan hartuz. Eredu berri eta sofistikatuenak mitokondrioen mekanismo konplexua eta intsulinaren exozitosiaren prozesu biologikoak deskribatzen ditu. Halaber, odoleko glukosa-kontzentrazio desberdinek eragiten dituzten β-zelulen aktibitatearen aldaketak eta ondorioz jariatutako intsulina kantitatea ere jasotzeko gai da. Esperimentuetan behatutakoarekin bat eginez, ereduak aurreikusten du intsulina-jarioa handitu egiten dela glukosa maila altuarekin, eta intsulinaren kontzentrazioa oinarrizko maila minimora murrizten dela glukosa kantitatea txikitzen denean.

Azkenik, eredu berria erabiliko dugu irla berdinean dauden β-zelulen arteko elkarrekintza simulatzeko. Hain zuzen ere, simulazio hauen arabera, akoplamendu elektrikoa nahikoa da irla berdineko β-zelulak sinkronizatzeko, eta zelulak sinkronizatzen direnean, intsulina-jarioaren oszilazioen anplitudea handiagoa dela ere erakutsiko dugu. Honek iradokitzen du intsulina-jarioa eraginkorragoa izango

dela zelula guztiak aldi berean aktibatzen direnean, esperimentuetako neurketek erakusten duten bezalaxe.

Resumen

Todos los organismos pueden mantener un ambiente interno estable adecuado para sustentar vida. Esta capacidad se denomina *homeostasis*. Los animales han desarrollado numerosos mecanismos fisiológicos para ser capaces de mantener un estado de equilibrio en su ambiente interno al enfrentarse con distintos cambios externos. Uno de estos mecanismos es el bucle de retroalimentación negativa que implica dos hormonas, *insulina* y *glucagón*, el cual permite que los niveles de glucemia varíen en un rango de concentración fisiológica. Si el nivel de glucosa es demasiado alto (por ejemplo, después de una comida), el organismo libera insulina en el torrente sanguíneo. La insulina provoca la absorción y el almacenamiento de la glucosa por las células del organismo (es decir, tejido adiposo y muscular), lo que disminuye la concentración de glucosa en la sangre. Si el nivel de glucosa es demasiado bajo (por ejemplo, en una situación de ayuno), el nivel de insulina será bajo y esto provoca la liberación de glucagón, que permite la liberación de glucosa desde las células en las que ha sido almacenada.

Si este bucle se altera, el organismo perderá la capacidad de controlar el nivel de glucosa en la sangre y esto puede provocar graves consecuencias. Esto ocurre, por ejemplo, en presencia de disfunción o reducción del conjunto de células secretoras de insulina, lo que provoca una glucemia anómala y diabetes [81]. Por este motivo, las células β pancreáticas (es decir, las únicas células productoras y secretoras de insulina) han sido ampliamente estudiadas en el contexto de la regulación de la glucosa en el organismo y en relación con la diabetes.

La secreción de insulina se produce a causa del acoplamiento de actividad metabólica y eléctrica en las células β. Concretamente, la hormona es liberada de manera pulsátil, que refleja oscilaciones en la concentración de calcio intracelular, que, a su vez, se produce a causa de la ráfagas de potenciales de acción (*bursts*). Se han observado distintos tipos de oscilaciones en los laboratorios: oscilaciones lentas con periodos normalmente entre 4 y 6 min, oscilaciones rápidas con periodos normalmente entre 0,5 y 2 min y oscilaciones mixtas, que consisten en un grupo (de varios minutos) de oscilaciones rápidas repetido con el mismo rango de periodos que las oscilaciones lentas. Se ha observado que los periodos de oscilaciones mixtas y lentas concordan con las medidas de insulina plasmática en ratones [69]. Aunque el conocimiento sobre la dinámica del interior de las células β se encuentra en

continuo crecimiento, el mecanismo que subyace bajo estas oscilaciones (y provoca la secreción de insulina) aún no se entiende por completo.

En 1983, Chay y Keizer publicaron el primer modelo de actividad eléctrica de las células β [26]. El objetivo principal de este modelo fue buscar una explicación de la actividad de las células β desde un punto de vista mecánico. Desde entonces, se han desarrollado varios modelos matemáticos para investigar la sumamente compleja dinámica metabólica y eléctrica en las células β y el mecanismo que subyace bajo la actividad eléctrica celular. Los modelos matemáticos en la literatura sobre células β puede agruparse en dos clases principales de acuerdo con el mecanismo que lleva a las ráfagas, aquellas en las que las que oscilaciones en la concentración de Ca^{2+} citosólico conduce a oscilaciones metabólicas (oscilaciones producidas por Ca^{2+}) y aquellas en las que oscilaciones metabólicas intrínsecas conducen a oscilaciones en la concentración de Ca^{2+} (oscilaciones de origen metabólico). Nos referimos a las dos clases como *Clase I* y *Clase II,* respectivamente. En la *Clase I* [46, 76, 38, 31, 67, 37, 22], la actividad eléctrica en ráfagas está controlada por la retroalimentación negativa lenta de Ca^{2+} en procesos intermedios. Concretamente, durante la fase de activación (*active phase*) la concentración de Ca^{2+} citoplasmática aumenta debido a la activación de los canales de Ca^{2+} dependientes de voltaje. Esto conduce al aumento de la variable lenta (que aquí representa los procesos intermedios), lo que inicia la fase de activación. Durante la fase de desactivación (*silent phase*), la variable lenta disminuye, lo que detiene la actividad de desparo cellular (*spiking activity*) e inicia la fase de repolarización. Finalmente, la variable alcanza valores lo suficiente bajos que permiten el inicio de una nueva fase de activación. En la *Clase II* [94], las oscilaciones metabólicas intrínsecas generan oscilaciones en la concentración de ATP y en el cociente ATP/ADP, lo que afecta a la conducta de los canales de K^+ sensibles a ATP. El patrón de oscilaciones resultante modula los cambios en el potencial de membrana. Esto provoca una ráfagas y oscilaciones del Ca^{2+}, ambos de origen metabólico. Sin embargo, ninguna de las clases representa todos los patrones de ráfaga observados o los nuevos hallazgos experimentales.

En este contexto, Bertram et al. [10, 15, 17, 62] presentaron varios modelos matemáticos que combinan elementos de ambas clases para estimular una variedad de mecanismos que subyacen bajo la ráfaga. Concretamente, en estos modelos la ráfaga lenta es conducida por las oscilaciones glucolíticas y la acción ATP/ADP sobre los canales de K^+ sensibles a ATP, mientras que la ráfaga rápida se debe a la acción del Ca^{2+} sobre los canales de K^+ activados por Ca^{2+}. Una combinación adecuada de estos dos mecanismos provoca una ráfaga mixta. El modelo más completo de esta escuela para describir la dinámica de los metabolitos en las células β pancreáticas secretoras de insulina se denomina Integrated Oscillator Model (IOM). Este modelo consiste en una descripción matemática fundamentada fisiológicamente basada en datos experimentales relevantes y disponibles. A nuestro saber, el IOM es el

único modelo que representa el rango completo de ritmos de oscilaciones y todas las observaciones experimentales fundamentales presentadas en la literatura hasta ahora.

En esta tesis, presentamos y analizamos una versión actualizada del IOM, llamada IOM 1.5, que tiene en cuenta dinámicas más complejas del Ca^{2+} dentro de las mitocondrias, el orgánulo que genera la mayoría del suministro celular de ATP (a su vez utilizado como fuente de energía por la propia célula). De hecho, a medida que se recogen nuevas observaciones experimentales, el modelo se ajusta para representarlas. El proceso provoca una evolución constante del modelo, el cual presentamos en esta tesis. Utilizamos el IOM 1.5 para investigar los mecanismos detrás de las ráfagas que subyace bajo las oscilaciones intracelulares de Ca^{2+} y la secreción pulsátil de insulina, que aún no ha sido entendida por completo. El IOM 1.5 viene dado por un conjunto de ecuaciones diferenciales ordinarias que pueden dividirse en dos módulos: un módulo describe la actividad eléctrica de las células β y la dinámica del Ca^{2+} y el otro describe la ruta de la glucólisis y la producción de ATP. Estos dos módulos interactúan mediante numerosas rutas de realimentación prospectiva y retroalimentación, que generan oscilaciones metabólicas con una evolución temporal pulsátil o una evolución temporal en zigzag, lo que refleja mecanismos de oscilación muy distintos. Existen dos hipótesis de contraste principales en cuanto a la naturaleza del mecanismo detrás de la actividad celular en ráfagas: algunos presuponen que las oscilaciones metabólicas conducen las oscilaciones en concentración de Ca^{2+} citosólico, mientras otros apoyan la hipótesis opuesta. Realizamos un análisis de bifurcación del subsistema glucolítico para investigar la naturaleza de las oscilaciones metabólicas. Estos análisis nos permiten poner ambos puntos de vista en un mismo contexto y determinar las condiciones favorables para cada tipo de mecanismo. El IOM 1.5 también es capaz de producir un amplio rango de patrones de ráfaga (incluidas ráfagas mixtas, rápidas y lentas), además de nuevas observaciones experimentales en la actividad de las células β [66] que no podían representarse en modelos de células β anteriores. Además, sugerimos protocolos que pueden utilizarse en laboratorios para investigar la naturaleza de las oscilaciones de las células β. A pesar de la capacidad de IOM 1.5 para reproducir el conjunto completo de patrones de ráfaga y representar los hallazgos experimentales fundamentales, sigue teniendo limitaciones. Por ejemplo, no incluye una actividad metabólica detallada dentro de las mitocondrias. Esto provoca una concentración de ATP no fisiológica en la ausencia de metabolismo y, como tal, el IOM 1.5 no puede reproducir observaciones de laboratorio de concentraciones mitocondriales.

Llegados a este punto, avanzamos y presentamos una secuencia de extensiones del IOM 1.5, que enumeramos progresivamente para remarcar el proceso evolutivo.

Después de haber extendido el modelo de células β del IOM 1.0 al IOM 1.5, hemos desarrollado extensiones que incorporaban la dinámica de otras variables fundamentales de las mitocondrias. El primer ajuste, llamado IOM 2.0, añade un módulo que describe el metabolismo mitocondrial al IOM 1.5. Analizamos las posibilidades de este modelo mejorado y encontramos que, además de reproducir los hallazgos experimentales presentados con el IOM 1.5, el nuevo modelo también puede capturar una variedad de otros aspectos importantes. La recompensa de la alta complejidad es la capacidad del modelo para simular variables mitocondriales que pueden medirse experimentalmente con nuevas técnicas de laboratorio, y representar una descripción más realista de la producción y consumo de ATP, por lo que supera algunas de las limitaciones presentes en el IOM 1.5. El IOM 2.0 imita la dinámica de célula única en un islote sincronizado para un nivel de glucosa fijo. Por tanto, una mejora natural que consideramos en esta tesis es incluir la dinámica de la glucosa en el modelo. Presentamos el nuevo IOM 2.1, obtenido al añadir una dependencia explícita de actividad de las células β sobre el nivel de glucosa en el IOM 2.0 anterior. De este modo, nuestro modelo puede capturar las distintas respuestas de las células β a cambios en el nivel de glucosa observado en laboratorios. Estudiamos este aspecto utilizando una vez más técnicas de sistemas dinámicos y realizando un análisis rápido-lento (*fast-slow analysis*) del modelo.

Una extensión adicional del modelo incluye la adición de la cascada de la exocitosis de la insulina en el último IOM 2.1. Gracias a los módulos que describen la dinámica mitocondrial y la dinámica de la glucosa, pudimos simular la secreción de insulina que se amplifica por la actividad mitocondrial y se controla por cambios en la glucemia. El nuevo IOM, llamado IOM 2.2, pueden representar con éxito observaciones de laboratorio imposibles para otros modelos en la literatura. Gracias a las oscilaciones glucolíticas intrínsecas generadas por el IOM para un conjunto de parámetros adecuado, pudimos replicar las oscilaciones *in silico* en la concentración de insulina en una célula en una disolución con un nivel de glucosa subliminar. Sin embargo, el modelo no captura las oscilaciones en la insulina cuando la célula alcanza su máximo continuamente, como se observa en algunos laboratorios. Además, no tiene en cuenta la interacción célula-célula, esencial en el proceso de secreción de la insulina.

La extensión final del modelo que describimos en esta tesis representa la sincronización (mediante uniones gap - *gap junctions*) de células β dentro de un islote. Se ha observado que las células β del mismo islote disparan al mismo tiempo para secretar insulina de manera eficiente en respuesta a cambios en la glucemia. En esta tesis, simulamos cada célula β virtual con el último IOM 2.2 y presuponemos que la naturaleza del acoplamiento es eléctrico o eléctrico y metabólico. Investigamos las predicciones del modelo y observamos que, en nuestras simulaciones,

el acoplamiento eléctrico es suficiente para sincronizar las células β dentro de un islote.

El IOM 1.5 al IOM 2.2 (así como su extensión a islotes) son avances importantes en el campo del modelaje de células β, lo que permite realizar descripciones cualitativas y cuantitativas de hallazgos experimentales fundamentales registrados en las últimas décadas. A pesar de sus avances, estos modelos siguen estando limitados en su capacidad para simular el bucle de retroalimentación negativa cerrado, que implica que las hormonas glucagón e insulina mantengan una glucemia fisiológica estable. Concluimos esta tesis realizando algunas consideraciones sobre dos posibles caminos para esta investigación presentada. En concreto, podríamos seguir extendiendo el modelo al incluir la interacción páncreas-hígado o podríamos avanzar hacia una aplicación clínica del modelo para simular situaciones patológicas.

La homeostasis de la glucosa está regulada por la interacción mutua entre las células β pancreáticas secretoras de insulina y el hígado liberador y almacenador de glucosa. Esta interacción se produce de dos modos. El primero es una influencia directa de un órgano sobre el otro mediante la acción de hormonas (insulina y glucagón). Cuando la glucemia es elevada, las células β secretan insulina para estimular que el hígado almacene glucosa en la forma de glucógeno polimérico de almacenamiento (*glucogenogénesis*). La insulina también inhibe la secreción de glucagón desde células α. Si el nivel de glucosa disminuye por debajo del nivel fisiológico, se secreta entonces glucagón y hace que el hígado libere glucosa a la sangre al degradar glucógeno en glucosa (*glucogenólisis*). El segundo modo son los controles indirectos del hígado sobre la naturaleza oscilatoria de la actividad de las células β. Como regulador de las oscilaciones pancreáticas, el hígado puede ser capaz de sincronizar oscilaciones ya presentes en los islotes y, en algunos casos, de crearlas [89]. Para modelar este bucle, cambiaremos un sistema célula-célula por un sistema islote-hígado, en el que la entrada de glucosa en el modelo de células β viene dada por el modelo hepático que, a su vez, utiliza la insulina secretada por el islote para modular el propio nivel de glucosa.

Otra dirección que podemos tomar es la estimulación de diabetes mellitus neonatal permanente (DMNP), una forma poco frecuente de diabetes a menudo provocada por mutaciones genéticas que afectan a los canales de K^+ sensibles al ATP e impiden la secreción de insulina. Alrededor del 50% de las DMNP son provocadas por mutaciones en los genes KCNJ11 y ABCC8, que codifican las subunidades de los canales de K^+ sensibles a ATP e impiden la capacidad del ATP para cerrar los canales. Los canales de K^+ sensibles a ATP aseguran que sea secretada la cantidad correcta de insulina para la glucemia. De hecho, mutaciones en los genes KCNJ11 y ABCC8 pueden provocar tanto hipo como hiperglucemia, así como alteraciones neurológicas. Los pacientes afectados por estas mutaciones son normalmente tratados por altas

dosis de fármacos de sulfonilurea que pueden tener graves efectos secundarios. En este contexto, contar con una herramienta in silico que pueda representar con exactitud esta dinámica eléctrico-metabólica sumamente compleja, apoyaría llegado el momento a doctores en la investigación de distintos tratamientos farmacéuticos y en sus políticas de toma de decisiones. Desde un punto de vista matemático, estas mutaciones pueden simularse modificando la conductancia máxima de los canales de K^+ sensibles al ATP y los parámetros en la función de activación de estos canales.

Contents

1 Introduction

> *Research is creating new knowledge.* All organisms
>
> — **Neil Armstrong**

have the ability to maintain a stable internal environment suitable for sustaining life. This ability is called *homeostasis*. Animals have developed numerous physiological mechanisms to be capable of maintaining a condition of equilibrium within its internal environment when dealing with external and different changes. One of these mechanisms is the negative feedback loop involving two hormones, *insulin* and *glucagon*, that allows blood glucose levels to vary within a physiological concentration range. If the glucose level is too high (for example after a meal), the body releases insulin into the bloodstream. The insulin causes the uptake and the storage of glucose by body cells (i.e., muscles and adipose tissue), lowering the concentration of glucose in the blood. If the glucose level is too low (in a fasting state for instance), the insulin level will be low and this causes the release of glucagon which allows the release of glucose from the cells in which it has been stored. Figure 1.1 illustrates this feedback loop.

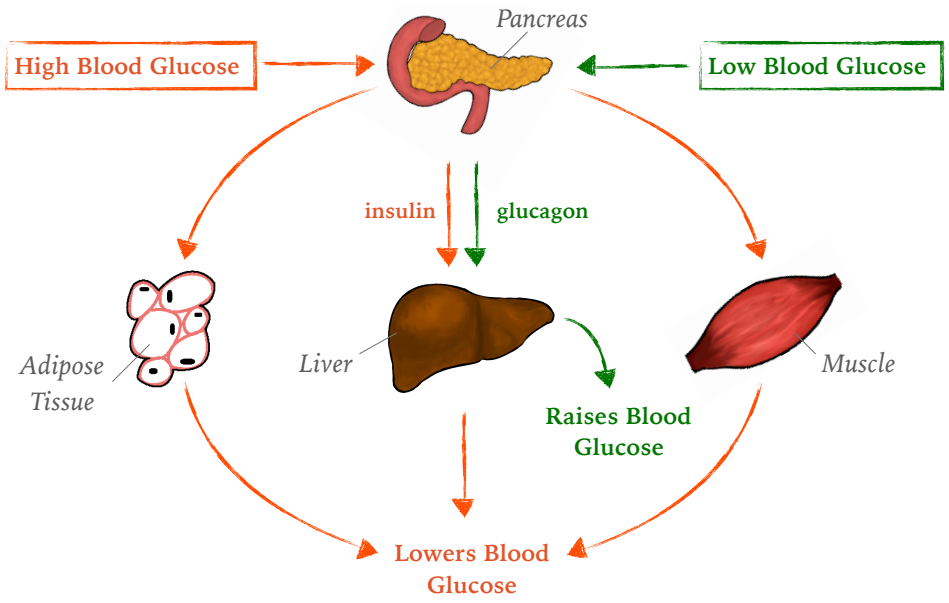

Figure 1.1.: Schematic of the negative feedback loop involving insulin and glucagon hormones.

If this loop is compromised, the body will lose the ability to control the glucose level in the blood and it may cause severe consequences. It occurs, for instance, in the presence of dysfunction or mass reduction of insulin-secreting cells, which results in an abnormal blood glucose level and diabetes [81]. Because of this, pancreatic β-cells (i.e., the only insulin-producing and -secreting cells) have been widely studied in the context of glucose regulation in the body and in relation to diabetes.

The insulin secretion results from the coupling of electrical and metabolic activity within β-cells. More precisely, the hormone is released in a pulsatile fashion, reflecting oscillations in the intracellular calcium concentration that, in turn, result from the cellular bursting activity. Different types of oscillations have been observed in the laboratories: slow oscillations with periods typically between 4 and 6 min, fast oscillations with a period typically between 0.5-2 min, and compound oscillations consisting in a cluster (of several minutes) of fast oscillations repeated with the same range of periods as the slow oscillations. It has been observed that the periods of slow and compound oscillations are consistent with measurements of plasma insulin in mice [69]. Although the knowledge of the dynamics within β-cells is continuously growing, the mechanism underlying these oscillations (and leading to the insulin secretion) is still not fully understood. Two are the main hypotheses: the first is that the oscillations in cytosolic Ca^{2+} concentration drive metabolic oscillations, while the second is that the metabolic oscillations drive the Ca^{2+} oscillations.

In 1983, Chay and Keizer published the first model of β-cell electrical activity [26]. The main aim of that model was to look for an explanation of the β-cell activity, from a mechanistic perspective. From that moment on, several mathematical models have been developed in order to investigate the extremely complex electrical-metabolic dynamics in β-cells and the mechanism underlying the cellular electrical activity [46, 76, 38, 31, 67, 94, 37, 22, 32, 10, 15, 17]. All these models for β-cell oscillations can be organized into two classes according to the mechanism for bursting: a first class of models accounting for Ca^{2+}-driven oscillations (first hypothesis), and a second class of models reproducing metabolic-driven oscillations (second hypothesis).

As new laboratory techniques are developed and new data are acquired, these old models have to be modified to account for the new experimental findings. In 2016, McKenna and collaborators [62] presented an innovative model to describe the dynamics of metabolites in insulin-secreting pancreatic β-cells. This model was called the Integrated Oscillator Model (IOM) and consisted of a physiologically grounded mathematical description based on relevant and available experimental data. To the best of our knowledge, the IOM is the only model accounting for the complete range of oscillation rhythms and all key experimental observations presented in the literature so far. It is also the only model in the literature that puts both perspectives about the nature of the mechanism underlying cellular oscillations

into a common framework. However, it lacks biophysical detail in its description of mitochondrial metabolism and insulin secretion in response of glucose changes.

In this dissertation, we improve the IOM by adding mitochondrial and insulin exocytosis modules, and we use this model to investigate the mechanisms behind the bursting activity that underlie oscillations in intracellular Ca^{2+} concentration and pulsatile insulin secretion. We perform a bifurcation analysis on the glycolytic subsystem to investigate the nature of the metabolic oscillations. This analysis allows us to determine conditions favourable to each type of mechanism. As new experimental observations are collected, the last available IOM is adjusted to account for them. The process results in a continuous evolution of the model, which we present in this thesis. The latest and most comprehensive IOM analyzed in this thesis captures the complex metabolism in the mitochondria and the several biological processes in the insulin exocytosis cascade, as well as the changes in the β-cell activity (and the resulting amount of secreted insulin) in response to different concentrations of glucose in the blood. We also use it to mimic the synchronization of β-cells within an islet through electrical and metabolic coupling.

1.1 Outline

The dissertation is organized as follows. In Chapter 2, we provide an overview of the physiology of pancreatic β-cells. We follow in Chapter 3 with a survey of the most relevant mathematical models that have been developed to describe the activity of β-cells in mice. In particular, we focus on the two classes of models that differ in their hypotheses for what primarily determines the bursting. We pay special attention to the IOM for the behaviour of a β-cell in a synchronized islet; the IOM combines crucial features from both classes of models and in Chapter 4, we present a detailed analysis of its dynamics. One feature that IOM lacks is a detailed description of the mitochondrial metabolism. As such, in Chapter 5, we build on the complexity of the IOM by incorporating detailed descriptions for the dynamics of the mitochondrial metabolism. In Chapter 6, we add further sophistication (and biophysical realism) to the model by incorporating descriptions of the glucose metabolism. Then, in Chapter 7, we suggest a way to distinguish between possible mechanisms underlying the bursting activity. We continue, in Chapter 8, to improve the IOM by including a description of insulin exocytosis. Then, in Chapter 9, we use our sophisticated model to simulate an islet of coupled β-cells. Finally, we summarise our conclusions and present a (partial) list of open questions in Chapter 10.

This dissertation also contains appendices. In Appendix A, we list the equations that constitute some of the mathematical models presented in Chapter 3. In Appendix B we present a general result for the stability of an excitable system used in Chapter 4.

In Appendix C, we give a brief description of the numerical continuation software, AUTO, which was used for the numerical bifurcation analysis throughout the thesis. Finally, in Appendix D, we list the Matlab codes used for the simulations in this thesis.

2 Basic Concepts of Pancreatic β-Cell Physiology

> *Biology is the study of complicated things that have the appearance of having been designed with a purpose.*
>
> **— Richard Dawkins**

2.1 Introduction

This dissertation focuses on biophysical models to describe the dynamics within a pancreatic β-cell. Here, we give a brief overview of the physiology. In this chapter, we describe the pancreas and the region of this organ that contains insulin-secreting β-cells (Section 2.2). We briefly describe the processes involved in the secretion of insulin (Section 2.3), and in the generation of the electrical activity that underlies insulin secretion (Section 2.4). Finally, we discuss type 2 diabetes, a disease that may occur in case of β-cell dysfunction (Section 2.5).

2.2 The Pancreas

The pancreas is a flat, pear-shaped gland located across the back of the abdomen, behind the stomach, in humans. Glands are specialized groups of organs that secrete chemical substances (i.e., hormones), and they fall into two main categories: endocrine and exocrine. Endocrine glands produce and secrete hormones internally into ducts, while exocrine glands secrete hormones directly into the bloodstream. The pancreas is both types of glands. Specifically, it has an exocrine function as part of the digestive system, and an endocrine function in the blood sugar regulation.

As an exocrine gland, the pancreas excretes enzymes that help to break down proteins, lipids, carbohydrates, and nucleic acids in food. This part, which represents more than the 95% of the total pancreas volume, is composed of exocrine glandular tissue and it has two main ducts, namely the *main pancreatic duct* and the *accessory*

pancreatic duct, that drain digestive enzymes through the ampulla of Vater into the duodenum.

As an endocrine gland, the pancreas secretes the hormones *insulin* and *glucagon* to control blood sugar levels. This second portion of the organ, whose volume represents the remaining 5% of the pancreas, is composed of hormonal tissue distributed along the pancreas in discrete irregularly shaped regions called *islets of Langerhans*.

Because of the presence of the two different tissues (glandular and hormonal), the pancreas is classified as a *heterocrine* gland. In this dissertation, we focus on the endocrine role of the pancreas with a special focus on the insulin hormone.

2.2.1 Islets of Langerhans

The islets of Langerhans are regions of the pancreas that contain mixed populations of endocrine cells. They were first described by the German physician Paul Langerhans in 1869. The number of islets in a human pancreas has been recently approximated to be 3.2 million [43]. In the same study, the total islet volume was found to be about 2 cm^3, which corresponds to approximately 4.5% of the total pancreas volume (45 cm^3). Each islet contains many capillaries that carry hormones to the rest of the body. The endocrine cells are classified into 5 types:

- α-cells: produce glucagon, which works to raise the concentration of glucose and fatty acids in the bloodstream
- β-cells: produce insulin, which controls the glucose level in the blood by allowing the cells in the muscles, fat, and liver to absorb it
- δ-cells: produce somatostatin, which inhibits the secretion of several other hormones (for instance growth hormone and insulin)
- γ- or PP- cells: produce pancreatic polypeptide, which acts as a regulator of pancreatic and gastrointestinal functions
- ε-cells: produce ghrelin, which controls appetite and plays an important role in regulating energy homeostasis.

It has been estimated that a human islet contains $\sim$200 β-cells [78], which alone make up more than half of the total number of cells in the islet ($\sim$60%). The second most numerous cells are α-cells ($\sim$30%). The remaining 10% is made up of δ-, γ- (or PP-) cells, and ε-cells [29]. These values differ from species to species, as does

the architecture of the islet itself. For instance, in rodents the β-cells are clustered in the core of the islets and surrounded by the endocrine cell of the other types (Figure 2.1A), unlike in humans where β-cells are contiguous and arranged into smaller clusters surrounded by non-β-cells, and non-β-cells are also found within the islet core (Figure 2.1B) [21, 29, 77].

Despite these differences, rodents are the most used animal models for experiments due to their much easier availability.

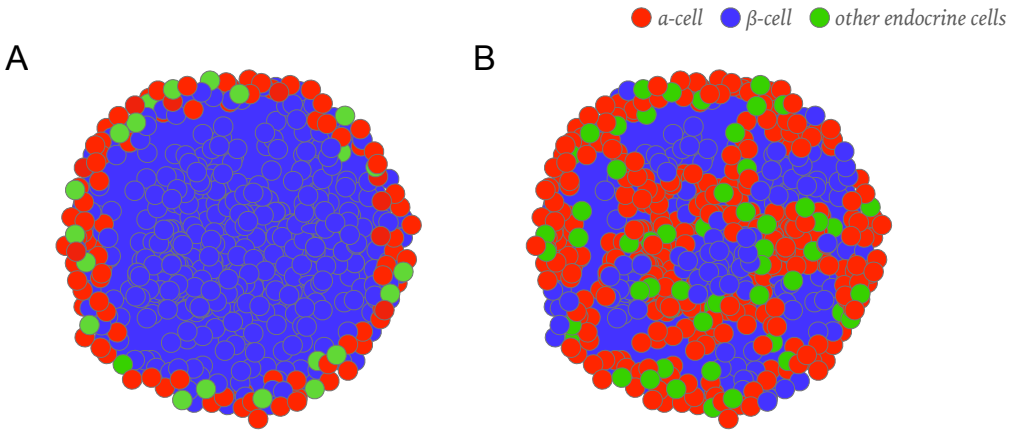

Figure 2.1.: Schematic of the islet architecture in rodent (A) and human (B).

2.3 β-cell Dynamics and Insulin Secretion

β-cells are electrically active cells that have been widely studied in the context of glucose regulation in the body, particularly in diabetes. In fact, they are the only cell type in the body that synthesizes and releases the hormone *insulin* (from Latin *insula*, island) that maintains glucose homeostasis by stimulating the absorption of glucose by muscle, liver, and adipose tissues after any meal.

The secretion of insulin is the result of the β-cell electrical activity in response to stimulatory blood glucose, and it occurs through *exocytosis* (from Ancient Greek *exo-* + *cyto-* +*osis*, out of cell process) in a biphasic matter. The first phase lasts about 10 minutes and is an immediate response to elevated blood glucose. This is followed by a slow sustained second phase lasting for a few hours.

Insulin is released in a multi-step process that is illustrated in Figure 2.2.

1. Blood glucose enters into the cellular cytosol via facilitated diffusion through the GLUT-2 glucose transporter. Here, it is broken down during *glycolysis*. The metabolic products of this process are used in the tricarboxylic acid (TCA)

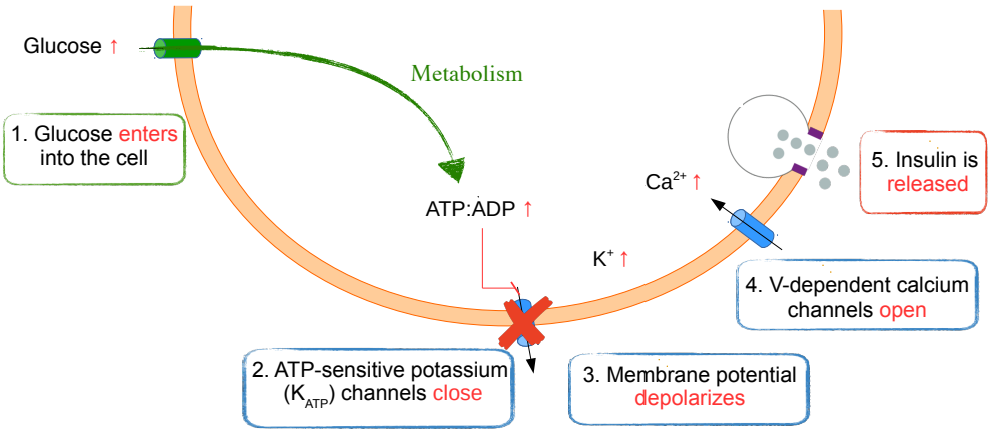

Figure 2.2.: Illustration of the main steps that leads to the insulin exocytosis. We use the same numeration in the text.

cycle (also called Krebs cycle) which, eventually, leads to a rise in the ratio of the adenosine triphosphate (ATP) concentration to the adenosine diphosphate (ADP) concentration. Most ATP is produced during oxidative phosphorylation, which takes place after the TCA cycle.

2. The increase of the ATP/ADP ratio closes the ATP-sensitive potassium (K(ATP)) channels in the plasma membrane.

3. The K(ATP) channels belong to the potassium inwardly-rectifying channel family, and they allow potassium ions to flow out of the cell. When they close, the loss of outward currents leads to a gradual depolarization of the plasma membrane.

4. The membrane depolarization is the condition to open the voltage-dependent calcium (Ca(V)) channels, allowing the calcium ions to flow into the cell.

5. Ca^{2+} that enters the cell leads to exocytosis of the insulin-filled vesicles.

2.4 Bursting Rhythms

The electrical activity of β-cells is characterized by burst episodes that consist of active phases of (Ca^{2+}-carrying) action potentials (i.e., rapid rises and subsequent falls in membrane potential) alternating with silent phases of repolarization. This activity results in oscillations in the cytosolic Ca^{2+} concentration and pulsatile insulin secretion.

The bursting rhythms that have been found in β-cells are classified as slow, fast, or compound. Figure 2.3 illustrates laboratory records of these three rhythms obtained by Ren and Satin and published in [16]. The difference between fast and slow bursts is the duration (about 0.5-2 min for the former and about 4-6min for the latter). On the other hand, compound oscillations consist of fast bursts (usually less than 30 sec in duration) clustered into episodes (duration of several minutes), with each episode separated by a long (2 or 3 minutes) silent phase. Compound oscillations are thus a composition of fast and slow oscillations.

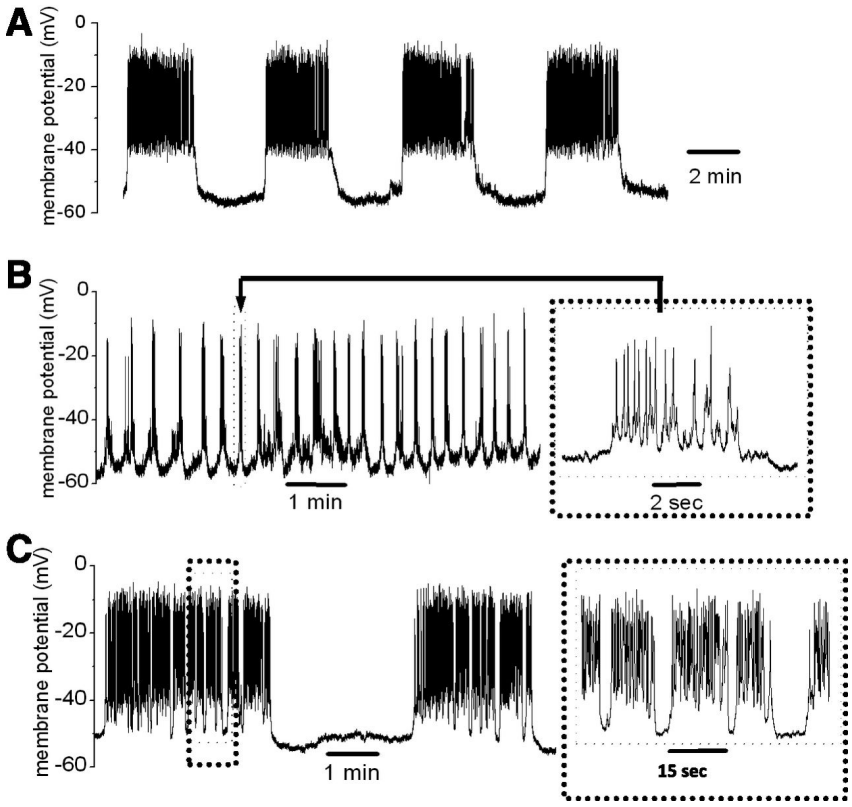

Figure 2.3.: Intracellular electrical recordings from islet β-cells exhibiting three types of oscillations. Example of islet with slow (A), fast (B) and compound (C) oscillations. Recordings were made using perforated patch and amphotericin B. Reprinted with permission from [16].

In this dissertation, we classify a burst as compound if the burst pattern consists of both long and short interburst intervals, and if the ratio of the longest to the shortest interburst interval is greater than 1.25. If the maximum ratio is smaller than 1.25, then the burst is either fast or slow. In our analysis, we set the threshold to 2 min to distinguish between slow and fast bursting. Therefore, the burst will be called fast if the period is shorter than 2 min, and slow otherwise.

2.5 Glucose Concentration in the Blood: Pathological Cases

Pancreatic β-cells are the only cells that synthesize and secrete insulin. Thus, dysfunction or loss of β-cell mass may be responsible for abnormal blood glucose homeostasis. The resulting inappropriate level of insulin in the blood for the actual glucose concentration may lead to pathological cases of extremely low or elevated plasma glucose concentration.

The first condition is called *hypoglycaemia* (from the Latinized form of Greek *hypo*, under, *glykys*, sweet, *haima*, blood) and it is defined as blood sugar that stays below 70 mg/dL ($\sim$3.9 mmol/L) [60]. The second condition is called *hyperglycaemia* (from the Latinized form of Greek *hyper*, above normal, *glykys*, sweet, *haima*, blood) and it is diagnosed when the sugar level in a fasting subject ranges between 100–126 mg/dl ($\sim$5.6-7 mmol/L). Furthermore, if the blood glucose concentration stays above 126 mg/dL ($\sim$7 mmol/l), diabetes is diagnosed.

2.5.1 Diabetes Mellitus

Diabetes (from Ancient Greek *diabainein*, to pass through) is a group of metabolic diseases characterized by hyperglycemia resulting from impaired insulin secretion, insulin action, or both [3]. The first clear and complete description of diabetes was made by the Ancient Greek physician Aretaeus of Cappadocia in the 1st century AD, who used that term as the name for the disease, meaning “excessive discharge of urine" [51] referring to the excessive amounts of urine produced by sufferers. In 1675, the English doctor Thomas Willis added the word mellitus (form Latin word *mellītus*, honey-sweet) as a classification for the disease because of the sweet taste of the urine of a diabetic (condition called *glycosuria*).

The American Diabetes Association classifies diabetes into four general categories [3]:

- Type 1 diabetes, caused by autoimmune β-cell destruction, usually leading to absolute insulin deficiency.

- Type 2 diabetes, caused by a progressive loss of β-cell insulin secretion frequently initiated by insulin resistance, which leads to overwork of β-cells and subsequent cell death.

- Gestational diabetes mellitus (GDM), a form of diabetes diagnosed in the second or third trimester of pregnancy that was not clearly overt diabetes prior to gestation.

- Specific types of diabetes due to other causes. In this category are included monogenic diabetes syndromes, for instance neonatal diabetes and maturity-onset diabetes of the young (MODY), diseases of the exocrine pancreas, including cystic fibrosis and pancreatitis, and drug- or chemical-induced diabetes, such as with glucocorticoid use in the treatment of HIV/AIDS or after organ transplantation.

Among the types of diabetes in the fourth class, one is caused by impaired function of K(ATP) channels due to genetic mutations. This form of diabetes is cause for concern in the clinical field since half of those diagnosed develop permanent diabetes and, in the most severe cases, it may lead to neurological disruptions. We describe this pathology more fully in Section 10.2.

3 The Most Relevant Models in the Literature

> *All models are wrong, but some are useful.*
>
> **— George E. P. Box**

3.1 Introduction

In this chapter, we provide an overview of the most relevant mathematical models presented in the literature to describe β-cell oscillatory behaviour in mice. They are single-cell models formulated to represent a cell in a synchronized islet. We briefly present the history of those models, from the very first to the most recent publications (Section 3.2). Then, we divide the models presented in the last two decades into three schools (Sections 3.3 to 3.5) and we highlight the most important features of each school. A special focus will be placed on the third group of models that represents the starting point for the work presented in this thesis (Section 3.5).

3.2 History

The mathematical models in the β-cell literature can be clustered into two main classes according to the mechanism driving the busting, those in which oscillations in cytosolic Ca^{2+} concentration drive metabolic oscillations (Ca^{2+}-driven oscillations), and those in which intrinsic metabolic oscillations drive oscillations in Ca^{2+} concentration (metabolic-driven oscillations). We refer to the two classes as *Class I* and *Class II*, respectively. Figure 3.1 depicts the active and silent phase process according to the mechanism underlying the burst. In *Class I* (Figure 3.1, left column), the bursting electrical activity is governed by the Ca^{2+} slow negative feedback on intermediate processes. More precisely, during the active phase the cytoplasmic Ca^{2+} concentration increases due to the activation of Ca(V) channels. This leads to the rise of the slow variable (here, representing the intermediate processes), initiating the active phase. During the silent phase, the slow variable decreases, stopping

the spiking activity and initiating the repolarization phase. Eventually, the variable reaches small enough values, allowing the beginning of a new active phase.

In *Class II* (Figure 3.1, right column), intrinsic metabolic oscillations generate oscillations in the ATP concentration and in the ATP/ADP ratio, affecting the conductance of K(ATP) channels. The resulting oscillatory pattern modulates the changes in the membrane potential. This results in metabolism-driven bust activity and Ca^{2+} oscillations.

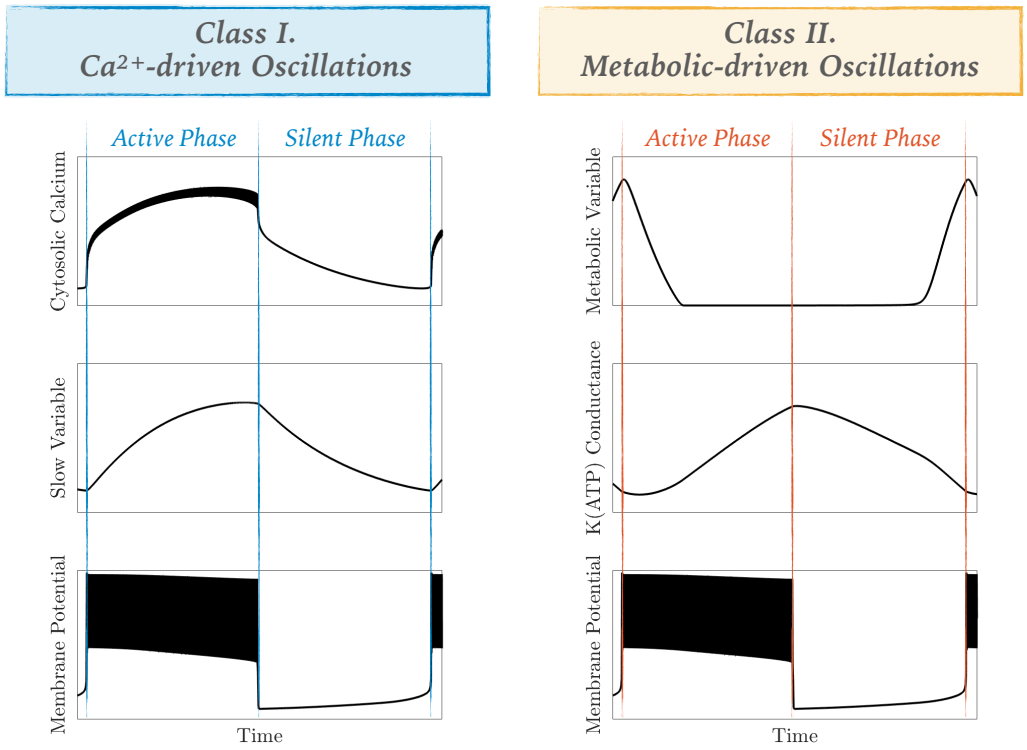

Figure 3.1.: Schematic for the active and silent phase process according the mechanism underlying the burst.

The very first model for electrical bursting in β-cells was published by Chay and Keizer in 1983 [26] and it belongs to *Class I*. It was a simple model describing only the membrane potential and the cytosolic Ca^{2+} dynamics. As β-cells are electrically active, the authors used a Hodgkin-Huxley (or conductance-based) formalism [41, 42] to describe the membrane potential dynamics. The Chay-Keizer model assumes that the bursting is regulated by the slow negative feedback resulting from the action of cytosolic calcium on Ca^{2+}-dependent K^+ (K(Ca)) channels, as it was already hypothesized in [4]. The Chay-Keizer model successfully reproduced fast bursting, the predominant type of oscillations observed at that time, and it was capable of capturing the cellular response to changes in glucose. This model was a pioneer in the β-cell field and it represents a foundation stone for all subsequent models. The Chay-Keizer model, however, provides a burst mechanism that only accounts for fast bursting, and it is not particularly robust to parameter changes.

In the decades following Chay-Keizer, several new models belonging to the first class were presented. These works hypothesized different Ca^{2+} feedback effects to be the mechanism behind cellular oscillations. In 1988, Chay and Cook developed a model in which the voltage-dependent inactivation of the Ca^{2+} current is the primary mechanism driving the bursting [25]. The same idea was later used by Keizer and Smolen [46]. Moreover, in those same years, K(ATP) channels were observed in β-cells. Their fundamental role in the cellular dynamics was immediately clear [1], and the new models started including dynamics of the concentrations of the nucleotides [45, 87, 56]. In these models, the bursting was assumed to be driven by the Ca^{2+} oscillations modulating the ATP/ADP ratio and thus indirectly controlling the K(ATP) channels.

At the end of the 1990s, Chay hypothesized that the Ca^{2+} concentration in the endoplasmic reticulum (ER) is the principal character in the negative feedback. In 1996, she hypothesized that the bursting was driven by the ER calcium acting on the Ca^{2+} release-activated channels [24]. This idea was later used by Roe and collaborators in 1998 [76]. Chay next suggested that the ER Ca^{2+} was responsible for the bursting activity by modulating the effect of the cytosolic calcium on the Ca^{2+} or K^{+} channels [23]. This last hypothesis was taken up by Gall and Susa in 1999 [38]. At about the same time, Detimary and collaborators published an exhaustive analysis on the interaction between the cytosolic Ca^{2+} concentration and the adenine nucleotides in mouse islets [31]. In this paper, the utilization of ATP by Ca^{2+} pumps was hypothesized as the mechanism driving the oscillations. A few years later, Miwa and collaborators published a new model in which the β-cell electrical activity was due to the changes in extracellular Na^{+} and K^{+} concentrations, a hypothesis supported by some later data [67].

All the models belonging to *Class I* can only reproduce fast bursting, not taking into account slow bursting [79] or compound bursting [28, 40]. Because of that, in 1997, Tornheim hypothesized the existence of intrinsic metabolic oscillations that drive Ca^{2+} oscillations [92] and may be responsible for grouping the fast bursts into episodes. This idea was supported by findings that showed the presence in β-cells of the muscle isoform of the allosteric enzyme phosphofructokinase (PFK) [98], which had been demonstrated to be capable of producing glycolytic oscillations [94]. More precisely, PFK catalyzes the phosphorylation of the substrate fructose 6-phosphate (F6P) into fructose 1,6-bisphosphate (FBP). However, FBP has an activating effect on the PFK enzyme. Thus, the more FBP is produced, the more F6P is consumed. When the substrate level is too low, the phosphorylation reaction stops and F6P can build up again, closing the production-consumption loop. With Tornheim's work, the *Class II* of models of metabolic-induced Ca^{2+} oscillations was born.

From this point forward, several mathematical models were published, each more sophisticated and detailed than the last. Some of these models are based on the original Chay-Keizer hypothesis of Ca^{2+}-induced cellular activity, while others inherited Tornheim's hypothesis that intrinsic glycolytic oscillations are responsible for cellular activity.

From a mathematical point of view, the most recent models can be divided into three main schools according to the description of ions and metabolites dynamics. First, the models from the Fridlyand school (2003, [37]) employ the Detimary and Miwa hypotheses [67], and belong to *Class I* of calcium-driven models. Next, the models from the Cha school (2011, [22]) also use the Detimary and Miwa hypotheses [67], and are calcium-driven models. Finally, the models from the Bertram-Satin-Sherman school (2004, [10]) combine features from both *Class I* and *Class II*, and can account for both Ca^{2+}-driven and metabolic-driven bursts, although the starting model was based on the Chay-Keizer model. This division of the models according to their classes and schools is summarized in Figure 3.2. A fourth school could be considered. In 2006, Diederichs presented an independent model based on detailed conversions of chemical reactions into equations [32]. According to the classification introduced above, this model belongs to the class of Ca^{2+}-driven oscillatory activity models. Unfortunately, because of the lack of information on the parameter values, the results shown in [32] could not be reproduced. Because of this, we will not consider this model further in this dissertation.

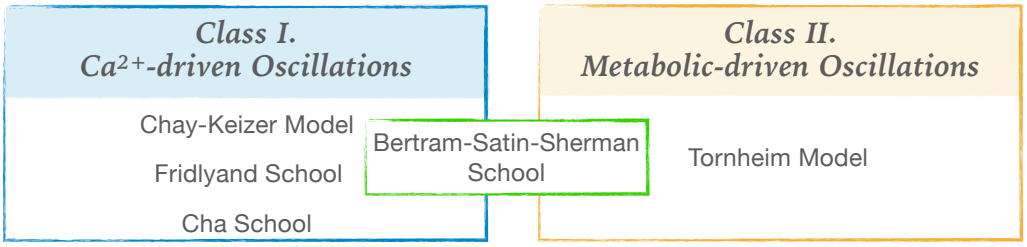

Figure 3.2.: Classification of the modelling schools according to the mechanism underlying the burst.

3.3 Fridlyand School

In this thesis, we are interested in the interaction between metabolism and Ca^{2+} oscillations. Here, we present the two most relevant models from the Fridlyand school, Fridlyand 2003 [37] and Fridlyand 2005 [36]. These models are based on the schematic shown in Figure 3.3.

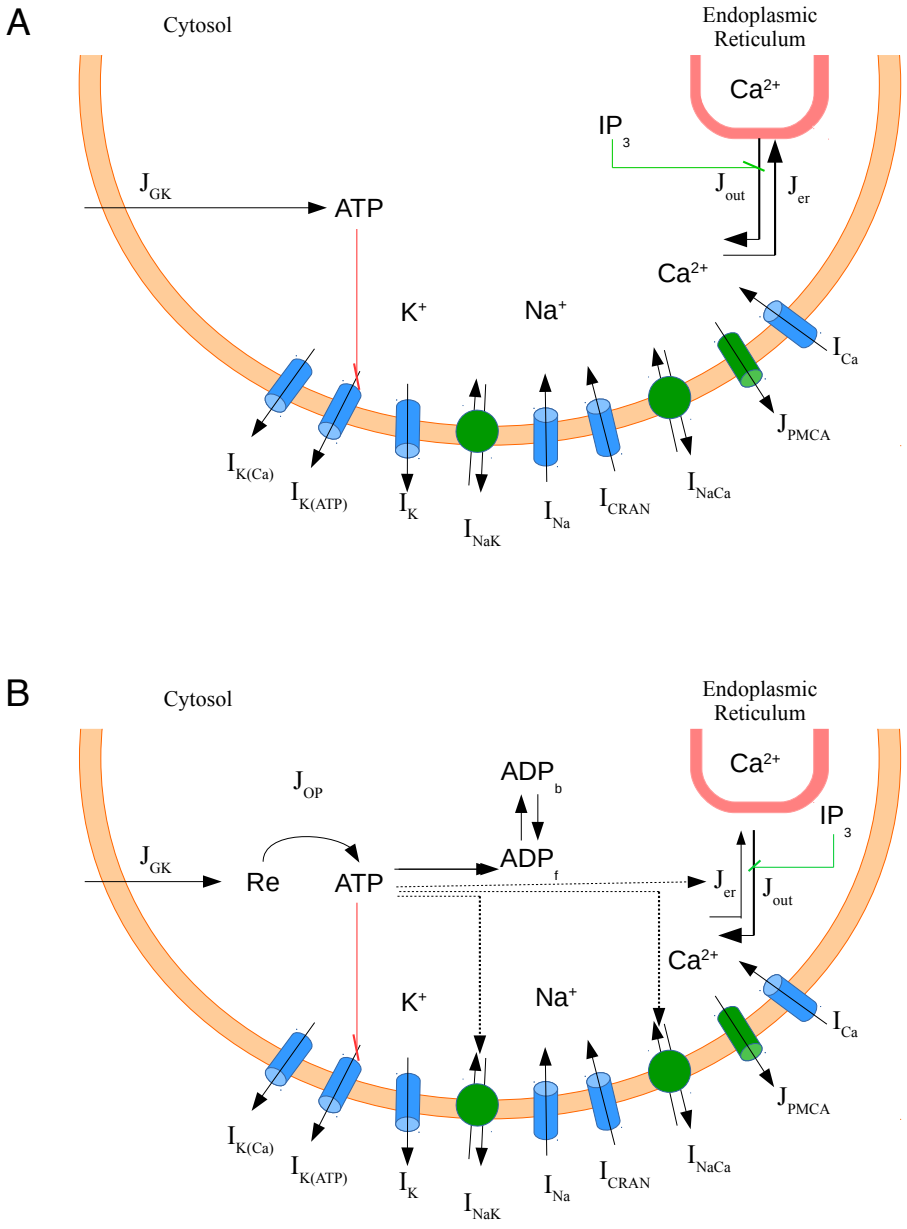

Figure 3.3.: Schematic of the selected models from Fridlyand school: (A) Fridlyand model 2003 [37], (B) Fridlyand model 2005 [36]. I: currents, J: fluxes. See Appendix B for the detailed description of ions and metabolites dynamics.

3.3.1 Fridlyand 2003

The first model we focus on, Fridlyand 2003 [37], is given by a system of seven ordinary differential equations (ODEs) that describe the cellular electrical activity, the calcium in both the cytosol and the endoplasmic reticulum, the cytosolic sodium, and the interactions of these with cytosolic ATP and inositol 1,4,5-trisphosphate (IP_3)

concentrations. No metabolic nor insulin compartments are present. The equations are fully listed in Appendix A.1.1.

A key role in the model is played by Na^+ that is responsible for the slow negative feedback underlying the oscillatory behaviour of the β-cell. More precisely, slow bursting is driven by the increase in Na^+ through the Na^+/Ca^{2+} exchanger as a consequence of the increase in Ca^{2+} concentration when the plasma membrane is depolarized (active phase). This results in a slow increase of the outward current through the Na^+/K^+ pumps, which causes the repolarization of the cellular membrane (silent phase). During this phase, Na^+ decreases and so does I_{NaK}, resulting in the membrane depolarization. On the other hand, fast bursting is driven by the combined action of the Na^+ movements through the Na^+/K^+ pump and the endoplasmic calcium-regulated current. Figure 3.4 shows representative time series obtained from the Fridlyand 2003 model. According to the burst rhythm classification (Section 2.4), this behaviour corresponds to a fast bursting.

The Fridlyand 2003 model was a first attempt to describe the activity of β-cells by tracking the ion dynamics through channels and pumps on both plasma and endoplasmic reticulum membranes. The driving force of the burst is attributed to the dynamics of Na^+ concentration and its role as a modulator in the Na^+/Ca^{2+} exchanger or Na^+/K^+ pump.

However, the bursts obtained with this model (Figure 3.4 left panel) do not resemble the bursts observed experimentally in β-cells. Also, it lacks a proper description of the glucose-dependent ATP production. The changes in the glucose level are simulated by varying the parameter k_{ADP} in the ATP dynamics (see Eq. (A.28) in the Appendix A.1.1), without considering the intermediate steps that bring about ATP production.

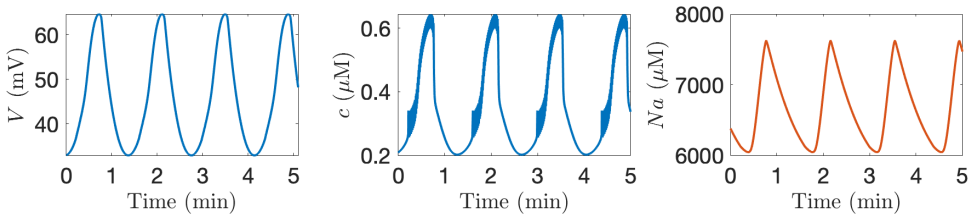

Figure 3.4.: Time series of the membrane potential, V, cytosolic Ca^{2+}, c, and Na^+, Na generated by the Fridlyand model 2003, with k_{ADP}=0.0004 ms. The cell is in a fast bursting mode.

3.3.2 Fridlyand 2005

To overcome the limitation of their first model, Fridlyand and collaborators presented an extension of their model [36] which we refer as the Fridlyand 2005 model. This new model takes into account the effect of cellular respiration and glucose consumption on ATP production. In particular, the list of model variables now includes the concentration of intermediate metabolism and the cytosolic free and bound ADP. Thus, the Fridlyand 2005 model consists of ten ODEs and is shown in Appendix A.1.2.

Once again, the nature of the mechanism driving the bursting is not metabolic and it is based on the changes of Na^+ concentration. The resulting Ca^{2+} oscillations are considered as drivers of the metabolic oscillations. Figure 3.5 illustrates an example of fast bursting simulated with the current model. As in Fridlyand 2003, the bursting does not resemble experimental recordings.

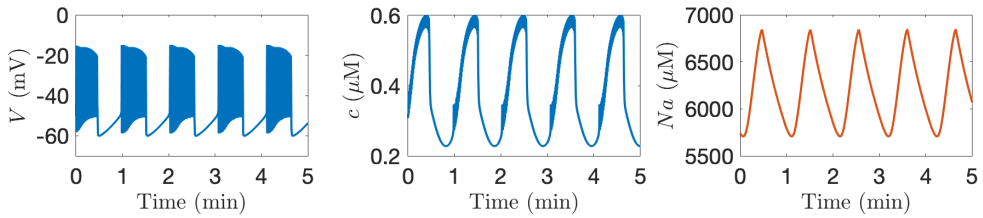

Figure 3.5.: Fast bursting in the Fridlyand 2005 model, with G=8 mM.

3.4 Cha School

The second school we analyze in this thesis is Cha's. In 2011, Cha *et al.* published a model to investigate the mechanism underlying the bursting activity in β-cells [22]. This model was used some years later by Silva *et al.* [85] to simulate a whole pancreatic islet and to investigate the effect of some specific genetic mutations on the cellular activity.

3.4.1 Cha 2011

The model presented by Cha and collaborators is very complex and describes the membrane potential, Ca^{2+}, Na^+, and K^+ ion concentrations, and metabolic variables, such as ATP and reduced metabolites (Re). The model consists of 18 ODEs, which reflects the higher complexity. Unlike the models in Section 3.3, the activation/inactivation gate variables are described by ordinary differential equations. The complete set of equations is given in Appendix A.2.1, while in Figure 3.9 we provide

a schematic representation of the model.

As in the Fridlyand models, the authors identify the Na^+/K^+ pumps as a first mechanism to trigger the bursting activity. This results in a Na^+ intracellular accumulation that in turn activates the Na^+/Ca^{2+} exchanger. However, it is not the only one. In the paper, it was hypothesized that there may be a combination of factors that may modulate the bursting rhythm in β-cells.

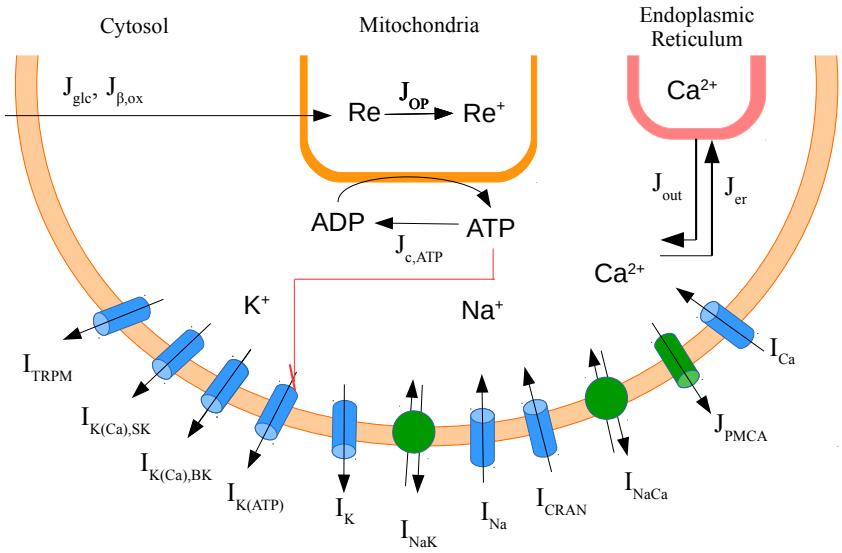

Figure 3.6.: Schematic of the selected model from Cha school: Cha 2011 [22]. I: currents and J: fluxes.

The model presented by Cha and collaborators is based on the pivotal idea of coupling the electrical activity of the cellular membrane with metabolism (as already used by Fridlyand *et al.*). It provides a very detailed description of ionic currents. Also, it takes into account new currents (never used before) strongly supported by experimental findings. In the paper, it is shown that the model can account for the cellular response to changes in the glucose level.

As demonstrated in Figure 3.7, the fast bursting generated by the Cha 2011 β-cell model reproduces the real bursting pattern (unlike the models from the Fridlyand school).

The slow feedback underlying the busting activity was found in the Na^+ modulation of the turnover in the Na^+/K^+ exchanger. It was also suggested that the oscillatory activity in the cell was due to the cytosolic Ca^{2+} acting on the I_{PMCA}, I_{NaCa}, I_{TRPM}, and $I_{\mathrm{K(Ca),SK}}$, or on the ER Ca^{2+} concentration through I_{SOC}. However, the evidence

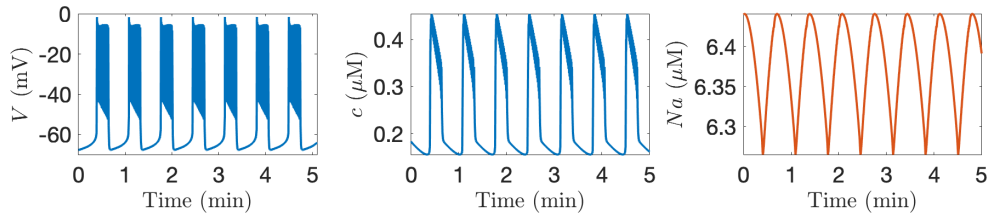

Figure 3.7.: These plots show cytosolic Ca^{2+}, c, and Na^{+}, Na, time courses with the Cha model with G=11 mM. The cell is in a fast bursting mode.

supporting these hypotheses were a few or very parameter-dependent.

Despite its successes, the Cha 2011 β-cell model lacks a detailed description of the metabolic compartment. Furthermore, the Ca^{2+} influence on ATP production is not taken into account.

3.4.2 Silva 2014: Cell-to-Cell Coupling

In 2014, Silva used the Cha single-cell model to simulate a whole pancreatic islet and to investigate genetic mutations affecting K(ATP) channels [85].

In the study, the authors considered two grid-shaped islets of $4\times4\times4$ and $10\times10\times10$ cells each (Figure 3.8). The cell-cell coupling was obtained by adding a gap junction current between neighbouring β-cells in the islet (see Appendix A.2.2).

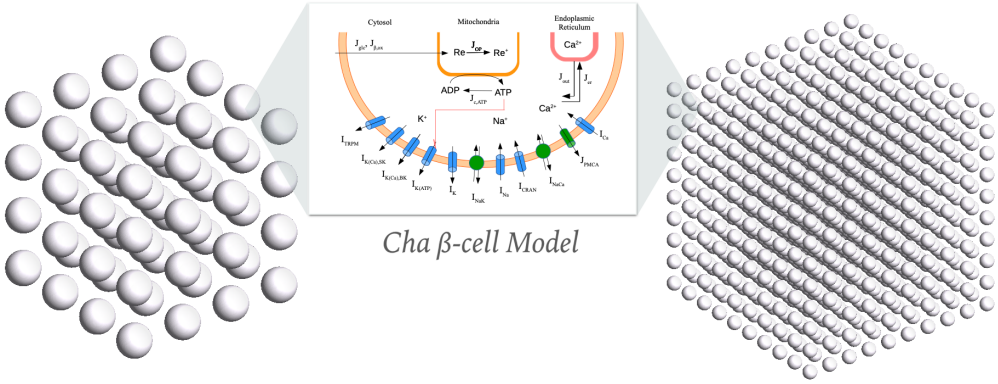

Figure 3.8.: Schematic of the the islets used by Silva and collaborators [85]. Each β-cell in the virtual islets is simulated implementing the model proposed by Cha [22].

The genetic mutations simulated in the paper were: the dominant-negative Kir6.2[AAA] and the gain-of-function (GOF) Kir6.2[ΔN30] or Kir6.2 [ΔN30, K185Q]. The first mutation affects only a subset of β-cells in the islet, which has no measurable K(ATP) conductance. In the model, the conductance $G_{K(ATP)}$ is set to zero in 50% of cells

(randomly chosen). The authors showed that the cells can overcome this impediment because of the gap junction coupling. Furthermore, if the randomness was increased and the proximity of the cell with a similar phenotype was reduced, the bursting activity could still be restored as long as the glucose concentration increased. On the other hand, GOF mutations affect the K(ATP) channels by reducing their ATP sensitivity, and they often result in neonatal diabetes. The authors simulate GOF mutations by decreasing the ATP affinity in up to 25% of β-cells of an islet. Interestingly, the β-cells are still electrically active because of the gap junctions. However, the stimulatory glucose range shifts and its values increase proportionally to the reduction of the ATP sensitivity.

The use of β-cells clusters proposed by Silva *et al.* allows predictions on the cell behaviour in the case of some specific genetic mutations. Unfortunately, there are some experimental findings in the busting behaviour that this model cannot account for. The first limitation is that the interburst interval does not decrease when the glucose concentration is raised. Moreover, the model cannot replicate slow bursting.

3.5 Bertram-Satin-Sherman School

The last family of models comes from the Bertram-Satin-Sherman school. We study 5 β-cells models developed by this school in detail. The first model, called the Biophan model, was published in 2004 [10] and it is part of the so-called "phantom bursters" family. The second model we describe belongs to the same family and it is called the Dual Oscillator Model (DOM). The following two models are extensions or improvements of the DOM. Finally, the last model of this school we discuss is the Integrated Oscillator Model (IOM) which presents an even more sophisticated bursting mechanism. Figure 3.9 depicts the schematic of the four most significant models of the selected five.

Several β-cell models had been developed before the Biophan model [13, 19, 11] (the first β-cell phantom bursting model was published in 1995, a decade before Biophan). However, none of these models accounted for metabolic changes. Thus, we identify the Biophan model as the seminal β-cell model as it was the first model to include all of the key elements (electrical and metabolic) of the bursting activity that will be taken up and improved in the next works.

As already mentioned in Section 3.2, most of the models in this family belong to both classes (Ca^{2+}-driven metabolic oscillations and metabolic-driven Ca^{2+} oscillations), unlike the Fridlyand models or the Cha models.

In the remainder of this Chapter, we study the main features of (and list the equations for) the 5 Bertram-Satin-Sherman β-cell models (Biophan, DOM 1.0, DOM1.5, DOM2.0, and IOM), which will be used later in this thesis.

3.5.1 Biophan Model

The Biophan model presented in 2004 [10] is a calcium-based phantom bursting model and is based on the Chay-Keizer β-cell model [26]. In Bertram's formulation, two slow variables, the endoplasmic reticulum Ca^{2+} and the cytosolic nucleotides ratio, and a revisited cytosolic Ca^{2+} dynamics are added to the minimal Chay-Keizer model to account for the experimental findings that could not be replicated with the original model.

In this model, the bursting activity results from a "phantom" effect of the interaction of the two slow variables with the faster electrical variables. Hence, "phantom bursting" reflects the fact that the slow variables can produce bursting with period very different from that of the time scale for either slow variable individually. The model consists of a single module for the cell electrical activity and Ca^{2+} dynamics. The only metabolic variable is the ratio ADP/ATP that bridges the gap between the glucose concentration (not present) and the fraction of open K(ATP) channels. In this work, the burst is modulated by the Ca^{2+} feedback onto K(Ca) and K(ATP) channels. Therefore, the model belongs to the class of Ca^{2+}-driven metabolic oscillations.

Mathematical Model

As in Chay-Keizer paper, the Biophan model consists of a conductance-based model, and the membrane potential, V, is described by

$$\frac{dV}{dt} = -\frac{1}{C}\left[I_{\mathrm{Ca}} + I_{\mathrm{K}} + I_{\mathrm{K(Ca)}} + I_{\mathrm{K(ATP)}}\right] , \tag{3.1}$$

where C is the membrane capacitance, I_{Ca} is a Ca^{2+} current, I_{K} is a delayed-rectifying K^+ current, $I_{\mathrm{K(Ca)}}$ is a Ca^{2+}-activated K^+ current, and $I_{\mathrm{K(ATP)}}$ is a K^+ current that is deactivated by ATP.

The expressions for these currents are:

$$I_{\mathrm{Ca}} = g_{\mathrm{Ca}} m_\infty(V)(V - V_{\mathrm{Ca}}) , \tag{3.2}$$

$$I_{\mathrm{K}} = g_{\mathrm{K}} n (V - V_{\mathrm{K}}) , \tag{3.3}$$

$$I_{\mathrm{K(Ca)}} = g_{\mathrm{K(Ca)}} q_\infty(c)(V - V_{\mathrm{K}}), \tag{3.4}$$

$$I_{\mathrm{K(ATP)}} = g_{\mathrm{K(ATP)}} a (V - V_{\mathrm{K}}) , \tag{3.5}$$

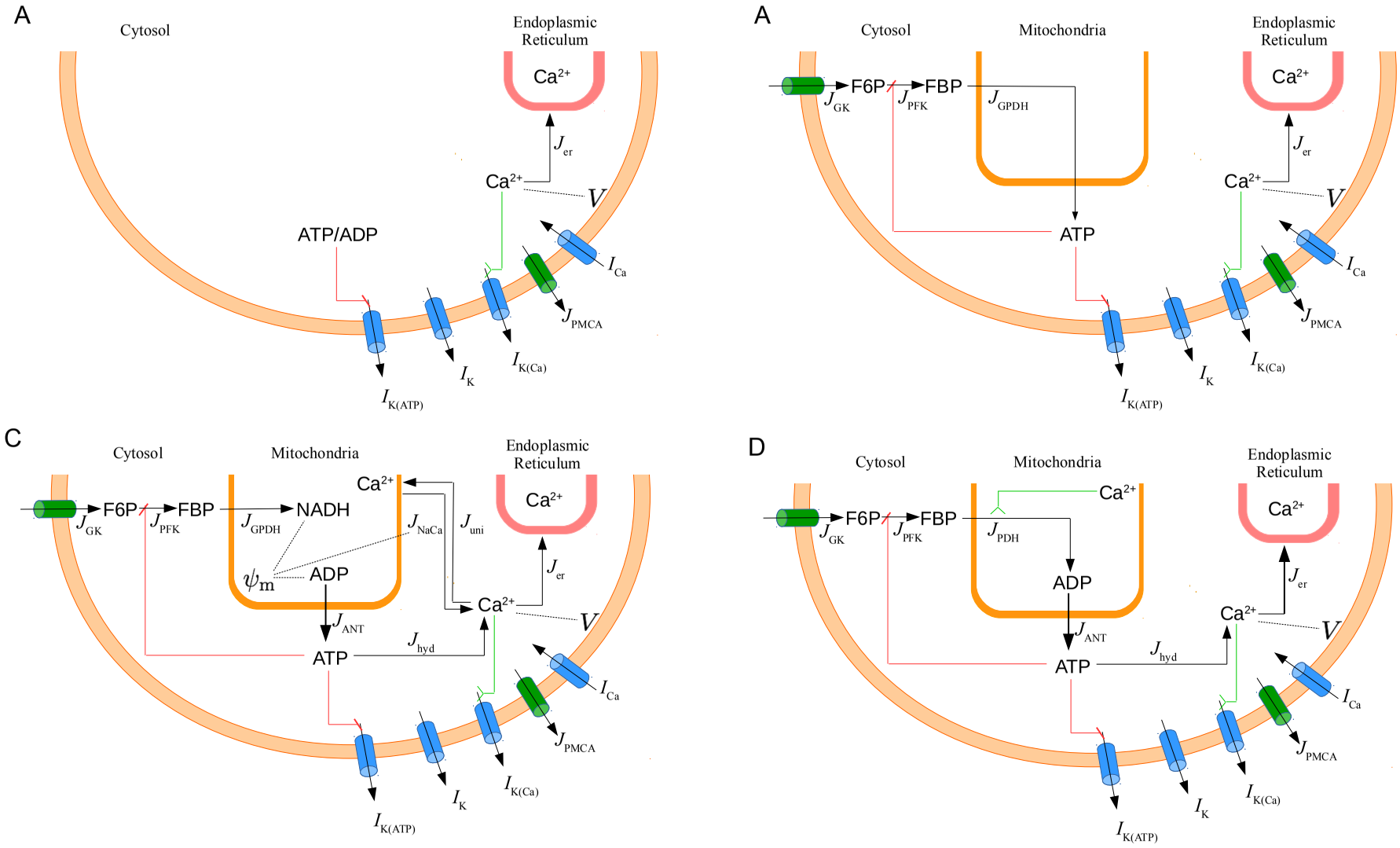

Figure 3.9.: Schematic of the selected models from the Bertram school: (A) Biophan model [10], (B) DOM 1.0 [15], (C) DOM2.0 [17], (D) IOM [62]. I: currents. J: fluxes. GK: glucokinase. PFK: phosphofructokinase. PDH=phosphate dehydrogenase. GPDH: glycerol-3-phosphate dehydrogenase. ANT: adenine nucleotide translocator. hyd: hydrolysis. uni: uniporter. PMCA: plasma membrane Ca^{2+} ATPase. NaCa: Na^{+}-Ca^{2+} exchanger. V and ψ_{m}: cellular and mitochondrial membrane potential respectively. The red and green lines represent negative and positive feedbacks respectively. The red and green lines represent negative and positive feedback, respectively.

where a is the ratio ADP/ATP. The parameters g_i with $i \in \{\text{Ca, K, K(Ca), K(ATP)}\}$ represent maximal conductances of the corresponding currents, while V_{Ca} and V_{K} are the Ca^{2+} and K^+ Nernst potentials, respectively. Table 3.1 gathers the values for all the parameters presented in the model.

The activation of Ca^{2+} current, m_∞, is voltage-dependent and it is assumed to be at the equilibrium:

$$m_\infty(V) = \frac{1}{1 + \exp[(\nu_m - V)/s_m]} \, . \tag{3.6}$$

The increasing sigmoid function is shaped by the parameters ν_m and s_m.

The rapid equilibrium assumption is made for the Ca^{2+}-dependent activation of K(Ca) current, $q_\infty(c)$:

$$q_\infty(c) = \frac{c^5}{K_d^5 + c^5} \, , \tag{3.7}$$

where the variable c represents the cytosolic Ca^{2+} concentration.

On the other hand, the activation of the delayed rectifying K^+ current, n, has the first-order kinetics

$$\frac{dn}{dt} = \frac{n_\infty(V) - n}{\tau_n} \, , \tag{3.8}$$

where $n_\infty(V)$ is again a sigmoid of the form Eq. (3.6), but with shape parameters ν_n and s_n.

The free calcium concentration in the cytosol, c, and in the endoplasmic reticulum, c_{er}, are described by

$$\frac{dc}{dt} = f_{\text{Ca}}(J_{\text{mem}} - J_{\text{er}}) \, , \tag{3.9}$$

$$\frac{dc_{\text{er}}}{dt} = f_{\text{Ca}} \sigma_{\text{er}} J_{\text{er}} \, , \tag{3.10}$$

where J_{mem} and J_{er} are the Ca^{2+} flux across the plasma and ER membranes, respectively, the expression of which is given by

$$\begin{aligned} J_{\text{mem}} &= -\left[\frac{\alpha}{V_{\text{cyt}}} I_{\text{Ca}} + k_{\text{PMCA}} c\right] \, , \\ J_{\text{er}} &= k_{\text{SERCA}} c - p_{\text{leak}}(c_{\text{er}} - c) \, . \end{aligned} \tag{3.11}$$

The dynamics of the nucleotide ratio, a, is given by a first-order kinetic equation

$$\frac{da}{dt} = \frac{a_\infty(c) - a}{\tau_a} \, , \tag{3.12}$$

Parameter	Value	Parameter	Value
C	5300 fF	K_d	0.5 μM
g_{Ca}	1000 pS	f_{Ca}	0.01
g_{K}	2700 pS	σ_{er}	31
$g_{\mathrm{K(Ca)}}$	varies	α	5.18×10^{-18} μmol fA^{-1} ms^{-1}
$g_{\mathrm{K(ATP)}}$	25000 pS	V_{cyt}	1.15×10^{-12} l
V_{Ca}	25 mV	k_{PMCA}	0.2 ms^{-1}
V_{K}	-75 mV	k_{SERCA}	0.4 ms^{-1}
ν_m	-20 mV	p_{leak}	2×10^{-4} ms^{-1}
s_m	12 mV	s_a	0.1 mV
ν_n	-16 mV	τ_a	3×10^{4} sec
s_n	5 mV	r	varies
τ_n	20 ms		

Table 3.1.: Parameters for the Biophan model [10].

where the equilibrium function $a_\infty(c)$ is an increasing sigmoidal function of cytosolic calcium

$$a_\infty(c) = \frac{1}{1+\exp[(r-c)/s_a]} \,. \tag{3.13}$$

The parameter r reflects the glucose influence into the ATP/ADP ratio. For instance, r=0 μM represents a glucose-free scenario, while r=0.14 μM corresponds to a mid-low glucose concentration.

Comments

Due to the two slow variables and the action of Ca^{2+} on K(Ca) and on K(ATP), the Biophan model can overcome some of the limitations shown by the Chay-Keizer model. For instance, the range of burst rhythms it can produce is extended and the model can account for both slow and fast bursting (Figure 3.10).

Despite the important accomplishment, the model still presents some limitations. For instance, the metabolic compartment is minimal. The only metabolic variable considered in the model is the ratio ATP/ADP that depends on glucose through the r parameter.

3.5.2 Dual Oscillator Model 1.0

The second model we analyze is the Dual Oscillator Model (DOM) [15]. The name "dual oscillator" comes from the fact that this model consists of two compartments: the β-cell electrical activity and Ca^{2+} dynamics module (electrical oscillator, EO), and the glycolytic component (glycolytic oscillator, GO). Because of the interaction

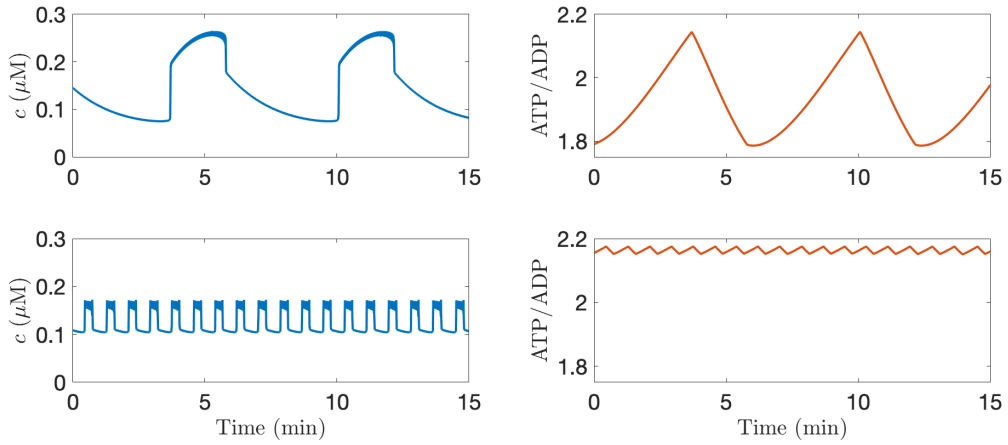

Figure 3.10.: Representative slow (top row) and fast (bottom row) bursting rhythm. These plots show cytosolic Ca^{2+} and ATP/ADP time courses with the Biophan model with r=0.14. In the top row $g_{K(Ca)}$=10 pS; in the bottom row $g_{K(Ca)}$=700 pS.

of these two oscillators, the diverse bursting patterns observed in β-cells can be reproduced. In particular, the EO drives fast bursting (Ca^{2+}-driven oscillations) while the GO governs slow bursting (Ca^{2+}-independent).

Being the first model to consider EO and GO, we will refer to this DOM as the DOM1.0.

Mathematical Model

The membrane potential and Ca^{2+} dynamics are described by Eqs. (3.1) to (3.11) of the Biophan model. The only change is in the Hill coefficient in the expression for $q_\infty(c)$ that here becomes

$$q_\infty(c) = \frac{c^2}{K_d^2 + c^2} \,. \tag{3.14}$$

The value of K_d stays unchanged.

The major difference between the Biophan model and the DOM1.0 lies in the metabolic module. The nucleotide ratio a of the Biophan model is now replaced by more complex ADP dynamics that directly depend on the glycolytic process.

Following the same hypothesis presented by Smolen in 1995 [86], the basis for oscillations in glycolysis is found in the allosteric enzyme phosphofructokinase (PFK) that converts the substrate fructose 6-phosphate (F6P) into fructose 1,6-bisphosphate (FBP) during the phosphorylation. More specifically, FBP feeds back onto the PFK leading to substrate (F6P) depletion, which lowers the reaction rate. When F6P

level increases again, the process restarts. This metabolic process is assumed to be responsible for the glycolytic oscillations. The corresponding ODEs to describe the F6P and FBP are

$$\begin{aligned} \frac{d\mathrm{F6P}}{dt} &= 0.3\left(J_{\mathrm{GK}} - J_{\mathrm{PFK}}\right) \ , \\ \frac{d\mathrm{FBP}}{dt} &= J_{\mathrm{PFK}} - \frac{1}{2}J_{\mathrm{GPDH}} \ , \end{aligned} \tag{3.15}$$

where J_{GK} is the constant glucose-dependent glucokinase (GK) reaction rate, J_{PFK} is the PFK reaction rate, and J_{GPDH} is the glycerol-3-phosphate dehydrogenase (GPDH) reaction rate. J_{PFK} is defined as in [86]:

$$J_{\mathrm{PFK}} = v_{\mathrm{PFK}} \frac{w_{1110} + k_{\mathrm{PFK}} \sum_{i,j,l\in\{0,1\}} w_{ij1l}}{\sum_{i,j,k,l\in\{0,1\}} w_{ijkl}}, \tag{3.16}$$

with weights

$$w_{ijkl} = \frac{\left(\mathrm{AMP}/K_1\right)^i \left(\mathrm{FBP}/K_2\right)^j \left(\mathrm{F6P}^2/K_3\right)^k \left(\mathrm{ATP}^2/K_4\right)^l}{f_{13}^{ik} f_{23}^{jk} f_{41}^{il} f_{42}^{jl} f_{43}^{kl}}, \tag{3.17}$$

where the adenosine monophosphate (AMP) is given by $\mathrm{AMP} = \frac{\mathrm{ADP}^2}{\mathrm{ATP}}$, since the adenylate kinase reaction, which converts two molecules of ADP to one of AMP and one of ATP, is assumed to be at equilibrium. The parameters are shown in Table 3.2. On the other hand, the GPDH reaction rate J_{GPDH} is described by

$$J_{\mathrm{GPDH}} = 0.2\sqrt{\mathrm{FBP}} \ . \tag{3.18}$$

Thus, cytosolic ADP is described by

$$\frac{d\mathrm{ADP}}{dt} = \mathrm{ATP} - \mathrm{ADP}\exp\left[\left(1 + 2.2\frac{J_{\mathrm{GPDH}}}{10 + J_{\mathrm{GPDH}}}\right)\left(1 - \frac{c}{0.35}\right)\right] , \tag{3.19}$$

where $\frac{J_{\mathrm{GPDH}}}{10+J_{\mathrm{GPDH}}}$ represents the glycolytic input. Finally, the total nucleotide concentration, A_{tot}, is assumed constant, so that the intracellular ATP concentration is given by

$$\mathrm{ATP} = \frac{1}{2}\left[A_{\mathrm{tot}} + \sqrt{-4\mathrm{ADP}^2 + (A_{\mathrm{tot}} - \mathrm{ADP})^2} - \mathrm{ADP}\right] \ . \tag{3.20}$$

Comments

The interaction of the two mechanisms for oscillations in β-cells (EO and GO) further extend the range of bursting rhythm. In addition to slow and fast bursting (already reproducible by the Biophan model), the DOM1.0 can simulate compound

Parameter	Value	Parameter	Value
J_{GK}	0.002 μM ms^{-1}	f_{13}	0.02
v_{PFK}	0.01 μM ms^{-1}	f_{23}	0.2
k_{PFK}	0.06	f_{41}	20
K_1	30 μM	f_{42}	20
K_2	1 μM	f_{43}	20
K_3	5×10^4 μM^2	τ_a	3×10^5
K_4	10^3 μM^2	A_{tot}	3×10^3 μM

Table 3.2.: Parameters for the metabolic module in the DOM1.0 [15].

bursting (Figure 3.11) that is possible only if the glycolytic subsystem modulates the burst. Furthermore, the model can account for other experimental findings not reproducible with the other models. For instance, the so-called "accordion bursting" and subthreshold oscillations in the membrane potential and Ca^{2+} concentration. The first occurs when the glycolytic subsystem is oscillating but the K(ATP) current is not high enough to turn off the electrical activity between two pulses of FBP. The second occurs when the glycolytic oscillator is on, but the K(ATP) current is too high to support electrical activity.

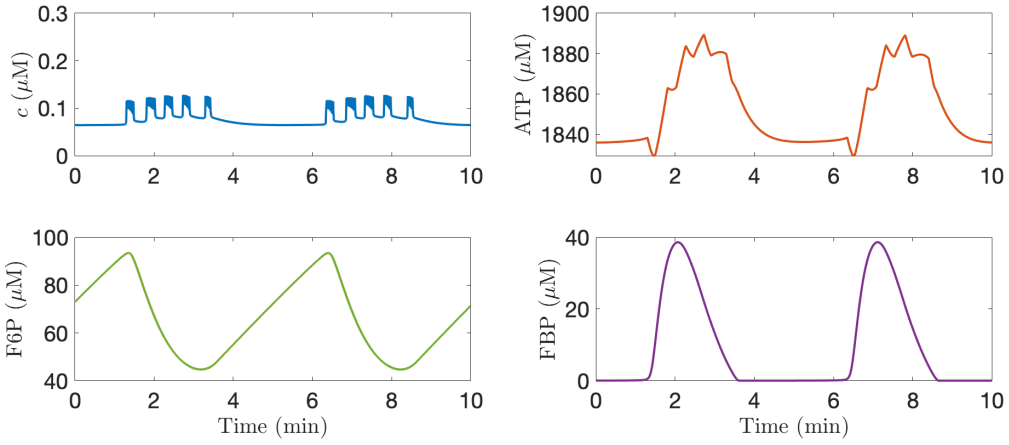

Figure 3.11.: Representative compound bursting rhythm. These plots show cytosolic Ca^{2+}, ATP, F6P, and FBP time courses with the DOM1.0 with $g_{\mathrm{K(ATP)}}$=25000 pS; $g_{\mathrm{K(Ca)}}$=600 pS.

3.5.3 Dual Oscillator Model 1.5

A second version of the Dual Oscillator Model was presented in 2014 [97] and can be considered the first step toward a more realistic model since it accounts for the dynamics of mitochondria. The mitochondria are organelles that play a key role in any cellular activity since it is where the ATP is mainly produced. Furthermore, the ADP conversion into ATP process, which occurs in the organelle, is regulated by the

mitochondrial membrane potential that, thus, indirectly modulates the nucleotide concentrations in the cytosol as well.

As this model is essentially an extension of the DOM1.0, we refer to it as the DOM1.5.

Mathematical Model

The mathematical model is given by the same set of ODEs described for the DOM1.0 (see Section 3.5.2). Only the dynamics of the nucleotides have been modified. More precisely, instead of Eq. (3.19) the ODE governing the cytosolic ADP concentration is now

$$\frac{d\mathrm{ADP}}{dt} = J_{\mathrm{hyd}} - \delta J_{\mathrm{ANT}} \,, \tag{3.21}$$

where δ is the mitochondrial/cytosolic volume ratio, J_{hyd} is the hydrolysis rate, and J_{ANT} is the flux through the adenine nucleotide transporter (ANT) exchanging mitochondrial ATP for cytosolic ADP. Thus,

$$J_{\mathrm{hyd}} = (k_{\mathrm{hyd}} c + k_{\mathrm{hyd,bas}})\mathrm{ATP} \,, \tag{3.22}$$

$$J_{\mathrm{ANT}} = p_{19} \frac{\frac{\mathrm{ATP_m}}{\mathrm{ADP_m}}}{\frac{\mathrm{ATP_m}}{\mathrm{ADP_m}} + p_{20}} \exp\left(\frac{\mathrm{F}}{2\mathrm{RT}}\,\psi_{\mathrm{m}}\right) . \tag{3.23}$$

The term ψ_{m} represents the mitochondrial membrane potential, here assumed to be constant, while $\mathrm{ADP_m}$ and $\mathrm{ATP_m}$ are the adenosine di- and tri-phosphate concentrations in the mitochondria, respectively. The parameter values are shown in Table 3.3.

In this model, $\mathrm{ADP_m}$ is set to equilibrium and is described by

$$\mathrm{ADP_m} = q_2 \exp\left(-\frac{J_{\mathrm{GPDH}}}{5}\right) , \tag{3.24}$$

where J_{GPDH} is the GPDH reaction rate defined in Eq. (3.18). The total nucleotide concentrations in the mitochondria, $A_{\mathrm{tot,m}}$, is assumed to be constant. Hence,

$$\mathrm{ATP_m} = A_{\mathrm{tot,m}} - \mathrm{ADP_m} \,. \tag{3.25}$$

Comments

The most significant achievement of the DOM1.5 is the introduction of mitochondrial dynamics in the model (Figure 3.12). Also, the authors perform an accurate analysis

Parameter	Value	Parameter	Value
δ	0.0733	p_{20}	2
k_{hyd}	$5{\times}10^{-5}$ μM ms^{-1}	$\frac{\mathrm{F}}{\mathrm{RT}}$	0.037
$k_{\mathrm{hyd,bas}}$	$5{\times}10^{-5}$ μM ms^{-1}	ψ_{m}	164 mV
p_{19}	0.35	q_2	12700

Table 3.3.: Parameters for the metabolic module in the DOM1.5 [97].

of the model providing regions of the parameter space in which metabolic oscillations are Ca^{2+}-dependent and others in which they persist although Ca^{2+} is clamped.

However, the mitochondrial dynamics introduced by the DOM1.5 is very simplistic and accounts only for the nucleotide concentration that is at equilibrium.

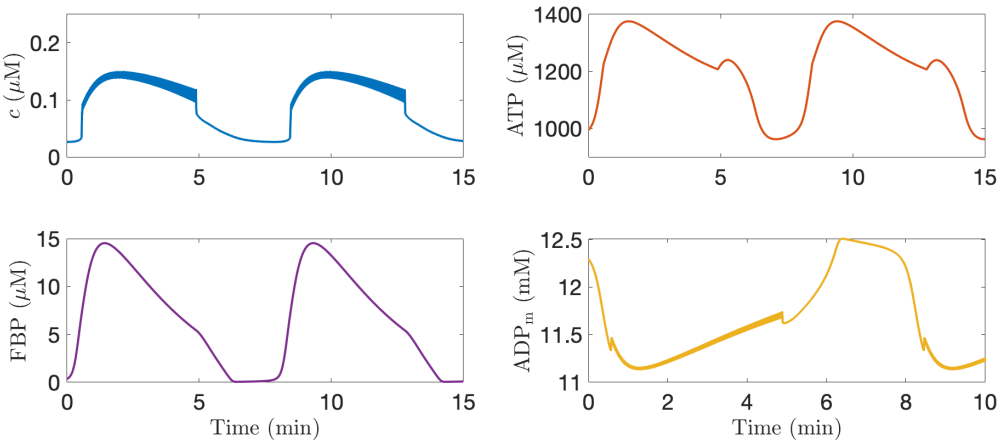

Figure 3.12.: Representative slow bursting rhythm. These plots show cytosolic Ca^{2+}, ATP, FBP, and ADP_m time courses with the DOM1.5 with $g_{K(ATP)}$=17000 pS; $g_{K(Ca)}$=650 pS, K_{PMCA}=0.3 ms^{-1}.

3.5.4 Dual Oscillator Model 2.0

A further step towards a more realistic model was presented in 2007 in [17] where the DOM1.0 was improved by adding a time-dependent rate for the mitochondrial membrane and a description of the reduced nicotinamide adenine dinucleotide (NADH) in the mitochondria. β-cell electrical activity, Ca^{2+} dynamics, and metabolic compartments are adapted from the DOM presented by Bertram *et al.* in [15], while the mitochondrial module is based on the model presented in [14] that represents a simplification of the several works presented by Magnus and Keizer [56, 57].

Chronologically speaking, this model comes before the DOM1.5 presented in the previous section. However, in terms of complexity, it offers a more detailed description

of the glucose pathway, as well as the mitochondrial membrane and concentrations dynamics. Therefore, we call this model the DOM2.0.

Mathematical Model

The rate of change of the cellular membrane potential is the same as in the DOM1.0 while the calcium module is extended to include the mitochondrial Ca^{2+}, c_{m}, and its dynamics

$$\frac{dc_{\mathrm{m}}}{dt} = f_{\mathrm{Ca}}\sigma_{\mathrm{m}}J_{\mathrm{m}}. \tag{3.26}$$

Here, the flux J_{m} represents Ca^{2+} cytosol-mitochondria exchange

$$J_{\mathrm{m}} = J_{\mathrm{uni}} - J_{\mathrm{NaCa}}\ , \tag{3.27}$$

where the fluxes through the Ca^{2+} pumps, J_{uni}, and through the Na^{+}/Ca^{2+} exchanger, J_{NaCa} are

$$J_{\mathrm{uni}} = (p_{21}\ \psi_{\mathrm{m}} - p_{22})c^2\ , \tag{3.28}$$

$$J_{\mathrm{NaCa}} = p_{23}\frac{c_{\mathrm{m}}}{c}\exp\left(p_{24}\ \psi_{\mathrm{m}}\right)\ . \tag{3.29}$$

The variable ψ_{m} represents the mitochondrial membrane potential and, unlike in the DOM1.5, it is now described by a differential equation in the mitochondrial module. The parameters are given in Table 3.4.

The ODE for c previously given by Eq. (3.9) is now replaced by

$$\frac{dc}{dt} = f_{\mathrm{Ca}}(J_{\mathrm{mem}} - J_{\mathrm{m}} - J_{\mathrm{er}})\ , \tag{3.30}$$

where the Ca^{2+} flux through the plasma membrane, J_{mem}, and through the endoplasmic reticulum membrane, J_{er}, are defined as in the DOM1.0.

In the metabolic module, the glycolytic subsystem Eq. (3.15) stays unaltered, while the ADP dynamics are adapted to better describe the effect of glycolysis and the mitochondrial activity.

The cytosolic ADP concentration is described as in the DOM1.5 by

$$\frac{d\mathrm{ADP}}{dt} = J_{\mathrm{hyd}} - \delta J_{\mathrm{ANT}}\ , \tag{3.31}$$

where J_{hyd} and J_{ANT} have already been defined in Eq. (3.22).

The mitochondrial ADP is described by the differential equation

$$\frac{d\mathrm{ADP_m}}{dt} = J_{\mathrm{ANT}} - J_{\mathrm{F1F0}} \,. \tag{3.32}$$

The flux J_{F1F0} is the rate at which the F1F0 ATPase phosphorylates ADP to form ATP. This flux depends on the ATP mitochondria concentration and the mitochondria membrane potential ψ_{m}:

$$J_{\mathrm{F1F0}} = p_{16} \frac{p_{13}}{p_{13} + \mathrm{ATP_m}} \frac{1}{1 + \exp\left(\frac{p_{14} - \psi_{\mathrm{m}}}{p_{15}}\right)} \,. \tag{3.33}$$

In both cytosol and mitochondria, ATP synthesis comes at the expense of ADP and the sums of nucleotides are conserved. Hence,

$$\mathrm{ATP} = A_{\mathrm{tot}} - \mathrm{ADP} \,, \tag{3.34}$$

$$\mathrm{ATP_m} = \mathrm{A_{tot,m}} - \mathrm{ADP_m} \,, \tag{3.35}$$

where A_{tot} and $A_{\mathrm{tot,m}}$ are the total nucleotide concentrations in the cytosol and mitochondria, respectively.

Finally, the rate of change of the mitochondrial membrane potential ψ_{m} is described by

$$\frac{d\psi_{\mathrm{m}}}{dt} = \frac{1}{C_{\mathrm{m}}} \left[J_{\mathrm{Hres}} - J_{\mathrm{Hatp}} - J_{\mathrm{Hleak}} - J_{\mathrm{ANT}} - J_{\mathrm{NaCa}} - 2J_{\mathrm{uni}} \right] \,, \tag{3.36}$$

where C_{m} is the mitochondrial inner membrane capacitance. The first term, J_{Hres}, represents the flux through respiration-driven proton pumps

$$J_{\mathrm{Hres}} = p_8 \frac{\mathrm{NADH_m}}{p_9 + \mathrm{NADH_m}} \frac{1}{1 + \exp\left(\frac{\psi_{\mathrm{m}} - p_{10}}{p_{11}}\right)} \,. \tag{3.37}$$

J_{Hatp} and J_{Hleak} are the proton flux entering the mitochondria through the ATPase and through leakage down the proton gradient, respectively:

$$J_{\mathrm{Hatp}} = 3J_{\mathrm{F1F0}} \,, \tag{3.38}$$

$$J_{\mathrm{Hleak}} = p_{17}\, \psi_{\mathrm{m}} - p_{18} \,. \tag{3.39}$$

Note that we use the convention that the membrane potential is positive if the inner membrane is hyperpolarized.

The production of mitochondrial NADH that occurs in the citric acid cycle is assumed to be proportional to the pyruvate dehydrogenase (PDH) reaction rate J_{PDH}, that is

$$J_{\mathrm{PDH}} = \left(\frac{p_1}{p_2 + \frac{\mathrm{NADH_m}}{\mathrm{NAD_m}}} \right) \left(\frac{C_{\mathrm{m}}}{p_3 + C_{\mathrm{m}}} \right) \left(J_{\mathrm{GPDH}} + J_{\mathrm{GPDH,bas}} \right) \,, \tag{3.40}$$

Parameter	Value	Parameter	Value
p_1	400	p_{15}	8.5 mV
p_2	1	p_{16}	35 μM ms^{-1}
p_3	0.01 μM	p_{17}	0.002 μM ms^{-1} mV^{-1}
p_4	0.6 μM ms^{-1}	p_{18}	0.03 μM ms^{-1}
p_5	100 μM	p_{21}	0.04 μM^{-1} ms^{-1} mV^{-1}
p_6	177 mV	p_{22}	1.1 μM^{-1} ms^{-1}
p_7	5 mV	p_{23}	0.01 ms^{-1}
p_8	7 μM ms^{-1}	p_{24}	0.016 mV^{-1}
p_9	100 μM	f_{Ca}	0.01
p_{10}	177 mV	$J_{\mathrm{GPDH,bas}}$	0.0004 μM ms^{-1}
p_{11}	5 mV	$\mathrm{A_{tot,m}}$	15000 μM
p_{13}	10000 μM	$\mathrm{N_{tot,m}}$	10000 μM
p_{14}	190 mV	C_{m}	1.8 μM mV^{-1}

Table 3.4.: Parameters for the mitochondrial module in the DOM2.0 [17].

where NAD is the nicotinamide adenine dinucleotide.

On the other hand, NADH is converted into NADH^+ during the electron transport chain which consumes oxygen at the final stage. Thus, the mitochondrial concentration of NADH is described by

$$\frac{d\mathrm{NADH_m}}{dt} = J_{\mathrm{PDH}} - J_{\mathrm{O}} \ , \tag{3.41}$$

where J_{O} is the $\mathrm{O_2}$ consumption rate

$$J_{\mathrm{O}} = p_4 \frac{\mathrm{NADH_m}}{p_5 + \mathrm{NADH_m}} \frac{1}{1 + \exp\left(\frac{\psi_{\mathrm{m}} - p_6}{p_7}\right)} \ . \tag{3.42}$$

In the DOM2.0, the total nucleotide concentration in the mitochondria is assumed constant:

$$\mathrm{NAD_m} = \mathrm{N_{tot,m}} - \mathrm{NADH_m} \ , \tag{3.43}$$

where $\mathrm{N_{tot,m}}$ is the total nucleotide concentration.

Comments

The DOM2.0 represents a milestone in the family of β-cell models. In this model, the interaction among the three compartments (cytosol, endoplasmic reticulum, and mitochondria) provides a realistic representation of the cellular physiology. In addition to being able to reproduce the complete range of bursting patterns, it can simulate the dynamics of mitochondrial variables (Figure 3.13) that can be measured

with imagining techniques in the laboratory. This result can be used to validate the model and further understand the bursting activity that is driven by glycolytic oscillations.

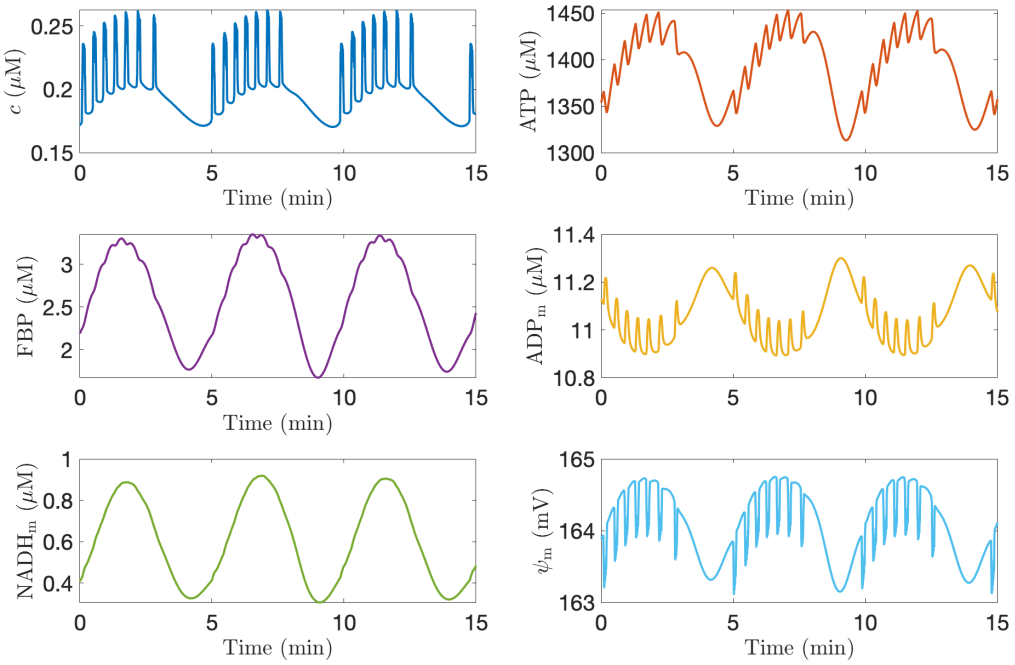

Figure 3.13.: Representative compound bursting rhythm with the DOM2.0. These plots show cytosolic Ca^{2+}, ATP, FBP, ADP_m, $NADH_m$, and ψ_m time courses with J_{GK}=0.7 μM ms^{-1}, $g_{K(ATP)}$=16000 pS; $g_{K(Ca)}$=300 pS, p_{21}=0.04 μM^{-1} ms^{-1} mV^{-1}, p_{23}=0.01 ms^{-1}.

3.5.5 Integrated Oscillator Model

The last model of this school we are describing is the Integrated Oscillator Model (IOM) published in 2016 [62].

Recent studies provide measurements of the glycolytic enzyme pyruvate kinase and metabolic oscillations in β-cells simultaneously with membrane potential, showing a sawtooth time course of the glycolytic metabolite FBP [64, 66]. These important results could be achieved thanks to two new sensors. The first is the Förster Resonance Energy Transfer (FRET) biosensor (a pyruvate kinase activity reporter, PKAR) which tracks the activity of the pyruvate kinase [55, 2]. The second sensor is Perceval High Resolution (Perceval-HR), which is a fluorescent sensor that tracks the dynamics of the nucleotide ATP/ADP ratio [90, 7].

The models shown so far are not able to reproduce these new findings, which forces a re-thinking of the oscillation mechanism, resulting in the development of the

Integrated Oscillator Model (IOM) in which Ca^{2+} feeds back onto glycolysis [62]. This feedback gives FBP the sawtooth shape. But the driving force for oscillations is ATP consumption by Ca^{2+} pumps [61].

The "integrated" specification in the name means that the two oscillators (metabolic and electrical) from the DOM actually operate as a combined mechanism for bursting. Thus, the name DOM would have misrepresented this more integrated bursting mechanism. More specifically, this model is based on the DOM1.5 described in Section 3.5.3 and combines electrical activity with intracellular Ca^{2+} and glucose metabolism via numerous feedforward and feedback pathways. For this formulation, a Ca^{2+} dependence is added to the PDH reaction rate J_{PDH} that here replaces the GPDH reaction rate as glycolytic efflux.

Mathematical Model

The mathematical model is based on the DOM1.5. In this formulation, the PDH reaction (that replaces the GPDH reaction in Eq. (3.15)) is assumed dependent on the mitochondrial calcium concentration, c_{m}, through the function s_∞:

$$J_{\mathrm{PDH}} = v_{\mathrm{PDH}} s_\infty \sqrt{\mathrm{FBP}} \,, \tag{3.44}$$

where $v_{\mathrm{PDH}} = 3.74 \times 10^{-4}$ μM ms^{-1} is the maximum rate of the PDH reaction and the nozzle s_∞ is described by:

$$s_\infty = \frac{c_m}{c_m + K_{\mathrm{PDH}}} \,, \tag{3.45}$$

with $K_{\mathrm{PDH}} = 0.1$ μM. This s_∞ function is referred to as a "nozzle" since it controls efflux of metabolites through the glycolysis.

The concentration c_{m} described by a simple polynomial expression, instead of the ODE shown in DOM2.0 (Eq. (3.26)):

$$c_{\mathrm{m}} = 5c \,, \tag{3.46}$$

where c the cytosolic Ca^{2+} concentration. The s_∞ term plays a fundamental role in the model since it represents the Ca^{2+} control on the glycolytic subsystem.

Comments

From a mathematical point of view, the IOM is a simple extension of the DOM1.5 in which the authors included a calcium dependency in the glycolysis efflux. However,

this small change has significant consequences on the nature of the bursting simulated by the model. Specifically, it further extends the range of bursting patterns to include the new experimental observations in the β-cell activity, such as the recently discovered FBP sawtooth-shape (Figure 3.14). We point out that the IOM lacks the mitochondrial module, a key element in the DOM2.0. This suggests the evolution of the mathematical model still has not reached the final step.

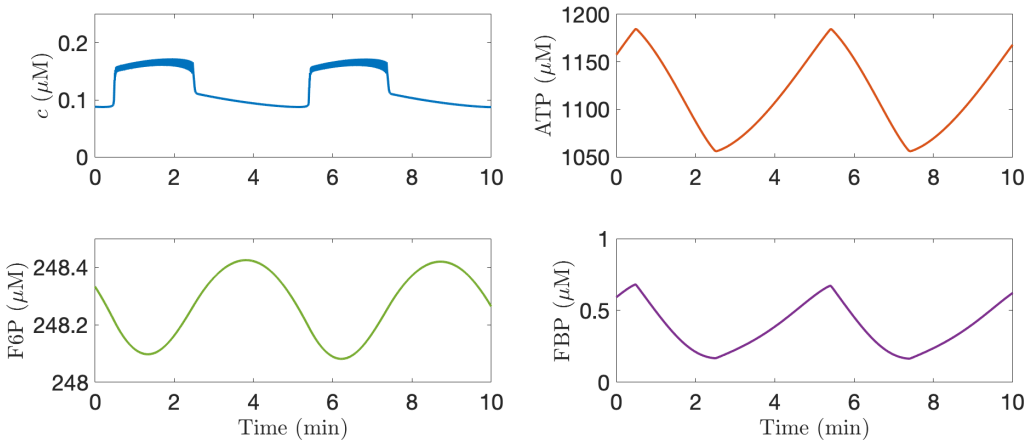

Figure 3.14.: Representative slow bursting rhythm with sawtooth-like FBP. These plots show cytosolic Ca^{2+}, ATP, FBP, ADP_m, $NADH_m$, and ψ_m time courses with the IOM with J_{GK}=9.45×10^{-5} μM ms^{-1}, $g_{K(ATP)}$=2,960 pS; $g_{K(Ca)}$=18 pS.

3.6 Summary

In the literature, we have two main classes of models: those in which Ca^{2+} oscillations induce metabolic oscillations (*Class I*), and those in which metabolic oscillations are intrinsic and drive the bursting pattern (*Class II*). In this chapter, we introduced some of the most relevant models published so far. Among the presented models belonging to the first class, we find that there are different hypotheses regarding the mechanism in which Ca^{2+} modulates the bursts [26, 25, 46, 45, 87, 56, 24, 23, 31, 67]. From *Class II*, we mention in particular Tornheim's work [92]. In this case, the metabolic oscillations are the result of the activity of the M-type isoform which is in turn induced by the conversion of F6P into FBP.

We briefly discussed the main achievements and limitations of Fridlyand and Cha schools, both belonging to *Class I*. Then, we focused on a third group of models represented by Bertram-Satin-Sherman school, which combines elements of both classes in order to simulate a variety of mechanisms underlying the bursting. To be more precise, in these models slow busting is driven by the glycolytic oscillations and ATP/ADP action on the K(ATP) channels, while fast bursting is due to the Ca^{2+}

action on the K(Ca) channels. A suitable combination of these two mechanisms results in compound bursting.

Recently, Bertram *et al.* [16] published a list of canonical experimental results that any β-cell model should be able to reproduce. We show this list in Table 3.5, highlighting whether the models considered in this chapter are capable of reproducing them. In the table, each column represents a model, while the experimental findings correspond to the rows. We also colour-coded the models according to the bursting mechanism: the models accounting for Ca^{2+}-driven oscillations are in light blue, those reproducing metabolism-driven oscillations are in light yellow, while those accounting for both mechanisms are in light green. As the IOM is the only model accounting for all key experiments, we considered this particular model as the starting point for the work presented in this thesis.

Experiment \ Model	CK83	KM89	T97	D98	SK92	BS04	F03	Dd06	DOM	C11	IOM
Fast bursting and Ca^{2+} patterns	✓	✓		✓	✓	✓	✓	✓	✓	✓	✓
Slow bursting and Ca^{2+} patterns			✓	✓		✓		✓	✓	✓	✓
Compound bursting and Ca^{2+} patterns									✓		✓
Subthreshold oscillations			✓						✓		✓
Metabolic oscillations with Ca^{2+} clamped by Dz									✓		✓
Oscillations in KATP conductance measured with voltage ramps during islet bursting			✓						✓		✓
Ca^{2+} oscillations stimulated by KIC	✓	✓		✓	✓	✓	✓	✓		✓	✓
Sawtooth oscillations in Perceval		✓		✓	✓	✓	✓	✓		✓	✓
Sawtooth oscillations in PKAR											✓

Table 3.5.: CK83, Chay and Keizer, 1983 [26]; KM89, Keizer and Magnus, 1989 [45]; T97, Tornheim, 1997 [92]; D98, Detimary *et al.*, 1998 [31]; SK92, Smolen and Keizer, 1992 [87]; BS04, Bertram and Sherman, 2004 [10]; F03, Fridlyand *et al.*, 2003 [37]; Dd06, Diederichs, 2006 [32]; DOM, Bertram *et al.*, 2007 [17]; C11, Cha *et al.*, 2011 [22]; IOM, McKenna *et al.*, 2016 [62].

4 Advanced Analysis of the Integrated Oscillator Model

> *One never notices what has been done; one can only see what remains to be done.*
>
> **— Marie Curie**

In this chapter, we develop an extension of the IOM (Section 3.5.5), called the IOM1.5, which accounts for more realistic calcium dynamics in both cytosol and mitochondria. We provide the motivations for this new version (Section 4.1) and list the complete set of equations describing the model (Section 4.2). Then, we show that the new IOM can account for different types of experimentally observed oscillations and we investigate how transitions can be made between them (Section 4.3). By studying variations in key bifurcation parameters from the electrical and metabolic subsystems, we establish which conditions are necessary for bursting to be driven by glycolytic oscillations or by the indirect action of cytosolic Ca^{2+} onto ATP production. Since the model reflects the interaction of electrical and metabolic subsystems, bifurcation parameters from these two subsystems are used in the analysis. Finally, we show what can be expected in experimental measurements of β-cell bursting activity, and suggest protocols through which oscillations can be converted from one type to the other (Section 4.4).

Some of the results presented in this chapter have been published in Marinelli *et al.* paper published in the Journal of Theoretical Biology in 2018 [58].

4.1 Motivations

A widely discussed topic in the islet biology field has been the origin of β-cell oscillations, whether due to intrinsic glycolytic oscillations (i.e., oscillations that persist when the variables in the electrical module are clamped) or due to Ca^{2+} feedback. This is a crucial aspect in the proper interpretation of the many experimental findings that have been published about β-cell oscillations.

Today, we still do not have the answer to this crucial question. On one side, Ca^{2+} feedback is needed to explain the fast bursting as well as some dynamics of glycolytic products. On the other side, there is evidence that supports the hypothesis of intrinsic glycolytic oscillations, such as slow, accordion, and compound bursts, or the duration of the insulin pulses themselves (about 5 min) that is close to the duration of slow and compound bursting.

In Chapter 3, we presented the most relevant models in the β-cell literature, pointing out whether they can account for either one mechanism or the other. We also showed that many models in Bertram-Sherman-Satin school combine the two classes and we presented the IOM as the last step of an evolution process started many years ago. Ca^{2+} feedback onto glycolysis allows the IOM to replicate new findings, unreproducible by other models previously developed in the literature. Therefore, we take this model as the starting point for the updated IOM presented in this chapter, which we call the IOM1.5.

The equations giving the IOM1.5 have already been described in Chapter 3. To make this chapter self-contained and for the sake of clarity in the presentation, we describe all model equations once again.

4.2 Mathematical Model

The schematic for the IOM1.5 is illustrated in Figure 4.1, which shows the interactions among the membrane potential and the metabolites.

The IOM1.5 is made up of two modules. The first module describes the β-cell electrical activity and Ca^{2+} dynamics. The second module describes the production and consumption of glycolysis selected products and of ATP.

4.2.1 The Electrical and Calcium Module

The β-cell electrical activity is described with a Hodgkin–Huxley-type model. The time change of the cellular membrane potential (V) is expressed by

$$\frac{dV}{dt} = -\frac{1}{C}\left[I_{\mathrm{Ca}} + I_{\mathrm{K}} + I_{\mathrm{K(Ca)}} + I_{\mathrm{K(ATP)}}\right] , \tag{4.1}$$

where C is the membrane capacitance, I_{Ca} is a Ca^{2+} current responsible for the upstroke of action potentials, I_{K} is a delayed-rectifying K^+ current responsible for the downstroke of action potentials, $I_{\mathrm{K(Ca)}}$ is a Ca^{2+}-activated K^+ current that plays a key role in packaging action potentials into bursts, and $I_{\mathrm{K(ATP)}}$ is a K^+ current that is inactivated by ATP and is thereby regulated by the glucose level.

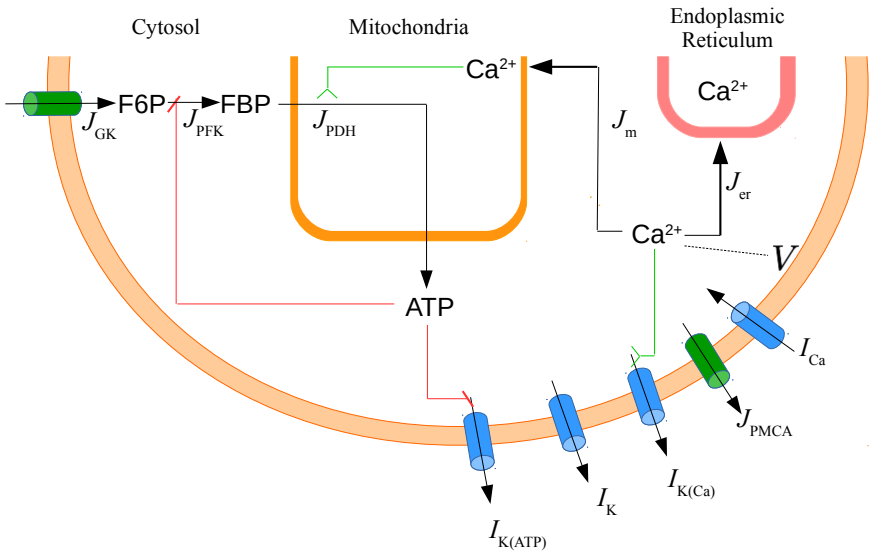

Figure 4.1.: The IOM1.5 consists of modules for electrical activity, Ca^{2+} dynamics and metabolism. I: currents, J: fluxes, GK: glucokinase. PFK: phosphofructokinase, PDH: phosphate dehydrogenase. The red and green lines represent negative and positive feedback, respectively.

The Ca^{2+} current is assumed to change instantaneously with changes in V, and is described by

$$I_{\mathrm{Ca}} = g_{\mathrm{Ca}} m_\infty(V)(V - V_{\mathrm{Ca}}) \,, \tag{4.2}$$

where g_{Ca} is the maximal conductance, V_{Ca} is the Ca^{2+} Nernst potential, and m_∞ is the activation function given by the increasing sigmoid

$$m_\infty(V) = \frac{1}{1 + \exp\left[(\nu_m - V)/s_m\right]} \,. \tag{4.3}$$

Table 4.1 gathers the values for the shape parameters ν_m and s_m, as well as all other model parameters.

The delayed rectifying current is

$$I_{\mathrm{K}} = g_{\mathrm{K}} n (V - V_{\mathrm{K}}) \,. \tag{4.4}$$

The activation variable, n, has the first-order kinetics

$$\frac{dn}{dt} = \frac{n_\infty(V) - n}{\tau_n} \,, \tag{4.5}$$

where $n_\infty(V)$ is sigmoid of the form Eq. (4.3), with shape parameters ν_n and s_n.

Activation of the K(Ca) current occurs through binding of Ca^{2+} ions to intracellular binding sites and is assumed to occur instantaneously with the binding. The K(Ca) current is then

$$I_{\mathrm{K(Ca)}} = g_{\mathrm{K(Ca)}} q_\infty(c)(V - V_{\mathrm{K}}) \,, \tag{4.6}$$

where

$$q_\infty(c) = \frac{c^2}{k_d^2 + c^2} \,, \tag{4.7}$$

is the activation function and c is the free intracellular Ca^{2+} concentration. The maximal conductance, $g_{\mathrm{K(Ca)}}$, is one of the key parameters that we vary to explore the types of electrical bursting produced by the model.

The ATP-activated K^+ current is described by

$$I_{\mathrm{K(ATP)}} = g_{\mathrm{K(ATP)}} o_\infty(\mathrm{ADP}, \mathrm{ATP})(V - V_{\mathrm{K}}) \,, \tag{4.8}$$

where the activation function, o_∞, depends on the concentrations of cytosolic ADP as well as on ATP, and is given by

$$o_\infty(\mathrm{ADP}, \mathrm{ATP}) = \frac{0.08 + 0.89 \left(\frac{\mathrm{MgADP}}{k_{dd}}\right)^2 + 0.16 \left(\frac{\mathrm{MgADP}}{k_{dd}}\right)}{\left(1 + \frac{\mathrm{MgADP}}{k_{dd}}\right)^2 \left(1 + \frac{\mathrm{ATP}^{4-}}{k_{tt}} + \frac{\mathrm{ADP}^{3-}}{k_{td}}\right)} \,. \tag{4.9}$$

Here, $\mathrm{MgADP} = 0.165\ \mathrm{ADP}$, $\mathrm{ADP}^{3-} = 0.135\ \mathrm{ADP}$, and $\mathrm{ATP}^{4-} = 0.05\ \mathrm{ATP}$.

During an action potential, Ca^{2+} enters the cell via Ca^{2+} channels, and is removed from the cell via pumps in the plasma membrane. The Ca^{2+} also flows into and out of the mitochondria and endoplasmic reticulum (ER). The dynamics of the free cytosolic Ca^{2+} concentration is given by

$$\frac{dc}{dt} = f_{\mathrm{Ca}}(J_{\mathrm{mem}} - J_{\mathrm{m}} - J_{\mathrm{er}}) \,, \tag{4.10}$$

where f_{Ca} is the fraction of Ca^{2+} ions not bound to buffers, and J_{mem}, J_{m}, and J_{er} represent the Ca^{2+} flux densities across the plasma membrane, into the mitochondria, and into the ER, respectively. They are described by

$$\begin{aligned} J_{\mathrm{mem}} &= -\left[\frac{\alpha}{V_{\mathrm{cyt}}} I_{\mathrm{Ca}} + k_{\mathrm{PMCA}} c\right] \,, \\ J_{\mathrm{er}} &= k_{\mathrm{SERCA}} c - p_{\mathrm{leak}}(c_{\mathrm{er}} - c) \,, \\ J_{\mathrm{m}} &= k_{\mathrm{uni}} c - k_{\mathrm{NaCa}}(c_{\mathrm{m}} - c) \,. \end{aligned} \tag{4.11}$$

The parameter V_{cyt} is the volume of the cytosolic compartment and α is the conversion rate of current to ion flux. The k parameters reflect the strength of Ca^{2+}

Parameter	Value	Parameter	Value
C	5300 fF	k_{dd}	17 μM
g_{Ca}	1000 pS	k_{tt}	1 μM
g_{K}	2700 pS	k_{td}	26 μM
$g_{\mathrm{K(Ca)}}$	varies	f_{Ca}	0.01
$g_{\mathrm{K(ATP)}}$	25000 pS	α	5.18×10^{-18} μmol fA^{-1} ms^{-1}
V_{Ca}	25 mV	V_{cyt}	1.15×10^{-12} l
V_{K}	-75 mV	k_{PMCA}	0.2 ms^{-1}
ν_m	-20 mV	k_{SERCA}	0.4 ms^{-1}
s_m	12 mV	p_{leak}	2×10^{-4} ms^{-1}
ν_n	-16 mV	k_{uni}	0.4 ms^{-1}
s_n	5 mV	k_{NaCa}	0.001 ms^{-1}
τ_n	20 ms	σ_{m}	100
k_d	0.5 μM	σ_{er}	31

Table 4.1.: Parameters for the electrical and calcium modules in the IOM1.5.

pumps or Na^+-Ca^{2+} exchanger, while p_{leak} quantifies the leak of Ca^{2+} across the ER membrane.

The free Ca^{2+} concentrations in the mitochondria and ER are described by

$$\frac{dc_{\mathrm{m}}}{dt} = f_{\mathrm{Ca}}\sigma_{\mathrm{m}}J_{\mathrm{m}} \ , \tag{4.12}$$

$$\frac{dc_{\mathrm{er}}}{dt} = f_{\mathrm{Ca}}\sigma_{\mathrm{er}}J_{\mathrm{er}} \ , \tag{4.13}$$

where the σ parameters are ratios of cytosolic volume to ER or mitochondria volumes.

4.2.2 The Metabolic Module

For the metabolic module, we use a simplified model that focuses on the allosteric enzyme phosphofructokinase (PFK), which is the basis for oscillations in glycolysis [86]. Parameter values for the model are given in Table 4.2. The cytosolic concentrations of the enzyme's substrate fructose 6-phosphate (F6P) and product fructose 1,6-bisphosphate (FBP) are described by

$$\begin{aligned} \frac{d\mathrm{F6P}}{dt} &= 0.3\left(J_{\mathrm{GK}} - J_{\mathrm{PFK}}\right) \ , \\ \frac{d\mathrm{FBP}}{dt} &= J_{\mathrm{PFK}} - \frac{1}{2}J_{\mathrm{PDH}} \ , \end{aligned} \tag{4.14}$$

where the parameter J_{GK} is the glucose-dependent glucokinase reaction rate, J_{PFK} is the PFK reaction rate, and J_{PDH} is the pyruvate dehydrogenase (PDH) reaction

rate. The value of J_{GK} corresponds to the stimulatory glucose concentration of 11 mM.

The complicated PFK rate depends on its substrate F6P as well as on ATP, AMP, and most importantly its product FBP. The positive feedback of FBP onto PFK is responsible for glycolytic oscillations [86]. The PFK reaction rate is

$$J_{\mathrm{PFK}} = v_{\mathrm{PFK}} \frac{w_{1110} + k_{\mathrm{PFK}} \sum_{i,j,l \in \{0,1\}} w_{ij1l}}{\sum_{i,j,k,l \in \{0,1\}} w_{ijkl}} \,, \tag{4.15}$$

with weights

$$w_{ijkl} = \frac{\left(\mathrm{AMP}/K_1\right)^i \left(\mathrm{FBP}/K_2\right)^j \left(\mathrm{F6P}^2/K_3\right)^k \left(\mathrm{ATP}^2/K_4\right)^l}{f_{13}^{ik} f_{23}^{jk} f_{41}^{il} f_{42}^{jl} f_{43}^{kl}} \,, \tag{4.16}$$

where $\mathrm{AMP} = \frac{\mathrm{ADP}^2}{\mathrm{ATP}}$.

The PDH reaction rate also has a key feedback pathway, with facilitation of the reaction by mitochondrial Ca^{2+} as discussed in [16]. This reaction is described by

$$J_{\mathrm{PDH}} = v_{\mathrm{PDH}} s_\infty(c_{\mathrm{m}}) \sqrt{\mathrm{FBP}} \,, \tag{4.17}$$

where v_{PDH} is one of the key parameters that we vary to explore the impact of changing the glycolytic efflux rate. The Ca^{2+} feedback is through the s_∞ function,

$$s_\infty(c_{\mathrm{m}}) = \frac{c_{\mathrm{m}}}{K_{\mathrm{PDH}} + c_{\mathrm{m}}} \,. \tag{4.18}$$

The physiological details of mitochondrial metabolism are not included in this model. Instead, we use a phenomenological model, in which ATP production is driven by the output of the glycolytic subsystem, J_{PDH}. The newly synthesized ATP comes at the expense of ADP, where the ADP concentration is described by

$$\frac{d\mathrm{ADP}}{dt} = \frac{\left\{\mathrm{ATP} - \exp\left[\left(r + 2.2 \frac{J_{\mathrm{PDH}}}{0.05 + J_{\mathrm{PDH}}}\right)\left(1 - \frac{c}{0.35}\right)\right] \mathrm{ADP}\right\}}{\tau_a} \,. \tag{4.19}$$

That is, when the Ca^{2+} concentration is elevated the electrical gradient across the mitochondrial membrane is reduced, leading to a reduction in the rate of ATP production. This is often referred to as the Keizer-Magnus effect [45]. It is assumed that the sum of the cytosolic nucleotides is conserved, so

$$\mathrm{ATP} = \frac{1}{2}\left[A_{\mathrm{tot}} + \sqrt{-4\mathrm{ADP}^2 + (A_{\mathrm{tot}} - \mathrm{ADP})^2} - \mathrm{ADP}\right] \,, \tag{4.20}$$

where A_{tot} is the total (and constant) nucleotide concentration.

Parameter	Value	Parameter	Value
J_{GK}	0.001 μM ms^{-1}	f_{41}	20
v_{PFK}	0.01 μM ms^{-1}	f_{42}	20
k_{PFK}	0.06	f_{43}	20
K_1	30 μM	v_{PDH}	varies
K_2	1 μM	K_{PDH}	200 μM
K_3	5×10^4 μM^2	τ_a	3×10^5 ms
K_4	10^3 μM^2	r	1
f_{13}	0.02	A_{tot}	3×10^3 μM
f_{23}	0.2		

Table 4.2.: Parameters for the metabolic module.

4.3 Mechanism Driving the Burst

We want to determine the values of key parameters for which intrinsic glycolytic oscillations occur and values for which bursting oscillations are driven by Ca^{2+} feedback. The parameters selected for this study are the maximal conductance of the Ca^{2+}-activated K^+ current, $g_{\mathrm{K(Ca)}}$, and the maximum flux rate through the pyruvate dehydrogenase reaction, v_{PDH}. They are chosen because of their pivotal roles in the electrical and metabolic portions of the model. More precisely, it is well-known [10] that variations in $g_{\mathrm{K(Ca)}}$ alter the active phase duration from tens of seconds (when $g_{\mathrm{K(Ca)}}$ is large) to several minutes (when $g_{\mathrm{K(Ca)}}$ is small). The parameter v_{PDH} controls the maximum efflux out of glycolysis. Thus, v_{PDH} determines the degree to which FBP can build up and feed back onto PFK in a regenerative manner. It is this positive feedback, which results in the depletion of the substrate F6P, which is responsible for intrinsic PFK-induced oscillations [87]. The greater is the value of v_{PDH}, the less positive feedback of FBP there is onto PFK.

When $g_{\mathrm{K(Ca)}}$ is small, the IOM1.5 can produce slow oscillations in the cytosolic Ca^{2+} concentration resembling those often observed in Ca^{2+} measurements from pancreatic islets [99]. However, these slow oscillations can be driven by two entirely different mechanisms. Figure 4.2 shows the time courses of Ca^{2+}, ATP, and FBP for $v_{\mathrm{PDH}} = 0.009$ μM/ms (left column) and $v_{\mathrm{PDH}} = 0.002$ μM/ms (right column). The Ca^{2+} and ATP time series are remarkably similar, but the FBP time courses are quite different. For low v_{PDH}, the FBP time course exhibits a sawtooth pattern (Figure 4.2F), whereas for larger v_{PDH} there are pulses of FBP appearing from an almost-zero baseline (Figure 4.2E). This substantial difference in the FBP time course is indicative of the fact that there are distinct mechanisms driving the slow Ca^{2+} oscillations [61].

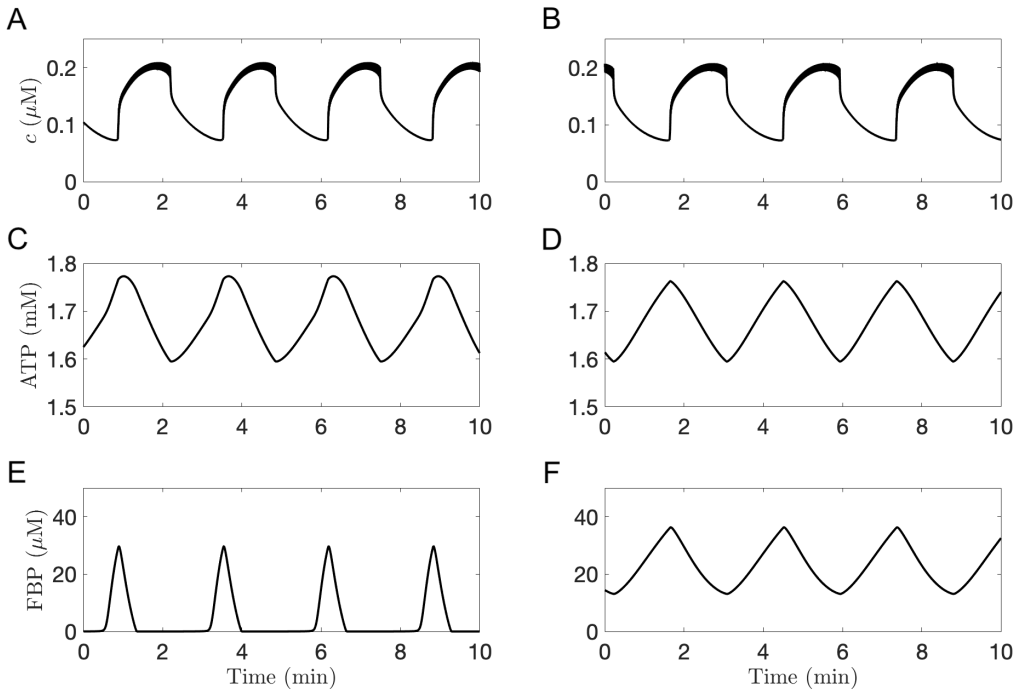

Figure 4.2.: Time courses of cytosolic calcium (top row), cytosolic ATP (middle row), and FBP (bottom row), with $g_{\mathrm{K(Ca)}} = 50$ pS. In the left column $v_{\mathrm{PDH}} = 0.009$ μM/ms; in the right column $v_{\mathrm{PDH}} = 0.002$ μM/ms.

Both types of oscillations have been observed experimentally, though in different preparations. Pulses of FBP were observed in measurements from muscle extracts [92], which contain the same isoform of the rhythmogenic enzyme PFK-M that is dominant in β-cells [98]. In contrast, sawtooth FBP oscillations were observed in islets, using a FRET biosensor [64, 66]. Thus, the PFK-M isoform, found in both muscle extracts and islet β-cells can contribute to metabolic oscillations resulting in either pulsatile or sawtooth FBP patterns, reflecting different oscillation mechanisms.

Our current goal is to characterize conditions in which one can expect the different FBP patterns. We use this information about the FBP time course as a fingerprint for the oscillation mechanism.

We begin by exploring the ($g_{\mathrm{K(Ca)}}$, v_{PDH})-parameter space. Figure 4.3 shows that the ($g_{\mathrm{K(Ca)}}$, v_{PDH}) plane is split into three regions, according to the behaviour of the FBP in the attractor of the IOM1.5. In the upper region (corresponding to larger v_{PDH}), the FBP time course is pulsatile. In the lower region (corresponding to smaller v_{PDH}), the FBP time course has a sawtooth profile. These pulsatile and sawtooth regions are separated by a bistable region (shaded), where the FBP may exhibit either pulsatile or sawtooth behaviour, depending on the initial conditions.

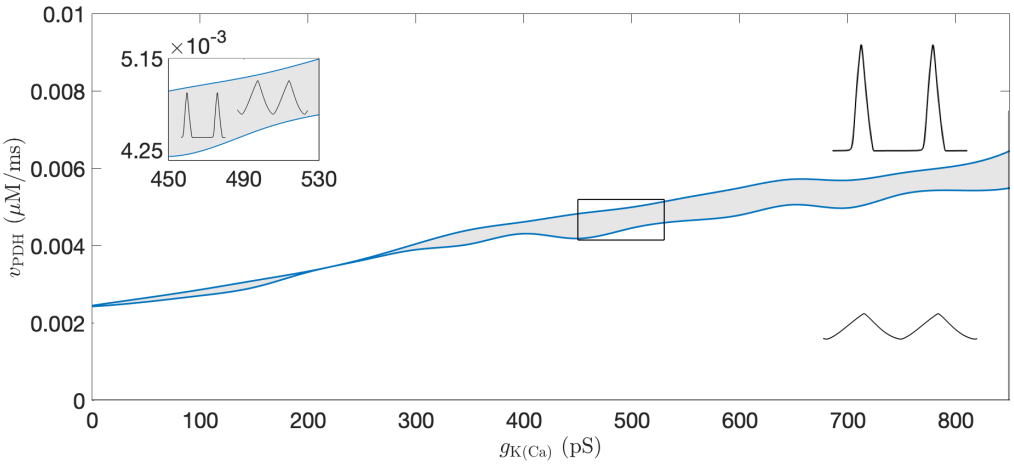

Figure 4.3.: Division of the ($g_{\mathrm{K(Ca)}}$, v_{PDH}) parameter plane into a region producing FBP pulses and a region producing sawtooth FBP time courses, separated by a bistable region (shaded). Inset: zoom of the bistable region, where FBP can be either sawtooth or pulsatile, depending on the initial conditions. Here and elsewhere, sawtooth and pulsatile time courses are distinguished by eye.

4.3.1 Oscillations in the Glycolytic Subsystem and the Shape of the FBP Patterns

We investigate now the basis for the qualitatively different FBP time courses and the nature of the boundary between sawtooth and pulsatile FBP time courses in Figure 4.3. For this purpose, we focus on the glycolytic subsystem and we look for conditions under which the model produces intrinsic glycolytic oscillations.

We note that the glycolytic subsystem (4.14) depends explicitly on v_{PDH} and implicitly on $g_{\mathrm{K(Ca)}}$. More specifically, $g_{\mathrm{K(Ca)}}$ plays a role in determining the cytosolic Ca^{2+} level, c. For a fixed c, the equilibrium mitochondrial Ca^{2+} level is

$$c_{\mathrm{m}} = \frac{(k_{\mathrm{uni}} + k_{\mathrm{NaCa}})\, c}{k_{\mathrm{NaCa}}}, \tag{4.21}$$

which, in turn, affects the glycolytic efflux via the PDH reaction rate, J_{PDH}, and the Ca^{2+} feedback via s_∞ (Eqs. (4.17) and (4.18)). Cytosolic Ca^{2+} also affects the equilibrium ATP production through Eqs. (4.19) and (4.20). Finally, the nuclueotides AMP, ADP, and ATP influence PFK activity through Eqs. (4.15) and (4.16). Thus, $g_{\mathrm{K(Ca)}}$ affects glycolysis indirectly through its influence on c.

In what follows, we isolate the glycolytic subsystem Eq. (4.14) by clamping c at a fixed value and assuming ATP is at equilibrium, and perform bifurcation studies of

the intrinsic oscillations with respect to c and v_{PDH}. Figure 4.4 shows the results (Section C.4 in the Appendix for the computational details).

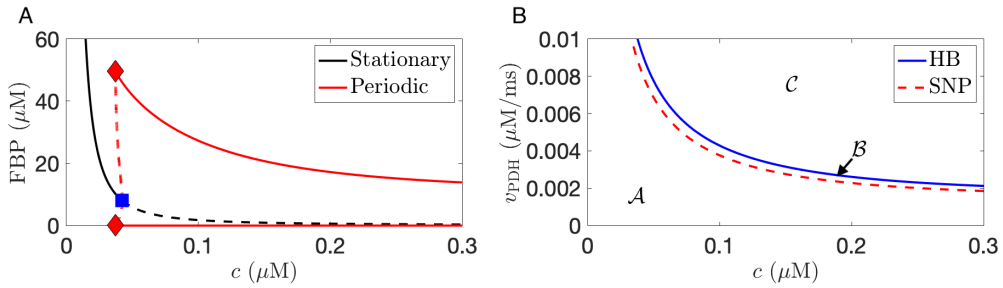

Figure 4.4.: (A) Bifurcation structure of the glycolytic module with respect to c for $v_{\mathrm{PDH}} = 0.009$ μM/ms. The blue and red squares indicate the subcritical HB and the SNP, respectively. (B) Two-parameter bifurcation diagram of the glycolytic subsystem illustrating the regions of Ca^{2+}-dependent ($\mathcal{A}$), conditional Ca^{2+}-independent ($\mathcal{B}$), and Ca^{2+}-independent ($\mathcal{C}$) oscillations.

We first fix $v_{\mathrm{PDH}} = 0.009$ μM/ms and construct a bifurcation diagram of the glycolytic subsystem with c as a bifurcation parameter. Lines in Figure 4.4A represent the steady states (and their nature) as functions of c. We use the convention that a solid line represents a stable branch and a dashed line an unstable branch. For low values of c, the glycolytic subsystem is stationary (black solid line). Because of the influence of c on J_{PDH}, lower values of c produce higher equilibrium values of FBP. More precisely, the efflux through glycolysis is low for lower values of c, so FBP can build up. At $c \approx 0.04$ μM there is a subcritical Hopf bifurcation (HB, blue square), giving rise to a branch of unstable periodic solutions of the glycolytic subsystem (dashed red) that meets a branch of stable periodic solutions (solid red) at a saddle-node of periodics bifurcation (SNP, red diamonds). Hence, for c values to the right of the SNP point, the stationary solution is unstable (black dashed line) and the attractor of the glycolytic subsystem is a limit cycle. These stable limit cycles correspond to the pulsatile FBP.

Figure 4.4B shows the two-parameter continuations of the Hopf and SNP bifurcations in the (c, v_{PDH}) plane. The HB and SNP curves partition the plane into three regions, each characterized by different dynamics: in region $\mathcal{A}$ (below the red SNP curve) the equilibrium is the unique attractor of the glycolytic subsystem (4.14); in region $\mathcal{C}$ (above the blue HB curve) the equilibrium is unstable and the limit cycle is the only attractor; in region $\mathcal{B}$ (between the two curves) both the equilibrium and the limit cycle are stable. Therefore, this figure characterizes the asymptotic structure of the glycolytic subsystem with the input variable c clamped and the input nucleotide variables fixed at their corresponding equilibrium values. We note that the oscillations in region $\mathcal{C}$ are intrinsic to the glycolytic subsystem.

We return now to the whole IOM1.5, where c and the nucleotides vary over time. The top panel of Figure 4.5A illustrates c and FBP time courses for a combination of the parameters ($g_{\mathrm{K(Ca)}}$, v_{PDH}) that results in a pulsatile FBP pattern. The bottom panel of Figure 4.5A corresponds to a sawtooth FBP time course. In the first case, the model produces compound bursting, consisting of fast bursts grouped into episodes that occur during each FBP pulse. In the second case, the model produces fast bursting with active phases separated by equal time intervals. Figure 4.5B shows, for each of these two cases, the projection of the orbit onto the (c, v_{PDH}) plane from Figure 4.4B, indicating the range of c values taken on during oscillations. From this panel, we see that when FBP oscillations are pulsatile, the projection lies in region $\mathcal{C}$, where the glycolytic subsystem is oscillatory. In the case of the sawtooth FBP time course, the projection into the (c, v_{PDH}) plane lies in region $\mathcal{A}$, corresponding to the case where glycolysis is stationary.

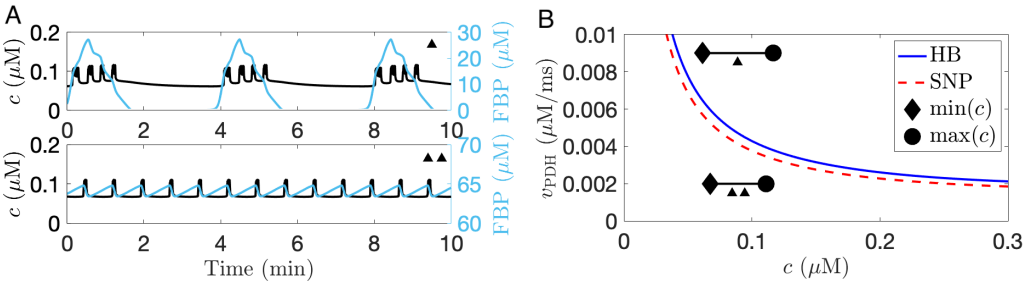

Figure 4.5.: (A) c and FBP time courses with $g_{\mathrm{K(Ca)}} = 800$ pS and $v_{\mathrm{PDH}} = 0.002$ μM/ms (bottom) or $v_{\mathrm{PDH}} = 0.009$ μM/ms (top). (B) Ca^{2+} oscillations from panel A projected onto the (c, v_{PDH}) plane (black segments). The triangles identify the corresponding time courses in panel A.

More generally, if the periodic orbit of the IOM1.5 lies in region $\mathcal{A}$ of Figure 4.4B then FBP will have a sawtooth shape, and the oscillations will cease if c is clamped. If the projection of the periodic orbit lies in region $\mathcal{C}$ then FBP will have a pulsatile shape due to the presence of intrinsic glycolytic oscillations that would persist even if c were clamped. If it crosses through region $\mathcal{B}$ then the FBP time course could be either sawtooth or pulsatile.

Figures 4.4 and 4.5 shows that intrinsic glycolytic oscillations only occur if the PDH reaction rate is sufficiently large. If v_{PDH} is too small, then the FBP level will build up to such a high level that the PFK reaction will always stay elevated and there will be no glycolytic oscillations. However, if v_{PDH} is too large, no glycolytic oscillations are permitted. In fact, with the resulting large efflux through glycolysis, the FBP level will be too low to provide the necessary positive feedback onto PFK for glycolytic oscillations. If we consider a larger range of the parameter v_{PDH} for our bifurcation diagram, we see that there is a second HB in the glycolytic subsystem, which occurs for large v_{PDH}, and above which the glycolytic subsystem is stationary.

Figure 4.6A shows two examples of bursting oscillations produced by the IOM1.5 with $g_{\mathrm{K(Ca)}} = 800$ pS, both corresponding to large values of v_{PDH}. In the bottom panel of Figure 4.6A ($v_{\mathrm{PDH}} = 0.02$ μM/ms) compound bursting is produced, but now the FBP pulses are much smaller than those obtained during compound bursting in Figure 4.5A. For the top panel of Figure 4.6A, we use an even larger maximum efflux value of $v_{\mathrm{PDH}} = 0.05$ μM/ms, and fast bursting is produced. In this case, there are no FBP pulses and FBP stays near zero since the glycolytic efflux rate is so high. When the projections of these orbits are plotted in the (c, v_{PDH}) plane (Figure 4.6B), the compound bursting rhythm lies in region $\mathcal{C}$ where there are intrinsic glycolytic oscillations. The projection of the fast bursting, on the other hand, lies in a new region of stationary attractors, region $\mathcal{D}$, which is separated from region $\mathcal{C}$ by a new curve of Hopf bifurcations (upper blue curve in the diagram).

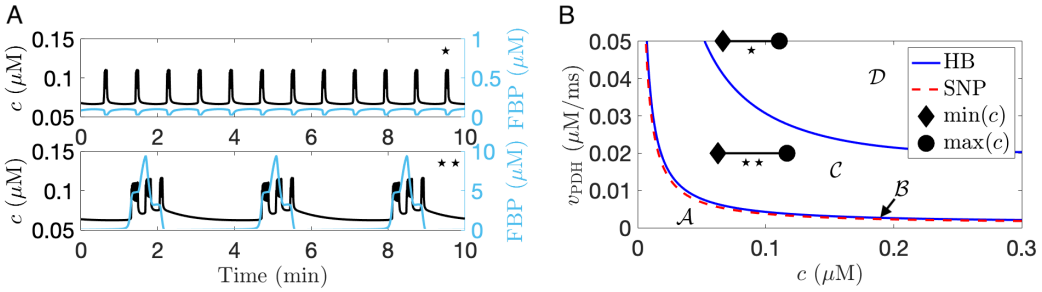

Figure 4.6.: (A) Ca^{2+} and FBP time courses with $g_{\mathrm{K(Ca)}} = 800$ pS and $v_{\mathrm{PDH}} = 0.02$ μM/ms (bottom) or $v_{\mathrm{PDH}} = 0.05$ μM/ms (top). (B) Projections of the Ca^{2+} oscillations from panel A into the (c, v_{PDH}) plane (black segments). The stars identify the corresponding time courses in panel A. Note that the vertical scale in (B) is different from that of Figures 4.4B and 4.5B.

In summary, the transition from fast bursting to compound bursting shown in Figure 4.5A when v_{PDH} was increased from 0.002 μM/ms to 0.009 μM/ms occurred because the lower threshold for intrinsic glycolytic oscillations was crossed, turning on the oscillations. The transition from compound bursting oscillations back to fast bursting when v_{PDH} was increased from 0.02 μM/ms to 0.05μM/ms occurred because the upper threshold for intrinsic glycolytic oscillations was crossed, turning off the oscillations.

4.3.2 Bursting Patterns and Their Relationship to Metabolic Activity

The parameter $g_{\mathrm{K(Ca)}}$ influences the cellular electrical activity directly through the ionic current $I_{\mathrm{K(Ca)}}$ (Eq. (4.6)). The parameter v_{PDH} instead affects the electrical activity indirectly through its effects on ATP production and through its downstream inhibitory effects of ATP on the K(ATP) current (Eq. (4.8)). We now determine how variations of these parameters affect the overall bursting rhythms produced by the

IOM1.5. For the purposes of quantification, we use the following definitions. We say that the bursting pattern is

- *fast* if the period is less than 2 min;
- *slow* if the period is greater than 2 min;
- *compound* if the burst pattern consists of both long and short interburst intervals, and if the ratio of the longest to the shortest is greater than 1.25.

The results of this classification are shown in Figure 4.7, where the size and colour of the circles indicate the duration and type of the busting, respectively.

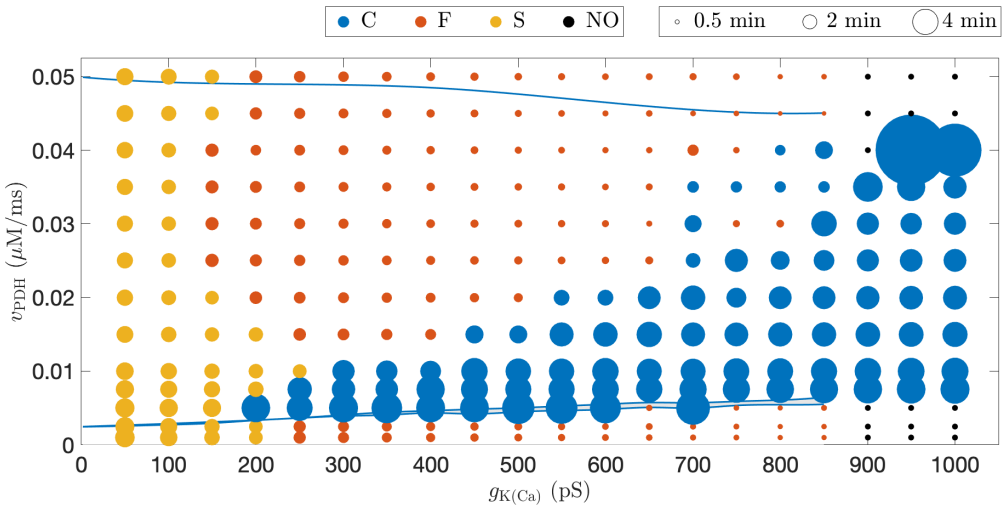

Figure 4.7.: Classification of bursting oscillations with changes in $g_{\mathrm{K(Ca)}}$ and v_{PDH}. The colours and radii of the circles identify the burst pattern and duration, respectively. C, F, S, and NO stand for compound bursting, fast bursting, slow bursting, and no oscillations, respectively. The region of pulsatile FBP oscillations lies between the upper and lower blue curves. Note that there are two bottom lines corresponding to the two curves in Figure 4.3 defining the bistable region.

The first observation we make is that compound bursting only occurs between the lower and upper thresholds for pulsatile FBP oscillations. Thus, during compound oscillations, the FBP time course will be pulsatile. This prediction can be tested experimentally by simultaneously measuring either the membrane potential or Ca^{2+} (to see if compound oscillations are produced) together with a FRET indicator of the FBP concentration.

A second observation is that FBP oscillations showing a pulsatile pattern can occur in conjunction with either fast, slow, or compound bursting oscillations, since all three scenarios are present between the lower and upper thresholds for pulsatile FBP. Both fast and slow bursting can also be produced in the presence of a sawtooth FBP time course (bottom and top regions of the figure). Thus, unless compound

oscillations are produced, it is not possible to determine from the Ca^{2+} time course alone whether or not the glycolytic oscillator is active, as was seen in Figure 4.2.

A third observation from Figure 4.7 is that the burst period decreases with increases in $g_{\mathrm{K(Ca)}}$, up until the point at which compound oscillations are induced or the system becomes silent. In the former case, the glycolytic oscillations are sufficiently large that they begin to periodically initiate and terminate electrical bursting oscillations through their effect on the K(ATP) current. An analysis of compound bursting and the contribution of Ca^{2+} pulses to the glycolytic oscillations that underlie it was performed in [97]. Once the bursting is converted to compound bursting the oscillation period increases dramatically as the compound burst period matches the period of the intrinsic glycolytic oscillator. For large or small values of v_{PDH} there are no glycolytic oscillations, and increasing $g_{\mathrm{K(Ca)}}$ eventually terminates all electrical activity and the model cell comes to rest.

Finally, we point out the large-period oscillations that occur at $g_{\mathrm{K(Ca)}} = 950$ pS and 1000 pS, with $v_{\mathrm{PDH}} = 0.04$ μM/ms. For these parameter combinations, the silent phase between burst episodes becomes extremely long, suggesting that the system is close to a homoclinic bifurcation. Indeed, for larger values of v_{PDH}, the system is at rest with no electrical or metabolic oscillations. However, the precise nature of this bifurcation is an open question.

Figure 4.8 shows c and FBP time courses for a range of values of $g_{\mathrm{K(Ca)}}$ and v_{PDH}, complementing the quantification of Figure 4.7. The value of $g_{\mathrm{K(Ca)}}$ is fixed along each column and increases from left to right, while v_{PDH} is the same along each row and decreases from top to bottom.

Panel A corresponds to the point in the upper left corner of Figure 4.7. Since this is above the upper threshold for pulsatile FBP, the FBP time course exhibits a sawtooth pattern. The FBP values are small since the glycolytic efflux is large ($v_{\mathrm{PDH}} = 0.05$ μM/ms). The resulting bursting pattern is slow because $g_{\mathrm{K(Ca)}}$ has a small value. When $g_{\mathrm{K(Ca)}}$ is increased from 50 pS to 600 pS (panel B) the burst period decreases dramatically, but the FBP time course retains the sawtooth pattern. At $g_{\mathrm{K(Ca)}} = 900$ pS all electrical activity stops since the K^+ current is so large that electrical impulses are not triggered.

The glycolytic efflux is smaller in the second row of Figure 4.8, where v_{PDH} is reduced to 0.035 μM/ms. The bursting along this row coincides with FBP pulses since this lies in the pulsatile FBP region enclosed by the blue curves in Figure 4.7. At the smallest value of $g_{\mathrm{K(Ca)}}$ (i.e. panel D) shown oscillations are slow, but are now organized by the intrinsic glycolytic oscillator (in contrast to panel A). Increasing $g_{\mathrm{K(Ca)}}$ speeds up the oscillations (panel E) until, eventually, compound bursting

is produced (panel F, $g_{\mathrm{K(Ca)}}$=900 pS) and the period increases significantly. In contrast, panel C shows that for the same value of $g_{\mathrm{K(Ca)}}$ (but a larger value of v_{PDH}), there is no electrical activity at all.

The third row of Figure 4.8 has even less glycolytic efflux ($v_{\mathrm{PDH}} = 0.02$ μM/ms), and as a result, the FBP pulses are much larger in amplitude than in the second row. Interestingly, the slow bursts in panel G seem to split into two shorter bursts in panel H, creating compound oscillations. The number of oscillations per compound bursting episode increases as $g_{\mathrm{K(Ca)}}$ is further increased, and the duration of each active phase decreases (panel I).

In the last row of Figure 4.8 the glycolytic efflux rate is sufficiently low that the system is below the lower threshold for FBP pulses and intrinsic glycolytic oscillations. The low glycolytic efflux means that the FBP levels are also much higher than in the other panels of Figure 4.8. Panel J shows slow bursting with $g_{\mathrm{K(Ca)}}$=50 pS, which becomes much faster when $g_{\mathrm{K(Ca)}}$ is increased to 600 pS (panel K). At the largest $g_{\mathrm{K(Ca)}}$, value ($g_{\mathrm{K(Ca)}}$=900 pS) shown all electrical activity stops (panel L), just as in panel C which was also outside the window for intrinsic glycolytic oscillations. We note that the mean FBP level increases with $g_{\mathrm{K(Ca)}}$ along this row, even though v_{PDH} is fixed. This is because the mean Ca^{2+} level is lower at higher values of $g_{\mathrm{K(Ca)}}$, and the lower Ca^{2+} results in less glycolytic efflux, causing FBP to increase.

Finally, for the same parameter grid shown in Figure 4.7, we compute the mean value and the amplitude of FBP oscillations (Figure 4.9). Clearly, the highest mean values of FBP oscillation are reached when the glycolytic efflux is small and the glycolytic oscillator is off (bottom region of Figure 4.7). As v_{PDH} increases and we move beyond the bistable region (middle part), the glycolytic oscillator is activated and the sawtooth-like pattern of FBP is transformed into pulses. This results in a drastic decrease of the mean value and a significant increase in the amplitude. Interestingly, the amplitude decreases as the glycolytic efflux becomes larger and larger, but FBP keeps oscillating around almost the same mean value. We eventually cross the top threshold that turns off the glycolytic oscillator and FBP shows a sawtooth pattern again. In this scenario, FBP values are very low due to the very high glycolytic efflux.

We stress that experimental data published thus far only show FBP oscillations when β-cell islets exhibit slow bursting. No data have been published showing FBP oscillations during compound bursting, which is a prominent behaviour in islets. One of the main results of this section is that, in the IOM1.5, compound bursting is always due to intrinsic glycolytic oscillations. It has been shown previously that compound bursting can be produced by a model without glycolytic oscillations [12], but this was in a limited parameter range and there is no experimental evidence

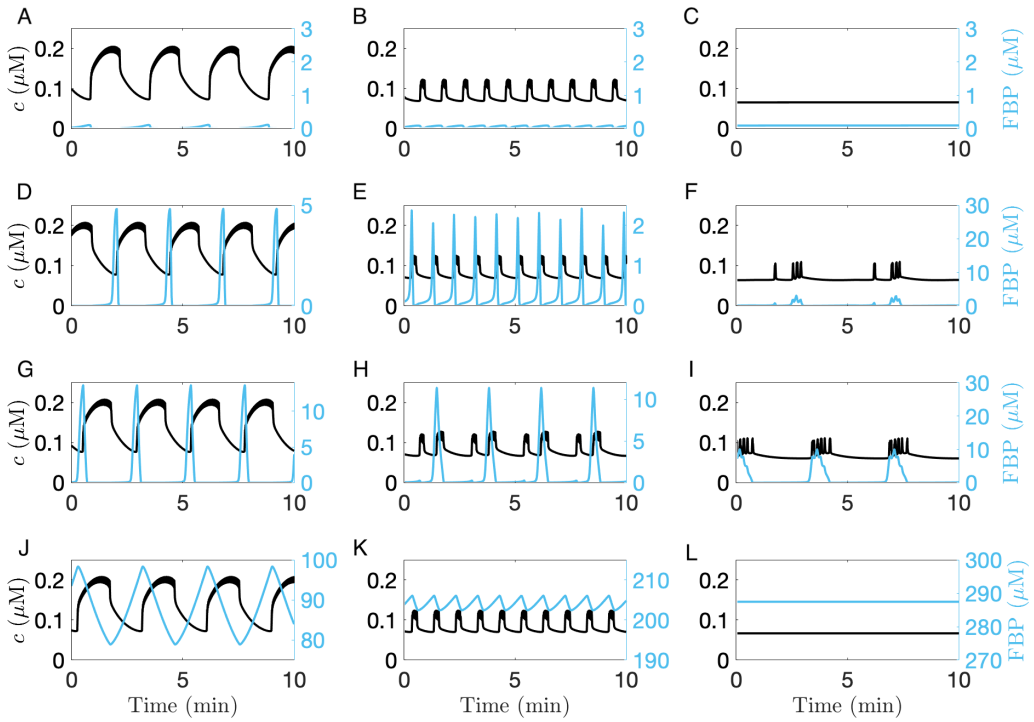

Figure 4.8.: Calcium and FBP time courses taken over a grid of $g_{K(Ca)}$ and v_{PDH} values. Specific values are: $v_{PDH} = 0.05$ μM/ms (top row), $v_{PDH} = 0.035$ μM/ms (second row), $v_{PDH} = 0.02$ μM/ms (third row), $v_{PDH} = 0.001$ μM/ms (bottom row); $g_{K(Ca)} = 50$ pS (left column), $g_{K(Ca)} = 600$ pS (middle column), $g_{K(Ca)} = 900$ pS (right column).

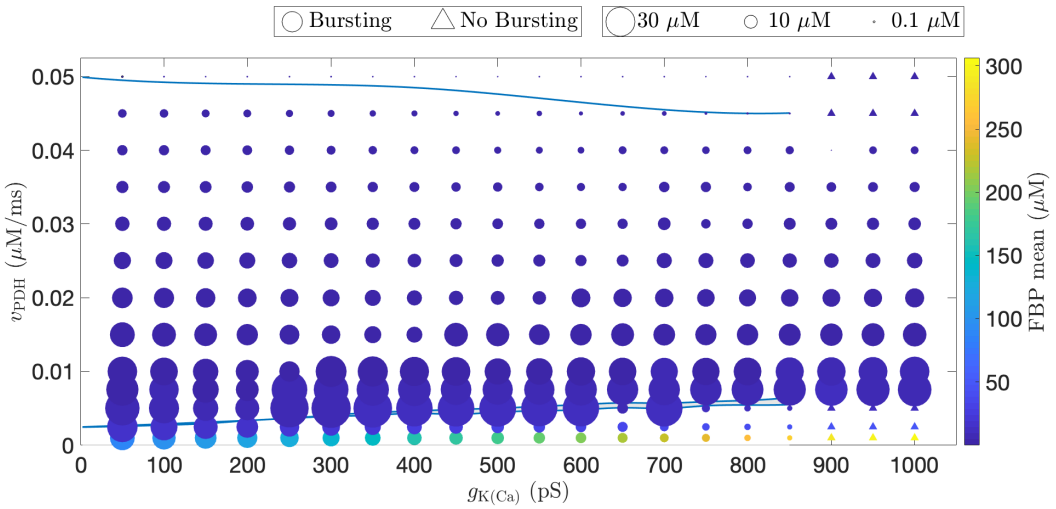

Figure 4.9.: Amplitude and mean of FBP time courses with changes in $g_{K(Ca)}$ and v_{PDH}. The colours and radii of the circles identify the mean value and amplitude of FBP oscillation, respectively. The upper and lower curves enclose the region of pulsatile FBP oscillations. The lower curves are the two curves shown in Figure 4.3, defining the bistable region.

that this alternate mechanism occurs in β-cells. Thus, we predict that if FBP were

measured in a compound bursting islet, then the FBP time course would be pulsatile, not sawtooth.

4.4 Model Predictions and Experimental Findings

Experimental data support a model in which metabolic oscillations in islets are sometimes driven by Ca^{2+} feedback and sometimes due to an intrinsic glycolytic oscillator. We have shown that in the IOM1.5, the oscillation mechanism depends on parameter values in both the electrical ($g_{\mathrm{K(Ca)}}$) and metabolic (v_{PDH}) subsystems, and for the appropriate combination, the model can replicate different scenarios such as various bursting rhythms and FBP patterns (Figure 4.7) that are observed in experiments.

In the following, we suggest two protocols that could be used to analyze the β-cell oscillatory activity. We perform experiments *in silico*, and we show the model predictions. The first protocol explores the origin of islet oscillations (Section 4.4.1), while the second focuses on the nature of these oscillations by investigating the isoform of the PFK enzyme (Section 4.4.2).

4.4.1 Diazoxide and KCl as Tools for Studying the Nature of Islet Oscillations

In the previous section, we used the FBP time course to determine whether the glycolytic oscillator was activated. We also showed (Figure 4.2) that slow Ca^{2+} oscillations, and the accompanying ATP oscillations, can look quite similar regardless of whether the glycolytic oscillator is on or off.

We now present another way to distinguish between mechanisms behind islet oscillations.

The protocol consists of two steps.

1. We first add the pharmacological agent diazoxide (Dz) to an islet in stimulatory glucose. This agent activates K(ATP) channels in β-cells, thus increasing the K(ATP) current and terminating all spiking activity. We simulated the application of Dz at $t = 10$ min by increasing $g_{\mathrm{K(ATP)}}$ from 25000 pS to 37000 pS.

2. In the second step, we induce cell depolarization by adding potassium chloride (KCl), which increases the K^+ Nernst potential and elevates the calcium

concentration. We simulated the addition of KCl at $t = 40$ min by increasing V_K from -75 mV to -60 mV.

The results of this protocol are shown in Figure 4.10 for a range of v_{PDH}.

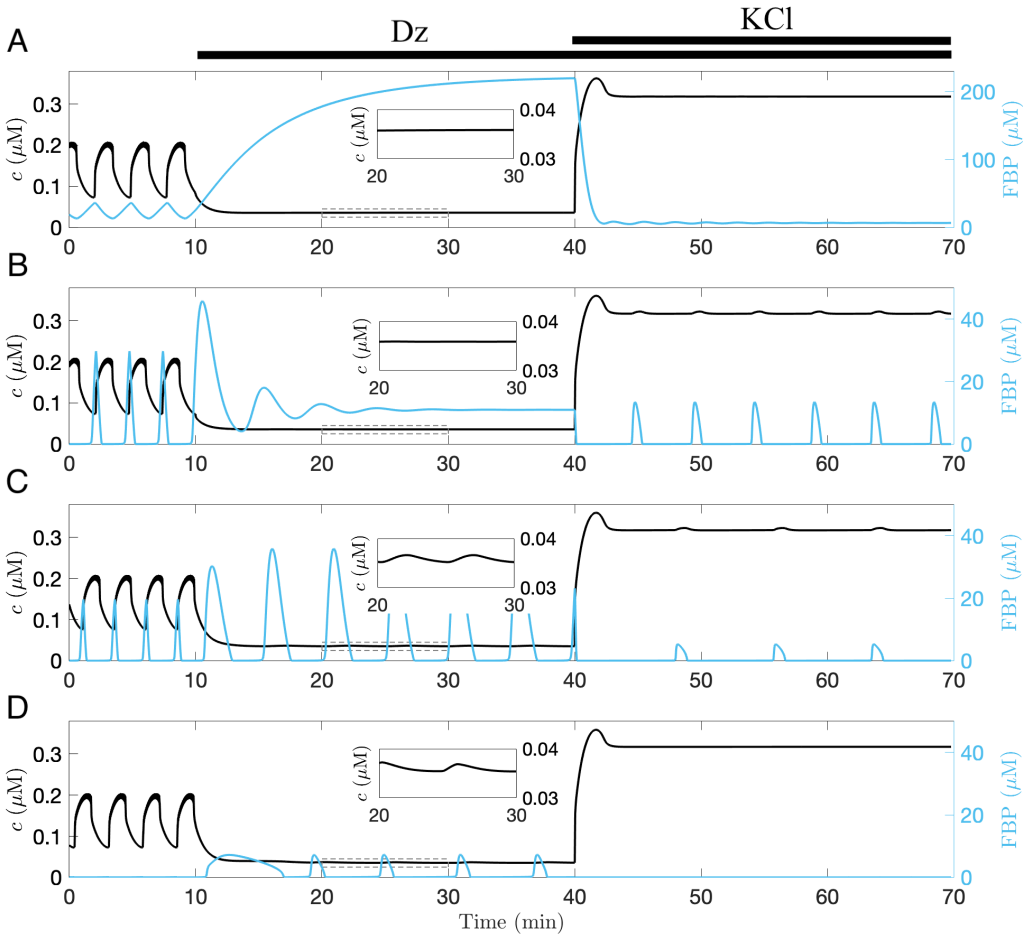

Figure 4.10.: Ca^{2+} and FBP time courses for different value of v_{PDH}. At $t = 10$ min, the Dz is injected and at $t = 40$ min the KCl is added as well. Specific values are: $v_{\mathrm{PDH}} = 0.002$ μM/ms (A), $v_{\mathrm{PDH}} = 0.009$ μM/ms (B), $v_{\mathrm{PDH}} = 0.015$ μM/ms (C), and $v_{\mathrm{PDH}} = 0.05$ μM/ms (D). In all cases, $g_{\mathrm{K(Ca)}} = 50$ pS.

For $v_{\mathrm{PDH}} = 0.002$ μM/ms (Figure 4.10A) the glycolytic oscillator is not initially engaged, so the FBP oscillations have a sawtooth shape. When Dz is applied, the electrical bursting and large Ca^{2+} oscillations stop, and so do the FBP oscillations. The FBP now increases to a plateau. When KCl is added, the Ca^{2+} concentration increases and the FBP level crashes. The rise of FBP with Dz application reflects the fact that the decline in c shuts off most glycolytic flux through its action on the PDH enzyme, so FBP builds up. When c is elevated by KCl, the resulting increase in the flux through glycolysis consumes the FBP whose concentration rapidly declines. This simulation can be thought of in terms of Figure 4.6B. Prior to the application of

Dz, the system moves within region $\mathcal{A}$, below the curve of Hopf bifurcations, and it remains in that region even after Dz and KCl applications.

In Figure 4.10B, we consider the same protocol with a larger value of the glycolytic flux ($v_{\mathrm{PDH}} = 0.009$ μM/ms). The model cell is initially bursting with pulsatile glycolytic oscillations. When Dz is applied, the electrical bursting again stops and, after some transient damped oscillations, also the metabolic oscillations terminate. However, unlike the previous case, the metabolic oscillations can be rescued by increasing the Ca^{2+} concentration with KCl. In terms of Figure 4.6B the system initially moved within region $\mathcal{C}$, but with Dz application, it fell into region $\mathcal{A}$, where there are no glycolytic oscillations. The addition of KCl increases c so that the system shifted back into region $\mathcal{C}$, thus restarting the glycolytic oscillator.

For $v_{\mathrm{PDH}} = 0.015$ μM/ms (Figure 4.10C), the FBP oscillations persist even though the electrical bursting and large Ca^{2+} oscillations have stopped by adding Dz. Instead, there are small subthreshold Ca^{2+} oscillations (see inset), reflecting small fluctuations in the cell's membrane potential due to the continuing metabolic oscillations (the oscillatory ATP acts on K(ATP) channels). When the cell is depolarized at $t = 40$ min by the simulated application of KCl, the Ca^{2+} concentration is also increased and subthreshold oscillations in Ca^{2+} persist, as do FBP oscillations. Prior to the application of Dz, the system moves within region $\mathcal{C}$. Upon application of Dz, the mean of the small amplitude fluctuations in c continues to lie in region $\mathcal{C}$. When the addition of KCl is simulated, the system moves rightward in the diagram, again staying within region $\mathcal{C}$. Thus, under all conditions, the glycolytic subsystem is in an oscillatory state.

Figure 4.10D ($v_{\mathrm{PDH}} = 0.05$ μM/ms) corresponds to the opposite scenario with respect to panel B. Here, the glycolytic oscillations are initially small and have a sawtooth pattern, since the system lies in region $\mathcal{D}$ of Figure 4.6B. Application of Dz stops both the bursting and the large Ca^{2+} oscillations, but it also activates the glycolytic oscillator, so there are now pulsatile FBP oscillations. This occurs because the reduction in c moved the system into region $\mathcal{C}$ where the glycolytic oscillator is active. When the application of KCl is simulated, the elevation in c moves the system towards region $\mathcal{D}$ once again, and it terminates the FBP oscillations.

In light of the above results, the model predicts that when bursting oscillations are driven by an intrinsic glycolytic oscillator, metabolic oscillations may or may not persist with the application of Dz, and thus subthreshold Ca^{2+} oscillations may or may not be produced. However, if metabolic oscillations are terminated, they can be rescued with cell depolarization via KCl. In contrast, in conditions where bursting is not driven by an intrinsic glycolytic oscillator, the application of Dz may actually activate the glycolytic oscillator, but depolarization by the application of KCl will

inactivate it. In other words, application of KCl facilitates metabolic oscillations (in the presence of Dz) when the cell initially has an active glycolytic oscillator, and it suppresses metabolic oscillations when the glycolytic oscillator is not initially activated.

These predictions are consistent with recent experimental findings. In [18], subthreshold Ca^{2+} oscillations have been measured in islets exposed to a low glucose level. This preparation is similar to the exposure of islets to a stimulatory glucose concentration along with the K(ATP) channel activator diazoxide, in that lowering the glucose level opens K(ATP) channels, just as diazoxide does. In another experiment, diazoxide was added to islets in stimulatory glucose just as in our simulations, and the reduced nicotinamide adenine dinucleotide (phosphate) (NAD(P)H) fluorescence was measured as a readout of metabolism [65]. It was found that in some cases the metabolic oscillations persisted during the application of diazoxide, as in Figure 4.10C. In some cases, where metabolic oscillations did not persist, they could be rescued by depolarizing the islet with KCl, as in Figure 4.10B. Finally, in some cases, the NAD(P)H oscillations were not rescued by KCl, as in Figures 4.10A, D. In a later study [66], the fluorescent sensor PKAR was used to detect the level of FBP. It was found that the PKAR signal initially had a sawtooth pattern, and upon application of Dz, it stopped oscillating and increased significantly. When KCl was later applied, the PKAR level crashed. Our model (Figure 4.10A) resembles this experimental behaviour.

4.4.2 Different Isoforms of the Enzyme PFK

In this section, we investigate the nature of metabolic oscillations using the second protocol mentioned in Section 4.4.

Up to this point, we assumed the glycolytic oscillations to be produced only by the muscle isoform of the allosteric enzyme PFK, named PFK-M. The ability of PFK-M to generate metabolic oscillations was demonstrated in muscle extracts by Tornheim in 1973 [94], and is the basis for the intrinsic glycolytic oscillations produced by our model. At least two other isoforms of PFK are expressed in β-cells: the brain isoform PFK-C and the liver isoform PFK-L. Although all three isoforms are expressed in β-cells, the isoform responsible for most of the PFK activity is PFK-M [98].

We consider now a lower expression of the M-type PFK and we investigate the effect that this would have on the parameter window for intrinsic glycolytic oscillations. This type of effect has been already explored in [17]. However, the model used for that study was the DOM1.5 without Ca^{2+} feedback onto glycolysis. We re-

examine the question in the context of the IOM1.5. In order to better understand the consequences of the considered reduction, we start by briefly describing the main characteristics of PFK enzyme activation and inhibition.

The PFK Activation and Inhibition

In the early 1970s, Tornheim *et al.* showed that in muscle extracts the allosteric enzyme PFK is activated by FBP and AMP, and inhibited by ATP [94]. The opposite effect of FBP and ATP was interpreted as a competition where FBP tries to reduce the effectiveness of the inhibition by ATP, without fully reversing it [93]. It was shown that PFK-C and PFK-L have a lower affinity for FBP feedback [20] and a higher affinity for ATP [34, 35] than PFK-M. Because of the similar nature of PFK-C and PFK-L, we do not include PFK-L in our model but we consider a second generic isoform that we labelled PFK-C, in addition to PFK-M.

Figure 4.11 illustrates an example of how the ATP inactivation and FBP activation affect a generic PFK isoform flux rate J_{PFK}. In the simulations, we use the J_{PFK} definition given in Eq. (4.15) with all the variables clamped except for ATP (in panel A) or FBP (in panel B). In this equation, the parameters K_2 and K_4 represent FBP and ATP dissociation constants, respectively. Thus, we vary them in order to simulate different affinities for the metabolic variables.

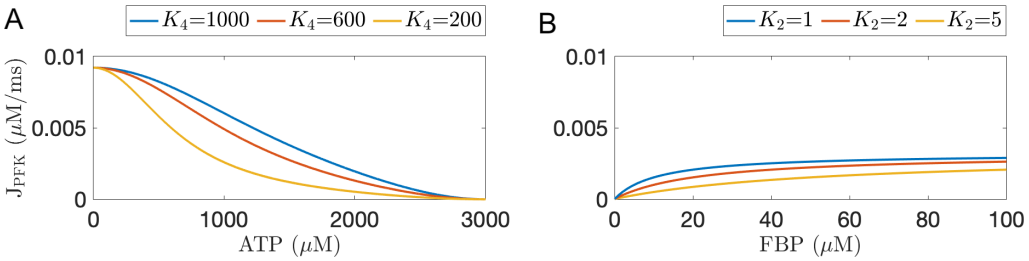

Figure 4.11.: Example of ATP inhibitory and FBP activation effects on the PFK flux rate, J_{PFK}. The parameters K_2 and K_4 represent FBP and ATP dissociation constants, respectively.

By assuming a rapid equilibrium in Eq. (4.16) as in [86], the dissociation constants, K_2 and K_4, correspond to the Michaelis constant, K_m, in the reaction rate equation

$$v = v_{max}\frac{S}{S + K_m}\ , \tag{4.22}$$

where v is a generic reaction speed whose maximum is v_{max}, and S is the corresponding substrate. Also, the Michaelis constant K_m corresponds to the substrate concentration at which the reaction rate is at half-maximum. Therefore, a small

K_m is an indicator of high affinity, since it means little substrate must be present to saturate the enzyme; a high K_m suggests a low affinity.

Figure 4.11A shows the changes in J_{PFK} when the affinity for ATP is increased by decreasing K_4 from 1000 μM to 200 μM. The inhibition effect of ATP on PFK is stronger as K_4 is reduced, and the total reaction rate decreases. In Figure 4.11B, FBP affinity is decreased by increasing K_2 from 1 μM to 5 μM, and once again the total flux J_{PFK} decreases, since a small affinity for FBP results in the reduction of the effect of the activation factor.

Ideally, the blue curves in the two panels correspond to the M-type isoform, while the yellow represent the C-type.

Slow Bursting with Reduced PFK-M Fraction

Following Tornheim's idea, we interpret the interaction between M and C isoforms of PFK as a contest in which they compete for the resource, namely the substrate F6P. We hypothesize that F6P binds preferentially to PFK-M in a wild-type, namely the phenotype that prevails in a species in natural conditions. However, in the absence of this isoform, F6P binds to the C-type. To simulate these dynamics, we present two different mathematical approaches.

The first considers the possibility that some fraction, $M_{\mathrm{frac}} \in [0, 1]$, of the total PFK is of M-type and the remainder is of C-type. The total PFK flux then is

$$J_{\mathrm{PFK}} = M_{\mathrm{frac}} J_{\mathrm{PFK-M}} + (1 - M_{\mathrm{frac}}) J_{\mathrm{PFK-C}}, \tag{4.23}$$

where $J_{\mathrm{PFK-M}}$ and $J_{\mathrm{PFK-C}}$ are the portions of flux due to the M- and C-type isoforms, respectively. The two fluxes, $J_{\mathrm{PFK-M}}$ and $J_{\mathrm{PFK-C}}$, are defined as in Eq. (4.15) but with different values for the parameters K_2 and K_4. In particular, $K_2 = 1$ μM and $K_4 = 1000$ μM for $J_{\mathrm{PFK-M}}$, while $K_2 = 2$ μM and $K_4 = 100$ μM for $J_{\mathrm{PFK-C}}$ since the C-type isoform has a lower affinity for FBP and a higher affinity for ATP.

Figure 4.12A illustrates two examples of slow Ca^{2+} oscillations. In each case, the oscillations are produced even though some M-type PFK has been replaced with C-type. In the top example, only 40% of the PFK is M-type ($M_{\mathrm{frac}} = 0.4$), while in the bottom example none of the PFK is of M-type ($M_{\mathrm{frac}} = 0$). Clearly, in this model slow Ca^{2+} oscillations do not require M-type PFK for their production. Note, however, that in both cases the FBP oscillations have a sawtooth form since the glycolytic oscillator is not active.

Replacing some fraction of PFK-M with PFK-C causes a change in the window for intrinsic glycolytic oscillations. To see this, we return to the glycolytic subsystem, treating c as a parameter as in Figure 4.6B. In Figure 4.12B we show the threshold curves for glycolytic oscillations for five values of M_{frac}. As the fraction of M-type PFK is reduced, the upper threshold curve moves downward, reducing the size of the window for intrinsic glycolytic oscillations. When $M_{\text{frac}} = 0.35$ the upper and lower threshold curves have coalesced, and as M_{frac} is decreased further the region of intrinsic glycolytic oscillations decreases in size and becomes restricted to larger values of the cytosolic Ca^{2+} concentration. Thus, the likelihood that slow Ca^{2+} oscillations are driven by intrinsic glycolytic oscillations in the full IOM1.5 declines as PFK-M is replaced by PFK-C. Moreover, if the percentage of M-type PFK falls below roughly 25% it becomes very unlikely or impossible for this to occur.

Figure 4.12 indicates that slow Ca^{2+} oscillations should be possible in islets in which most or all of the M-type PFK is replaced with another isoform. This prediction was made recently with a somewhat different β-cell model [62]. Another observation is that slow Ca^{2+} oscillations produced in β-cells under this condition should coincide with a sawtooth FBP time course since in this condition there is no intrinsic glycolytic oscillation. We note that so far it has not been determined whether FBP oscillates in the islets in which PFK-M protein has been knocked out and, if so, whether the time course is a sawtooth-like or not.

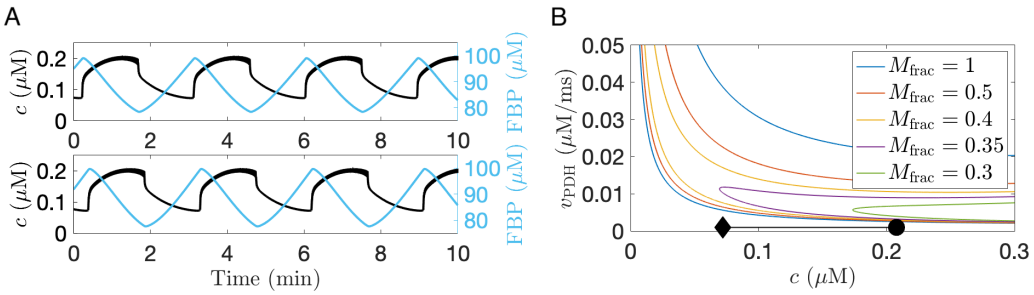

Figure 4.12.: (A) Ca^{2+} and FBP time courses for $g_{\text{K(Ca)}} = 50$ pS, $v_{\text{PDH}} = 0.001$ μM/ms, and $M_{\text{frac}} = 0.4$ (top) and $M_{\text{frac}} = 0$ (bottom). (B) Two-parameter bifurcation structure of the glycolytic subsystem showing the Hopf bifurcation curves for various values of M_{frac}, together with the projections of the Ca^{2+} oscillations from panel A (black segment).

We have shown that changes in the glycolytic efflux or the clamping of Ca^{2+} can move the system from one oscillatory regime to the other. In fact, oscillations can persist even after the partial or complete replacement of the rhythmogenic enzyme PFK-M with a non-rhythmogenic isoform (Figure 4.12). This result is consistent with the data published in [75] showing that slow Ca^{2+} oscillations can occur in islets in which the PFK-M protein has been genetically knocked out (and where it is expected that other PFK isoforms will be upregulated).

With this approach, the increase in PFK-C fraction comes at the expense of PFK-M. However, it has been recently hypothesized that the PFK-M and PFK-C populations are always expressed in β-cells, independently from each other, and that only their activities vary. That is, there is no increase in gene expression of one isoform in response to knock-out of the other. To simulate this scenario, we redefine the total PFK flux, J_{PFK}, as follows:

$$J_{\mathrm{PFK}} = J_{\mathrm{PFK-M}} + J_{\mathrm{PFK-C}} \ , \tag{4.24}$$

where the contribution of each isoform is given by

$$J_{\mathrm{PFK}-i} = v_{\mathrm{PFK}-i} \frac{w_{1110-i} + k_{\mathrm{PFK}} \sum_{i,j,l\in\{0,1\}} w_{ij1l-i}}{\sum_{i,j,k,l\in\{0,1\}} w_{ijkl-i}}, \qquad i = \{\mathrm{M}, \mathrm{C}\}. \tag{4.25}$$

The maximum rates $v_{\mathrm{PFK}-i}$ are different for each PFK isoform, and the weights w_{ijkl-i} are defined as in the previous case. Figure 4.13 depicts the mean value of the flux J_{PFK} and the FBP amplitude obtained by running a grid of simulations over the range $v_{\mathrm{PFK-M}}$ and $v_{\mathrm{PFK-C}} \in [0, 0.001]$ μM/ms.

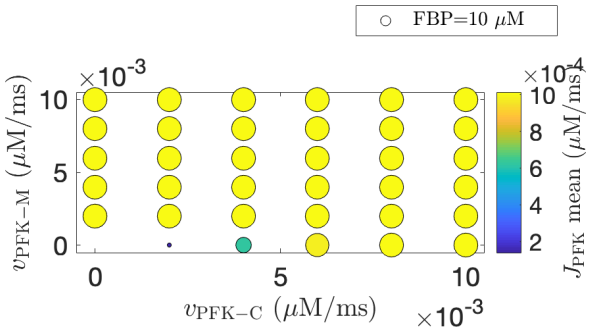

Figure 4.13.: Overview of the mean values of FBP and J_{PFK} oscillations obtained by running a grid of simulations over the range $v_{\mathrm{PFK-M}}$ and $v_{\mathrm{PFK-C}} \in [0, 0.001]$ μM/ms. The color and radii of the circles identifies the mean value of J_{PFK} and FBP oscillations, respectively. In all cases, v_{PDH}=0.002 μM/ms and $g_{\mathrm{K(Ca)}}$=50 pS.

Clearly, if both maximum rates are zero, the glycolysis process stops, no ATP is produced, and the β-cell is silent. However, if at least one of the two isoforms is present, the cell enters in a slow bursting regime (with sawtooth-like FBP for the choice of v_{PDH} and $g_{\mathrm{K(Ca)}}$). Interestingly, the mean value of the flux does not change significantly across the grid, except for two scenarios on the bottom that correspond to a cell with knocked out PFK and very little PFK-C activity. Consequently, FBP amplitude is not affected by the changes in $v_{\mathrm{PFK-C}}$ and $v_{\mathrm{PFK-M}}$.

We now investigate the contribution of each isoform to the total PFK activity using the new approach. For this purpose, we propose the following protocol in which either PFK-C or PFK-M, or both, is knocked out in a wild-type β-cell.

The protocol we use consists of a progressive knocking out of the PFK isoform.

1. In the first step, PFK-C is genetically knocked out in a wild-type cell at $t = 15$ min. In this step, the glycolytic oscillations are mediated only by PFK-M. This is simulated by decreasing $v_{\mathrm{PFK-C}}$ from 0.008 μM/ms to 0 μM/ms, while $v_{\mathrm{PFK-M}}$ is kept equal to 0.008 μM/ms.

2. At $t = 60$ min, the M-type isoform is knocked out (so that both isoforms are no longer present). In this case, both maximum rates, $v_{\mathrm{PFK-C}}$ and $v_{\mathrm{PFK-M}}$, are set to 0 μM/ms.

The results of this protocol are shown in Figure 4.14 for $g_{\mathrm{K(Ca)}}$=50 pS and v_{PDH}=0.002 μM. For this simulation, we lower the parameter r in Eq. (4.19) from 1 to 0.87 to control the glycolysis independent component in the ADP consumption, or equivalently the ATP production. In the wild-type cell (blue), the $J_{\mathrm{PFK}-C}$ (panel D) is negligible with respect to $J_{\mathrm{PFK}-M}$ (panel B) and the flux J_{PFK} (panel F) is mostly due to the M-type isoform. Thus, knocking out the PFK-C (orange) has little effect on the bursting activity and Ca^{2+}, ATP, and FBP patterns (left column) do not change post PFK-C knock out. When the M-type isoform is subsequently knocked out (green), the bursting activity stops and the cell is silent.

We now present the results of a second version of the same protocol. In this case, at $t = 15$ min the M-type isoform is knocked out by setting $v_{\mathrm{PFK-M}}$ to 0 μM/ms, instead of PFK-C as in the previous version. The results of this protocol are shown in Figure 4.15 for the same parameter combination $g_{\mathrm{K(Ca)}}$=50 pS and v_{PDH}=0.002 μM. Interestingly, Ca^{2+}, ATP, and FBP time series (left column) in the wild-type are remarkably similar to the ones obtained after the first step of the protocol, i.e., after knocking out PFK-M, except for a very short initial transient in the metabolic variables. However, this result hides a very different nature of the metabolic oscillations. In the wild-type cell, the flux through the PFK reaction (panel F) is essentially mediated by the M-type isoform (pane B) and the contribution of component $J_{\mathrm{PFK}-C}$ is insignificant (pane D), as we have already pointed out in the previous protocol. However, in this scenario, the C-type takes over in absence of PFK-M due to the knock out, and keeps the PFK activity oscillating about the same mean value providing the rythmogenic mechanism. Once again, if both isoforms are knocked out, the bursting activity stops (green curve).

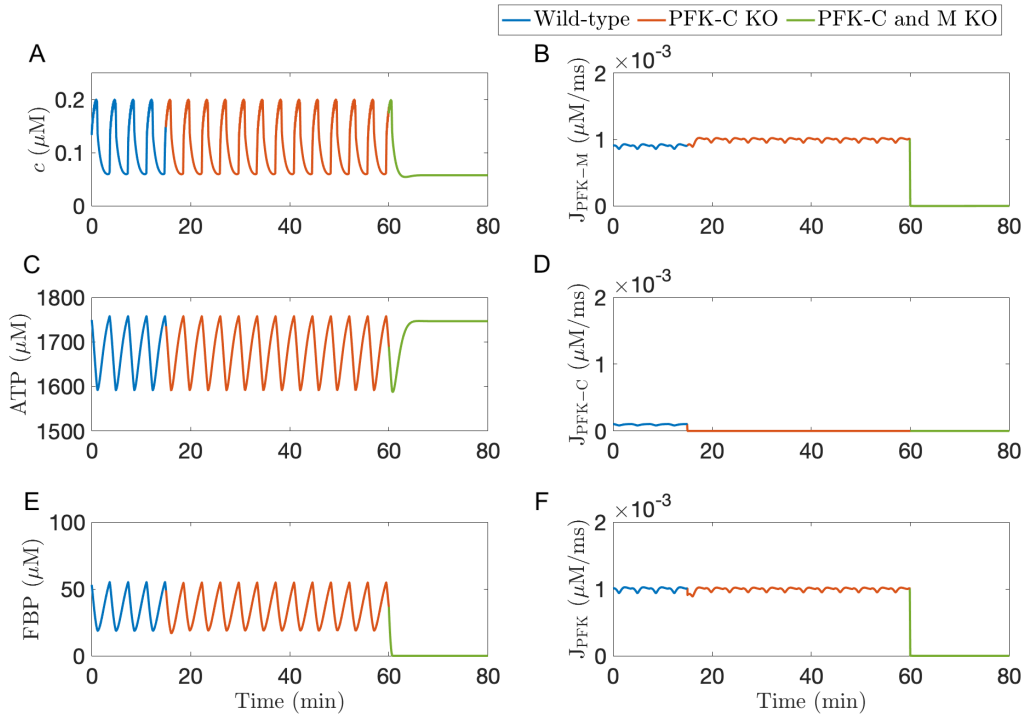

Figure 4.14.: Time courses of Ca^{2+}, ATP, and FBP (left column) and $J_{\mathrm{PFK}-M}$, $J_{\mathrm{PFK}-C}$, and J_{PFK} (right column) for different value of $v_{\mathrm{PFK-C}}$ and $v_{\mathrm{PFK-M}}$. Specific values are: $v_{\mathrm{PFK-M}}$=$v_{\mathrm{PFK-C}}$=0.008 μM/ms (blue curve), $v_{\mathrm{PFK-M}}$=0.008 μM/ms and $v_{\mathrm{PFK-C}}$=0 μM/ms (orange curve), and $v_{\mathrm{PFK-M}}$=$v_{\mathrm{PFK-C}}$=0 μM/ms (green curve). In all cases, v_{PDH}=0.002 μM and $g_{\mathrm{K(Ca)}}$=50 pS, and r=0.87.

The results show the ability of PFK-C to compensate for the absence of PFK-M and to support slow oscillations, providing a reasonable explanation for the slow Ca^{2+} oscillations observed in islets with knocked out PFK-M protein in [75].

We also observe that the model predicts ATP plateauing at a relatively high value when the glycolytic oscillator is turned off. Physiologically, the ATP concentration should decrease in the absence of glycolytic activity since there would be no ATP production due to the absence of glycolytic products, while ATP would still be consumed by the ATPase (which is responsible for lowering the Ca^{2+} concentration).

To improve this non-physiological behaviour, we suggest including explicitly the hydrolysis of ATP to ADP by Ca^{2+} pumps in the plasma and ER membranes as production force for the ADP. We discuss this in Chapter 5.

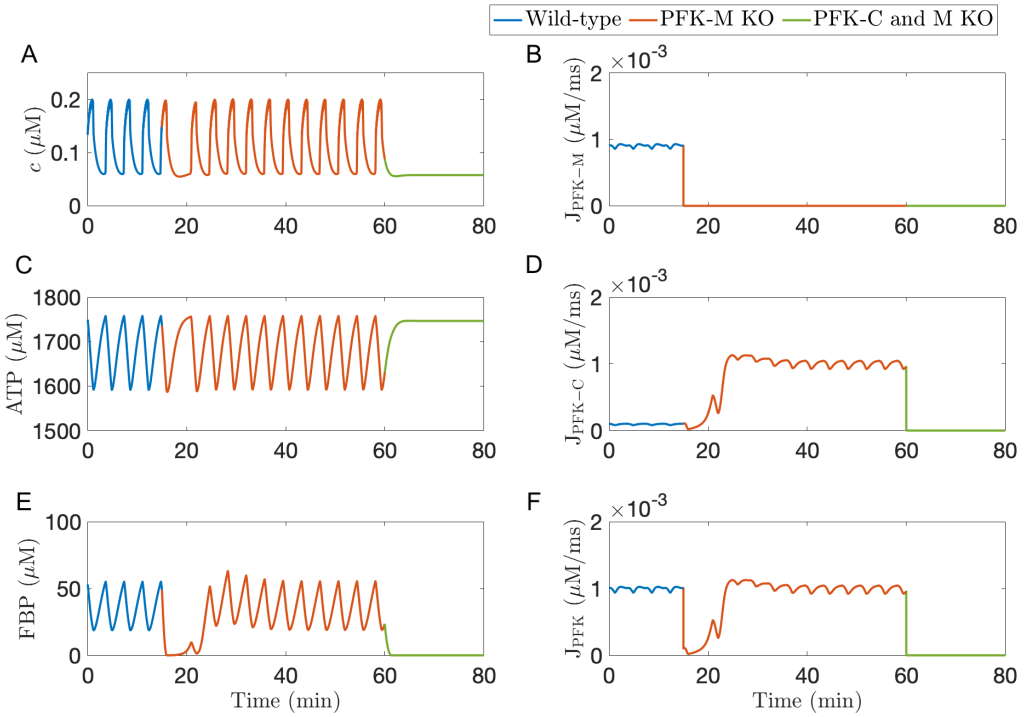

Figure 4.15.: Time courses of Ca^{2+}, ATP, and FBP (left column) and J_{PFK-M}, J_{PFK-C}, and J_{PFK} (right column) for different value of v_{PFK-C} and v_{PFK-M}. Specific values are: v_{PFK-C}=v_{PFK-M}=0.008 μM/ms (blue curve), v_{PFK-C}=0.008 μM/ms and v_{PFK-M}=0 μM/ms (orange curve), and v_{PFK-C}=v_{PFK-M}=0 μM/ms (green curve). In all cases, v_{PDH}=0.002 μM and $g_{K(Ca)}$=50 pS, and r=0.87.

Compound Bursting with Reduced PFK-M Fraction

In the previous section, we looked at the IOM1.5 predictions after knocking out the M-type isoform in a cell in slow bursting mode driven by Ca^{2+} oscillations. Recently, Satin and collaborators have observed compound bursting in β-cells in which PFK-M has been genetically knocked out (unpublished data). In Section 4.3 we concluded that compound oscillations can arise only if the glycolytic oscillator is on. Thus, if the isoform believed responsible for the intrinsic glycolytic oscillations is not present, how can compound bursting still be possible? In this section, we show that the IOM1.5 can account for this result with the right choice of parameters.

We assume that PFK-C is the only isoform expressed by the β-cell by setting v_{PFK-M} to 0 μM/ms in Eq.(4.24). If PFK-C had the same affinities for FBP and ATP as PFK-M, we could easily find a combination of the parameters v_{PDH} and $g_{K(Ca)}$ such that the cell was in the compound bursting mode (Figure 4.7). However, the C-type isoform has a lower affinity for FBP and a higher affinity for ATP, and the Michaelis constants K_2 and K_4 have to be increased and decreased, respectively. Figure 4.16 illustrates this process. The plot at the top left corner represents the scenario in

which the affinities for FBP and ATP do not change from one isoform to the other (i.e. $K_2 = 1\mu$M and $K_4 = 1000\mu$M). From there, the parameter K_2 increases (top to bottom) and the parameter K_4 decreases (left to right).

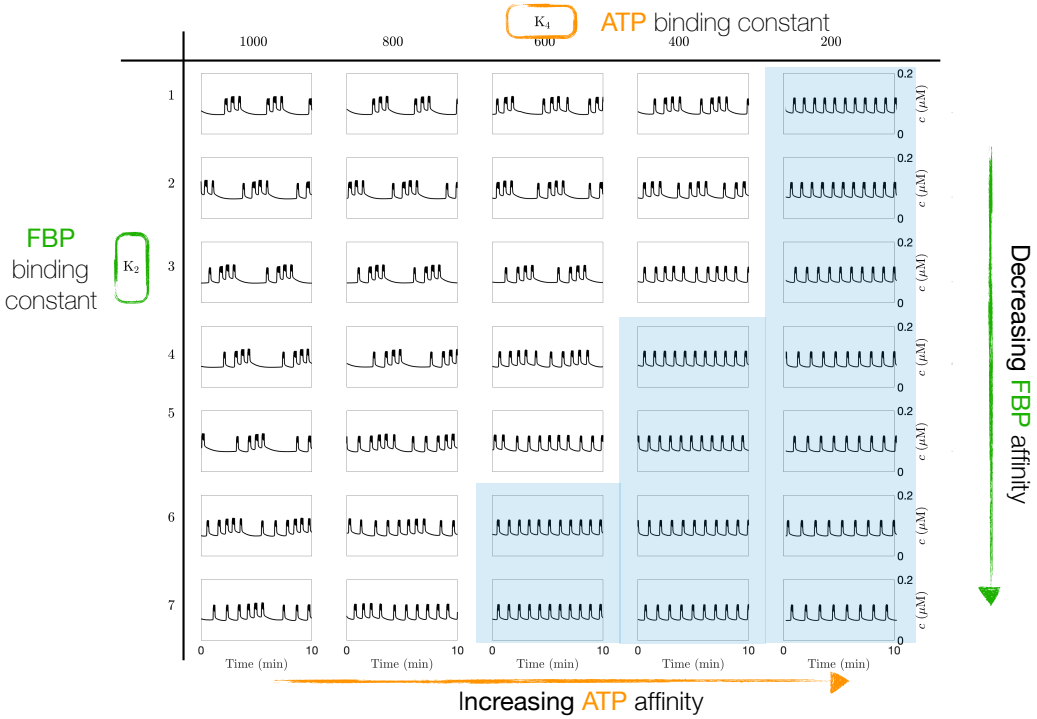

Figure 4.16.: Compound oscillations may or may not persist in β-cell in which PFK-M has been genetically knocked out. The parameter K_2 and K_4 are varied to simulate different PFK-C affinities for FBP and ATP. In all cases, v_{PDH}=0.009 μM/ms, $g_{\mathrm{K(Ca)}}$=650 pS.

The grid is partitioned into two regions: a region in which the compound bursting rhythm is not affected by the different values of the parameters K_2 and K_4, and a region in which the compound bursting disappears and fast bursting arises (scenarios highlighted in blue in Figure 4.16).

Once again, we use bifurcation analysis to study this transition. More specifically, we focus on the glycolytic subsystem (Eq. (4.14)) and on the intersection of F6P and FBP nullclines.

For an excitable system with a cubic-shaped nullcline, the equilibrium is stable if the nullcline of the slow variable intersects the outer branches of the nullcline of the fast variable (Appendix B). In the case of the glycolytic oscillator, FBP is the variable with a cubic-like nullcline. Hence, the glycolytic oscillator is off unless the nullclines intersect on the middle branch of the FBP nullcline. Having predicted that compound bursting can occur only in the presence of an active GO, compound bursting can arise only if the nullclines intersect in the middle branch. Therefore, we

analyze in detail the position of the nullclines as the parameters K_2 and K_4 change.

Among the possible outputs shown in Figure 4.16, we select the scenario with $K_2 = 3$ μM and $K_4 = 400$ μM because of its particular location: the bursting is compound but becomes fast if K_2 increases or K_4 decreases. Hence, we look at the F6P and FBP nullclines (Figure 4.17C). For the considered parameter set, the F6P nullcline (blue curve) intersects the FBP nullcline (orange curve) in the middle branch. Therefore, the GO is active and the cell is in a compound bursting mode. If the parameter K_2 decreases or K_4 increases, the F6P nullcline changes very little, while FBP nullcline moves significantly towards the left (Figure 4.17A and B). Since they still intersect in the middle branch, the bursting is still compound (Figure 4.16). On the other hand, if K_2 increases or K_4 decreases, the FBP nullcline moves rightward (Figure 4.17D and E). Once again, the F6P nullcline does not change much and, consequently, the intersection now occurs on the bottom branch. Therefore, the glycolytic oscillator is now off and the compound bursting is transformed into fast bursting (Figure 4.16).

Nonetheless, the compound bursting lost by increasing K_2 can be restored by changing the value of the maximum rate in the glycolytic efflux, v_{PDH}, or influx, v_{PFK}. For instance, the cell in Figure 4.16 with $K_2 = 7$ μM and $K_4 = 400$ μM (corresponding to Figure 4.17D) is in fast bursting mode with v_{PDH}=0.009 μM/ms and v_{PFK}=0.01 μM/ms (baseline values). However, if we lower the maximum rate in the glycolytic outflux, v_{PDH}, from 0.009 μM/ms to 0.008 μM/ms, thus reducing the glycolytic efflux, the FBP nullcline moves leftward (Figure 4.18A). The intersection is now occurring on the middle branch, but too close to the knee to have the glycolytic oscillations drive the burst, and the bursting is still fast. On the contrary, if v_{PDH}=0.006 μM/ms, the two nullclines intersect in the middle branch far from the knee and the intrinsic glycolytic oscillations are recovered (Figure 4.18B). The column on the right illustrates the corresponding Ca^{2+} time courses and the transition from fast bursting (panel A) to compound bursting (panel B).

The same result can be obtained by increasing the glycolytic influx, i.e., by raising the maximum flux rate through PFK reaction v_{PFK} (Figure 4.19). As in the previous case, if v_{PFK} does not vary much from the initial value, neither the intrinsic glycolytic oscillations nor the compound busting are restored (panel A). However, if the parameter v_{PFK} is increased from v_{PDH}=0.01μM/ms to 0.04μM/ms (panel B), the FBP nullcline is brought back to the left so that the intersection occurs in the middle branch. Hence, intrinsic glycolytic oscillations and compound bursting are restored.

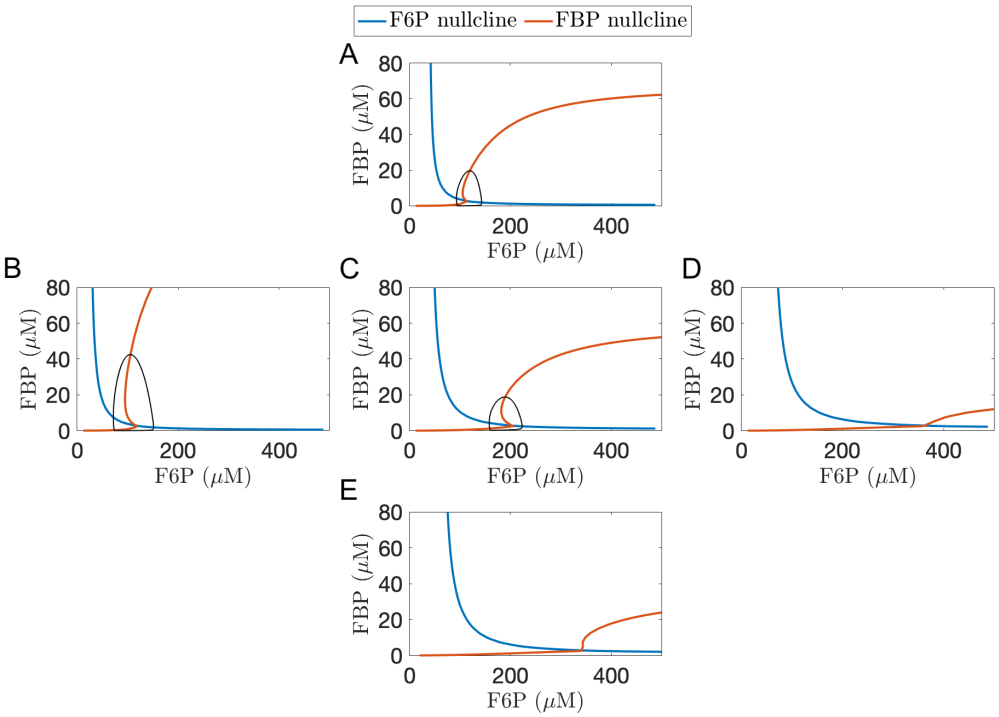

Figure 4.17.: Fast/slow analysis of the glycolytic subsystem with F6P (blue curve) and FBP (orange curve) nullclines, and the projection of the orbit onto the (F6P, FBP)-plane (black curve). Starting from panel (C), PFK-C affinity for ATP is decreased in panel (B) and increased in panel (D); while PFK-C affinity for FBP is increased in panel (A) and decreased in panel (E). The samples values are: (A) $K_2 = 1\mu$M and $K_4 = 400$ μM, (B) $K_2 = 3$ μM and $K_4 = 1000$ μM, (C) $K_2 = 3$ μM and $K_4 = 400$ μM, (D) $K_2 = 3$ μM and $K_4 = 200$ μM, (E) $K_2 = 6$ μM and $K_4 = 400$ μM. In all cases, c=0.077μM and v_{PDH}=0.009 μM/ms.

This protocol can be applied to all the scenarios shown in Figure 4.16. Figure 4.20 illustrates the minimum v_{PDH} and the maximum v_{PFK} values necessary to have compound bursting over the grid of K_2 and K_4 values considered in Figure 4.16.

We note that compound bursting can be restored when FBP and ATP affinities are close to C-type isoform by reducing the consumption or increasing the production of the glycolytic product FBP. However, if the affinity of ATP is very high (K_4=200 μM) compound bursting is lost, and decreasing v_{PDH} or increasing v_{PFK} is not enough to restore it (black dots in Figure 4.20). This occurs because the glycolytic nullclines degenerate when K_4 is too low and changing the flux rates is not enough to restore the initial situation (Figure 4.17E). Biologically, this scenario represents a β-cell with PFK-M protein knocked out and a very strong inhibitory effect of ATP on PFK-C (due to the high affinity) that prevents the activation of the enzyme and then the generation of intrinsic glycolytic oscillations.

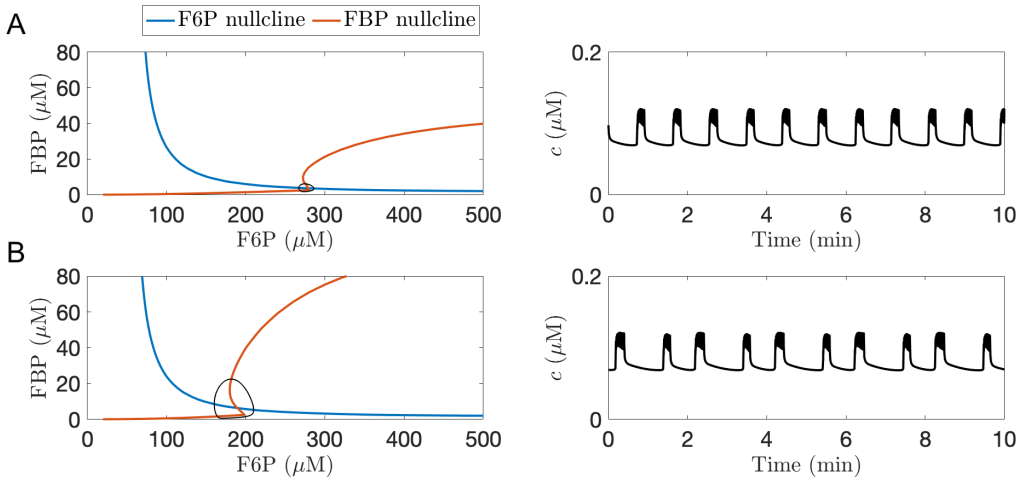

Figure 4.18.: Fast/slow analysis of the glycolytic subsystem with F6P (blue curve) and FBP (orange curve) nullclines, and the projection of the orbit onto the (F6P, FBP)-plane (black curve) Decreasing the maximum rate in the PDH reaction, v_{PDH}, the compound bursting is restored. v_{PDH}=0.008 μM in (A) and 0.006 μM in (B). In both cases, $g_{\mathrm{K(Ca)}}$=650 pS, $K_2 = 6$ μM, $K_4 = 400$ μM, and v_{PFK}=0.01 μM/ms.

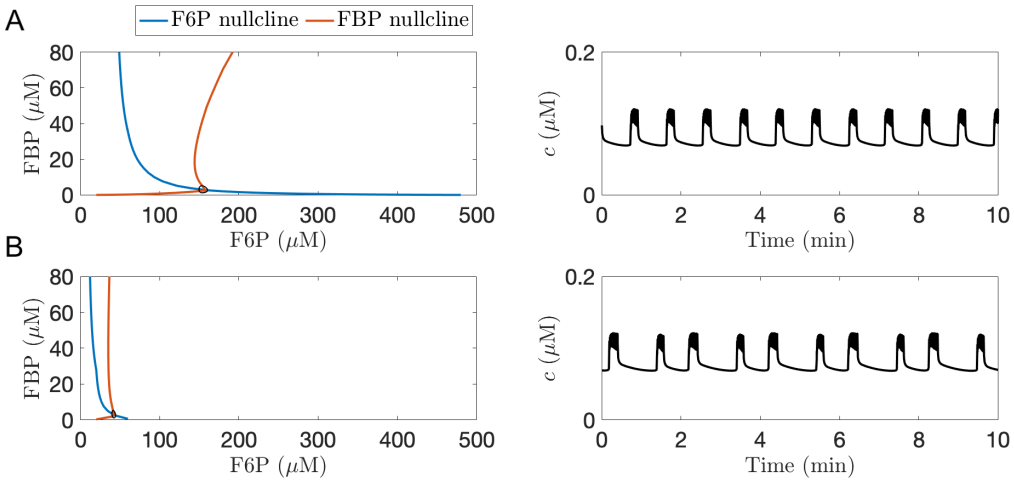

Figure 4.19.: Fast/slow analysis of the glycolytic subsystem with F6P (blue curve) and FBP (orange curve) nullclines. Increasing the maximum rate in the PFK reaction, v_{PFK}, the compound bursting is restored. v_{PFK}=0.02 μM in (A) and 0.18 μM in (B). In both cases, $g_{\mathrm{K(Ca)}}$=650 pS, $K_2 = 6$ μM, $K_4 = 400$ μM, and v_{PDH}=0.009 μM/ms.

4.5 Summary

The IOM1.5 and its predecessor, the IOM1.0, are much more complex than the other models in Bertram-Satin-Sherman school presented in Chapter 3. The payoff for this complexity is a much greater range of potential activity patterns and much greater robustness in the generation of slow or compound oscillations. Indeed, mouse islets

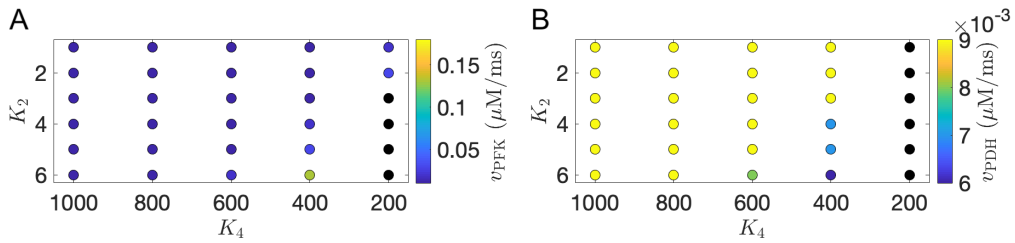

Figure 4.20.: The colors of the circles identify minimum and maximum values of v_{PDH} (left) and v_{PFK} (right) in order to restore compound oscillations. The black dots correspond to the scenarios in which the glycolytic oscillator cannot be turned on by varying only v_{PDH} or v_{PFK}.

produce slow oscillations in activity under various physiological conditions, and even following genetic modification to knock out K(ATP) channels [33, 82] or the PFK-M isoform [75]. However, we also showed the non-physiological ATP response to the PFK knocking out.

In the following chapter, we introduce an extension of the IOM1.5, with a more sophisticated description of the ADP production-consumption process.

5 A More Sophisticated Integrated Oscillator Model

> *The biggest room in the world is the room for improvement.*
>
> **— Helmut Schmidt**

In this chapter, we present an extension of the IOM1.5 described in Chapter 4. This new model takes into account a more sophisticated representation of the ATP production-consumption process by describing in detail the mitochondrial metabolism. We discuss the motivations that bring us to this new model (Section 5.1) and the equations describing it (Section 5.2). Then, we show the potentialities of the new IOM (Sections 5.3, 5.4, and 5.5) and we suggest experimental protocols that can be used to investigate the nature of the oscillations (Section 5.6).

5.1 Motivations

There are three main motivations for the extension of the previous IOM1.5 and the inclusion of the mitochondrial metabolism. The first is due to ATP production. In Chapter 4, we showed that even though the IOM1.5 accounts for fundamental experimental findings, it also predicts non-physiological results (Section 4.5) due to an inaccurate description of ATP dynamics. To overcome this issue, we have to focus on the mitochondria, i.e., the organelle in which most of the ATP is produced, and its metabolism. Moreover, it has been observed that the signal leading to insulin secretion is amplified by the mitochondrial metabolic activity. As the simulation of insulin exocytosis is one of the aims of this dissertation, including the mitochondrial dynamics in the model is a natural extension. Finally, a further reason to extend the previous IOM1.5 is given by the new technologies that track mitochondrial membrane potential and NADH concentration. In order to use these experimental observations to validate the mathematical model, the model itself has to be able to simulate the time evolution of those quantities.

We refer to the extended IOM presented in this chapter as the IOM2.0.

5.2 Mathematical Model

In the IOM2.0, cellular membrane potential, cytosolic Ca^{2+} and metabolites are influenced by, and influence, the mitochondrial activity as well as the Ca^{2+} exchange with the endoplasmic reticulum. Figure 8.1 shows a schematic of the dynamics. Mathematically, the IOM2.0 consists of three modules. A first module describes the β-cell electrical activity and Ca^{2+} dynamics, while the second concerns the metabolism in the cytosol, and the third one accounts for the metabolism in the mitochondria (adapted from [17]).

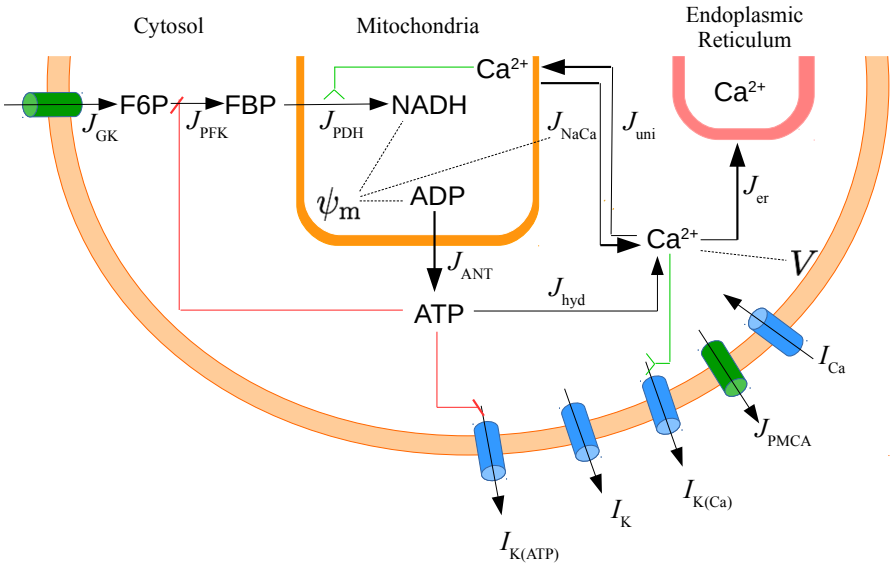

Figure 5.1.: Schematic description of the Integrated Oscillator Model (IOM). I: currents. J: fluxes. GK: glucokinase. PFK: phosphofructokinase. PDH=phosphate dehydrogenase. ANT: adenine nucleotide translocator. hyd: hydrolysis. uni: uniporter. PMCA: plasma membrane Ca^{2+} ATPase. NaCa: Na^{+}-Ca^{2+} exchanger. V and ψ_{m}: cellular and mitochondrial membrane potential respectively. The red and green lines represent negative and positive feedbacks respectively.

5.2.1 The Electrical and Calcium Module

The β-cell electrical activity and the cytosolic Ca^{2+} dynamics are adapted from the IOM1.5 (Sections 4.2.1). For this formulation, the ratio of cytosolic volume to mitochondrial volume, σ_{m}, is set to 290, while the maximal conductance $g_{\mathrm{K(ATP)}}$ is decreased to 19700 pS. Moreover, the Ca^{2+} flux density into the mitochondria, J_{m}, is modified to include the electrical driving force due to the mitochondrial membrane potential, ψ_{m}, whose dynamics are described in the mitochondrial module (Eq. (5.17)). Thus, Eq.(4.11) is now replaced by

$$J_{\mathrm{m}} = J_{\mathrm{uni}} - J_{\mathrm{NaCa}} \ , \tag{5.1}$$

Parameter	Value	Parameter	Value
p_{21}	0.013 μM^{-1} ms^{-1} mV^{-1}	p_{23}	0.0015 μM ms^{-1}
p_{22}	1.6 μM^{-1} ms^{-1}	p_{24}	0.016 mV^{-1}

Table 5.1.: Parameters for the electrical and calcium module.

where J_{uni} and J_{NaCa} are the fluxes through the Ca^{2+} pumps and the Na^{+}/Ca^{2+} exchanger, respectively:

$$J_{\text{uni}} = (p_{21}\ \psi_{\text{m}} - p_{22})c^2\ , \tag{5.2}$$

$$J_{\text{NaCa}} = p_{23}(c_{\text{m}} - c)\exp\left(p_{24}\ \psi_{\text{m}}\right)\ . \tag{5.3}$$

The parameters p_i are given in Table 5.1.

All other fluxes, currents, and parameters are defined as in the IOM1.5 (Sections 4.2.1).

5.2.2 The Metabolic Module

In the IOM2.0, the cytosolic concentrations of F6P and FBP are described by

$$\begin{aligned} \frac{d\text{F6P}}{dt} &= 0.3\left(J_{\text{GK}} - J_{\text{PFK}}\right)\ , \\ \frac{d\text{FBP}}{dt} &= J_{\text{PFK}} - \frac{1}{2}\frac{J_{\text{PDH}}}{\sigma_{\text{m}}}\ , \end{aligned} \tag{5.4}$$

where J_{GK} and J_{PFK} are the glucose-dependent glucokinase (GK) and phosphofructokinase (PFK) reaction rates defined in Eqs. (4.15) and (4.14), and J_{PDH} is pyruvate dehydrogenase (PDH) reaction rate. The PDH reaction occurs in the mitochondria and converts pyruvate (whose concentration is here assumed proportionate to FBP) into NADH. The PDH flux is described by

$$J_{\text{PDH}} = v_{\text{PDH}}\frac{1}{K_{\text{NADH}_{\text{m}},\text{PDH}} + \frac{\text{NADH}_{\text{m}}}{\text{NAD}_{\text{m}}}}J_{\text{GPDH}}\ , \tag{5.5}$$

where v_{PDH} is one of the key parameters that we vary to explore the impact of changing the glycolytic efflux rate. The dynamics of the mitochondrial NADH and NAD^{+} concentrations (NADH_{m} and NAD_{m}, respectively) are described in the mitochondrial module (Section 5.2.3). Finally, the glycerol-3-phosphate dehydrogenase (GPDH) reaction rate, J_{GPDH}, in Eq. (5.5) is given by

$$J_{\text{GPDH}} = s_{\infty}(c_{\text{m}})\sqrt{\text{FBP}}\ , \tag{5.6}$$

Parameter	Value	Parameter	Value
K_{GPDH}	1.5 μM	p_{19}	0.6 μM ms^{-1}
v_{PDH}	varies	p_{20}	2
$K_{\mathrm{NADH_m,PDH}}$	1.3	$\frac{\mathrm{F}}{\mathrm{RT}}$	0.037
k_{hyd}	1.864×10^{-6} μM ms^{-1}	$\mathrm{A_{tot}}$	3000 μM
$k_{\mathrm{hyd,bas}}$	6.48×10^{-7} μM ms^{-1}	$\mathrm{A_{tot,m}}$	15000 μM

Table 5.2.: Parameters for the metabolic module.

where the nozzle s_∞ is described as in Eq.(4.18):

$$s_\infty(c_{\mathrm{m}}) = \frac{c_{\mathrm{m}}}{K_{\mathrm{GPDH}} + c_{\mathrm{m}}} \,. \tag{5.7}$$

In Table 5.2 we give the values of all parameters of this module.

A major change in the cytosolic metabolic module with respect to the IOM1.5, is the description of ADP concentration. In the IOM2.0, we use a more sophisticated ADP dynamics presented in the DOM2.0 (Eq. (3.31)), namely,

$$\frac{d\mathrm{ADP}}{dt} = J_{\mathrm{hyd}} - \frac{J_{\mathrm{ANT}}}{\sigma_{\mathrm{m}}} \,, \tag{5.8}$$

where J_{hyd} is the flux due to the hydrolysis and J_{ANT} is the flux of ATP produced in the mitochondria and transported to the cytosol through the adenine nucleotide translocator (ANT), and described by

$$J_{\mathrm{hyd}} = (k_{\mathrm{hyd}}c + k_{\mathrm{hyd,bas}})\mathrm{ATP} \,, \tag{5.9}$$

$$J_{\mathrm{ANT}} = p_{19}\frac{\frac{\mathrm{ATP_m}}{\mathrm{ADP_m}}}{\frac{\mathrm{ATP_m}}{\mathrm{ADP_m}} + p_{20}} \exp\left(\frac{\mathrm{F}}{2\mathrm{RT}}\psi_{\mathrm{m}}\right) . \tag{5.10}$$

Thus, ADP production depends on the hydrolysis of the ATP to ADP by Ca^{2+} pumps present on the plasma and ER membranes, while ADP consumption is influenced by the mitochondrial metabolism and the mitochondrial membrane potential.

The sums of both cytosolic and mitochondrial nucleotides are conserved. Hence:

$$\mathrm{ATP} = \frac{1}{2}\left[A_{\mathrm{tot}} + \sqrt{-4\mathrm{ADP}^2 + (A_{\mathrm{tot}} - \mathrm{ADP})^2} - \mathrm{ADP}\right] \,, \tag{5.11}$$

$$\mathrm{ATP_m} = \mathrm{A_{tot,m}} - \mathrm{ADP_m} \,, \tag{5.12}$$

where A_{tot} and $A_{\mathrm{tot,m}}$ are the total nucleotide concentrations in the cytosol and in the mitochondria, respectively, and they are assumed to be both constant.

5.2.3 The Mitochondrial Module

The mitochondrial module is adapted from the correspondent module of the DOM2.0 published by Bertram *et al.* in [17] and described in Section 3.5.4. For this formulation, we assume the mitochondrial NADH produced during two processes, a first strictly dependent on the glycolytic efflux and a second only indirectly governed by the glucose metabolism. The first process is the PDH reaction that transforms the pyruvate into Acetyl-CoA, CO_2, and NADH. Acetyl-CoA, in turn, becomes the substrate for the TCA cycle, which represents the second source of NADH production. Specifically, during the TCA cycle, NAD^+ is reduced to NADH by several dehydrogenases (DH). Both PDH and DH reactions are modulated by the mitochondrial calcium concentration. On the other hand, NADH is converted into NAD^+ during the electron transport chain that consumes oxygen at the final stage.

Thus, the mitochondrial concentration of NADH in our model is described by

$$\frac{d\mathrm{NADH_m}}{dt} = J_{\mathrm{PDH}} + J_{\mathrm{DH}} - J_{\mathrm{O}} \ , \tag{5.13}$$

where J_{PDH} is the PDH reaction rate Eq. (5.5), J_{DH} represents the several dehydrogenases occurring during the TCA cycle, and J_{O} is the O_2 consumption rate:

$$J_{\mathrm{DH}} = v_{\mathrm{DH}} \frac{c_{\mathrm{m}}}{K_{\mathrm{DH}} + c_{\mathrm{m}}} \frac{1}{K_{\mathrm{NADH_m,DH}} + \frac{\mathrm{NADH_m}}{\mathrm{NAD_m}}} \ , \tag{5.14}$$

$$J_{\mathrm{O}} = p_4 \frac{\mathrm{NADH_m}}{p_5 + \mathrm{NADH_m}} \frac{1}{1 + \exp\left(\frac{\psi_{\mathrm{m}} - p_6}{p_7}\right)} \ . \tag{5.15}$$

The values of the parameters of this module are given in Table 5.3.

In this model, we assume nucleotide conservation:

$$\mathrm{NAD_m} = \mathrm{N_{tot,m}} - \mathrm{NADH_m} \ , \tag{5.16}$$

where $\mathrm{N_{tot,m}}$ is the total concentration in the mitochondria.

The rate of change of the mitochondrial membrane potential, ψ_{m}, is described by

$$\frac{d\psi_{\mathrm{m}}}{dt} = \frac{1}{C_{\mathrm{m}}} \left[J_{\mathrm{Hres}} - J_{\mathrm{Hatp}} - J_{\mathrm{Hleak}} - J_{\mathrm{ANT}} - J_{\mathrm{NaCa}} - 2J_{\mathrm{uni}} \right] \ , \tag{5.17}$$

where C_{m} is the mitochondrial inner membrane capacitance. In this dissertation, we use the convention that the membrane potential is positive if the inner membrane is hyperpolarized. The term J_{Hres} represents the flux through respiration-driven proton pumps

$$J_{\mathrm{Hres}} = p_8 \frac{\mathrm{NADH_m}}{p_9 + \mathrm{NADH_m}} \frac{1}{1 + \exp\left(\frac{\psi_{\mathrm{m}} - p_{10}}{p_{11}}\right)} \ . \tag{5.18}$$

Parameter	Value	Parameter	Value
v_{DH}	1.1 μM ms^{-1}	p_{11}	5 mV
K_{DH}	0.08 μM	p_{13}	10000 μM
$K_{\mathrm{NADH_m,DH}}$	1.3	p_{14}	190 mV
p_4	0.55 μM ms^{-1}	p_{15}	8.5 mV
p_5	250 μM	p_{16}	4 μM ms^{-1}
p_6	165 mV	p_{17}	0.0014 μM ms^{-1} mV^{-1}
p_7	5 mV	p_{18}	0.02 μM ms^{-1}
p_8	7.4 μM ms^{-1}	$\mathrm{N_{tot,m}}$	10000 μM
p_9	100 μM	C_{m}	180 mV
p_{10}	165 mV		

Table 5.3.: Parameters for the mitochondrial module.

The terms J_{Hatp} and J_{Hleak} are the proton fluxes entering the mitochondria through the ATPase and through leakage down the proton gradient, respectively

$$J_{\mathrm{Hatp}} = 3J_{\mathrm{F1F0}} \,, \tag{5.19}$$

$$J_{\mathrm{Hleak}} = p_{17}\,\psi_{\mathrm{m}} - p_{18} \,, \tag{5.20}$$

where J_{F1F0} is the rate at which the F1F0 ATP synthase phosphorylates ADP to form ATP and it is described by

$$J_{\mathrm{F1F0}} = p_{16}\frac{p_{13}}{p_{13}+\mathrm{ATP_m}}\frac{1}{1+\exp\left(\frac{p_{14}-\psi_{\mathrm{m}}}{p_{15}}\right)} \,. \tag{5.21}$$

The multiplying factor 3 in Eq. (5.19) is because three protons move through the F1F0 ATP synthase for each ATP molecule produced.

Finally, we assume the synthesized ATP comes at the expense of ADP in the mitochondria, as in the cytosol. Thus, the rate of change in ADP in the mitochondria can be read as

$$\frac{d\mathrm{ADP_m}}{dt} = J_{\mathrm{ANT}} - J_{\mathrm{F1F0}} \,, \tag{5.22}$$

with J_{ANT} and J_{F1F0} described in Eqs. (5.10) and (5.21), respectively.

5.3 Bursting Regimes and Mitochondrial Variables

The IOM2.0 is capable of replicating the whole range of bursting patterns shown with the IOM1.5. Moreover, because of the mitochondrial module, the new IOM also contains mitochondrial variables that can be measured experimentally, such as the mitochondrial membrane potential and the mitochondrial NADH concentration.

Figure 5.2 illustrates a representative of each burst mode. From left to right, we show an example of slow bursting with sawtooth-like (column A) and pulsatile FBP (column B), fast bursting (column C), and compound bursting (column D).

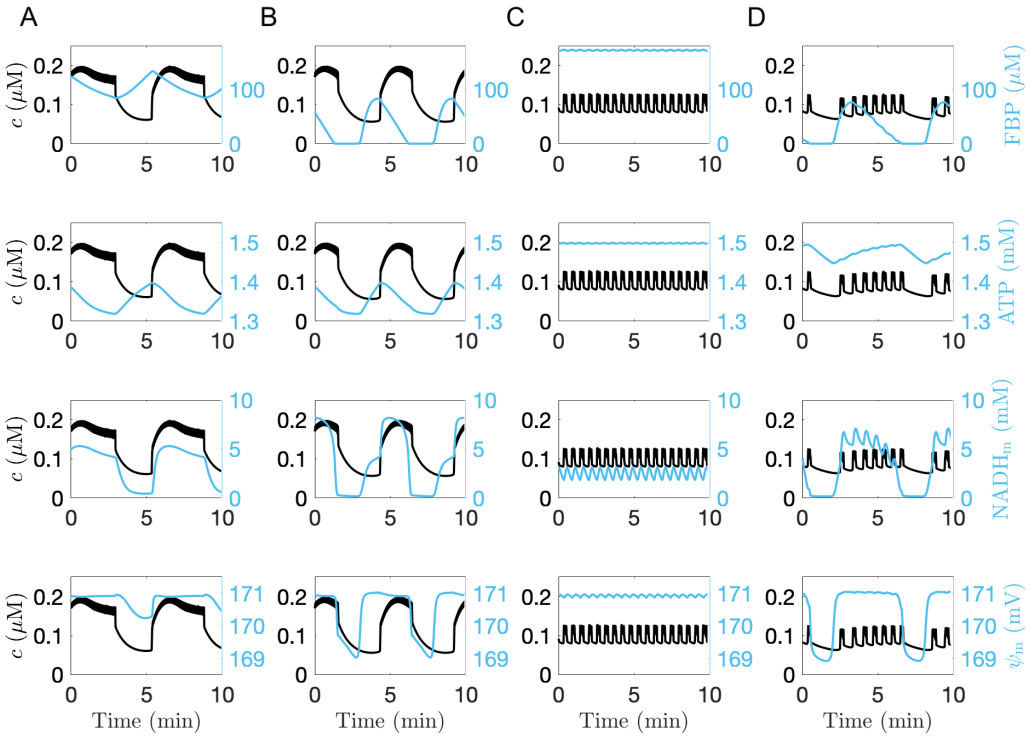

Figure 5.2.: Representative slow bursting with sawtooth-like (column A) and pulsatile FBP (column B), fast bursting (column C), and compound bursting (column D) with the IOM2.0. These plots show cytosolic Ca^{2+}, FBP, ATP, $NADH_m$, and ψ_m time courses with $g_{K(Ca)}$=150 pS (panels A and B) or $g_{K(Ca)}$=600 pS (panels C and D), and v_{PDH}=0.4 μM/ms (columns A and C) or v_{PDH}=2 μM/ms (columns B and D) .

We observe that the $NADH_m$ and ψ_m time courses obtained for a cell in a slow bursting regime with pulsatile FBP (column B) are consistent with the experimental findings shown by Merrins *et al.* in [66]. In their data, NADH mitochondrial concentration increases during the silent phase and decreases during the silent phase, peaking at the beginning of the active phase most of the times. Moreover, simultaneous records of NADH with mitochondrial membrane potential show that ψ_m hyperpolarizes (increases) when the NADH arises during the active phase and it depolarizes (decrease) during the silent phase, as shown with the IOM2.0 (Figure 5.2, column B).

5.4 Ca^{2+} Effect on the Mitochondrial Membrane Potential

During a burst, the cytosolic Ca^{2+} level increases because of the influx due to the voltage-dependent Ca^{2+} channels. This phenomenon triggers exchanges of calcium ions through the mitochondrial inner membrane. This movement, in turn, affects the mitochondrial membrane potential in two ways.

- The dehydrogenase effect, due to the Ca^{2+} activation of dehydrogenases and the resulting $NADH_m$ increase. This hyperpolarizes the mitochondrial inner membrane.

- The electrical effect (also called Keizer-Magnus effect), due to the flux of positive ions through the uniporter (J_{uni}). This depolarizes the mitochondrial inner membrane.

These two effects are in competition with each other. If the dehydrogenase effect overtakes the electrical effect, the mitochondrial membrane potential will hyperpolarize in response to an increase in the cytosolic Ca^{2+} concentration. Otherwise, it will depolarize. Both situations have been observed experimentally. In 2010, Merrins and collaborators published laboratory observations of mitochondrial membrane potential depolarization during the active phase [65]. A decade before, Krippeit-Drews *et al.* recorded the opposite scenario in their laboratory [50]. Figure 5.3 illustrates a schematic of the two effects. Panel A represents the scenario in which the dehydrogenase effect exceeds the electrical effect, so that ψ_m increases during a burst active phase, as in Merrins *et al.*. Panel B corresponds to Krippeit-Drews findings in which the mitochondrial membrane potential depolarizes during the active phase because the electrical effect is stronger than the dehydrogenase. This bursting is fast, as in the Krippeit-Drews data.

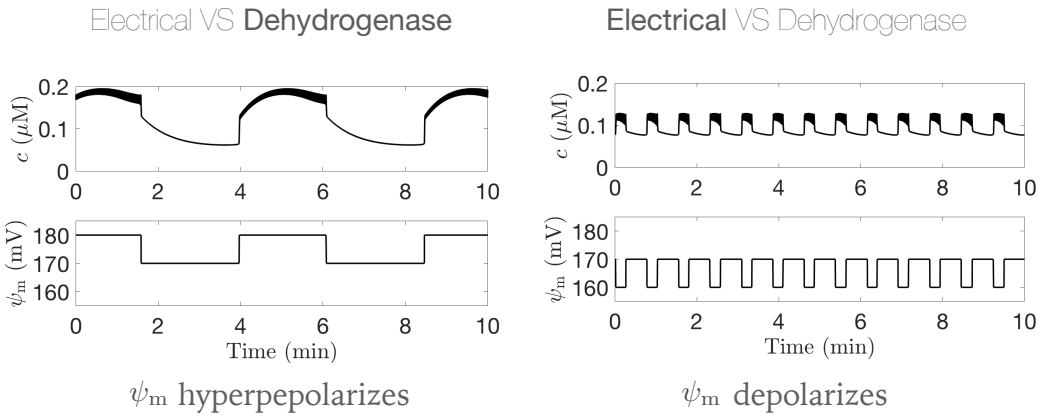

Figure 5.3.: Schematic of experimental findings on the mitochondrial membrane potential.

In the IOM2.0, the trade-off is regulated by the parameter p_{21} that influences the amplitude of the Ca^{2+} flux through the uniporter, J_{uni} (Eq. (5.2)). Biologically, this parameter modulates the Keizer-Magnus effect by governing the Ca^{2+} flux into the mitochondria. Thus, for high values of the parameter, the Ca^{2+} influx into the mitochondria is substantial and the mitochondrial membrane potential becomes more positive (ψ_{m} hyperpolarizes). If the parameter is small, the Ca^{2+} uptake through the uniporter is very low and the mitochondrial membrane potential declines (ψ_{m} depolarizes).

Figure 5.4 depicts the results obtained for a cell in a fast bursting mode with two different vales of p_{21}. If the value of the parameter is low (panel A, $p_{21} = 0.013$ μM/ms), ψ_{m} hyperpolarizes during the active phase as a consequence of the little electrical effect, and it slowly depolarizes during the silent phase. If p_{21} is relatively high (panel B, $p_{21} = 0.03$ μM/ms), the opposite effect is observed, due to the Ca^{2+} flux through the uniporter. In this scenario, the mitochondrial membrane stays depolarized during the active phase (high Ca^{2+} concentration) and hyperpolarized during the silent phase (low Ca^{2+} concentration).

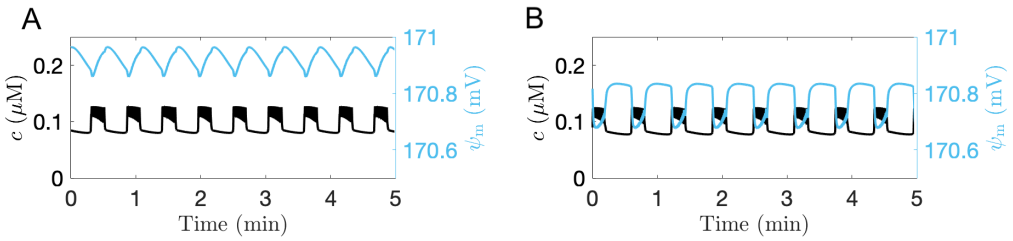

Figure 5.4.: The parameter p_{21} controls the trade-off between the electrical effect and the dehydrogenase effect. The value of the parameter differs: $p_{21} = 0.013$ μM/ms (A) and $p_{21} = 0.013$ μM/ms (B). In all cases, v_{PDH}=0.7 μM/ms and $g_{\text{K(Ca)}}$=150 pS.

5.5 Subthreshold Oscillations

In the history of studies focusing on β-cell activity, the subthreshold oscillations in membrane potential and Ca^{2+} concentration have always been taken in special consideration. In fact, they are evidence that glycolytic oscillations can occur in the absence of electrical activity, supporting Tornheim's hypothesis of intrinsic metabolic oscillations [92]. More recently, oscillations in Ca^{2+} concentration and in the K(ATP) conductance have been observed in β-cells in the presence of a subthreshold glucose concentration [47, 68]. These findings suggest the existence of an active glycolytic oscillator for a low glucose level that can oscillate without electrical activity.

In this chapter, the glucose concentration is represented by the parameter J_{GK} that is fixed to 0.001 μM/ms in all simulations. This value corresponds to an extracellular concentration of 11 mM, which is the general external glucose concentration used in the experimental set-up. Nonetheless, we show that the IOM2.0 can capture the subthreshold oscillations by increasing the K(ATP) conductance. Biologically speaking, increasing the K(ATP) conductance means increasing the flux through the K(ATP) channels. This mimics the effect of a low glucose level that lowers the ATP/ADP ratio, resulting in a higher fraction of open K(ATP) channels and in a higher flux through them.

Figure 5.5A illustrates a virtual cell in compound bursting mode. In panel B, the K(ATP) conductance, $g_{\mathrm{K(ATP)}}$, is increased from 19700 pS up to 21000 pS in the same cell. In this second scenario, the electrical activity stops and there is a drop in the cytosolic Ca^{2+} concentration. However, the glycolytic oscillator is still active and generates intrinsic metabolic oscillations. The effect of these oscillations on the K(ATP) conductance leads to the subthreshold oscillations in membrane potential and in Ca^{2+} concentration. We observe that the peaks in the induced Ca^{2+} oscillations (panel B) are not synchronized with the peaks in the metabolic oscillations. In fact, the oscillations in the electrical component are induced by oscillations in ATP and ADP concentrations, resulting from many mitochondrial reactions that shift the nucleotide oscillations with respect to the glycolytic variables.

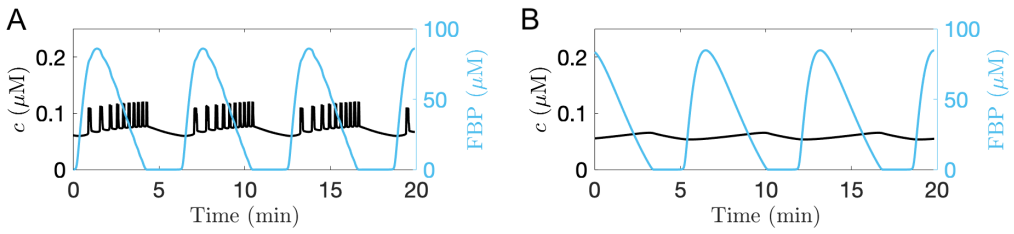

Figure 5.5.: Subthreshold oscillations in a virtual cell in compound mode with v_{PDH}=3 μM/ms and $g_{\mathrm{K(Ca)}}$=700 pS. The K(ATP) conductance is increased from 19700 pS (A) to 21000 pS (B).

5.6 Model Predictions and Experimental Findings

The IOM2.0 brings together the detailed mitochondrial module presented in the DOM2.0 with the Ca^{2+} feedback into the glycolysis introduced in the IOM1.5. This makes the IOM2.0 the most sophisticated among all the IOMs and DOMs. In this section, we present three new protocols that can be used to study β-cell activity and to further validate the IOM2.0. The first experiment consists of terminating the Ca^{2+} oscillations by voltage clamping a cell's plasma membrane (Section 5.6.1). The second protocol studies the nature of the bursts by clamping the metabolic

activity (Section 5.6.2). The last experiment focuses on the origin of the glycolytic oscillations by investigating the enzyme PFK (Section 5.6.3).

5.6.1 Oscillations in K(ATP) Conductance Measured with Voltage Ramps During Islet Bursting

In Section 4.4.1, we presented an experiment to discriminate between the two different mechanisms underlying the bursting activity by clamping the Ca^{2+} oscillations with diazoxide. Although the IOM2.0 is capable of replicating this experiment, we do not show the results. Instead, we propose a new experiment to clamp the Ca^{2+} concentration by setting a single β-cell in an islet in a voltage clamp mode (indirect clamping of the calcium). If the islet is in a solution of stimulatory glucose, the cells in the islet will burst except the patched cell that is held at the clamp command potential. In our simulations, the voltage clamp mode is reached through the application of rapid voltage ramps of 2 s from -120 mV to -50 mV (Figure 5.6).

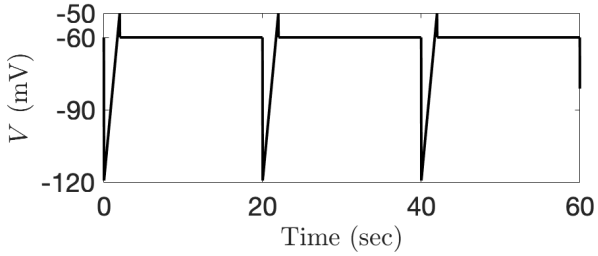

Figure 5.6.: Rapid voltage ramps of 2 s from -120 mV to -50 mV.

To simplify the scenario, the clamped-cell/islet system is converted into a 2-cell system. We distinguish the two cells by labelling one as the "small" cell and the other one as the "super-cell". The small cell represents the single cell set in a voltage clamp mode, while the super-cell identifies the rest of the islet that is free to burst. The super-cell is modestly influenced by the small cell that, on the contrary, is strongly affected by the cellular activity of the first. The two cells are coupled by gap junctions and we assume this coupling to be both electrical and metabolic. Mathematically, the coupling is simulated by adding a coupling term to V, F6P, and FBP dynamics.

More specifically, the membrane potentials of the super-cell and small cell, named V_S and V_c, respectively, are described by

$$\frac{dV_S}{dt} = -\frac{1}{C}\left[I_{\mathrm{Ca}} + I_{\mathrm{K}} + I_{\mathrm{K(Ca)}} + I_{\mathrm{K(ATP)}}\right] - g_{Sc}(V_S - V_c)\,, \tag{5.23}$$

$$\frac{dV_c}{dt} = -\frac{1}{C}\left[I_{\mathrm{Ca}} + I_{\mathrm{K}} + I_{\mathrm{K(Ca)}} + I_{\mathrm{K(ATP)}}\right] - g_{cS}(V_c - V_S)\,, \tag{5.24}$$

where the terms $g_{ij}(V_i - V_j)$ (with $i, j \in \{c, S\}$ and $i \neq j$) represent the electrical coupling in the two-cell system. The factors g_{ij} are electrical coupling conductances. To simulate the different influence of one cell onto the other, we introduce asymmetry in the coupling currents (as in [74]) by setting

$$g_{cS} = \frac{g_c}{2p} , \qquad g_{Sc} = \frac{g_c}{2(1-p)} , \tag{5.25}$$

where g_c is a generic electrical coupling conductance, and $p = \frac{1}{(N-1)}$ where N is the total number of β-cells assumed in the islet. In our simulation, N=101 and $g_c = 10$ pS, so that $g_{cS} = 500$ pS and $g_{Sc} \approx 5$ pS.

Similarly, the extra metabolite current due to the gap junction in the metabolic compartment is added to the previous descriptions of F6P and FBP:

$$\frac{d\mathrm{F6P}_i}{dt} = 0.3\,(J_{\mathrm{GK}} - J_{\mathrm{PFK}}) - p_{\mathrm{F6P},ij}(\mathrm{F6P}_i - \mathrm{F6P}_j) , \tag{5.26}$$

$$\frac{d\mathrm{FBP}_i}{dt} = J_{\mathrm{PFK}} - \frac{1}{2}J_{\mathrm{GPDH}} - p_{\mathrm{FBP},ij}(\mathrm{FBP}_i - \mathrm{FBP}_j) , \tag{5.27}$$

where $p_{\mathrm{F6P},ij}$ and $p_{\mathrm{FBP},ij}$ (with $i, j \in \{c, S\}$ and $i \neq j$) are the gap junction permeabilities for F6P and FBP, respectively. Once again, the asymmetric coupling currents are given by asymmetric gap junction permeabilities:

$$p_{\mathrm{F6P},cS} = \frac{p_{\mathrm{F6P}}}{2p} , \qquad p_{\mathrm{F6P},Sc} = \frac{p_{\mathrm{F6P}}}{2(1-p)} , \tag{5.28}$$

$$p_{\mathrm{FBP},cS} = \frac{p_{\mathrm{FBP}}}{2p} , \qquad p_{\mathrm{FBP},Sc} = \frac{p_{\mathrm{FBP}}}{2(1-p)} . \tag{5.29}$$

In our simulations, $p_{\mathrm{F6P}} = 0.01$ ms^{-1} and $p_{\mathrm{FBP}} = 0.02$ ms^{-1}.

We start by considering two uncoupled cells, i.e., g_c = 0. At $t = 30$ min, we coupled the two cells by adding gap junction terms. More precisely, we set $g_c = 10$ pS, $p_{\mathrm{F6P}} = 0.01$ ms^{-1}, and $p_{\mathrm{FBP}} = 0.02$ ms^{-1}. The results of this protocol are shown in Figure 5.7.

When the voltage is clamped (not shown), the bursting activity of the small cell is stopped, while it persists in the super-cell. In this scenario, the model predicts no oscillation in the K(ATP) conductance in the small cell (Figure 5.7, blue) if the cells are uncoupled. When the gap junctions are introduced (at $t = 30$ min), the electrical activity of the super-cell induces glycolytic oscillations in the small cell, and $g_{\mathrm{K(ATP)}}$ oscillations can be observed in the latter.

The predictions shown in Figures 5.7 are consistent with the experimental observation published in 2013 by Ren *et al.* [74]. In this experimental set-up, the islet is placed in a medium with 11.1 mM glucose and the rapid voltage ramps are of

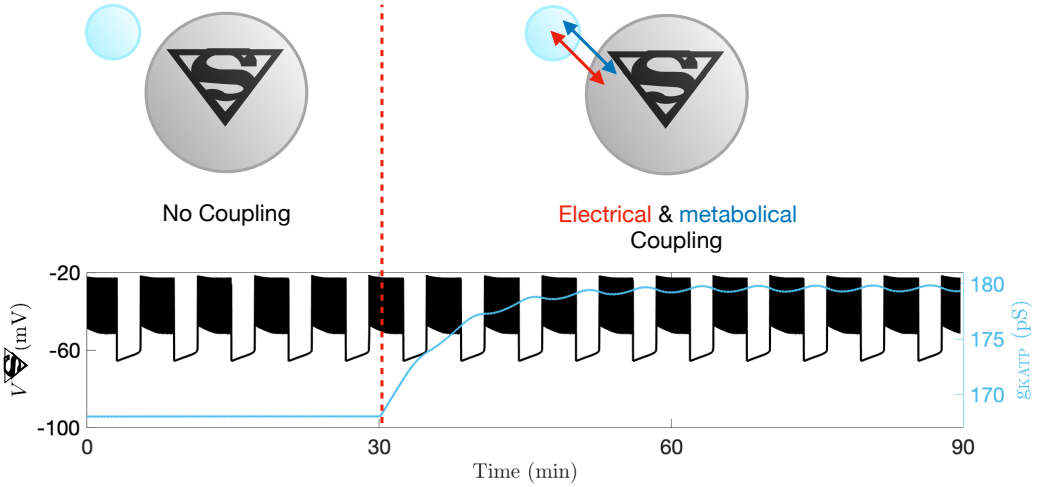

Figure 5.7.: Schematic description of the two-cell system state for each step of the protocol. Time courses of cellular membrane potential of the super cell (black) and K(ATP) channel conductance of the small cell (blue). At t=30 min, the gap junctions terms are added. Specific values are: $g_{\mathrm{K(Ca)}}$=150 pS and v_{PDH}=0.4 μM/ms.

the same nature as the ones described in our *in silico* experiment (Figure 5.6). The authors report slow bursting in the non-clamped cells, and slow oscillations in K(ATP) conductance in the clamped cell. Since the Ca^{2+} concentration is not oscillating in the clamped β-cell, these oscillations are likely a result of metabolic activity. In this finding, the observed slow oscillations in K(ATP) conductance have lower value during the active phases of the bursts than during the silent phase, as model predictions show.

5.6.2 Ca^{2+} Oscillations Stimulated by KIC

The experiment described in the previous sections investigates the nature of metabolic oscillations by clamping the electrical busting (Section 5.6.1). We now approach the same problem from the opposite perspective, proposing an experiment in which the metabolic activity is clamped. We use this strategy to discover conditions under which the bursting activity can persist. This experiment consists of injecting the metabolic intermediate α-ketoisocaproic acid (α-KIC) into the β-cell. The α-KIC goes through many processes that result in the production of acetyl-CoA, used in the TCA cycle to eventually produce ATP. Thus, adding α-KIC into the cell stimulates the ATP production bypassing the glycolytic process.

In this thesis, the perfusion of α-KIC is simulated by clamping $\mathrm{NADH_m}$, which is an intermediate product of the TCA cycle. This way, the resulting ATP production is independent from the glucose level.

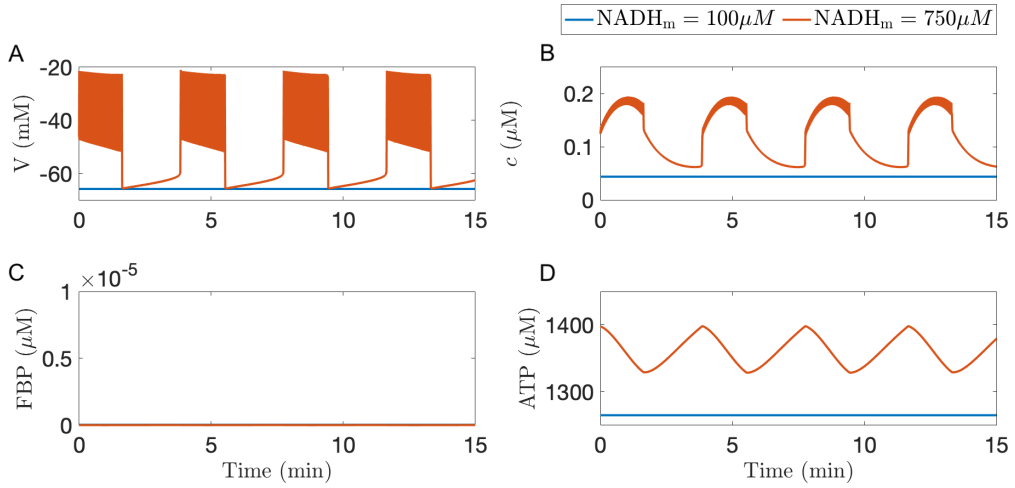

Figure 5.8.: Overview of the model prediction for the injection of α-KIC into the β-cell with $\mathrm{NADH_m} = 100$ μM (blue curve) and $\mathrm{NADH_m} = 750$ μM (orange curve). Time courses of cellular membrane potential (A), cytosolic calcium (B), FBP (C), and cytosolic ATP (D) with $g_{\mathrm{K(Ca)}} = 150$ pS and $v_{\mathrm{PDH}} = 0.4$ μM/ms.

Figure 5.8 depicts the results obtained for $\mathrm{NADH_m} = 100$ μM (blue curve) and $\mathrm{NADH_m} = 750$ μM (orange curve) in a glucose-free scenario ($J_{\mathrm{GK}} = 0$ μM/ms). In both cases, the glycolysis cannot occur due to the lack of glucose. Consequentially, the FBP level is very low. However, depending on the $\mathrm{NADH_m}$ concentration, the cell may still burst.

For low concentration of $\mathrm{NADH_m}$ ($\mathrm{NADH_m} = 100$ μM), the cell is silent. Biologically, this scenario represents the lack of resources for the TCA cycle and, as a result, the lack of ATP. Thus, the bursting activity cannot be supported. For high $\mathrm{NADH_m}$ ($\mathrm{NADH_m} = 750$ μM) the cell is active due to the series of mitochondrial chemical reactions that can occur because of the higher $\mathrm{NADH_m}$ concentration. This activity is able to trigger the bursting activity that, in turn, induces oscillations in the ATP concentration through the Ca^{2+}-mediated hydrolysis.

Several different research groups have performed the KIC experiment in their laboratories in the last 20 years, with different results. In some cases, Ca^{2+} oscillations are still observed in β-cells in a glucose-free solution [59, 39], supporting the hypothesis formulated by Detimary [31] that the mechanism driving the oscillations is the consumption of ATP by Ca^{2+} pumps. However, there have been cases in which the cells were silent [30, 53].

We have shown that the IOM2.0 can account for this experiment and that there are conditions for either one or the other output depending on the $\mathrm{NADH_m}$ concentration. More precisely, if $\mathrm{NADH_m}$ level is high, the ATP production can occur allowing the

cellular activity (as observed in [59, 39]), while if $NADH_m$ is low, the cell is silent (as in [30, 53]).

5.6.3 Different Isoforms of the Enzyme PFK

We now describe the last protocol presented in this chapter. In Section 4.4.2, we briefly introduced the nature of the allosteric enzyme PFK, considered to be responsible for the metabolic oscillations. Also, we described the various PFK isoforms and the differences between their affinities for ATP and FBP. We also presented the IOM1.5 predictions on the impact that the reduction of M-type PFK activity would have on the nature of the bursting, and its limitations (Section 4.5). We now show that the IOM2.0, in addition to accounting for the experimental findings, can overcome the limitations of the IOM1.5.

For our analysis, we use only the second approach described in Section 4.4.2, considered the most realistic. Thus, the flux due to the PFK reaction is made up of two components $J_{\mathrm{PFK-M}}$ and $J_{\mathrm{PFK-C}}$, the former mediated by the M-type isoform and the latter by the C-type (Eq. (4.24)). Also, as in Chapter 4, the FBP dissociation constant, K_2, is set to 1 μM for PFK-M and to 2 μM for PFK-C, while the ADP dissociation constant, K_4, is equal to 1000 μM for PFK-M and 200 μM for PFK-C.

In this section, we investigate only the behaviour of a cell in a compound mode, since the conclusions we can make for a cell in a slow bursting regime are the same as those described in Section 4.4.2. Nonetheless, we point out that now the IOM2.0 predicts a drop in the ATP concentration when both isoforms of PFK are knocked out and the cell is silent, as expected from a physiological point of view but not replicated with the IOM1.5. This result can be observed in Figure 5.9, in which we show the output of the protocol used for Figure 4.15.

Compound Bursting with genetically knocked-out PFK-M

We now focus our attention on a β-cell in a compound bursting mode that, according to model predictions, can occur only in the presence of intrinsic metabolic oscillations. We want to investigate the conditions for this bursting rhythm to persist after the PFK-M has been knocked out. For this purpose, we consider a cell in a compound bursting regime and we gradually lower the maximum rate $v_{\mathrm{PFK-M}}$ to simulate the reduction of M-type isoform activity. Moreover, the maximum rate is set to zero to mimic the PFK-M knocking out. The results are shown in Figure 5.10 for several values of $v_{\mathrm{PFK-M}}$.

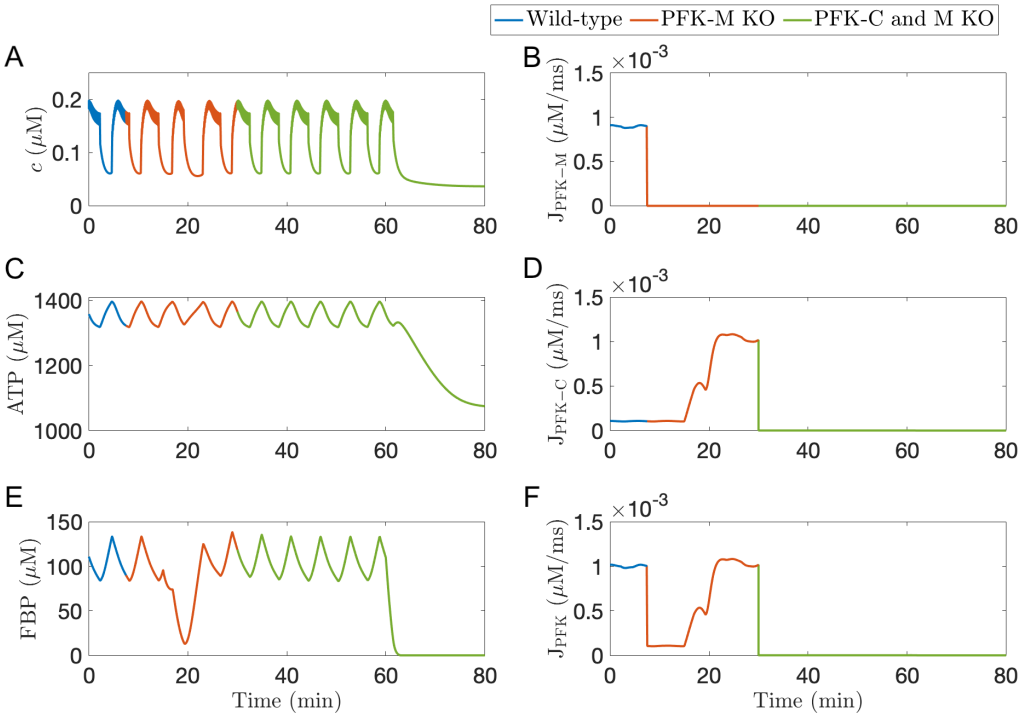

Figure 5.9.: Time courses of Ca^{2+}, ATP, and FBP (left column) and J_{PFK-M}, J_{PFK-C}, and J_{PFK} (right column) for different value of v_{PFK-C} and v_{PFK-M}. Specific values are: v_{PFK-M}=v_{PFK-C}=0.008 μM/ms (blue curve), v_{PFK-M}=0.008 μM/ms and v_{PFK-C}=0 μM/ms (orange curve), and v_{PFK-M}=v_{PFK-C}=0 μM/ms (green curve). In all cases, v_{PDH}=0.4 μM and $g_{K(Ca)}$=150 pS.

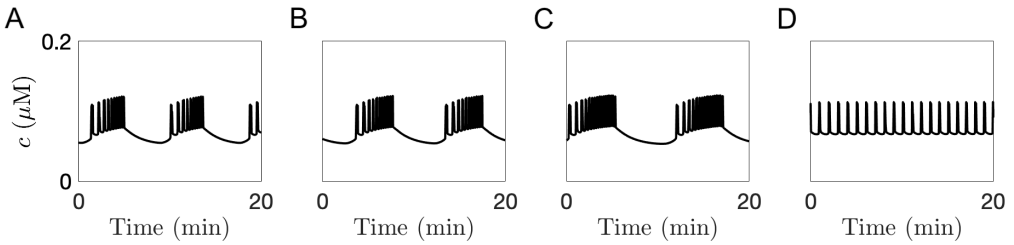

Figure 5.10.: Compound oscillations may or may not persist reducing PFK-M fraction. The Ca^{2+} oscillations are obtained with $g_{K(Ca)}$=650 pS, v_{PDH}=20 μM/ms, and v_{PFK-C}=0.008 μM/ms. The maximum rate v_{PFK-M} varies: v_{PFK-M}=0.008 μM/ms (A), v_{PFK-M}=0.006 μM/ms (B), v_{PFK-M}=0.004 μM/ms (C), and v_{PFK-M}=0 μM/ms (D).

In Figure 5.10, the parameter v_{PFK-M} decreases left to right. We observe that the reduction of PFK-M activity (panels A, B, and C, with a lower v_{PFK-M}) affects the bursting pattern but there is no change in the bursting type, and the cell is still in a compound mode. However, if the PFK-M is knocked out entirely (panel D, with v_{PFK-M}=0μM/ms) the compound bursting is converted into fast bursting as a consequence of the turning off of the glycolytic oscillator.

We now look for an approach to recover the initial bursting mode or, equivalently, a way to engage the glycolytic oscillator again. A path we can take to recover the compound mode is to increase the value of the maximum rate $v_{\mathrm{PFK-C}}$. This way, the lack of PFK activity is compensated by increasing the values of the PFK flux. A second way is to reduce the outward efflux by lowering v_{PDH}, thus allowing FBP to build up.

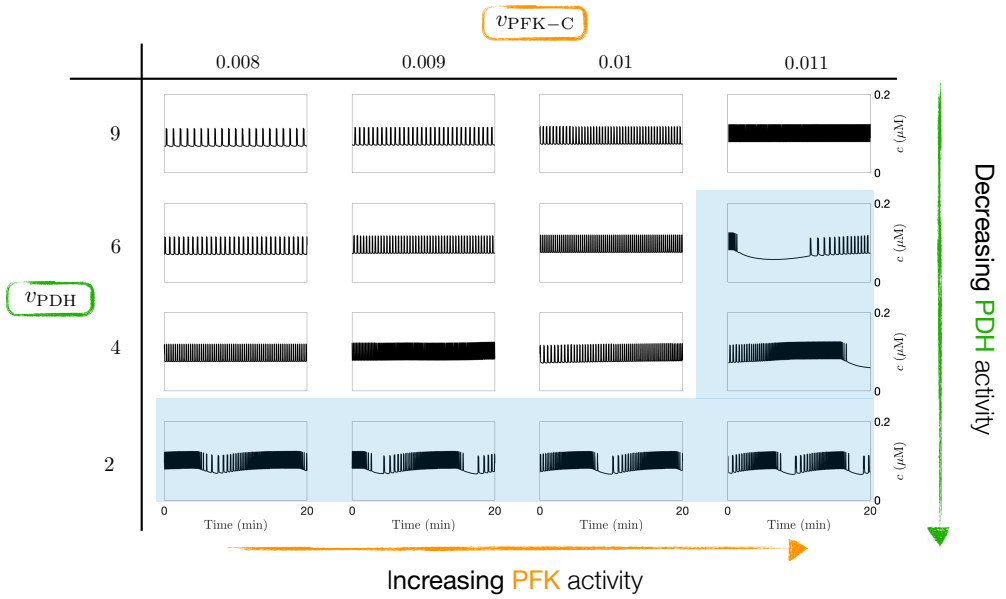

Figure 5.11.: Calcium time courses taken over a grid of $v_{\mathrm{PFK-C}}$ and v_{PDH} values. The blue shaded region indicates the parameter combination for which compound oscillations can be recovered even if PFK-M is knocked out. In all cases: $g_{\mathrm{K(Ca)}}$=700 pS and $v_{\mathrm{PFK-M}}$=0 μM/ms.

Figure 5.11 shows Ca^{2+} time courses for different vales of $v_{\mathrm{PFK-C}}$ and v_{PDH} with $v_{\mathrm{PFK-M}}$=0 (PFK-M is assumed to be knocked out). The top left corner corresponds to the scenario in Figure 5.10D. The parameter $v_{\mathrm{PFK-C}}$ increases left to right, while v_{PDH} decreases top to bottom. We highlight the parameter combinations for which the compound bursting is recovered (blue shaded region). We observe that only one of the two paths, either increasing $v_{\mathrm{PFK-C}}$ or lowering v_{PDH}, is not enough to recover compound oscillations. Thus, we have to both increase $v_{\mathrm{PFK-C}}$ and decrease v_{PDH} in order to restore the desired bursting rhythm.

From a physiological point of view, this approach suggests an upregulation of PDH to compensate for the absence of the M-type isoform. However, recent experiments show that compound bursts were observed in cells in which PFK-M was knocked out, without modifying the gene expression. Therefore, we now show that the IOM2.0 can account for the experimental findings without changing the initial value of v_{PDH}. In fact, it is possible to select regions in the parameter space where compound bursting is transformed into fast bursting by knocking out PFK-M, and others where

compound oscillations persist.

To show this result, we look at the behaviour of two virtual β-cells, called Cell 1 and Cell 2, each of them defined by parameters belonging to one of the two regions. Specifically, we consider a box in the ($v_{\mathrm{PFK-C}}$, $v_{\mathrm{PFK-M}}$, v_{PDH}) parameter space (Figure 5.12). In this scheme, we also indicate the parameter combinations used to simulate Cell 1 (blue dot) and Cell 2 (purple dot). The protocol we used consists of knocking out PFK-M at $t = 20$ min by setting $v_{\mathrm{PFK-M}}$ to zero in both Cell 1 (orange dot) and Cell 2 (green dot).

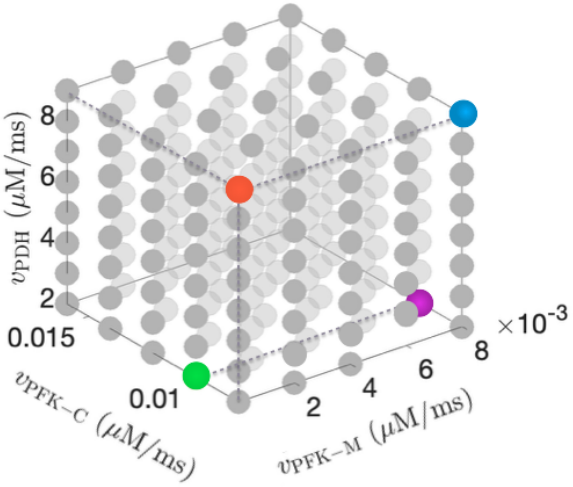

Figure 5.12.: Parameter space in terms of $v_{\mathrm{PFK-C}}$, $v_{\mathrm{PFK-M}}$ and v_{PDH}. The blue and orange dots are used to simulate Cell 1 before (blue) and after (orange) knocking out PFK-M. While, the purple and green dots are used to simulate Cell 2 before (purple) and after (green) knocking out PFK-M.

The results of this protocol are shown in Figure 5.13 for Cell 1 and in Figure 5.14 for Cell 2. Initially, Cell 1 is in a compound bursting mode and most of PFK activity is through the M-type isoform (Figure 5.13, blue) although both PFK isoforms are expressed. In fact, $J_{\mathrm{PFK-M}}$ is roughly 7.5 times larger than $J_{\mathrm{PFK-C}}$ (panels B and D). At t=20 min, the PFK-M is knocked out (orange) setting to zero the rate $v_{\mathrm{PFK-M}}$. In this scenario, the maximum value of $J_{\mathrm{PFK-C}}$ does not change and so the total flux due to the PFK reaction decreases considerably. The PFK activity cannot support intrinsic metabolic oscillations and the compound bursting is transformed into fast bursting.

A different output is shown for Cell 2 (Figure 5.14). Once again, the burst is compound in the wild-type β-cell (purple curve) and $J_{\mathrm{PFK-M}}$ is about 10 times larger than $J_{\mathrm{PFK-C}}$ (panels B and D). However, because of the choice of v_{PDH} and $v_{\mathrm{PFK-C}}$ in the parameter space, PFK-C takes over the absence of M-type isoform allowing intrinsic metabolic oscillations to occur (green). The value of the total PFK flux

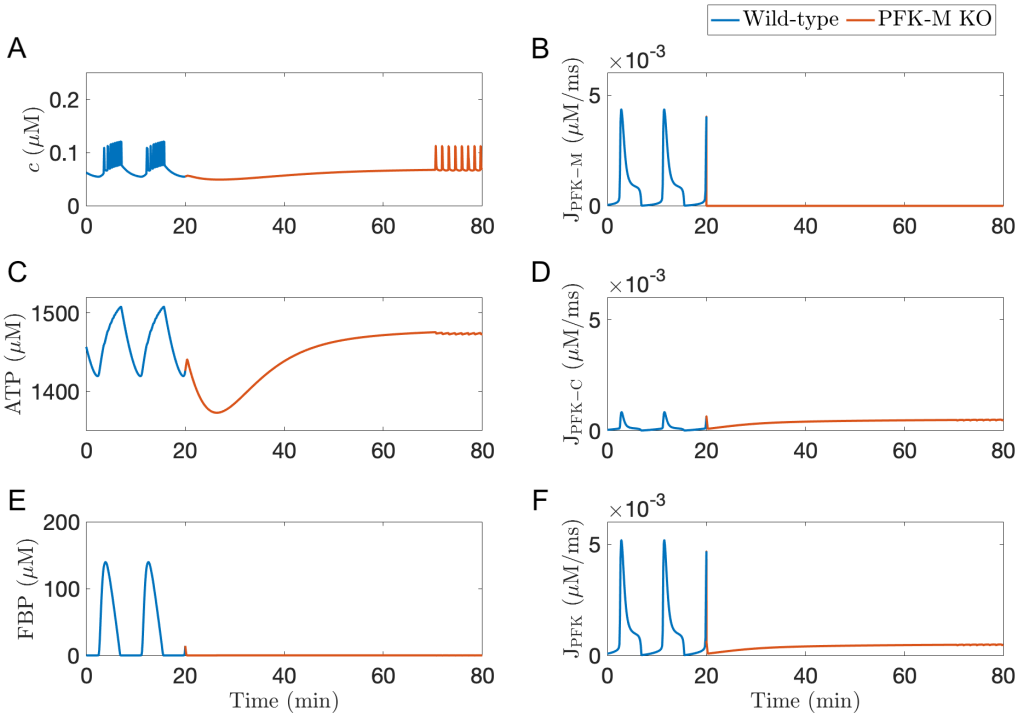

Figure 5.13.: Overview of the mean values of c, ADP, and FBP concentration and J_{PFK} in cell 1. Specific values are: $v_{\mathrm{PFK-M}}$=0.008 μM/ms (blue) and $v_{\mathrm{PFK-M}}$=0 μM/ms (orange). In all cases: $g_{\mathrm{K(Ca)}}$=700 pS, v_{PDH}=9 μM/ms, $v_{\mathrm{PFK-C}}$=0.008 μM/ms.

is smaller than that in the wild-type since the PFK-C is less active than the other isoform, and FBP pulses are smaller. However, the C-type isoform is enough to support the whole PFK activity.

These results show that according to the nature of the β-cell itself, compound bursting may or may not be terminated by knocking out the PFK-M proteins. This could justify the variety of laboratory recordings that sometimes show compound bursting persisting and that sometimes transform into fast bursting. Most important of all, our results illustrate the compensation by PFK-C occurs in the absence of gene upregulation.

5.7 Summary

In this chapter, we described and analyzed the IOM2.0, built from the IOM1.5 with more detailed metabolic reactions. On the one hand, it takes into account a detailed description of the mitochondrial metabolism that consumes ADP to create ATP. On the other hand, it includes the hydrolysis of ATP to ADP by Ca^{2+} pumps in the plasma and ER membranes as production force for the ADP.

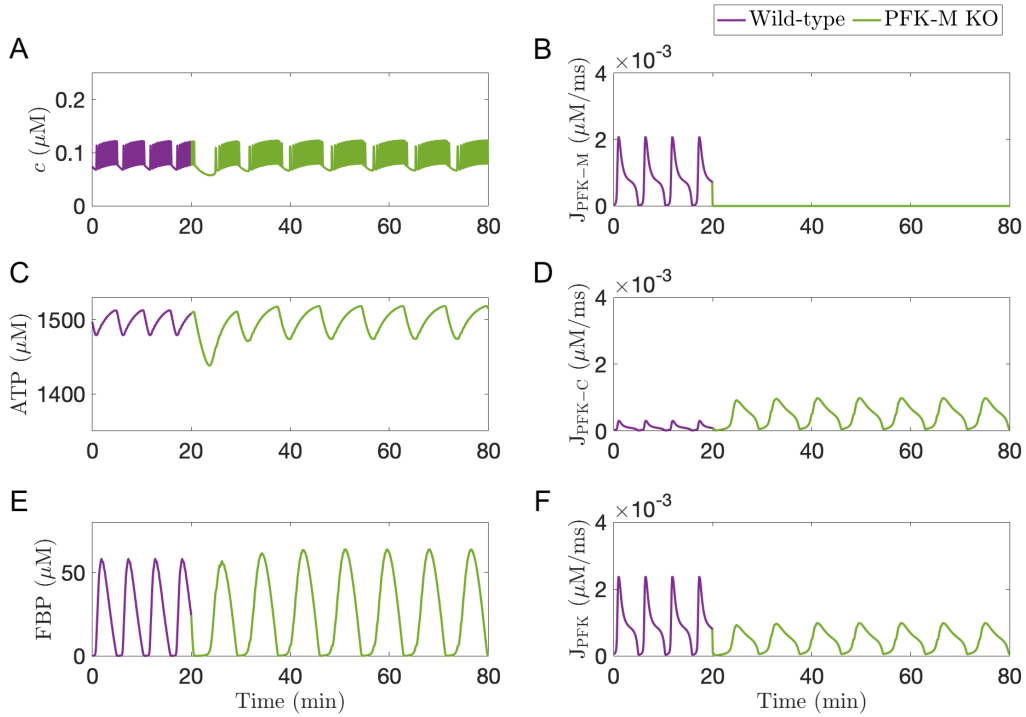

Figure 5.14.: Overview of the mean values of c, ADP, and FBP concentration and J_{PFK} in cell 2. Specific values are: $v_{\mathrm{PFK-M}}$=0.008 μM/ms (purple) and $v_{\mathrm{PFK-M}}$=0 μM/ms (green). In all cases: $g_{\mathrm{K(Ca)}}$=700 pS, v_{PDH}=2 μM/ms, $v_{\mathrm{PFK-C}}$=0.01 μM/ms.

The IOM2.0 can account for experimental observations involving processes occurring in the mitochondria, impossible for the IOM1.5. The model predictions are consistent with experimental data. Moreover, because of a better description of the ATP dynamics, the IOM2.0 can overcome the limitations of the IOM1.5.

In the next chapters, we examine the response of the IOM2.0 to changes in glucose concentration (Chapter 7), and a further extension of the model that includes both glucose dynamics and insulin exocytosis (Chapter 8).

6 The Glucose Dynamics in the Integrated Oscillator Model

> *If we knew what it was we were doing, it would not be called research, would it?*
>
> **— Albert Einstein**

In this chapter, we start from the IOM2.0 and introduce an explicit dependence of the cellular metabolism on the extracellular glucose level. The β-cells can burst only when the glucose concentration in the blood is in a stimulatory range (about 5 mM to 14 mM [63]). In the DOMs and the IOMs described so far, the parameter J_{GK} (representing the glucokinase reaction rate) has been varied to simulate different glucose concentrations in the blood. However, given the key role of glucose in β-cell function, we now improve this simplistic description and we introduce the glucose dynamics. This extension of the previously introduced mathematical model is described in Section 6.1.1, while the results obtained with it are shown in Sections 6.2 and 6.3. We refer to this extended model as the IOM2.1.

6.1 Mathematical Model

The IOM2.1 is an extension of the IOM2.0 (Chapter 5) in which the glucose dynamics is added into the metabolic module. The dynamics of the electrical and metabolism components are the same as in the IOM2.0 (see Sections 5.2.1 and 5.2.3).

6.1.1 Metabolic Module

Glucose enters into the cell via facilitated diffusion through the GLUT-2 glucose transporter. Here, the glucose becomes the influx to the glycolytic subsystem. We assume that the change in the glucose concentration in the blood will immediately transfer to changes inside the cell. That is, we use a quasi-equilibrium approximation for the intracellular glucose, and the glucokinase (GK) reaction rate is now described by:

$$J_{\mathrm{GK}} = v_{\mathrm{GK}} \frac{G_{\mathrm{i}}^2}{K_{\mathrm{GK}}^2 + G_{\mathrm{i}}^2} \,, \tag{6.1}$$

Parameter	Value	Parameter	Value
v_{GK}	0.0037 μM ms^{-1}	K_{GK}	19×10^3 μM

Table 6.1.: Parameters for the glucose dynamics.

where G_{i} is the intracellular glucose concentration that, due to the *quasi-equilibrium* approximation, is equal to the extracellular glucose concentration, G_{e}. Figure 6.1 illustrates the trend of J_{GK} as a function of the extracellular glucose. The values of the maximum rate v_{GK}, and the parameter K_{GK} are given in Table 6.1, while the value of G_{e} is user-specified and will be varied to study its effect on the model output. The other variables of this module (F6P, FBP, and ADP) are described as in the IOM2.0 (Section 5.2.2).

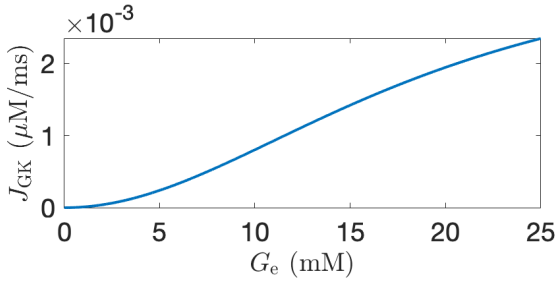

Figure 6.1.: GK reaction rate, J_{GK}, as function of the extracellular glucose G_{e} Eq (6.1).

6.2 Mechanism Driving the Burst and Glucose Level

In the previous chapters, we have been focusing on the impact of the glycolytic efflux (J_{PDH}) on the glycolytic oscillator. In this section, we focus on the glycolytic influx (J_{GK}) and investigate how it influences the activity of the glycolytic oscillator. As observed in the previous section, the extracellular glucose indirectly controls the glycolytic influx by acting on the intracellular glucose level. Thus, we vary the parameter G_{e} to control the influx of glucose into glycolysis.

For this purpose, we once again focus on the glycolytic subsystem which now includes the parameter G_{i} (equal to G_{e}). To isolate the (F6P, FBP) subsystem we clamp c and ψ_{m} at fixed values, while c_{m} and the nucleotides (both cytosolic and mitochondrial) are at equilibrium. Thus, the key parameters in this analysis are c (representing the influence of electrical activity on glycolysis), G_{e} and v_{PDH} (controlling the glycolytic influx and efflux, respectively). Furthermore, as we have already investigated in depth the role played by v_{PDH} in the nature of glycolytic oscillations (Section 4.3.1), we here set v_{PDH}=2 μM/ms, and we vary only c and G_{e} in our following analysis.

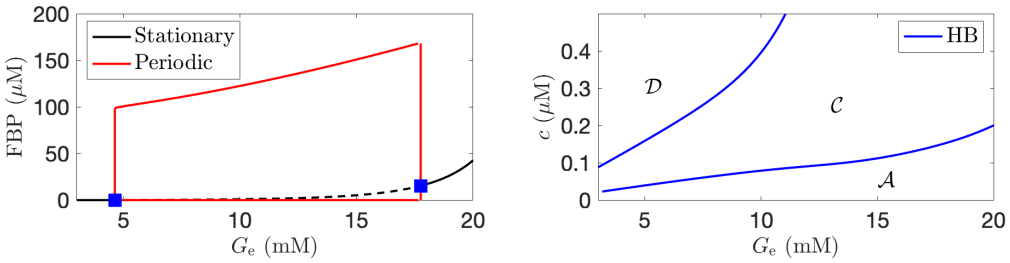

Figure 6.2.: (A) Bifurcation structure of the glycolytic module with respect to G_e, for v_{PDH}=2 μM/ms and $c = 0.15$ μM. Blue squares indicate the subcritical HB. (B) Two-parameter bifurcation diagram of the glycolytic subsystem illustrating the regions of Ca^{2+}-dependent ($\mathcal{A}$ and $\mathcal{D}$), and Ca^{2+}-independent ($\mathcal{C}$) oscillations.

We first fix $c = 0.15$ μM and construct a bifurcation diagram (Figure 6.2A) of the glycolytic subsystem with extracellular glucose concentration, G_e, as a bifurcation parameter. For low values of G_e, the glycolytic subsystem is at steady state with very small constant FBP concentration (solid black). The subsystem becomes oscillatory for intermediate values of glucose concentration in the range delimited by two subcritical Hopf bifurcations (HB, blue squares). The first HB (HB_1) occurs at $G_e \approx 4.56$ mM, while the second (HB_2) at $G_e \approx 13.67$ mM. A branch of unstable periodic solutions arises from each of the subcritical HBs and it meets a branch of stable periodic solutions (solid red) at a saddle-node of periodics bifurcation (SNP). Since the SNPs occur at almost the same value of G_e, we do not indicate them in the figure. For high values of G_e, the glycolytic subsystem is once again at steady state (solid black). At these high G_e values, the equilibrium value of FBP is higher than in the other stationary scenario.

Figure 6.2B shows the two-parameter continuations of the Hopf bifurcations in the (G_e, c) plane. The HB curves divide the plane into three regions, characterized by different dynamics. To stress the analogy with the results shown for the IOM1.5 (Figure 4.6), we use the same nomenclature for the regions: in region $\mathcal{A}$ (on the right of the HB_2 curve) the equilibrium is a unique attractor; in region $\mathcal{C}$ (between the two HB curves) the equilibrium is unstable and the limit cycle is the only attractor; in region $\mathcal{D}$ (on the left of the HB_1 curve) the equilibrium is once again a unique attractor. We point out that, unlike in the IOM1.5, there is no bistable region.

We now come back to the full IOM2.1, where c, ψ_m, and the nucleotides vary over time. If the projection of the orbit onto the (G_e, c) plane lies in either region $\mathcal{A}$ or region $\mathcal{D}$, the metabolic oscillations will be induced by c (passive glycolytic oscillator) and the FBP pattern will be sawtooth. If the projection lies in region $\mathcal{C}$, there will be intrinsic glycolytic oscillations (active glycolytic oscillator) and the FBP time course

will be pulsatile.

In light of the above results, we conclude that the status (active or passive) of the glycolytic oscillator can be modulated by changing the glycolytic influx (by varying G_{e}) for a fixed v_{PDH}, in addition to the previous transition obtained when varying the glycolytic efflux (by changing v_{PDH}) for a fixed glucose level.

Figure 6.3 summarises the results for a cell in bursting mode. The glycolytic influx is increased from top to bottom, while the glycolytic efflux is increased from left to right. For low glycolytic influx and efflux (panel A), the glycolytic oscillator is activated (pulsatile FBP). It can be turned off by increasing the glucose concentration (panel C, sawtooth-like FBP) and it remains passive even for higher glycolytic influx (panel E). If the glycolytic efflux is high (right column), the glycolytic oscillator is active for low and intermediate influx (panel B and D), and it becomes passive only at high glucose levels (panel F). Finally, we observe that the transition from active to passive can be also accomplished by decreasing v_{PDH} for an intermediate glucose level (panel D to panel C).

In summary, the glycolytic influx and efflux play opposite roles in the activation of the glycolytic oscillator. In order to have intrinsic metabolic oscillations, we can either increase v_{PDH} (glycolytic efflux) or decrease G_{e} (glycolytic influx).

6.3 Glycolytic Patterns in a β-cell not in Bursting Mode

Thus far, we have been focusing our attention on β-cells in bursting mode. In this section, we investigate the model response to gradual changes in glucose level starting from sub-threshold glucose conditions (i.e., the concentration is insufficient to trigger bursting activity in β-cells) up to very high concentrations under which the cell spikes continuously.

Specifically, we consider the scenario in which the extracellular glucose is increased from 4 mM up to 17 mM. The protocol consists of two steps.

1. We first increase the glucose concentration from a subthreshold level up to a stimulatory level. We simulate this by increasing G_{e} from 4 mM to 11 mM at $t = 50$ min.

2. In the second step, we further increase the glucose level. This is simulated at $t = 100$ min by bringing G_{e} from 11 mM to 17 mM.

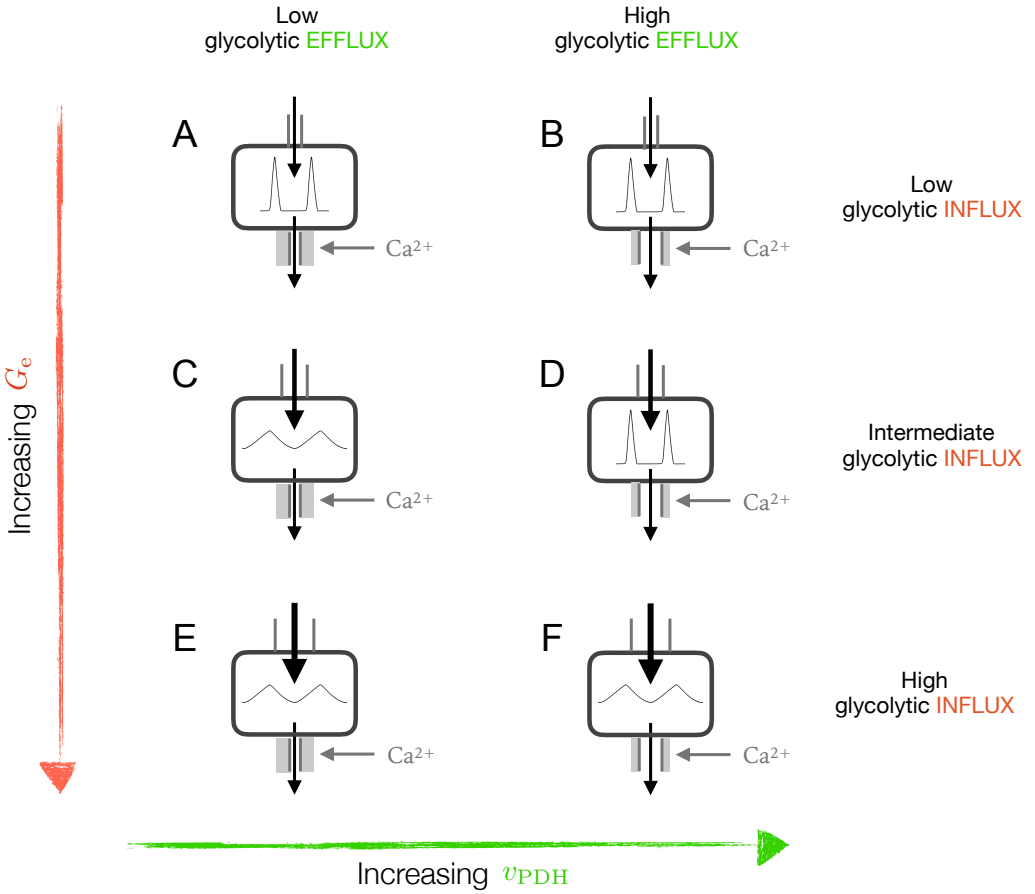

Figure 6.3.: Effects of glycolytic input (controlled by G_e) and output (modulated by v_{PDH}) on FBP. In each box, we give the pulsatile or sawtooth-like character of FBP oscillations corresponding to the particular combination of efflux and influx. The strength of glycolytic influx and efflux is given by the width of the channels on the top and on the bottom of the box, respectively. The shaded area around the efflux channel illustrates the Ca^{2+} control on the glycolytic efflux.

Figure 6.4 illustrates the results of this protocol. Subthreshold glucose concentration (G_e=4 mM) is not enough to allow the cell to burst. However, it is enough to activate the glycolytic oscillator. The metabolic oscillations (Figure 6.4, bottom row) induce subthreshold oscillations in Ca^{2+} concentration (top row) and in the plasma membrane (not shown). The cell starts busting when the glucose is increased up to a stimulatory level (G_e=11 mM) at $t = 50$ min. Finally, for elevated G_e (G_e=17 mM), the cell spikes continuously (after a relatively short transition phase).

We can analyze these transitions in terms of Figure 6.2. When the glucose concentration is 4 mM (below the stimulatory level), the projection of the orbit lies in region $\mathcal{C}$. The glycolytic oscillator is active, and pulses in FBP concentration are generated. However, the metabolic activity is not enough to trigger the cellular electrical activity, and we observe only sub-threshold oscillations in Ca^{2+}. When the glucose is increased to 11 mM the projection remains in region $\mathcal{C}$, but now metabolic

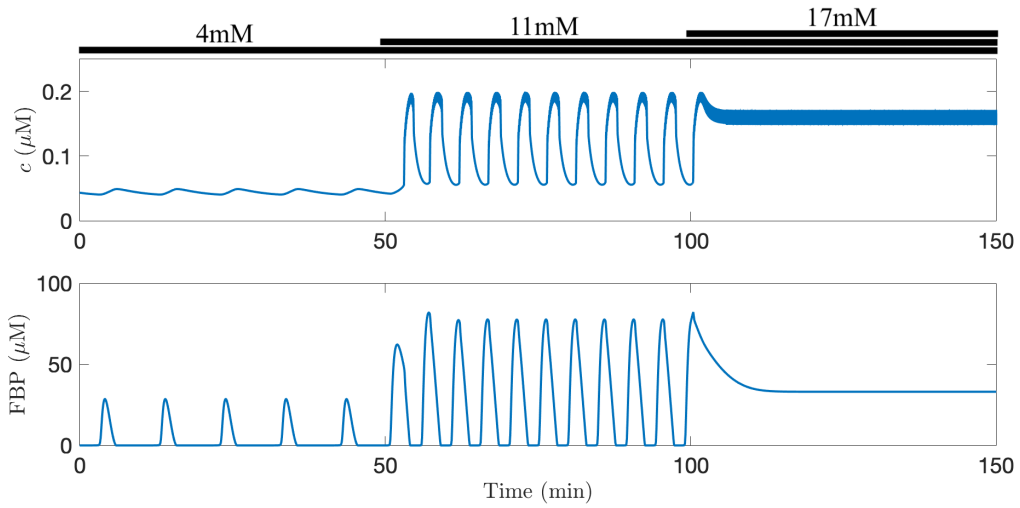

Figure 6.4.: Time courses of cytosolic calcium (top row) and cytosolic FBP (bottom row), with $g_{\mathrm{K(Ca)}}$=150 pS and v_{PDH}=2 μM/ms. The top bars illustrate the extracellular glucose concentration that is progressively increased from 4 mM to 11 mM at $t = 50$ min, and to 17 mM at $t = 100$ min.

oscillations are able to drive the electrical activity. Finally, if the glucose is too high, the system moves into $\mathcal{A}$, a region of Ca^{2+}-induced metabolic oscillations, and the glycolytic oscillator is passive. Due to the elevated metabolic activity, the cell spikes continuously in this last scenario.

This result is consistent with the experimental findings published by McKenna and collaborators in 2016 [63]. In this paper, the authors show that the slow oscillatory behaviour in a β-cell can be observed if the glucose concentration is higher than about 5 mM and it stops when the glucose level is 12.90 mM (with standard deviation 2.47 mM).

6.4 Summary

In this chapter, we simulated the glucose effect on the insulin-secreting β-cell activity. Because of the crucial role of extracellular glucose level in the insulin secretion process, the IOM2.0 was extended to include a description of the intracellular glucose concentration depending on the glucose level in the blood. This new model was called the IOM2.1.

We demonstrated that the status of the glycolytic oscillator (active or passive) can be changed by varying the glycolytic influx (modulated by the glucose level in the

blood), instead of varying the glycolytic efflux (controlled by the parameter v_{PDH}) as we showed in previous chapters.

The predictions obtained with the IOM2.1 were in line with the experimental observations published in the literature. We showed that for sub-stimulatory glucose there is no electrical activity in the β-cell, although the metabolic oscillations can be triggered with a suitable choice of parameters. If the glucose concentration is very high, the β-cell will be continuously spiking.

We keep investigating the cellular response to changes in glucose levels in Chapter 7, and we further extend the model to add the insulin secretion in Chapter 8.

7 Glucose Response as a Way to Distinguish Between Bursting Mechanisms

> *Look deep into nature, and then you will understand everything better.*
>
> — **Albert Einstein**

In this chapter, we step back from focusing only on the IOM (and its various versions) and we look at a more general behaviour shown by most of the models presented in this dissertation, including the IOMs. More precisely, we address once again the question about the nature of the mechanism underlying the bursting activity. We hypothesize that monitoring the cytosolic ATP or ATP/ADP level when the extracellular glucose concentration varies can be an effective method to distinguish between driving forces.

We begin by motivating the analysis of the IOM2.1 (Section 7.1). Then, we examine the response of the IOM2.1 to changes in the glucose level (Section 7.2.1). To better understand the nucleotide dynamics, we focus in Section 7.2.2 on the geometric features of a simple β-cell model, such as the Biophan model (Section 7.2.2). Finally, in Section 7.2.3, we use the Fridlyand and Cha models presented in 2005 and 2011, respectively, to compare our results with other β-cell models present in the literature.

7.1 Motivations

We show that β-cells are mostly inactive when the blood glucose level is low, but the activity of β-cells increases as the glucose level increases (Chapter 6). This elevated electrical activity is due to the increase in the ratio of ATP to ADP, which is a direct result of glucose uptake and metabolism. K(ATP) channels in the plasma membrane are inactivated by ATP, so the increase in ATP/ADP that results from glucose metabolism decreases the hyperpolarizing K(ATP) current, $I_{\mathrm{K(ATP)}}$, thereby depolarizing the cell. It is generally thought that a continuous increase in the glucose

level results in a continuous increase in the ATP/ADP ratio, but this has never been shown.

In the previous chapters, we investigated in detail the mechanisms underlying the busting activity. In Section 3.2, we discussed the main hypotheses that have been presented in the literature so far. One suggestion is that the burst is driven by the oscillations in the activation state of K(ATP) channels, and indeed the observed oscillations in ATP/ADP are consistent with this hypothesis. However, something else could be driving bursting and the ATP/ADP oscillations could be a consequence of the cellular activity and not the trigger. In this case, they could be governed by oscillations in the intracellular Ca^{2+} concentration that modulates the Ca^{2+} pumping by ATPases in the plasma and ER membranes powered by hydrolysis of ATP itself. Other mechanisms that have been suggested are the actions of K(Ca) channels (Chay-Keizer [26]) or the current produced by electrogenic plasma membrane pumps (Fridlyand [37, 36]). The difficulty in identifying the mechanism underlying bursting is that all of these factors oscillate and so are correlated with the bursting electrical activity.

In principle, one could block one of these factors, such as the K(ATP) channels, and determine if this interferes with the bursting rhythm. However, this is a fundamentally flawed approach. For example, blocking K(ATP) channels reliably terminates the bursting pattern, but this is due to the drastic change in the mean level of the blocked factor: blocking K(ATP) channels removes most of the hyperpolarizing current in the cell, putting the cell into a highly active state. What is needed is an approach that does not require artificial manipulation of any of the potential rhythmogenic factors. In this chapter, we demonstrate using mathematical modelling that by monitoring the cytosolic ATP or ATP/ADP ratio while the glucose level is changed one can determine whether K(ATP) channel activity drives bursting in β-cells.

7.2 Dynamic Homeostasis in the Nucleotide Ratio

In this section, we investigate the nucleotide homeostasis starting with the most sophisticated IOM2.1 presented in Chapter 6. In trying to understand in depth the obtained results, the complexity of the IOM2.1 does not play in our favour. Therefore, we repeat the same analysis with a simpler model, namely the Biophan model described in Section 3.5.1. As the output is the same, we use the latter to provide a detailed analysis of the results. Finally, we analyze the ATP/ADP dynamics with the Fridlyand and Cha models presented in 2005 and in 2011, respectively (Sections 3.3.2 and 3.4.1) since it has been shown that the burst is not driven by K(ATP) in these models.

7.2.1 Dynamic Homeostasis in the Nucleotide Ratio in the IOM2.1

It has been shown that the ATP level increases with an increase in glucose when islet β-cells are inactive [91, 77]. Indeed, this increase is what ultimately activates the cells. Although intuition suggests that this should be the case, it has not been established whether the same holds when the cells are in an active bursting state. We begin by testing this hypothesis with the IOM2.1 that contains compartments for electrical activity of the cell, Ca^{2+} dynamics, and metabolism module.

Figure 7.1 shows simulations with the IOM2.1 with two values of the extracellular glucose, G_e, for a cell in slow bursting (left column) and a cell in fast bursting (right column). In the first case, the burst *duty cycle* (i.e., ratio of the duration of the active phase to the burst period) is below 0.5 for low G_e low. The duty cycle increases to approximately 0.8 for high G_e (Figure 7.1A), which agrees with the increases in duty cycle observed in experiments of glucose increase [68]. In both cases, the ATP/ADP exhibited oscillations of the same amplitude. In fact, the peaks and nadirs are almost the same (Figure 7.1C). Thus, when the IOM2.1 is in a slow bursting state a simulated increase in the glucose level does not increase the ATP/ADP level. This is in contrast to what occurs at low glucose levels when the model cell is silent and an increase in glucose does indeed increase ATP/ADP (not shown).

In a fast bursting state, the duty cycle increases for high G_e (Figure 7.1B), as in the slow case, and so do both the peak and nadir values of ATP/ADP (Figure 7.1D), unlike the previous case. In the following, we determine the basis for these different behaviours.

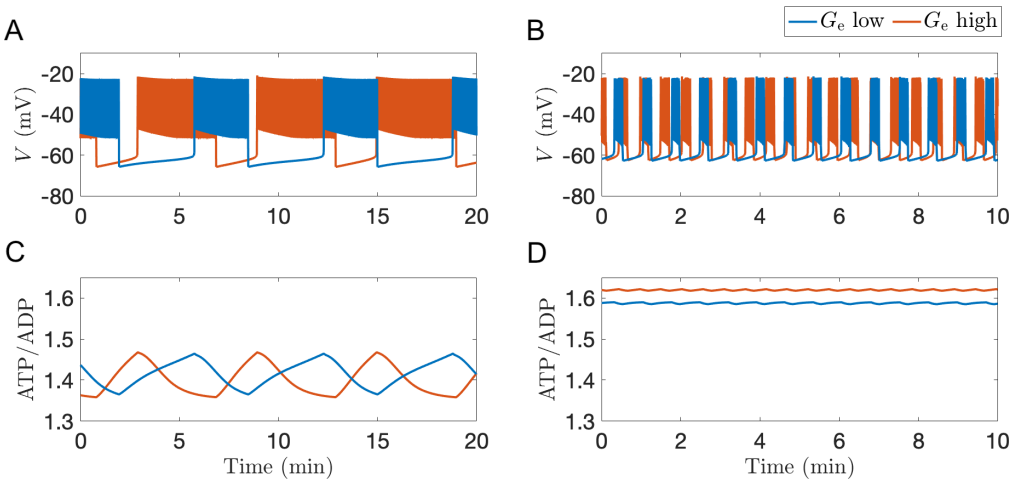

Figure 7.1.: Plasma membrane potential nucleotide ratio time courses with the IOM2.1 when G_e=9 mM (blue) and G_e=13 mM (orange). Specific values are: $g_{K(Ca)}$=150 pS (left column) and $g_{K(Ca)}$=600 pS (right column). In all cases, v_{PDH}=0.4 μM.

7.2.2 Conditional Nucleotide Homeostasis with the Simple Model

To better understand the dynamic nucleotide homeostasis shown above for slow bursting, we turn to the Biophan model. In this model, glucose affects the ATP to ADP ratio through the parameter r (Eq. (3.13)). We vary r to investigate the response of the model to changes in the glucose level. As shown in Figure 7.2A, an increase in r increases the burst duty cycle, as with the IOM2.1 when G_e is increased. Also similar to the IOM2.1, the peaks and nadirs of ATP/ADP (which is $\frac{1}{a}$ in this model) change little when the glucose parameter is increased (Figure 7.2C). Quantitatively, we compute the ratios

$$d_p = \left| \frac{\Delta p}{\Delta r} \right|, \qquad d_n = \left| \frac{\Delta n}{\Delta r} \right|, \tag{7.1}$$

to measure the rate of change in the peak (p) and nadir (n) level relative to the change in r. The small values of these quantities ($d_p = 0.026$ and $d_n = 0.392$) suggest that, in this model as in the IOM2.1, during slow bursting there is dynamic nucleotide homeostasis.

We now increase $g_{K(Ca)}$ from 10 pS to 700 pS to move the model cell from a slow bursting state to a much faster bursting state. Once again, an increase in r increases the burst duty cycle (Figure 7.2B), as predicted with the IOM2.1. However, in this case, the change in r causes an increase in both the peak and nadir values of ATP/ADP (Figure 7.2D). More precisely, $d_p = 0.79$ and $d_n = 2.11$, which are ≈ 30 and $\approx$5 times larger than during slow bursting. Thus, in this faster bursting mode the nucleotide homeostasis is lost: peak, nadir, and mean ATP/ADP all noticeably increase with increased glucose.

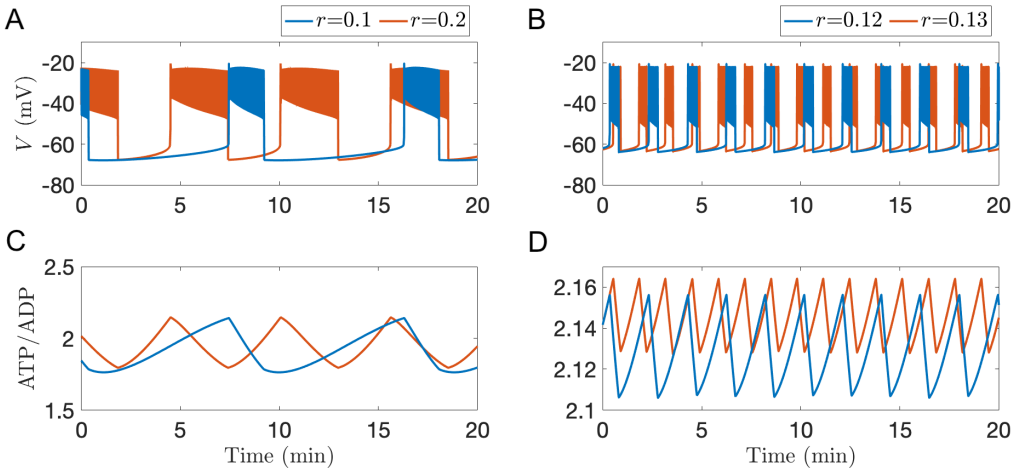

Figure 7.2.: Plasma membrane potential and ATP/ADP time courses with the Biophan model for slow bursting with $g_{K(Ca)}$=150 pS (left column) and fast bursting with $g_{K(Ca)}$=700 pS (right columns).

At low values of r the model cell is silent (duty cycle=0), at high values it spikes continuously (duty cycle=1), and at intermediate r values it bursts (0<duty cycle<1). In Figure 7.3, we show the duty cycle for a range of r values covering all of these behaviours. Superimposed on the duty cycle curves are curves showing the mean values of ATP/ADP, denoted as <ATP/ADP>. This is normalized to facilitate comparison between the slow bursting (panel A) and fast bursting (panel B) cases. The normalization is done by dividing <ATP/ADP> by its maximum, and it is denoted as $<\text{ATP/ADP}>_{\text{n}}$. For small r values, when the cell is silent, increases in r lead to increases in $<\text{ATP/ADP}>_{\text{n}}$. At the r value at which bursting commences, there is a drop in $<\text{ATP/ADP}>_{\text{n}}$ since the bursting elevates the intracellular Ca^{2+} level. At higher r values there is little change in the mean nucleotide level in the case of slow bursting, but a steady increase in the case of fast bursting. In the slow bursting case, $<\text{ATP/ADP}>_{\text{n}}$ declines once the cell enters a continuous spiking state (duty cycle=1) due to the associated increase in the intracellular Ca^{2+} level.

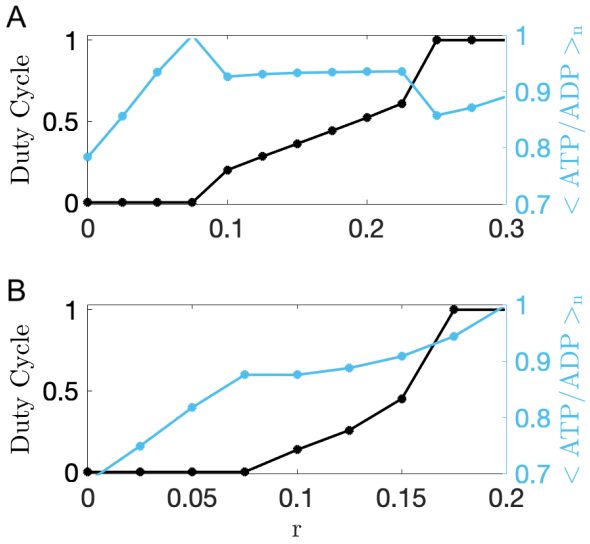

Figure 7.3.: Duty cycle (black) and the normalized mean level of ATP/ADP (blue) with the Biophan model in the case of (A) slow bursting (with $g_{\text{K(Ca)}}$=10 pS), and (B) fast bursting (with $g_{\text{K(Ca)}}$=700 pS).

Geometric Rationale for Nucleotide Homeostasis

The dynamic homeostasis of the nucleotide ratio can be explained geometrically using a fast/slow analysis [9]. In the phantom bursting model, three variables vary on a fast time scale during slow bursting: V, n, and c. The remaining two variables, c_{er} and a, vary on slower time scales. We take advantage of this time scale separation and perform a bifurcation analysis of the fast subsystem, treating $\frac{1}{a}$ =ATP/ADP as

the bifurcation parameter. The other slow variable, c_{er}, is clamped as described below.

The fast-subsystem bifurcation diagram is shown in Figure 7.4A, for the case of slow bursting ($g_{\mathrm{K(Ca)}} = 10$ pS). The c_{er} variable is clamped at the value taken on at the beginning of an active phase, $c_{\mathrm{er}} = 51$ μM. At low values of ATP/ADP, there is a stable equilibrium at a hyperpolarized voltage. The branch of stable hyperpolarized equilibria (bottom solid curve) persists up until a saddle-node bifurcation (SNB, purple square), at which point it coalesces with a branch of saddle point equilibria (middle dashed curve). This branch turns around at another saddle-node bifurcation and gains stability at a Hopf bifurcation (HB, green square), and the remainder of the upper branch is a stable depolarized equilibrium (top solid curve). A branch of stable periodic solutions (blue curve) is born at the supercritical Hopf bifurcation, which reflects tonic spiking solutions. This branch terminates at a homoclinic bifurcation (HM, green triangle).

The burst trajectory (yellow curve) is superimposed on this fast-subsystem diagram, also called the critical manifold, in Figure 7.4B. During the silent phase, the trajectory follows the bottom branch of the critical manifold, moving rightward as ATP/ADP increases (since Ca^{2+} is low during this phase, the ATP hydrolysis by Ca^{2+} pumps is reduced, so ATP/ADP increases). Once the stationary branch terminates at the saddle-node bifurcation the trajectory moves to the periodic spiking branch and now travels leftward (due to the increased ATP hydrolysis when Ca^{2+} is elevated) until the periodic branch ends at the homoclinic bifurcation. This terminates the active phase and a new silent phase is started. Thus, during one cycle of bursting the ATP/ADP level goes from its value at the homoclinic bifurcation to its value at the saddle-node bifurcation, covering the region of bistability between the bottom equilibrium branch and the stable periodic branch.

When the glucose parameter r is increased from 0.1 to 0.2 (Figure 7.4C), there is no effect on the critical manifold. The only effect is on the speed at which the trajectory moves along the bottom branch and the spiking branch since r appears only in the differential equation for a and not for V. With the larger r value, the trajectory moves more quickly along the bottom branch and more slowly along the top branch than it did with the lower r value, since the rate of ATP production is greater. This increases the burst duty cycle. However, the minimum and maximum ATP/ADP values taken on during bursting are the same as before, since the slow manifold did not change. In summary, since slow variation of ATP/ADP is responsible for turning the burst active phase on and off, the range of values taken on by the nucleotide ratio does not change when the glucose parameter is changed. This is true, however, only if the model cell is in a bursting state, where the bursting trajectory cycles over the bistable interval in the critical manifold. If the onset and offset of each active

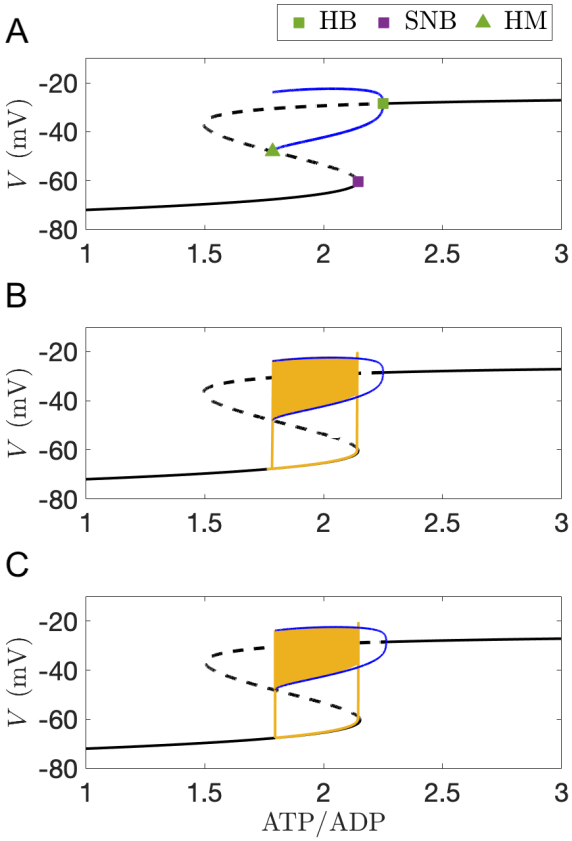

Figure 7.4.: Fast-slow analysis of bursting with the Biophan model. The conductance $g_{K(Ca)}$=10 pS and the parameter r is increased from 0.1 (A and B) to 0.2 (C). The black curve represents the fast V-nullcline (z-curve) at the beginning of the active phase, with the convention that solid line represents stable branch and dashed line unstable branch. The purple square indicates the supercritical Hopf bifurcation (HB), the green square the lower saddle-node bifurcation (SNB), and the green triangle the homoclinic bifurcation (HM). The yellow curves represent the projections of the bursting on the (ATP/ADP, V)-plane.

phase of bursting are driven by a variable other than ATP/ADP, then none of this applies.

7.2.3 Other Models in the Literature

The results shown so far are not model dependent. Instead, they reflect the properties of negative feedback that results in electrical bursting oscillations. To prove that, we select some other models in the literature and look at how they respond to the glucose increase. Because of their impact on the β-cell modeling society, we choose the models presented by Fridlyand *et al.* in 2005 [36], and by Cha *et al.* in 2011 [22] and introduced in Sections 3.3.2 and 3.4.1, respectively. In the model described by Fridlyand, glucose directly controls the glucokinase reaction rate that is the source of the glucose metabolite concentration, which in turn affects the ATP production

through oxidative phosphorylation. In the more complex model presented by Cha, glucose enters into play by controlling the glycolysis phosphorylation that produces the intermediate metabolites, which are now identified with NADH.

We implemented both models to study their reaction to the glucose increase. The results are shown in Figure 7.5. Panel A shows the values of the duty cycle (black) and the normalized <ATP/ADP> (blue) at different glucose concentrations obtained with Fridlyand's model. Panel B shows the same type of information obtained with Cha's model.

We first observe that the duty cycle is an increasing function of glucose, as with the IOM2.1 and Biophan model. However, unlike these models, $<\text{ATP/ADP}>_n$ increases monotonically with glucose concentration when the model cell is bursting. This occurs because K(ATP) channels do not drive the bursting. In fact, in both the Fridlyand and Cha models, bursting is driven by activity-dependent oscillations in the current through plasma membrane pumps.

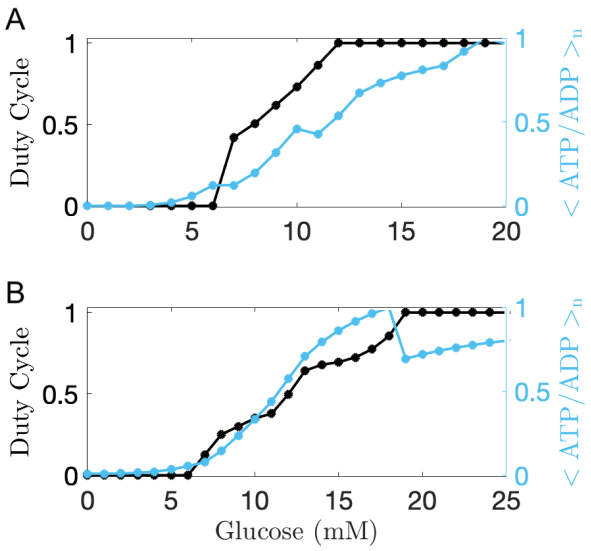

Figure 7.5.: Duty cycle (black) and the normalized mean level of ATP/ADP (blue) curves with the Fridlyand model (A) and the Cha model (B).

7.3 Summary

In this chapter, we suggested using the ATP/ADP response to changes in extracellular glucose concentration as a tool to discern among possible mechanisms underlying the β-cell bursting activity. We demonstrated that, if oscillations in the K(ATP) current are responsible for starting and stopping bursts of activity, then increases in the glucose level should have little or no effect on the peaks and nadirs of ATP/ADP

oscillations, provided that the cell is bursting. If some other factor drives bursting, such as K(Ca) current or plasma membrane pumps, then it is expected that the peaks/nadirs of ATP and ADP will change with the glucose level.

In our study, we used the IOM2.1 to demonstrate that when a cell is in a slow bursting mode (i.e., K(ATP)-driven activity), ATP/ADP oscillations do not exhibit significant change over the range of glucose, unlike the duty cycle of the oscillations (that increases with increases in glucose concentration). To show the very general nature of this behaviour, we considered other models, i.e., the Biophan model [10], the model presented by Fridlyand *et al.* in 2005 [36] and by Cha *et al.* in 2011 [22], and we demonstrate that the results are in line with our hypothesis. Moreover, we performed a fast/slow analysis to provide a geometric explanation for the nucleotide homeostasis using the simpler Biophan model.

Our result is very important in the islet biology field since it predicts that, contrary to intuition, increases in the glucose concentration do not cause increases in the ATP/ADP level when the islets exhibit slow oscillations. This hypothesis must be validated with experimental data.

8 Insulin Secretion Simulated with the Integrated Oscillator Model

> *Science is evidence-based and provides a continuing understanding of complex natural phenomena. Our understanding is constantly evolving and continually improving.*
>
> — **Priyamvada Natarajan**

With both mitochondrial and glucose dynamics described in the IOM2.1, all the elements influencing the insulin exocytosis (i.e., blood glucose concentration, Ca^{2+} concentration, and both cytosolic and mitochondrial metabolisms) are present in the mathematical model. In this chapter, we take into account these factors to further extend the IOM2.1 by adding the insulin secretion description.

We start explaining why simulating the insulin release is so important (Section 8.1). Then, we describe the mathematical model (Section 8.2) and the result obtained with the model (Sections 8.3 and 8.4).

8.1 Motivations

The β-cells are the only cell responsible for producing and for secreting the insulin hormone. Thus, the cellular response with the appropriate secretion of insulin is a crucial factor in the maintenance of glucose homeostasis. Given such a crucial role, extending the IOM2.1, our most sophisticated model, to include the insulin release is a natural step toward a complete description of the β-cell activity.
Furthermore, the simulation of the insulin exocytosis from a virtual β-cell could be eventually used as a *in silico* tool to support medical doctors in the exploration of different drug therapies and decision-making process.
Finally, in addition to this clinical application, there is the will to understand the nature of the mechanism underlying the β-cell activity and downstream insulin pulses. To be precise, we have shown different metabolic patterns resulting from different mechanisms underlying the β-cell activity. Since the insulin exocytosis

process is influenced by cellular metabolism, it is legitimate to wonder whether or not the insulin patter is likewise affected by those mechanisms.

Therefore, we extend the IOM2.1 to simulate the insulin exocytosis process. We refer to the model presented in this chapter as the IOM2.2.

8.2 Mathematical Model

The IOM2.2 is an extension of the latest IOM2.1 (Chapter 6) in which an insulin-exocytosis describing module is added. To this aim, we first make some changes in the calcium module of the IOM2.1. We describe these adjustments and the new insulin module in the next sections.
In what follows, only variables whose dynamics have been modified or hereby introduced for the first time are described. All other variable dynamics have not been changed from their descriptions presented in Sections 5.2.1 (electrical module), 5.2.2 (cytosolic metabolism module), 5.2.3 (mitochondrial metabolism module), and Section 6.1.1 (glucose dynamics).

8.2.1 The Electrical and Calcium Module

The modification in Ca^{2+} dynamics takes into account the different types of Ca(V) channels divided on the basis of differing pharmacology, voltage-dependent, and kinetic properties. In this dissertation, we consider only the two most relevant kinds of channels in β-cell, namely L- and R-type. Although they are both crucial to modulate the cellular membrane potential, the L- and R-type have a different role in the insulin secretion. Specifically, it has been observed that Ca^{2+} influx through L-type channels has an amplifying role in the insulin exocytosis cascade [80] and that the granules containing insulin can form stable complexed with this kind of channels [5]. On the other hand, the R-type influences the insulin secretion only marginally and indirectly by increasing Ca^{2+} level in the cytosol without any direct contribution to the granules dynamics [44]. Because of this, we modify the model to include the two different types of Ca(V) channels.

For this formulation of the calcium module, the Ca^{2+} densities through the Ca(V) channels are decomposed into the L- and R-type components. Mathematically, the current I_{Ca} described in Eq. (4.2) is split into two components

$$I_{\mathrm{Ca,L}} = r_{\mathrm{L}} I_{\mathrm{Ca}} \ , \qquad I_{\mathrm{Ca,R}} = (1 - \mathrm{r_L}) I_{\mathrm{Ca}} \ , \tag{8.1}$$

where $I_{\mathrm{Ca,L}}$ and $I_{\mathrm{Ca,R}}$ are the current due to the movements of the Ca^{2+} ions through the L-type and through the R-type, respectively. The parameter r_{L} represents the portion of L-type channels and it is fixed to 0.5 in our model. In other words, we assume the Ca(V) channels are equally split into L- and R-type.

We assume that Ca^{2+} ions entering into the cell through an R-type of Ca(V) channels go directly into the cytosol, while ions through the L-type enter first into an intermediate compartment surrounding the channels and only a fraction of them move toward the cytosol. This new compartment is called micro-domain, M-D. Figure 8.1 provides a visual representation of the IOM2.2 including the M-D.

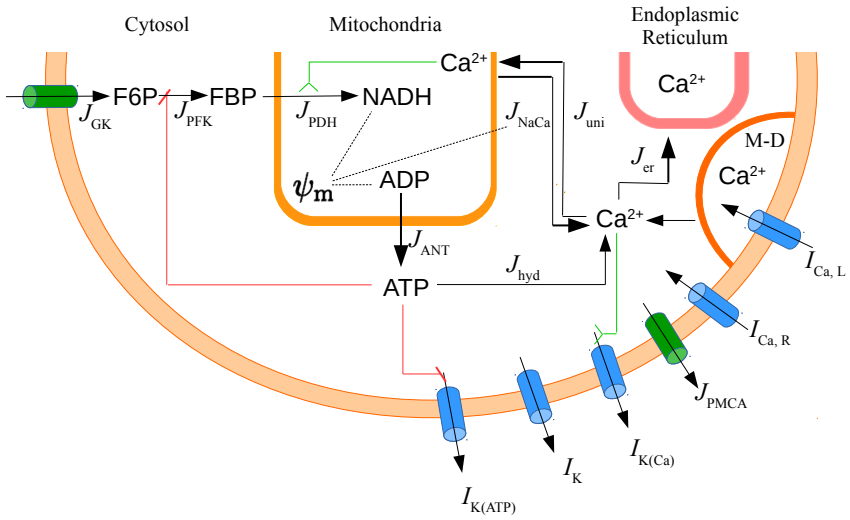

Figure 8.1.: Schematic of the Integrated Oscillator Model (IOM) adopted for the insulin secretion. M-D, micro-domain. I: currents. J: fluxes. GK: glucokinase. PFK: phosphofructokinase. PDH=phosphate dehydrogenase. ANT: adenine nucleotide translocator. hyd: hydrolysis. uni: uniporter. PMCA: plasma membrane Ca^{2+} ATPase. NaCa: Na^{+}-Ca^{2+} exchanger. V and ψ_{m}: cellular and mitochondrial membrane potential respectively. The red and green lines represent negative and positive feedbacks respectively.

Hence, the Ca^{2+} ion fluxes through the two different V-dependent Ca^{2+} channels are described by:

$$J_{\mathrm{R}} = \frac{\alpha}{V_{\mathrm{cyt}}} I_{\mathrm{Ca,R}} \ , \qquad J_{\mathrm{L}} = \frac{\alpha}{V_{\mathrm{md}}} I_{\mathrm{Ca,L}} \ , \tag{8.2}$$

where J_{R} and J_{L} are the fluxes through the L- and R-type channels, respectively. The parameters V_{cyt} and V_{md} are the cytosolic and M-D volumes, respectively. The values of the parameters introduced in this section for the first time are given in Table 8.1. The other parameters remain unchanged from the previous chapters.

Parameter	Value	Parameter	Value
V_{cyt}	1.15×10^{-12} l	r_{L}	0.5
V_{md}	4.2×10^{-15} l	B	10

Table 8.1.: Parameters for the micro-domain.

The dynamics of the free cytosolic Ca^{2+} concentration is given by Eq (4.10) that is

$$\frac{dc}{dt} = f_{\mathrm{Ca}}(J_{\mathrm{mem}} - J_{\mathrm{m}} - J_{\mathrm{er}}) \; . \tag{8.3}$$

However, the Ca^{2+} flux density across the plasma membrane, J_{mem}, previously described in Eq. (4.11) is now given by

$$J_{\mathrm{mem}} = -\left[J_{\mathrm{R}} + \sigma_{\mathrm{md}}\mathrm{B}(c - c_{\mathrm{md}}) + k_{\mathrm{PMCA}}c\right] \; , \tag{8.4}$$

where σ_{md} is the ratio of the micro-domain volume to the cytosolic, $\frac{V_{\mathrm{md}}}{V_{\mathrm{cyt}}}$, and B is the transport rate constant of Ca^{2+} between the two domains.

Finally, the micro-domain calcium concentration, c_{md}, is describe by

$$\frac{dc_{\mathrm{md}}}{dt} = f_{Ca}[-J_{\mathrm{L}} + \mathrm{B}(c - c_{\mathrm{md}})] \; . \tag{8.5}$$

8.2.2 Insulin Module

The insulin module added into the IOM2.2 is based on the model published by Chen *et al.* in [27].

We assume the insulin-containing granules in the cytosol are collected in two main pools: a large “reserve” pool (in the cytosol) and a smaller pool of “docked” (at the plasma membrane) granules. The latter, in turn, can be divided into several pools according to the granules maturity in the fusion process, during which plasma and insulin-containing vesicle membranes merge into a single continuous bilayer (to eventually release the insulin). Therefore, the granules in the reserve pool have to dock to the membrane and undergo some priming steps before proceeding to the fusion. Once the granules are “docked” and primed, they move to the micro-domain close to the L-type Ca(V) channels. Here, they bind with Ca^{2+} ions and fuse with the plasma membrane thanks to the high Ca^{2+} concentration in the micro-domain. After the fusion, the pore between the granules and the extracellular space expand so that the insulin can be finally released.

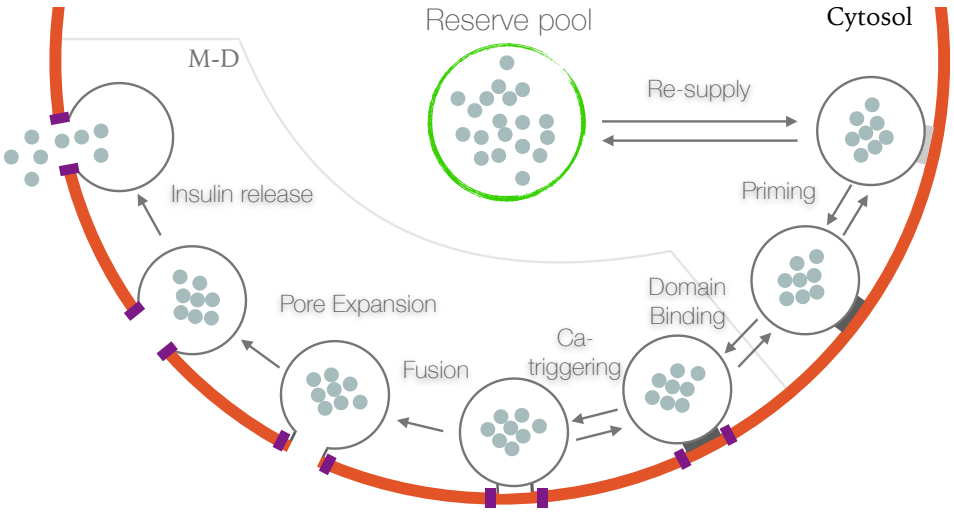

Figure 8.2.: Schematic description of the insulin exocytosis cascade introduced in the IOM2.2.

These steps are visually described in Figure 8.2. The arrows illustrate the directions of granule movements. We note that in the pre-triggering steps are assumed to be reversible, while the post-triggering steps are irreversible.

In Cheng's work, the cytosolic Ca^{2+} concentration amplifies the resupply step (during which insulin-containing granules move from the reserve pool to the one of docked granules) and the priming process. In our formulation, we introduce a second amplifying factor depending on the cellular respiration. There is some evidence that insulin secretion is amplified by the mitochondrial metabolic activity. Thus, we hereby assume that the resupply step is amplified by the metabolic activity represented by the oxygen consumption, in addition to the cytosolic calcium concentration (as already presented in Cheng model). Because of such a detailed cascade of steps, we can indicate the granules in the "reserve", "docked", and primed pools as responsible for the insulin released in the first phase (Section 2.3).

Mathematically, these steps are described by a set of ordinary differential equations. The number of docked insulin-containing granules not yet primed for the fusion, N_6, and the number of primed granules outside the micro-domain, N_5, are given by

$$\frac{dN_6}{dt} = r_3 + r_{-2}N_5 - [r_{-3} + r_2]N_6 \,, \tag{8.6}$$

$$\frac{dN_5}{dt} = r_{-1}N_1 - [r_1 + r_{-2}]N_5 + r_2N_6 \,, \tag{8.7}$$

where the parameters r_{-i} represent the rate at which the resupplying and priming steps can be reversed. Table 8.2 gathers the values of these rates, as well as all other

model parameters introduced in this section. The terms r_2 and r_3 are the priming and resupplying rates, respectively:

$$r_2 = r_2^0 \frac{c}{c + K_p} , \tag{8.8}$$

$$r_3 = r_{3,\mathrm{bas}} + A_\mathrm{m}\, r_3^0 \frac{c}{c + K_p} . \tag{8.9}$$

These rates describe the cytosolic Ca^{2+} control over the insulin exocytosis process. While the amplifying factor, A_m, represents the metabolic influence on the cascade, and it is given by

$$A_\mathrm{m} = 10 \frac{J_\mathrm{O}^2}{J_\mathrm{O}^2 + K_\mathrm{O}^2} , \tag{8.10}$$

where J_O is the O_2 consumption rates (Eq. (5.15)).

The variable N_1 represents the number of primed granules bound to the micro-domain

$$\frac{dN_1}{dt} = -[3h_1 A_\mathrm{md} + r_{-1}]N_1 + h_{-1}N_2 + r_1 N_5 , \tag{8.11}$$

with h_1 the micro-domain binding rate, and A_md the M-D Ca^{2+} control over the process occurring into the micro-compartment:

$$A_\mathrm{md} = c_{\mathrm{md,bas}} + c_{\mathrm{md,max}} \frac{c_\mathrm{md}^4}{c_\mathrm{md}^4 + K_{c_\mathrm{md}}^4} . \tag{8.12}$$

Once the granules enter into the micro-domain, they bind to the Ca^{2+} ions. N_2, N_3, and N_4 identify the number of vesicles with 1, 2, and 3 Ca^{2+} ions bounded

$$\frac{dN_2}{dt} = 3h_1 A_\mathrm{md} N_1 - [2h_1 A_\mathrm{md} + h_{-1}]N_2 + 2h_{-1}N_3 , \tag{8.13}$$

$$\frac{dN_3}{dt} = 2h_1 A_\mathrm{md} N_2 - [h_1 A_\mathrm{md} + 2h_{-1}]N_3 + 3h_{-1}N_4 , \tag{8.14}$$

$$\frac{dN_4}{dt} = h_1 A_\mathrm{md} N_3 - [3h_{-1} + u_1]N_4 . \tag{8.15}$$

In this model, the granules N_4 can be also considered a pre-fusion state. In fact, the number of granules fused with the plasma membrane, N_F, and containing insulin in a "releasable" state, N_R, are described by

$$\frac{dN_\mathrm{F}}{dt} = u_1 N_4 - u_2 N_\mathrm{F} , \tag{8.16}$$

$$\frac{dN_\mathrm{R}}{dt} = u_2 N_\mathrm{F} - u_3 N_\mathrm{R} . \tag{8.17}$$

Parameter	Value	Parameter	Value
K_p	$0.15\ \mu$M	h_{-1}	$0.1\ \text{ms}^{-1}$
r_2^0	$6 \times 10^{-6}\ \text{ms}^{-1}$	r_1	$0.0006,\ \text{ms}^{-1}$
$r_{3,\text{bas}}$	$3.2 \times 10^{-5}\ \text{ms}^{-1}$	r_{-1}	$0.001\ \text{ms}^{-1}$
r_3^0	$0.001205\ \text{ms}^{-1}$	r_{-2}	$10^{-6}\ \text{ms}^{-1}$
$c_{\text{md,bas}}$	$0.001\ \mu$M	r_{-3}	$10^{-7}\ \text{ms}^{-1}$
$c_{\text{md,max}}$	$0.1\ \mu$M	u_1	$2\ \text{ms}^{-1}$
$K_{c_{\text{md}}}$	$0.1\ \mu$M	u_3	$2 \times 10^{-5}\ \text{ms}^{-1}$
h_1	$0.02\ \mu\text{M ms}^{-1}$	K_{O}	$0.15\ \mu\text{M ms}^{-1}$

Table 8.2.: Parameters for the insulin module.

Finally, the number of secreted insulin-containing granules per β-cell can be described by

$$\frac{d\text{SE}}{dt} = u_3 N_{\text{R}} \ . \tag{8.18}$$

8.3 Mechanism Driving the Burst and Insulin Patterns

In this dissertation, we have widely studied the mechanism driving the bursting and we have often stressed that the metabolic variable FBP shows a different pattern according to the nature of the driving force (Chapters 4 and 5). As the insulin secretion is influenced by the metabolic activity, we here investigate whether or not the glycolytic oscillator status (active or passive) affects insulin pattern.

To this purpose, we focus on two bursting β-cells, each of them presenting a different mechanism underlying the bursting activity. Moreover, we introduce the rate of insulin secretion, ISR, (in units of granules per min) represented by:

$$\text{ISR} = u_3 N_{\text{R}} \ , \tag{8.19}$$

where N_{R} is the number of insulin-containing granules ready to be released Eq.(8.17).

Figure 8.3 shows the insulin secretion rate for the two virtual cells in a slow bursting mode in the presence of 11 mM of extracellular glucose. The glycolytic oscillator is passive in one cell (left column) and active in the other (right column).

As expected, Ca^{2+} time courses (panels A and B) are extremely similar, while FBP patters (panels C and D) are very different, highlighting the different nature of the metabolic oscillations.

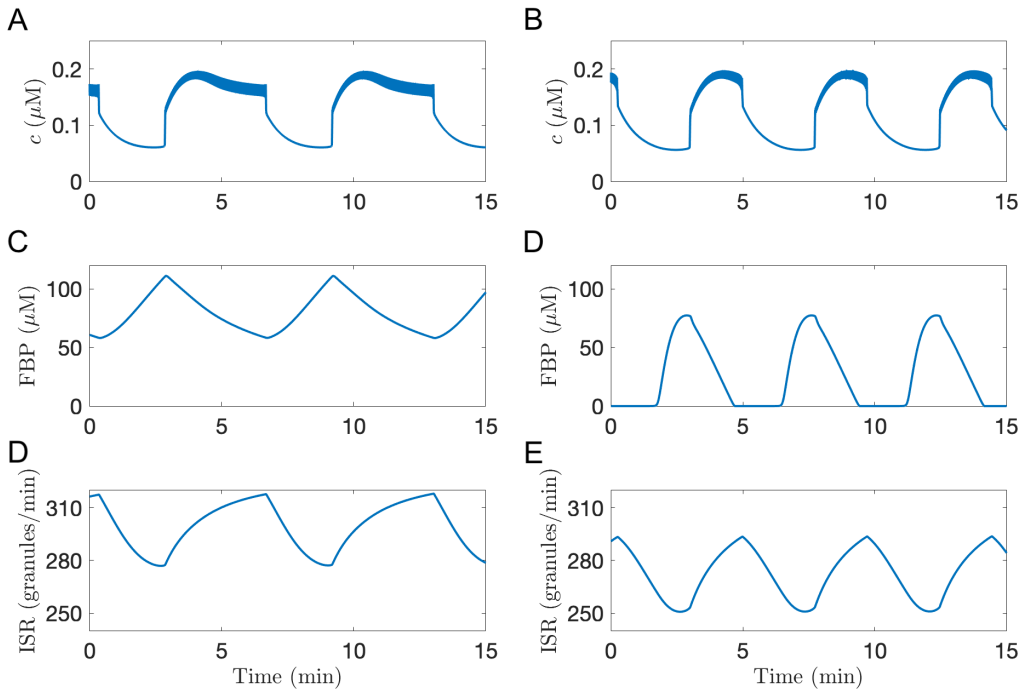

Figure 8.3.: Time courses of cytosolic calcium (top row), cytosolic FBP (middle row), and insulin secretion rate (bottom row), with $g_{\mathrm{K(Ca)}} = 150$ pS. In the left column $v_{\mathrm{PDH}} = 0.4$ μM/ms; in the right column $v_{\mathrm{PDH}} = 2$ μM/ms. The extracellular glucose concentration is equal to 11 mM.

Interestingly, the different mechanisms driving the bursting have very little influence on the feature of the insulin secretion rate (panels E and F) which always arises during the active phase (resulting from the high cytosolic Ca^{2+} concentration) and decreases during the silent phase (when Ca^{2+} level is low). Thus, despite the different FBP patter, sawtooth-like or pulsatile, the ISR time courses show always the same sawtooth-like pattern.

Nonetheless, the nature of cellular oscillations, either Ca^{2+}-driven or metabolism-driven, is fundamental in scenario in which the glucose concentration is too low to allow burst activity, and the insulin is still realized in a pulsatile fashion [8]. The only way it could be possible is if the metabolic oscillations (amplifying the insulin secretion) were self-driven. We study this scenario in the next section.

8.4 Model Predictions and Experimental Findings

In this section, we investigate the β-cell response with the insulin secretion to changes in blood glucose level. To do so, we often use the results obtained with the IOM2.1 in Chapter 6.

8.4.1 Insulin Secretion Rate Governed by Extracellular Glucose

In Chapter 6, we show that extracellular glucose controls the bursting activity in a β-cell. We observe that β-cell is silent for low glucose concentration, it bursts under intermediate glucose concentration, and it spikes continuously for elevated glucose (Section 6.3). In this section, we propose once again the protocol described in that section, and we simulate the virtual cell with the latest IOM2.2.

The results of this protocol are shown in Figure 8.4 for the same parameter set used in Figure 6.4. Initially, the cell is in a solution with subthreshold glucose concentration. For the choice of parameters, the cell is not electrically active whereas the glycolytic oscillator is engaged and pulses in the FBP patter can be observed (Figure 8.4, middle row). This leads to subthreshold oscillations in Ca^{2+} concentration (top row) and to ISR pulses (bottom row). When the glucose is augmented to a stimulatory level (at $t = 50$ min G_e increases to 11 mM), the β-cell starts bursting. Under these conditions, both mean and frequency of ISR oscillations increase drastically. Finally, when the glucose is elevated to 17 mM (at $t = 100$ min), the β-cell enters a continuously spiking mode and the ISR oscillations plateau at a constant high value.

The results obtained with the IOM2.2 are consistent with the one observed in laboratories. The β-cell responds to an increase in glucose concentration in the blood by increasing the rate at which the insulin is secreted. Also, the model predicts insulin pulses when there is no Ca^{2+} oscillation because the cell is either silent (low glucose) as observed in [8]. If we considered only the calcium dependence of the rates presented in the insulin module (as assumed by Chen *et al.*), we could not replicate these experimental observations. However, our model is able to capture this behavior thank to the active glycolytic oscillator that triggers pulses in the cellular metabolism, which, in turn, modulates the insulin secretion through the amplifying factor (Eq. (8.10)).

8.5 Summary

In this chapter, we extended the IOM2.1 to include the insulin secretion. The new model, the IOM2.2, predicts that an augment in the blood glucose level leads to a higher insulin secretion rate, in line with the experimental observations published in the literature.

More importantly, the new model is capable of simulating oscillations in insulin secretion observed under subthreshold glucose conditions [8]. This result, not re-

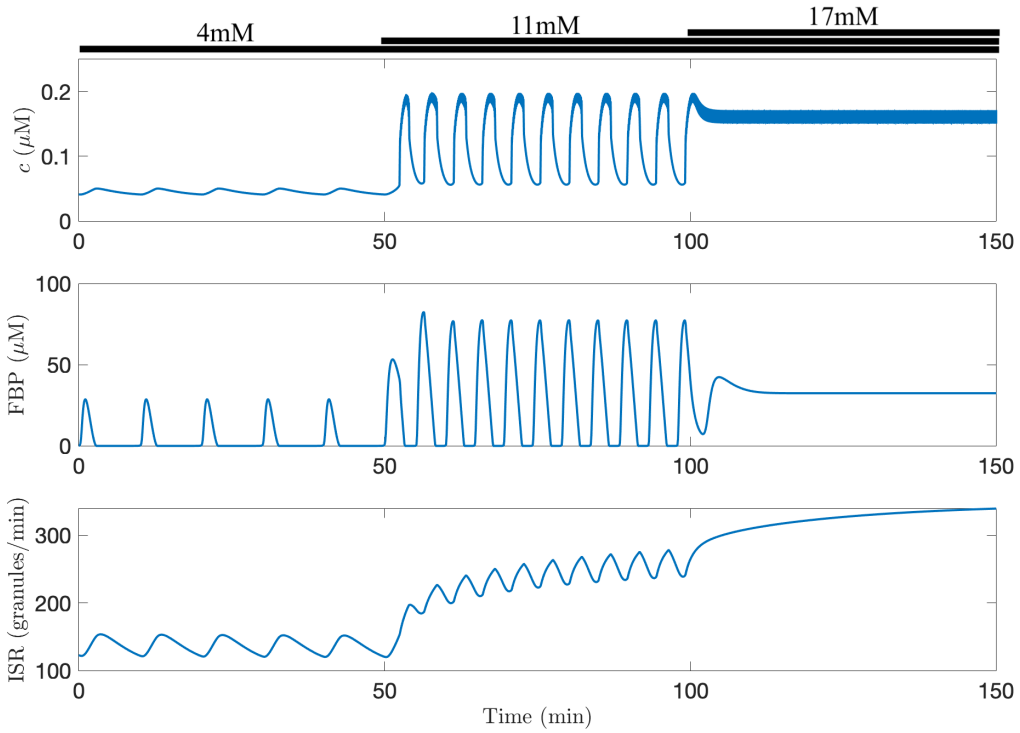

Figure 8.4.: Time courses of cytosolic calcium (top row), cytosolic FBP (middle row), insulin secretion rate (ISR) (bottom row) with $g_{\mathrm{K(Ca)}}$=150 pS and v_{PDH}=2 μM/ms. The top bars illustrate the extracellular glucose concentration that is progressively increased from 4 mM to 11 mM at $t = 50$ min, and to 17 mM at $t = 100$ min.

producible with other models, is possible because of intrinsic metabolic oscillations (occurring for a suitable parameter choice even if the β-cell does not burst) which indirectly influence the insulin exocytosis cascade.

In this chapter, we simulated the insulin secreted by a single cell within an islet. The next step is to couple β-cells and simulates the insulin secreted by a whole islet (Chapter 9).

9 Modelling a Pancreatic Islet

> *Great things are done by a series of small things brought together.*
>
> **— Vincent Van Gogh**

So far in this dissertation, we have been focusing on the bursting activity of a single β-cell assuming that it represents the activity of all β-cells in the same synchronized islet. In this chapter, we move our attention toward the interactions among the β-cells and we analyze the behaviour of several heterogeneous β-cells clustered within an islet. We start providing motivations for this analysis (Section 9.1). Then, we describe how the cells are coupled to mimic a whole islet (Sections 9.2) and we discuss the model predictions (Section 9.3).

9.1 Motivations

The bursting activity of β-cells within an islet is coordinated by gap junction [6, 48]. The resulting coupling allows the cells to overcome the physiological heterogeneity. In fact, it has been shown [88] that bursting can be induced in silent single cells if coupled with a sufficiently high number of active β-cells. Moreover, the synchronized bursting activity has a large impact on insulin secretion. It has been observed that oscillations of cytosolic Ca^{2+} lose their regularity when the β-cells were not synchronized [83]. In this scenario, the islets did not release insulin in a pulsatile fashion, even in a solution with stimulatory glucose concentration.

Moreover, it has been hypothesized that the electrical coupling can be supported with metabolic coupling [95]. Several experimental observations demonstrate the key role of electrical coupling in helping the coordination of bursting among clustered cells [96, 73, 52]. In contrast, the presence of metabolic coupling and its role in the inter-cellular synchronization is still unclear. It has been shown that signals generated in the early steps of the glycolytic pathway can propagate among β-cells [49] and that the intermediate products of glycolysis can also diffuse through gap junctions in pancreatic β-cells in transgenic RIP-Cx32 mice [73]. However, it has been also suggested that metabolites are too big to actually travel through gap

junction. In this chapter, we use the mathematical model to investigate the necessity of metabolic coupling in the synchronization process.

9.2 Mathematical Model

In this chapter, we simulate a virtual islet of 51 heterogeneous β-cells distributed in a sphere-shape grid. The electrical activity of each single cell within the islet is simulated with the most sophisticated IOM2.2 (Chapter 8). The cellular heterogeneity is simulated by allowing some of the most influential parameters in the IOM2.2 to vary. More precisely, the conductances of major currents in the electrical module (such as I_{Ca}, I_{K}, $I_{\mathrm{K(ATP)}}$) and the maximum rate of the most influencing metabolic reactions (i.e., J_{GK} and J_{PFK}) are uniformly selected in an interval centred at the baseline value (see Tables 4.1 and 4.2) with a standard deviation equal to 10%.

We assume that a cell interacts only with its nearest neighbours. Figure 9.1 illustrates an example of such a neighbourhood. The black cell is the selected one and it is surrounded by its neighbours (red cells).

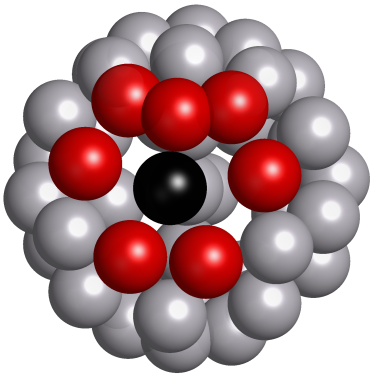

Figure 9.1.: Virtual islet of 51 β-cells. The red cells belong to the neighbourhood of the black cell.

The electrical cell-to-cell coupling is simulated by introducing gap junction current between β-cells [84, 88]. The membrane potential of the i^{th} cell in a islet is thus given by

$$\frac{dV_i}{dt} = -\frac{1}{C}\left[I_{\mathrm{Ca}} + I_{\mathrm{K}} + I_{\mathrm{K(Ca)}} + I_{\mathrm{K(ATP)}}\right] - \sum_{j\in\Omega_i}\left[g_{ij}(V_i - V_j)\right], \qquad (9.1)$$

where Ω_i is the neighbourhood of the i^{th} cell and g_{ij} are electrical coupling conductances. The values of the parameters g_{ij} were computed for the first time by Pérez-Armendariz and collaborators in 1991 [71]. They observe that among the 115 pairs of β-cells in the laboratory set-up, only 67% are electrically coupled. In

the coupled pairs, the value of g_{ij} is estimated to be between 200 pS and 600 pS in 44% of cases, and lower than 200 pS in the remaining. The authors also show that the values of g_{ij} follows a normal distribution with mean 215 pS and standard deviation 110 pS. Figure 9.2 depicts a graphic representation of this distribution. In our analysis, we use this probability distribution to select the electrical coupling conductances.

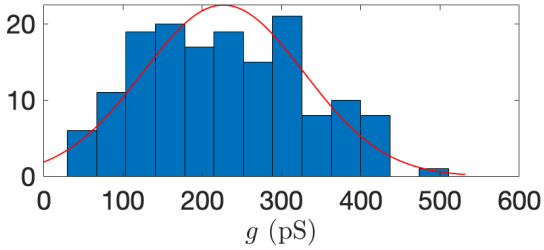

Figure 9.2.: Histograms of the values of electrical coupling conductances, g_{ij}, published in [71].

Similarly, the metabolic coupling is simulated by adding gap-junction coupling terms to the equation for FBP:

$$\frac{d\mathrm{FBP}_i}{dt} = J_{\mathrm{PFK}} - \frac{1}{2}J_{\mathrm{GPDH}} - \sum_{j\in\Omega_i}\left[p_{\mathrm{FBP},ij}(\mathrm{FBP}_i - \mathrm{FBP}_j)\right], \tag{9.2}$$

where $p_{\mathrm{FBP},ij}$ is the gap junction permeability for FBP. $p_{\mathrm{FBP},ij}$=0.02 in our dissertation.

9.3 Model Predictions

We use the model described in Section 9.2 to mimic a *in-silico* islet of 51 heterogeneous β-cells. In what follows, we first simulate an islet in which the β-cells are electrically coupled (Section 9.3.1), and then we add the metabolic coupling (Section 9.3.2).

9.3.1 Electrical Coupling

In our analysis, we start with the oscillatory activity of the uncoupled heterogeneous cells simulated with the IOM2.2. At $t = 10$ min, we induce the electric coupling by adding the gap-junction terms into the membrane potential equation as in (9.1). Figure 9.3 shows the results of this protocol for two islets, one with the glycolytic oscillator off (panels A and B) and a second with the glycolytic oscillator on (panels C and D). In this figure, each row represents a β-cell. The black segments in panels A

and C illustrate the active phase of the burst, while the points in panels B and C show the peaks in FBP time courses.

For the first cell (panels A and B), we observe that prior to the introduction of electrical coupling, the cells are not synchronized. Because of the heterogeneity, the bursting duration varies from cell to cell. In some cases (panel A, rows 1 for instance) the cells spiking continuously and FBP is plateauing (no peaks in panel B, rows 1). When the electrical coupling is introduced (at $t = 10$ min), the cells start bursting synchronously and the burst period and phase are the same in all the β-cells. Also the metabolic oscillations synchronize as the FBP peaks occur at the same time. The same observations can be made for the second cell (panels C and D) with the glycolytic oscillator engaged. Here, however, we observe a short initial transient before the metabolic oscillations synchronize.

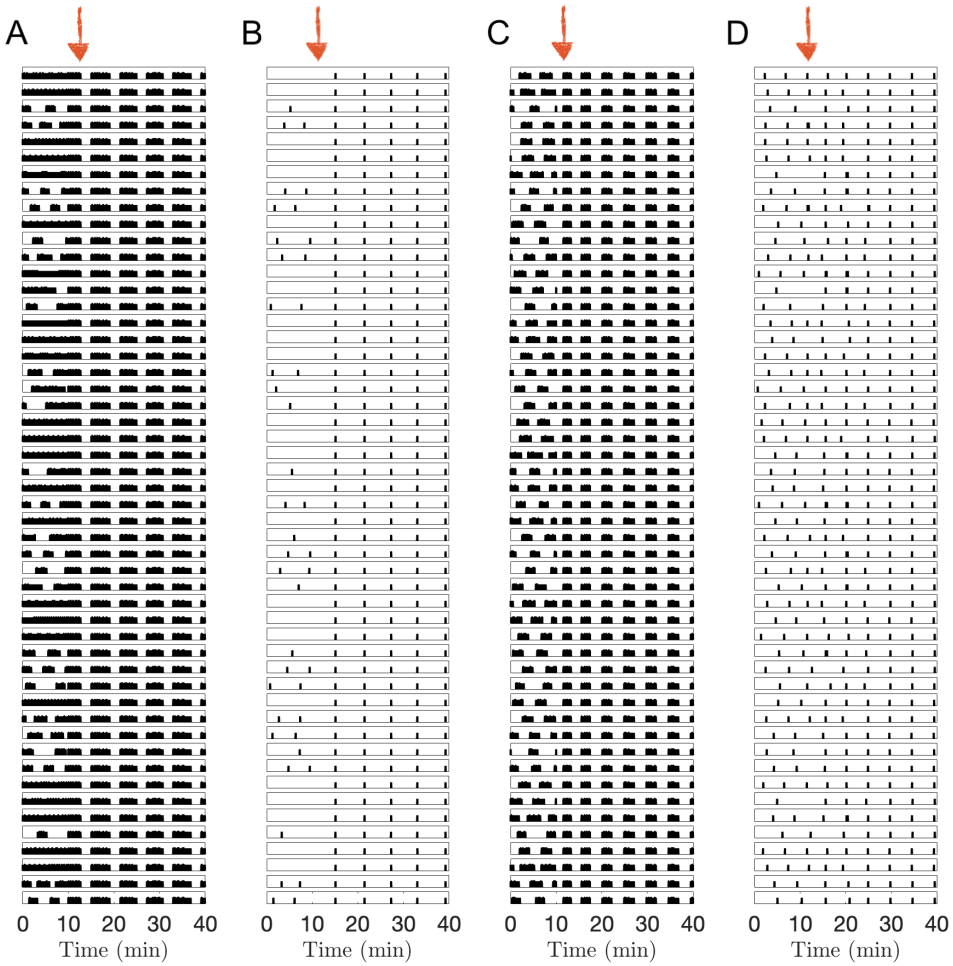

Figure 9.3.: Active phase (panels A and C) and FBP peaks (panels B and D) for each β-cell in the virtual islet (rows). The glycolytic oscillator is off in panels A and B, while it is on in panels C and D. Electrical coupling is introduced at $t = 10$ min (arrows).

To better visualize the results, we randomly select 7 virtual cells out of the 51 (highlighted in colour in Figure 9.4) and we show their calcium and FBP time courses in Figures 9.5A-D obtained in protocol just described. Here, we see clearly the impact that the cell-to-cell communication through gap junctions has on the islet synchronization process. It is worth noticing the slightly different values of peaks and nadirs in c and FBP time courses even after the cells synchronize. This is a consequence of the cellular heterogeneity.

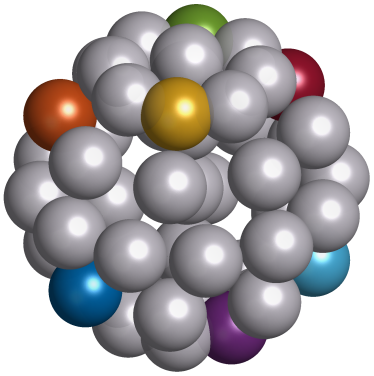

Figure 9.4.: Virtual islet of 51 β-cells. The coloured cells are the selected ones whose time course is plotted in Figures 9.5 and 9.7.

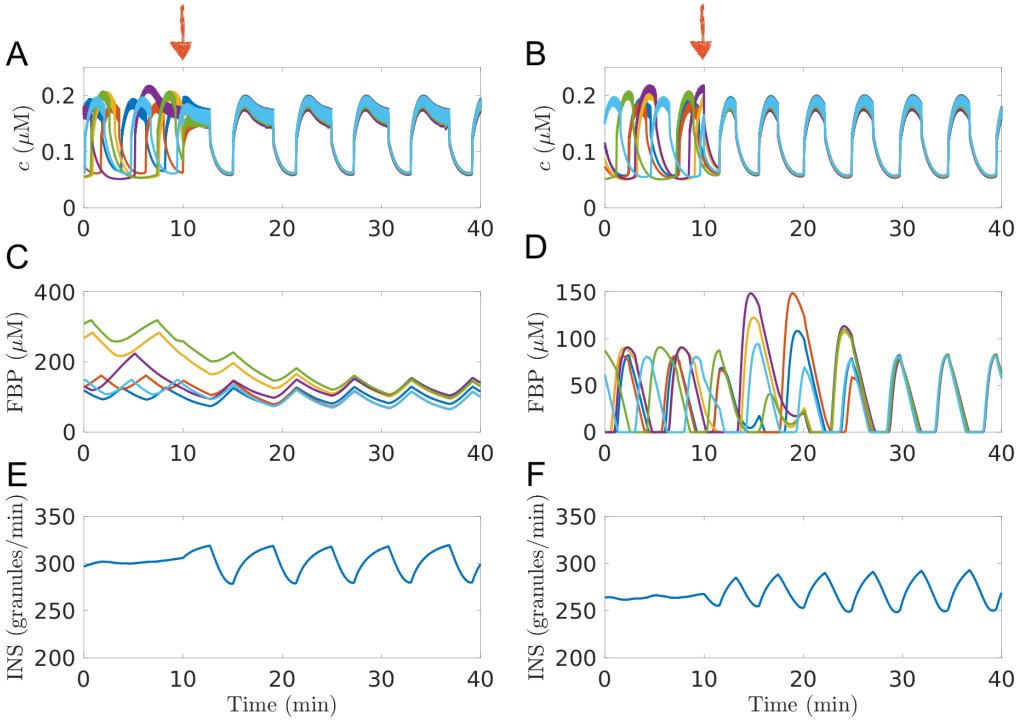

Figure 9.5.: Time courses of cytosolic calcium (top row), FBP (middle row), and insulin secretion rate (bottom row) of the selected cells (Figure 9.4). In the left column $v_{\mathrm{PDH}} = 0.4$ μM/ms; in the right column $v_{\mathrm{PDH}} = 2$ μM/ms. At $t = 10$ min, the electrical coupling is added (arrows).

In the figure, we also show (Figure 9.5E and F) the average value of the insulin secretion rates, INS, described by

$$\mathrm{INS} = \frac{1}{N}\sum_{i=1}^{N}\mathrm{ISR}_i \ , \tag{9.3}$$

where N=51 is the number of β-cells in the virtual islet, and ISR_i is the insulin secretion rate for the i^{th} β-cell (Eq. (8.19)). This quantity can be used as a measure of the "synchronization" among the cells. In fact, if the cells are not synchronized, we observe a flat averaged insulin secretion rate (panels E and F), even if most of β-cells are bursting (panels A, B, C, and D). When the coupling is added the cells come to burst synchronously and INS oscillations become bigger and regular. These results are consistent with recording observed in laboratories [83].

9.3.2 Electrical and Metabolic Coupling

In this section, we investigate the contribution that the metabolic coupling would make if introduced in the simulations. To replicate both electrical and metabolic coupling, the gap-junction term is added into both plasma membrane potential (Eq. (9.1)) and FBP (Eq. (9.2)) equations. We also use once again the same islets introduced in the previous section and we propose the same protocol to be able to compare the results.

Figure 9.6 illustrates the results for the islet with inactivated (panels A and B) or engaged (panels C and D) glycolytic oscillator. Due to the electrical coupling, the cells in both islets synchronized when they are coupled together (whether the glycolytic oscillator is active or not). The results are similar to what shown in Figure 9.3. The only relevant difference is that, due to the metabolic coupling, the metabolic oscillations synchronize instantaneously as soon as the coupling is added, even when the glycolytic oscillator is active (unlike in the previous section).

Considering these results, the metabolic coupling does not have a fundamental role in the synchronization process. Nonetheless, it has an effect on the time courses of Ca^{2+} and FBP (Figure 9.7A-D) facilitating the metabolic synchronization and making the slight differences observed in peaks and nadirs (Figure 9.3) disappeared. However, these results do not affect the averaged insulin secretion rate which oscillates within the same rage as in the previous section (Figure 9.5).

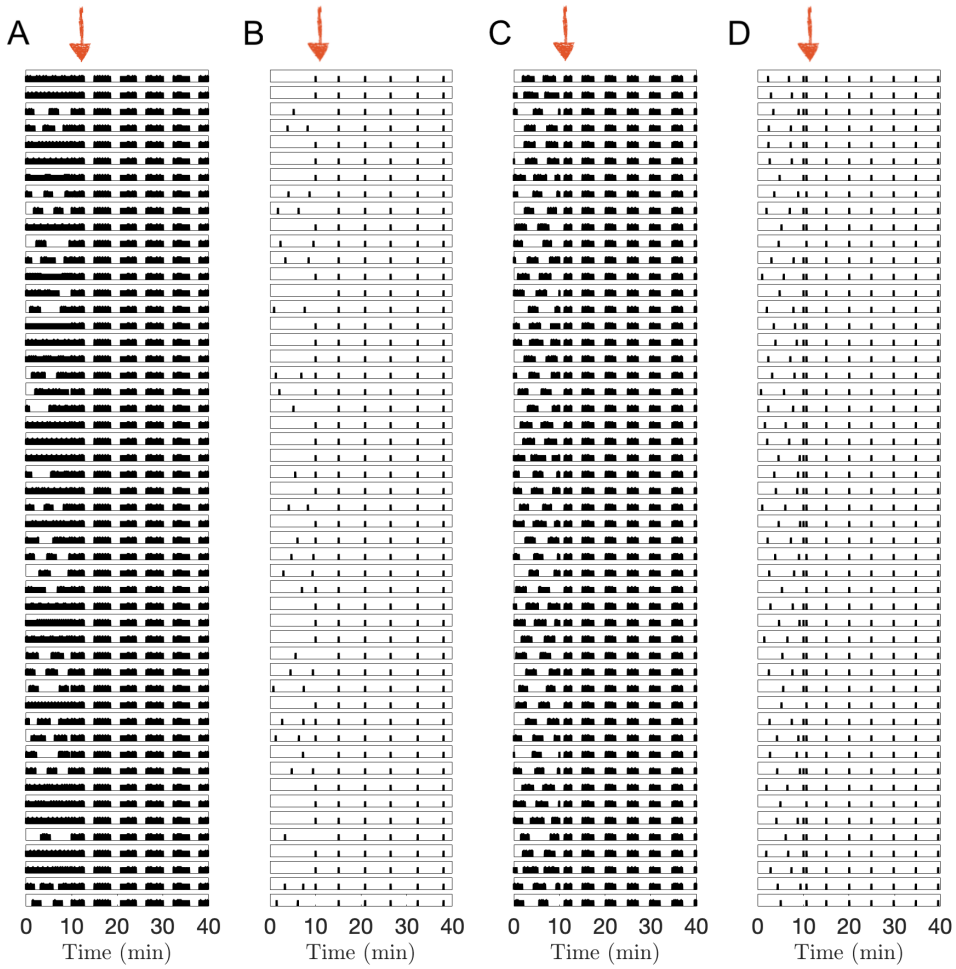

Figure 9.6.: Active phase (panels A and C) and FBP peaks (panels B and D) for each β-cell in the virtual islet (rows). The glycolytic oscillator is off in panels A and B, while it is on in panels C and D. Electrical and metabolic coupling are introduced at $t = 10$ min (arrows).

9.4 Summary

In this chapter, we introduced the cell-to-cell coupling to simulate the cellular interaction within an islet. As the role of the electrical coupling is well established, we first used our model to simulate a cluster of heterogeneous β-cells electrically coupled. Also, we investigated the effect of metabolic coupling on the cellular activity. The model predicts that electrical coupling alone is capable of synchronizing the β-cells, and that the only evident contribution given by the metabolic coupling is to homogenize the electrical and metabolic oscillations in the cells. However, if the degree of heterogeneity is greater it is possible that metabolic coupling will play a larger role in the cell-to-cell synchronization.

We also introduced the average insulin secretion rate, INS, to observe the effect of the cellular coupling. In line with experimental findings, we showed that INS has

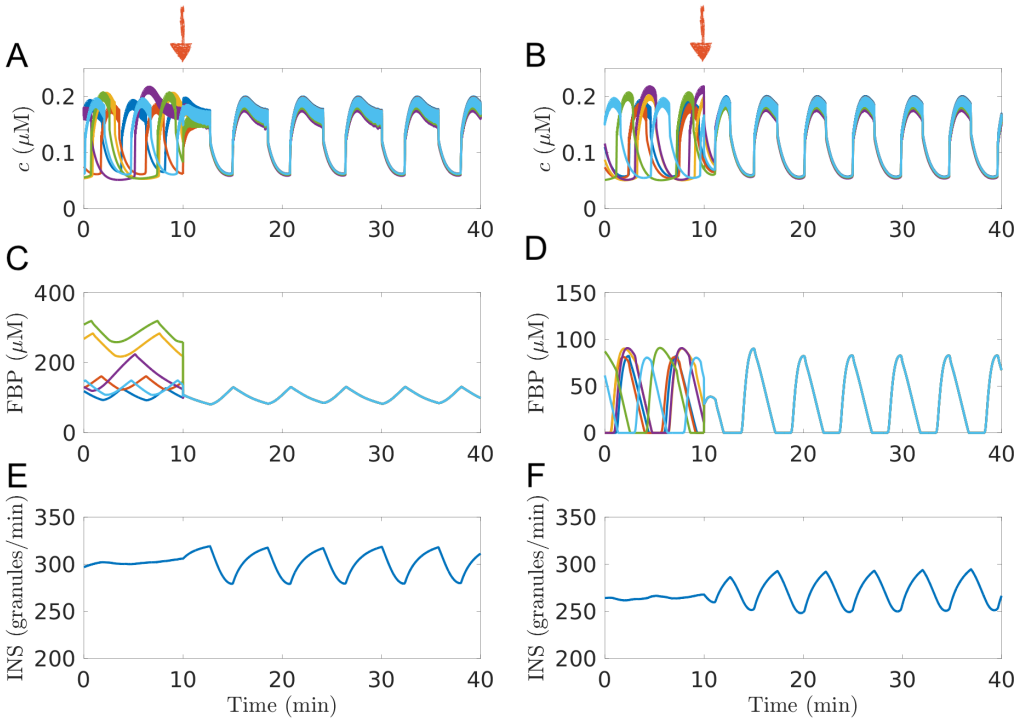

Figure 9.7.: Time courses of cytosolic calcium (top row), FBP (middle row), and insulin secretion rate (bottom row) of the selected cells (Figure 9.4). In the left column $v_{\mathrm{PDH}} = 0.4$ μM/ms; in the right column $v_{\mathrm{PDH}} = 2$ μM/ms. At $t = 10$ min, the electrical and metabolic coupling is added (arrows).

small and irregular oscillations when the cells are not synchronized, and big and regular oscillations when the cells are bursting in unison.

Conclusions and Future Work 10

> *Our imagination is the only limit to what we can hope to have in the future.*
>
> **— Charles Kettering**

In this concluding chapter, we summarize the contributions of this thesis (Section 10.1) and discuss important directions of future work (Section 10.2).

10.1 Summary

The central problem addressed in this thesis is modelling the extremely complex dynamics of the electrically active pancreatic β-cells, which are responsible for secreting the insulin hormone to maintain the glucose homeostasis in animals. We dedicated Chapter 2 to describe the physiology of β-cells. In Chapter 3, we discussed the mathematical models that have been constructed in the last four decades to describe the complex rhythms observed experimentally. We briefly outlined the history of the β-cell models, from the first model introduced by Chay and Keizer in 1983 until the most recent models. We also classified the latest and most relevant models into three schools (i.e., Fridlyand, Cha, and Bertram-Satin-Sherman schools) based on the description of ions and metabolites dynamics. We gave special attention to the models presented in Bertram-Satin-Sherman school, since they are the only ones accounting for the complete variety of bursting regimes observed in the laboratories. Because of this, we used the latest model of this school, the IOM, as starting point for this thesis. In Chapter 4, we investigated an updated version of the IOM, called the IOM1.5, including a more detailed description of calcium dynamics. From Chapter 5 on, we presented several extensions of the IOM1.5 each time more sophisticated than the previous in order to reproduce key experimental findings that could not be captured by prior models. First, we focused on the cellular level providing a better description of the dynamics within the cell, necessary to simulate the insulin exocytosis. Then, we moved towards the islet level by clustering several β-cells, each of them simulated with the most comprehensive IOM.

10.1.1 An Improved Integrated Oscillator Model

The first extension of the IOM that we developed (Chapter 4), which we called the IOM1.5, incorporates Ca^{2+} feed-back onto glycolysis and mitochondrial calcium dynamics to better account for oscillations in the intracellular calcium concentration and pulsatile insulin secretion. The IOM1.5 is able to reproduce a wide range of bursting patterns (including slow, fast, and compound bursting), as well as new experimental observations in the β-cell activity [66] that could not be accounted for in prior β-cell models. We used the IOM1.5 to investigate the mechanisms behind the bursting activity that underlies oscillations in intracellular Ca^{2+} concentration and pulsatile insulin secretion. Also, we suggested protocols that can be used in laboratories to investigate the nature of β-cell oscillations.

The model is given by a set of ordinary differential equations that can be divided into two modules: one module describes the β-cell electrical activity and Ca^{2+} dynamics, and the other describes the glycolysis pathway and ATP production. These two modules interact via numerous feedforward and feedback pathways, generating metabolic oscillations with a sawtooth time course or a pulsatile time course, which reflects very different oscillation mechanisms.

We performed a bifurcation analysis on the glycolytic subsystem to investigate the nature of the metabolic oscillations (Section 4.3). This analysis allowed us to put the two main perspectives about the mechanisms underlying the cellular activity into a common framework. We also determined conditions favourable to each type of mechanism. This way, not only can the IOM1.5 capture the various busting rhythms, but it also accounts for the different mechanisms underlying the β-cell oscillatory activity resulting in different metabolic patterns. Additionally, we explored the model potentialities showing the ability of the IOM1.5 to reproduce key experimental findings of β-cell activity (Section 4.4).

Despite its ability to reproduce the complete set of bursting patterns and to account for fundamental experimental findings, the IOM1.5 still has limitations. For instance, it does not include the metabolic activity within the mitochondria, which is the organelle where the cellular respiration and most of the ATP synthesis occur. This results in a non-physiological ATP concentration in the absence of metabolism, and as such, the IOM1.5 cannot reproduce laboratory observations of mitochondrial concentrations.

10.1.2 The Evolution of the Integrated Oscillator Model

At this point, we moved forward and presented a sequence of extensions of the IOM1.5, which we progressively enumerated to stress the evolution process.

The first refinement (Chapter 5), called the IOM2.0, adds a module describing mitochondrial metabolism to the IOM1.5. We analysed the potentialities of this improved model and find that, in addition to reproducing the experimental findings presented with the IOM1.5, the new model can also capture a variety of other important aspects (Sections 5.3-5.6). The payoff of the higher complexity is the capability of the model to simulate mitochondrial variables that can be measured experimentally with new laboratory techniques, and to account for a more realistic description of ATP production and consumption, overcoming some of the limitations presented in the IOM1.5.

The IOM2.0 mimics the dynamics of single-cell in a synchronized islet for a fixed glucose level. Thus, a natural improvement that we considered in this thesis is to include the glucose dynamics in the model. We presented the new IOM2.1 (Chapter 6), obtained by adding an explicit dependency of β-cell activity on glucose level in the previous IOM2.0. This way, our model can capture the various responses of the β-cells to changes in glucose level observed in laboratories (Section 6.3). We studied this aspect by using once again dynamical systems techniques and by performing a fast-slow analysis of the model (Chapter 7).

A further extension of the model includes the addition of the insulin exocytosis cascade into the latest IOM2.1 (Chapter 8). Thanks to the modules describing the mitochondrial dynamics and the glucose dynamics, we could simulate the insulin secretion that is amplified by mitochondrial metabolic activity and governed by changes in the glucose level in the blood. The new IOM, called the IOM2.2, can successfully account for laboratory observation impossible for the other models in the literature. Because of the intrinsic glycolytic oscillations generated by the IOM for a suitable parameter set, we could replicate *in silico* oscillations in the insulin concentration in a cell in a solution with subthreshold glucose level. However, the model does not capture the oscillations in the insulin when the cell is spiking continuously, as observed in some laboratories. Also, it does not take into account the cell-to-cell interaction, essential in the insulin secretion process.

The final extension of the model that we described in this dissertation, accounts for the synchronization (through gap junctions) of β-cells within an islet (Chapter 9). It has been observed that the β-cells in the same islet burst synchronously to efficiently secrete insulin in response to changes in the blood glucose level. In this thesis, we simulated each virtual β-cell with the latest IOM2.2 and we assumed the nature of the coupling to be either electrical or both electrical and metabolic. We investigated the model predictions and observe that, in our simulations, the electrical coupling is sufficient to synchronize the β-cells.

10.2 Direction for Future Work

The IOM1.5 to IOM2.2 (as well as its extension to islets) are significant advances in the β-cell modelling field, allowing for qualitative and quantitative descriptions of key experimental findings reported over the last decades. Despite their advances, these models are still limited in their ability to simulate the close negative feedback loop involving insulin and glucagon hormones to maintain a stable physiological glucose level in the blood (Chapter 1).

Here, we describe the two main paths we can take. Specifically, we could further extend the model by including the pancreas-liver interaction (Section 10.2.1) or we could move toward a clinical application of the model to simulate pathological scenarios (Section 10.2.2).

10.2.1 Islet-Liver Interaction

The glucose homeostasis is regulated by the mutual interaction between the insulin-secreting pancreatic β-cells and the glucose-storing and -releasing liver. This interaction occurs in two ways. The first way is a direct influence of one organ on the other through the action of hormones (insulin and glucagon). When the glucose level in the blood is elevated, the β-cells secrete insulin to stimulate the liver to store glucose in the form of the storage polymer glycogen (*glycogenesis*). The insulin also inhibits the glucagon secretion from α-cells. If the glucose level drops below the physiological level, the glucagon is now secreted and causes the liver to release glucose into the blood by breaking down of glycogen into glucose (*glycogenolysis*). The second way is the indirect controls of the liver on the oscillatory nature of β-cells activity. As a regulator of pancreatic oscillations, the liver may be capable of synchronizing oscillations already present in the islets and, in some cases, of creating them [89].

To model this loop, we will move from a cell-cell system into an islet-liver system in which the glucose input in the β-cell model is given by the liver model that, in turn, uses the insulin secreted by the islet to modulate the glucose level itself. Figure 10.1 illustrates a schematic of this closed loop.

10.2.2 Genetic Mutation: Neonatal Diabetes Mellitus

Another direction we can take is the simulation of neonatal diabetes mellitus caused by impaired function of K(ATP) channels due to genetic mutations. Neonatal (or congenital) diabetes is a form of diabetes occurring under 6 months of age. About 80-85% of cases of neonatal diabetes mellitus is monogenic, meaning they are

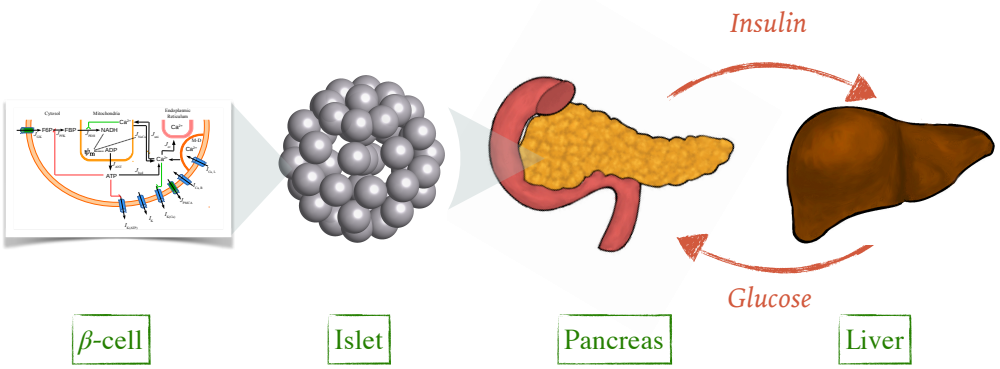

Figure 10.1.: Schematic of the full islet-liver system. The β-cells, each of them simulated with the IOM2.2, are coupled together into islets (through gap junctions) that are clustered at pancreas level. The insulin-glucose feedback creates the closed loop islet-liver.

caused by a mutation affecting only one gene. In contrast, the most common form of diabetes, such as Type 1 and type 2, are polygenic, i.e. they are related to a change in multiple genes.

Half of subjects with neonatal diabetes mellitus (NDM) recover from this condition during infancy although it can reappear later in life. This type of NDM is called transient neonatal diabetes mellitus (TNDM) and it is only temporary. The other form of NDM affecting the remaining cases is called permanent neonatal diabetes mellitus (PNDM) and is a lifelong condition. Transient diabetes is usually due to overexpression of genes on chromosome 6q24 and it is treated with a combination of insulin and other medications.

Around 50% of the PNDM is caused by mutations in the KCNJ11 and ABCC8 genes (encoding the subunits of the K(ATP) channels) that impair the ability of the ATP to close the channels. The K(ATP) channels make sure that the right amount of insulin is secreted for the level of glucose in the blood. Thus, if the function of these channels is damaged, the β-cells are not able to respond properly to physiological signals and the insulin quantity released is not appropriate for the level of extracellular glucose. In fact, mutations in the KCNJ11 and ABCC8 genes can result in both hypo- and hyperglycemia, as well as in neurological disruptions. The patients with these mutations have been treated by high doses of oral sulphonylurea drugs instead of insulin.

From a mathematical point of view, these mutations can be simulated by modifying the maximum conductance of the K(ATP) channels, $g_{\mathrm{K(ATP)}}$ (Eq. (4.8)), and the parameters in the activation function, o_∞ (Eq. (4.9)) of the K(ATP) channels. More precisely, increasing the maximum conductance will mimic a higher fraction of open channels, which is the main impairment in β-cells in patients affected by PNDM. On

the other hand, varying parameter such as k_{tt} and k_{td} that represent the dissociation constants for ATP and ADP, respectively, will simulate the change in the ATP and ADP affinity in case of β-cells with the considered genetic mutations. Furthermore, we could use data provided by our collaborators to tune these constants.

11 Biography

> *Not all those who wander are lost.*
>
> — **John R. R. Tolkien**

Education

1/2016–Present	**Ph. D. Student in Mathematics and Statistics** Basque Center for Applied Mathematics, Bilbao (Spain) *Advanced Mathematical Modelling of Pancreatic β-cells.* Supervisors: Dr. Luca Gerardo-Giorda and Prof. Richard Bertram.
9/2012–3/2015	**Master of Science in Mathematics** (Summa Cum Laude) University of Trento, Trento (Italy) *The role of endogenous boosting in the reactivation dynamics of the Varicella-Zoster Virus.* Supervisors: Prof. Andrea Pugliese and Dr. Michiel van Boven.
9/2008–6/2012	**Bachelor degree in Mathematics** University of Pisa, Pisa (Italy) *An age-structured epidemiological model for diffusion of hepatitis C.* Supervisor: Prof. Paolo Acquistapace.

Short Visits

- **Short Visit at the Florida State University, Tallahassee, Florida (US)**. *Study the latest Integrated Oscillator Model for pancreatic β-cells.* (July 27-August 31, 2019)

- **Informal Annual Meeting at The National Institute of Health, Bethesda, Maryland (US).** *Advanced study on pancreatic β-cells: from the physiology to the mathematical modelling.* (October 22-23, 2018)

- **Internship at the Florida State University, Tallahassee, Florida (US).** *Study the Integrated Oscillator Model for pancreatic β-cells.* (August 15-December 15, 2017)

- **Short Visit at the Institute of Bioengineering, Miguel Hernàndez University of Elche, Elche (Spain)**. *Oscillatory electrical activity of the islet of Langerhans.* (November 28-30, 2016)

Publications

- I. Marinelli, A. van Lier, H. de Melker, A. Pugliese, and M. van Boven, *Estimation of age-specific rates of reactivation and immune boosting of the varicella zoster virus*, Epidemics 19 (2017), pp. 1–12.

- J.M. Kroos, I. Marinelli, I. Diez, J. M. Cortes, S. Stramaglia, and L. Gerardo-Giorda, *Patient-specific computational modeling of cortical spreading depression via diffusion tensor imaging*, International Journal for Numerical Methods in Biomedical Engineering, 33(11):e2874 (2017).

- I. Marinelli, T. Vo, L. Gerardo-Giorda, and R. Bertram, *Transitions between bursting modes in the integrated oscillator model for pancreatic β-cells*, Journal of Theoretical Biology, 454 (2018), pp. 310– 319.

- N. C. Law, I. Marinelli, R. Bertram, K. L. Corbin, C. Schildmeye, C. S. Nunemaker, *Chronic stimulation induces compensatory potassium channel activity that restores calcium oscillations in pancreatic islets in vitro*, submitted to the American Journal of Physiology-Endocrinology and Metabolism.

- I. Marinelli, A. S. Sherman, L. S. Satin, L.Gerardo-Giorda, R. Bertram, *Using the glucose response to determine the mechanism of bursting in pancreatic islets*, in preparation 2019.

Professional Presentation

- **Poster presented at "Annual Meeting and Conference of the Society for Mathematical Biology", Montréal (Canada)**, *Can One Enzyme Isoform Compensate for Knockout of Another in Cellular Rhythmogenesis?* (July 22-26, 2019)

- **Poster presented at "Engineering and Information and Communication Technologies - Doctoral Student Workshop", Barcelona (Spain)**, *On the*

Integrated Oscillator Model for Pancreatic β-cells: Development, Results, and Applications. (April 3, 2019)

- **Seminar at University of Trento, Trento (Italy)**, *Modelling β-cellsin both healthy and pathological scenarios.* (November 22, 2018)

- **Talk at "11th European Conference on Mathematical and Theoretical Biology", Lisbon (Portugal)**, *Analysis of different bursting modes in the Integrated Oscillator Model for pancreatic β-cells.* (July 23-27, 2018)

- **Talk at "BCAM Light PhD Seminar", Bilbao (Spain)**, *Integrated Oscillator Model for pancreatic β-cells: analysis of the transitions between bursting modes.* (July 12, 2018)

- **Talk at "BCAM Workshop Populations in epidemics and ecology", Bilbao (Spain)**, *Estimation of age-specific rates of reactivation and immune boosting of the varicella zoster virus.* (July 4-5, 2017)

- **Poster presented at "2nd BCAM Workshop on Nonlinear Dynamics in Biological Systems", Bilbao (Spain)**, *Estimation of age-specific rates of reactivation and immune boosting of the varicella zoster virus.* (September 1-2,2016)

- **Poster presented at "Quantitative Biomedicine for Health and Disease", Bilbao (Spain)**, *Personalized Simulation of Cortical Spreading Depression.* (February 24-25, 2016)

Appendices

A Models in the Literature: ODE System

In this chapter, we fully list the ordinary differential equations that give the chosen mathematical models from Fridlyand and Cha Schools (Chapter 3).

A.1 Fridlyand School

A.1.1 Fridlyand 2003: Mathematical Model

In this model [37], the cell electrical activity is described by a Hodgkin–Huxley based model, where the rate of change of the cellular membrane potential, V, is given by

$$\begin{aligned}\frac{dV}{dt} = -\frac{1}{C}[&I_{\mathrm{VCa}} + I_{\mathrm{PMCA}} + I_{\mathrm{Na,Ca}} + I_{\mathrm{CRAN}} + I_{\mathrm{Na}} + \\ &+ I_{\mathrm{Na,K}} + I_{\mathrm{KDr}} + I_{\mathrm{K(Ca)}} + I_{\mathrm{K(ATP)}}]\ ,\end{aligned} \tag{A.1}$$

where C is the membrane capacitance, I_{VCa} is the voltage-dependent Ca^{2+} current, I_{PMCA} is the plasma membrane Ca^{2+} pump current, $I_{\mathrm{Na,Ca}}$ is the Na^{+}/Ca^{2+} pump current, I_{CRAN} is the Ca^{2+} release-activated nonselective cation current, I_{Na} is the inward Na^{+} current, $I_{\mathrm{Na,K}}$ is the Na^{+}/K^{+} pump current, I_{KDr} is the delay rectify K^{+} current, $I_{\mathrm{K(Ca)}}$ is the Ca^{2+}-activated K^{+} current, $I_{\mathrm{K(ATP)}}$ is ATP-activated K^{+} current.

The calcium current through voltage-activated Ca^{2+} channel, I_{VCa}, supplies most of intracellular Ca^{2+} in β-cells. It is activated by the cellular membrane depolarization, and is described by

$$I_{\mathrm{VCa}} = g_{\mathrm{mVCa}}\, p_{\mathrm{VCa}}(V)(V - V_{Ca})\ , \tag{A.2}$$

where g_{mVCa} is the maximum conductance and the current/voltage relationship p_{VCa} is a Boltzmann-type activation curve

$$p_{\mathrm{VCa}}(V) = \frac{1}{1 + \exp\left(\frac{V_{\mathrm{Cah}} - V}{K_{\mathrm{Cah}}}\right)}\ , \tag{A.3}$$

with K_{Cah} the slope at half-maximal potential and V_{Cah} the half-activation potential. The values of these parameters, as well as the others presented in this section are given in Table A.1.

On the contrary, the plasma membrane Ca^{2+}pumps, I_{PMCA}, is the main system to restore the Ca^{2+} homeostasis by expelling calcium ions toward the extracellular space. It is assumed dependent only on the Ca^{2+} concentration, c:

$$I_{\mathrm{PMCA}} = P_{\mathrm{mPMCA}} \frac{c^2}{c^2 + K^2_{\mathrm{PMCA}}} \,, \tag{A.4}$$

where P_{mPMCA} is a maximum current and K_{mPMCA} is the value for the half-activation calcium concentration.
A second outward Ca^{2+} current is due to the sodium-potassium exchanger that trades a Ca^{2+} ion from the cell for three Na^+ ions, which enter into the cell. The current thus generated, $I_{\mathrm{Na,Ca}}$, is given by

$$I_{\mathrm{Na,Ca}} = g_{\mathrm{NaCa}} \frac{c^5}{c^5 + K^5_{\mathrm{NaCa}}} (V - V_{\mathrm{NaCa}}) \,, \tag{A.5}$$

with g_{NaCa} the maximum conductance, K_{NaCa} the affinity constant, and V_{NaCa} the equilibrium potential

$$V_{\mathrm{NaCa}} = \frac{\mathrm{RT}}{\mathrm{F}} \left(3 \log \frac{Na_o^+}{Na^+} - \log \frac{c_o}{c} \right) \,, \tag{A.6}$$

where R is the universal gas constant, F is Faraday constant, T is the temperature. The terms c_o, Na_o^+, and Na_i^+ represent the extracellular Ca^{2+} concentration, the extracellular and intracellular Na^+ concentrations, respectively. Both extracellular concentrations are assumed to be constant.

Na^+ dynamics in β-cell is controlled by other three currents. The first is due to the Na^+ inward flux through the nonselective cation current, I_{CRAN}:

$$I_{\mathrm{CRAN}} = f_{\mathrm{CRAN}}(c_{\mathrm{er}}) p_{\mathrm{CRAN}}(V)(V - V_{\mathrm{Na}}) \,. \tag{A.7}$$

This current is made up by a voltage-dependent component, $p_{\mathrm{CRAN}}(V)$, and a voltage-independence component, f_{CRAN}, that is regulated by the endoplasmic Ca^{2+} concentration, c_{er}:

$$p_{\mathrm{CRAN}} = V - V_{\mathrm{CRAN}} \,, \tag{A.8}$$

$$f_{\mathrm{CRAN}} = -\frac{g_{mCRAN}}{1 + \exp\left(\frac{c_{\mathrm{er}} - K_{\mathrm{CRAN}}}{3}\right)} \,, \tag{A.9}$$

with V_{CRAN} the reversal potential, g_{mCRAN} the maximum conductance, and K_{CRAN} the half-activation endoplasmic reticulum level.
The second current is the voltage-activated Na^+ current, I_{Na}

$$I_{\mathrm{Na}} = g_{\mathrm{mNa}}\, p_{\mathrm{Na}}(V)(V - V_{\mathrm{Na}}) \,, \tag{A.10}$$

where the current/voltage relationship, p_{Na}, is once again a Boltzmann-type activation curve

$$p_{\mathrm{Na}}(V) = \frac{1}{1+\exp\left(\frac{104+V}{8}\right)} \,. \tag{A.11}$$

Finally, the third current is the sodium-potassium pump that transports 3 sodium ions to the outside of the cell and 2 potassium ions to the inside. Unlike the others described so far, this currents is ATP consuming. The current through the Na-K pump, $I_{\mathrm{Na,K}}$, is described by

$$I_{\mathrm{Na,K}} = \frac{P_{\mathrm{NaK}}(F_1 f_2 f_3 F_4 F_5 f_6 - b_1 B_2 B_3 B_4 b_5 B_6)}{D} \,,$$

with the function D is given by

$$D = f_2 f_3 F_4 F_5 f_6 + b_1 f_3 F_4 F_5 f_6 + b_1 B_2 F_4 F_5 f_6 + b_1 B_2 B_3 B_4 f_6 + b_1 B_2 B_3 B_4 b_5 \,, \tag{A.12}$$

and

$$\begin{aligned}
&F_1 = f_1 Na^3 \,, && F_4 = f_4 K_o^2 \,, && F_5 = f_5 \mathrm{ATP} \,, && \\
&B_2 = b_2 \mathrm{ADP} \,, && B_3 = b_3 Na_o^3 \,, && B_4 = b_4 P \,, && B_6 = b_6 K^2 \,, \\
&f_5 = f_5^* \exp\left(\tfrac{\mathrm{VF}}{2\mathrm{RT}}\right) \,, && b_5 = b_5^* \exp\left(-\tfrac{\mathrm{VF}}{2\mathrm{RT}}\right) \,. &&&&
\end{aligned} \tag{A.13}$$

The term P represents the inorganic phosphate concentration and it is assumed to be constant.

Consequentially, the Na^+ dynamics can be read as follows:

$$\frac{dNa}{dt} = \frac{-3I_{\mathrm{Na,Ca}} - 3I_{\mathrm{Na,K}} - I_{\mathrm{Na}} - I_{\mathrm{CRAN}}}{V_i \mathrm{F}} \,, \tag{A.14}$$

with V_i the cytosolic volume.

The voltage-dependent delay rectifier K^+ current, I_{KDr}, is the leading outward K^+ current:

$$I_{\mathrm{KDr}} = g_{mKDr} n (V - V_K) \,, \tag{A.15}$$

with g_{mKDr} the maximum conductance and the variable n is the activation gate that has a first-order kinetics

$$\frac{dn}{dt} = \frac{n_\infty(V) - n}{\tau_n(V)} \,, \tag{A.16}$$

where $n_\infty(V)$ is the steady-state value of the gating variable and $\tau_n(V)$ the relaxation time constant:

$$n_\infty(V) = \frac{1}{1+\exp\left(\frac{V_n - V}{S_n}\right)} \,, \qquad \tau_n(V) = \frac{p_\tau}{\exp\left(-\frac{V_\tau - V}{S_{\tau_1}}\right) + \exp\left(\frac{V_\tau - V}{S_{\tau_2}}\right)} \,. \tag{A.17}$$

The voltage-independent Ca^{2+}-activated K^+ channels, $I_{\mathrm{K(Ca)}}$, is described by

$$I_{\mathrm{K(Ca)}} = g_{mKCa} f(c)(V - V_K) \,, \tag{A.18}$$

where g_{mKCa} is the maximum conductance and $f(c)$ is the activation function

$$f(c) = \frac{c^4}{c^4 + K^4_{\mathrm{K(Ca)}}} \,. \tag{A.19}$$

This current results from the Ca^{2+} movement through the small-conductance K(Ca) channels, called SK channels. It is known that there is a second class of large-conductance K(Ca) channels, named BK channels. However, being the current through the latter channels not relevant, the authors did not included it in the model.

A fundamental role in the β-cells is played by the ATP-sensitive K^+-channel. The current though these channels, $I_{\mathrm{K(ATP)}}$, is given by

$$I_{\mathrm{K(ATP)}} = g_{\mathrm{K(ATP)}} O_{\mathrm{K(ATP)}} (V - V_K) \,, \tag{A.20}$$

where $g_{\mathrm{K(ATP)}}$ is the maximum conductance and $O_{\mathrm{K(ATP)}}$ is the fraction of K(ATP) open channels:

$$O_{\mathrm{K(ATP)}} = \frac{0.08\left(1 + 0.33\frac{\mathrm{ADP}}{K_{dd}}\right) + 0.89\left(0.165\frac{\mathrm{ADP}}{K_{dd}}\right)^2}{\left(1 + 0.165\frac{\mathrm{ADP}}{K_{dd}}\right)^2 \left(1 + 0.135\frac{\mathrm{ADP}}{K_{td}} + 0.05\frac{\mathrm{ATP}}{K_{tt}}\right)} \,. \tag{A.21}$$

This equation is based on the expression described by Magnus and Keizer in 1989 [56].

The dynamics of cytosolic and endoplasmic reticulum (ER) Ca^{2+} concentrations are given by

$$\frac{dc}{dt} = f_i \left[\frac{-I_{\mathrm{VCa}} + 2I_{\mathrm{Na,Ca}} - 2I_{\mathrm{PMCA}}}{2\mathrm{F}V_i} - J_{\mathrm{er,p}} + \frac{J_{out}}{V_i}\right] - k_{sg} c \,, \tag{A.22}$$

$$\frac{dc_{\mathrm{er}}}{dt} = \frac{f_{\mathrm{er}}}{V_{\mathrm{er}}} (J_{\mathrm{er,p}} V_i - J_{out}) \,, \tag{A.23}$$

where the constants V_i and V_{er} are the cytosolic and ER volumes, f_i and f_{er} the cytosolic and ER fractions of free Ca^{2+}, and F is the Faraday constant. The constant rate k_{sg} is the leak rate if Ca^{2+} due to the secretory granules, and $J_{\mathrm{er,p}}$ and J_{out} are the fluxes through the endoplasmic reticulum membrane. In particular, $J_{\mathrm{er,p}}$ is the flux due to the sarco(endo)plasmic reticulum Ca^{2+}-ATPase (SERCA) pump that consumes an ATP molecule to move two Ca^{2+} ions from the cytosol to the endoplasmic reticulum; and J_{out} is the ER Ca^{2+} mobilization flux controlled by the

IP_3 concentration, and represents the leak of Ca^{2+} from the endoplasmic reticulum to the cytosol.

$$J_{\mathrm{er,p}} = P_{c_{\mathrm{er}}} \frac{c^2}{c^2 + K_{Carp}^2} \,, \tag{A.24}$$

$$J_{out} = (P_{leak} + P_{\mathrm{IP_3}} O_\infty)(c_{\mathrm{er}} - c) \,. \tag{A.25}$$

The term O_∞ represents the fraction of open IP_3-activated Ca^{2+} channels

$$O_\infty = \frac{c}{c + K_{RCa}} \frac{\mathrm{IP_3^3}}{\mathrm{IP_3^3} + K_{\mathrm{IP_3}}^3} \,. \tag{A.26}$$

The rate of change of the cytosolic IP_3 depends on the cytosolic Ca^{2+} and on the IP_3 concentration itself:

$$\frac{d\mathrm{IP_3}}{dt} = k_{IP} \frac{c^2}{c^2 + K_{IPCa}^2} - k_{dIP}\mathrm{IP_3} \,, \tag{A.27}$$

where k_{IP} and k_{dIP} are the rates of IP_3 production and degradation, respectively, and K_{IPCa} is the Ca^{2+} dependent half-activation of the IP_3 concentration.

We have shown that the Na^+/K^+ pump, as well as the cellular and endoplasmic reticulum membranes calcium pumps require ATP to work. Also, it has been observed that ATP concentration decreases as Ca^{2+} increases in the cytosol, due to the ATP hydrolysis by Ca^{2+} pumps. Thus, the ATP concentration in the cytosol can be described by

$$\begin{aligned} \frac{d\mathrm{ATP}}{dt} =& k_{\mathrm{ADP}}\mathrm{ADP} - \frac{I_{\mathrm{Na,K}} + I_{\mathrm{PMCA}}}{V_i \mathrm{F}} + \\ & - \frac{J_{\mathrm{er,p}}}{2} - (k_{\mathrm{ATP},c}c + k_{\mathrm{ATP}})\mathrm{ATP} \,, \end{aligned} \tag{A.28}$$

where the parameter k_{ADP} is the constant rate for ATP production. The total concentration of intracellular nucleotides, $\mathrm{A_{tot}}$, is kept constant:

$$\mathrm{A_{tot}} = \mathrm{ADP} + \mathrm{ATP} \,. \tag{A.29}$$

A.1.2 Fridlyand 2005: Mathematical Model

The current model [36] is based on the precursor paper published in 2003 [37]. For this formulation, the authors made a few adjustments to include the metabolic process.

Parameter	Value	Parameter	Value	Parameter	Value
V_i	0.764 pL	g_{mNa}	1200 pS	p_τ	20 ms
V_{er}	0.280 pL	P_{NaK}	600 fA	g_{mKCa}	130 pS
C_m	6158 fF	P	4950 μM	$K_{\mathrm{K(Ca)}}$	0.1 μM
f_i	0.01	f_1	2.5×10^{-10} $\mu\mathrm{M}^{-3}$ ms^{-1}	$g'_{mK(ATP)}$	24000 pS
f_{er}	0.03	f_2	10 ms^{-1}	K_{dd}	17 μM
A_{tot}	4 mM	f_3	0.172 ms^{-1}	K_{td}	26 μM
K_i	132.4 mM	f_4	$1.5\times10^{-8}\mu\mathrm{M}^{-2}$ ms^{-1}	K_{tt}	1 μM
K_o	8 mM	f_5^*	0.002 $\mu\mathrm{M}^{-1}$ ms^{-1}	P_{CaER}	0.105 μM ms^{-1}
c_o	2.6 mM	f_6	11.5 ms^{-1}	K_{Carp}	0.5 μM
Na_o	140 mM	b_1	100 ms^{-1}	P_{leak}	0.0001 pL ms^{-1}
$\frac{RT}{F}$	26.73 mV	b_2	0.0001 $\mu\mathrm{M}^{-1}$ ms^{-1}	P_{IP_3}	0.0012 pL ms^{-1}
g_{mVCa}	770 pS	b_3	$1.72\times10^{-17}\mu\mathrm{M}^{-3}$ ms^{-1}	K_{RCa}	0.077 μM
V_{Cah}	-19 mV	b_4	0.0002 $\mu\mathrm{M}^{-1}$ ms^{-1}	K_{IP_3}	3.2 μM
K_{Cah}	9.5 mV	b_5^*	0.031 ms^{-1}	k_{IP}	0.0003 μM ms^{-1}
P_{mPMCA}	2000 fA	b_6	6×10^{-7} $\mu\mathrm{M}^{-1}$ ms^{-1}	k_{dIP}	0.00004 ms^{-1}
K_{PMCA}	0.1 μM	g'_{mKDr}	3000 pS	K_{IPCa}	0.4 μM
g_{NaCa}	271 pS	V_n	-14 mV	k_{sg}	0.0001 ms^{-1}
K_{NaCa}	0.75 μM	S_n	7 mV	k_{ADP}	varies
g_{mCRAN}	0.7 pS mV^{-1}	V_τ	-75 mV	$k_{\mathrm{ATP},c}$	0.00005 $\mu\mathrm{M}^{-1}$ ms^{-1}
V_{CRAN}	0 mV	S_{τ_1}	65 mV	k_{ATP}	0.00005 ms^{-1}
K_{CRAN}	200 μM	S_{τ_2}	20 mV		

Table A.1.: Parameters for the Fridlyand model 2003 [37].

In this model, the glucose goes through the phosphorylation by glucokinase that leads to the glucokinase reaction rate, J_{Glc}:

$$J_{\mathrm{Glc}} = P_{\mathrm{Glc}} \frac{\mathrm{MgATP}}{\mathrm{MgATP} + K_{\mathrm{mATP}}} \frac{G^{1.7}}{G^{1.7} + K_G^{1.7}} \ , \tag{A.30}$$

where G is the glucose concentration in the blood and MgATP represents the free magnesium-ATP concentration. Relevant parameters are show in Table A.2.

The product of this reaction is named the intermediate metabolites concentration, Re, and is described by

$$\frac{d\mathrm{Re}}{dt} = k_{\mathrm{Re}} J_{\mathrm{Glc}} - J_{\mathrm{OP}} \ , \tag{A.31}$$

where k_{Re} is the stoichiometric coefficient for Re production from glucose (i.e. how many ATP molecules are produced by one glucose molecule), and J_{OP} represents the oxidative phosphorylation rate:

$$J_{\mathrm{OP}} = P_{\mathrm{OP}} \mathrm{Re} \frac{\mathrm{MgADP}_f^2}{\mathrm{MgADP}_f^2 + K_{\mathrm{OP}}^2} \ . \tag{A.32}$$

In this equation, MgADP_f is the concentration of free magnesium-ADP, MgADP, which is assumed to be 1/20 of the total ADP concentration in β-cells. In turn, the MgADP concentration is set to be 55% of the total free ADP. In this development of

Parameter	Value	Parameter	Value
P_{Glc}	0.025 μM ms^{-1}	K_{OP}	20 μM
K_{mATP}	500 μM	$k_{\mathrm{ATP},c}$	0.00008 μM ms^{-1}
G	varies	k_{ATP}	5×10^{-5}
K_G	7 mM	$k_{\mathrm{ADP}b}$	0.0002 ms^{-1}
k_{Re}	31	$k_{\mathrm{ADP}f}$	0.00002 ms^{-1}
P_{OP}	0.0002 ms^{-1}	K_{tt}	50 μM

Table A.2.: Parameters for the Fridlyand model 2005 [36].

the model, Re is fuel for the oxidative phosphorylation that is the major source of ATP. Consequently, the ATP dynamics is described by

$$\frac{d\mathrm{ATP}}{dt} = J_{\mathrm{OP}} - \frac{I_{\mathrm{Na,K}} + I_{\mathrm{PMCA}}}{V_i \mathrm{F}} - \frac{J_{\mathrm{er,p}}}{2} - (k_{\mathrm{ATP},c}c + k_{\mathrm{ATP}})\mathrm{ATP}\ . \tag{A.33}$$

We point out that the only difference with the previous description of ATP (A.28) is the first term, J_{OP}, which now is not constant but indirectly glucose-dependent. Once again, the total concentration of ATP and ADP is assumed to be constant. However, the ADP concentration is not made up of two fractions: the cytosolic concentrations of free and bound ADP.

$$\begin{aligned}\frac{d\mathrm{ADP}_b}{dt} =& \frac{I_{\mathrm{Na,K}} + I_{\mathrm{PMCA}}}{V_i F} + \frac{J_{\mathrm{er,p}}}{2} + (k_{\mathrm{ATP},c}c + k_{\mathrm{ATP}})\mathrm{ATP} + \\ &+ k_{\mathrm{ADP}b}\mathrm{ADP}_b - J_{\mathrm{OP}} - k_{\mathrm{ADP}f}\mathrm{ADP}_f\ ,\end{aligned} \tag{A.34}$$

$$\frac{d\mathrm{ADP}_f}{dt} = k_{\mathrm{ADP}f}\mathrm{ADP}_f - k_{\mathrm{ADP}b}\mathrm{ADP}_b\ . \tag{A.35}$$

A.2 Cha School

A.2.1 Cha 2011: Mathematical Model

In the model presented by Cha *et al.* [22] the membrane potential dynamics is once again described by an Hodgkin-Huxley model:

$$\begin{aligned}\frac{dV}{dt} =& -\frac{1}{C}\Big[I_{\mathrm{VCa}} + I_{\mathrm{TRPM}} + I_{\mathrm{SOC}} + I_{\mathrm{bNSC}} + I_{\mathrm{KDr}} + I_{\mathrm{K(Ca),BK}} + \\ &+ I_{\mathrm{K(Ca),SK}} + I_{\mathrm{K(ATP)}} + I_{\mathrm{NaK}} + I_{\mathrm{NaCa}} + I_{\mathrm{PMCA}} + I_{\mathrm{inject}}\Big]\ ,\end{aligned} \tag{A.36}$$

where C is the membrane capacitance, I_{inject} is the constant injected current, I_{VCa} is the voltage-dependent Ca^{2+} current, I_{TRPM} is the Ca^{2+}-activated nonselective cation current, I_{SOC} is the store-operated current, I_{bNSC} is the background nonselective cation current, I_{KDr} is the delay rectify K^+ current, $I_{\mathrm{K(Ca),BK}}$ is the V- and Ca^{2+}-

dependent transient outward K^+ current, $I_{\mathrm{K(Ca),SK}}$ is the Ca^{2+}-activated K^+ currents, $I_{\mathrm{K(ATP)}}$ is the ATP-activated K^+ current, I_{NaK} is the Na^+/K^+ pump current, I_{NaCa} is the Na^+/Ca^{2+} pump current and I_{PMCA} is the plasma membrane Ca^{2+} pump.

The voltage-dependent Ca^{2+} current is made up by three terms, each of these takes into account the affinity for Ca^{2+}, Na^+, and K^+ ions:

$$I_{\mathrm{VCa}} = I_{\mathrm{VCa,Ca}} + I_{\mathrm{VCa,Na}} + I_{\mathrm{VCa,K}} \ , \tag{A.37}$$

where

$$I_{\mathrm{VCa,Ca}} = P_{\mathrm{VCa}}\, p_{\mathrm{VCa}}\, \mathrm{CF}_{Ca} \ , \tag{A.38}$$

$$I_{\mathrm{VCa,Na}} = 1.85 \times 10^{-5} P_{\mathrm{VCa}}\, p_{\mathrm{VCa}}\, \mathrm{CF}_{\mathrm{Na}} \ , \tag{A.39}$$

$$I_{\mathrm{VCa,K}} = 3.67 \times 10^{-4} P_{\mathrm{VCa}}\, p_{\mathrm{VCa}}\, \mathrm{CF}_{K} \ . \tag{A.40}$$

The constant field terms, CF_x, is given by

$$\mathrm{CF}_x = z_x \frac{V\mathrm{F}}{\mathrm{RT}} \frac{x_i - x_o \exp\left(-z_x \frac{V\mathrm{F}}{\mathrm{RT}}\right)}{1 - \exp\left(-z_x \frac{V\mathrm{F}}{\mathrm{RT}}\right)} \ , \tag{A.41}$$

where x_i and x_o are the cytosolic and extracellular concentrations of the ion x, respectively, and $x \in \{Ca^{2+}, K^+, Na^+\}$. This equation is also known as the Nernst-Planck equation [54, 72] and describes the contribution of voltage and concentration gradients to the current density carried by single ionic species. The values of the parameters presented in the model are reported in Table A.3.
The open probability of the Ca^{2+} channels, p_{VCa}, is

$$p_{\mathrm{VCa}} = d_{\mathrm{VCa}}^2 U_{\mathrm{VCa}} (0.4 + 0.6 f_{us}) k_{\mathrm{ATP}} \ , \tag{A.42}$$

where k_{ATP} represents the ATP sensitivity in the voltage-dependent Ca^{2+} current

$$k_{\mathrm{ATP}} = \frac{1}{1 + \left(\frac{1.4}{\mathrm{ATP}}\right)^3} \ , \tag{A.43}$$

and d_{VCa}, U_{VCa}, and f_{us} are the voltage-dependent activation, the Ca^{2+}-dependent inactivation, and the voltage-dependent ultra-slow inactivation gates of I_{VCa}, respectively. Based on the Hodgkin and Huxley model, the gates are described by

$$\frac{dd_{\mathrm{VCa}}}{dt} = \alpha_d (1 - d_{\mathrm{VCa}}) - \beta_d d_{\mathrm{VCa}} \ , \tag{A.44}$$

$$\frac{dU_{\mathrm{VCa}}}{dt} = \alpha_U (1 - U_{\mathrm{VCa}}) - \beta_U U_{\mathrm{VCa}} \ , \tag{A.45}$$

$$\frac{df_{us}}{dt} = \alpha_f (1 - f_{us}) - \beta_f f_{us} \ , \tag{A.46}$$

with the rate constants

$$\alpha_d = \frac{1}{0.9344\exp\left(-\frac{V}{50}\right) + 0.09045\exp\left(-\frac{V}{600}\right)}\ , \quad \beta_d = \frac{1}{4.2678\exp\left(-\frac{V}{12}\right) + 1.1265\exp\left(-\frac{V}{30}\right)}\ ,$$

$$\alpha_U = 8.4\times10^{-3} \qquad \beta_U = 0.2318(-1.15 i_{Ca} d_{\mathrm{VCa}}^2 + c)\ , \qquad i_{Ca} = 6.76\times10^{-2}\ \mathrm{CF}_{Ca}\ ,$$

$$\alpha_f = \frac{1}{7.5\times10^4\exp\left(\frac{V}{34}\right)}\ , \quad \beta_f = \frac{1}{5\times10^3\exp\left(-\frac{V}{19}\right) + 5e02\exp\left(-\frac{V}{100}\right)}\ .$$

The Ca^{2+}-activated nonselective cation current, I_{TRPM}, is described by

$$I_{\mathrm{TRPM}} = I_{\mathrm{TRPM,Na}} + I_{\mathrm{TRPM,K}}\ , \tag{A.47}$$

where the Na^+ and K^+ contributions are given by

$$I_{\mathrm{TRPM,Na}} = 0.8 P_{\mathrm{TRPM}}\ p_{\mathrm{TRPM}}\ \mathrm{CF}_{\mathrm{Na}}\ , \tag{A.48}$$

$$I_{\mathrm{TRPM,K}} = P_{\mathrm{TRPM}}\ p_{\mathrm{TRPM}}\ \mathrm{CF}_{\mathrm{K}}\ , \tag{A.49}$$

and the open probability, p_{TRPM}, is calcium-dependent:

$$p_{\mathrm{TRPM}} = \frac{1}{1+\left(\frac{7.6\times10^{-4}}{c}\right)^{1.7}}\ . \tag{A.50}$$

This was the first time that such a current was introduced in a mathematical model.

The store-operated current I_{SOC} is described by

$$I_{\mathrm{SOC}} = I_{\mathrm{SOC,Na}} + I_{\mathrm{SOC,K}} + I_{\mathrm{SOC,Ca}}\ , \tag{A.51}$$

with

$$I_{\mathrm{SOC,Na}} = 0.8 P_{\mathrm{SOC}}\ p_{\mathrm{SOC}}\ \mathrm{CF}_{\mathrm{Na}}\ , \tag{A.52}$$

$$I_{\mathrm{SOC,K}} = P_{\mathrm{SOC}}\ p_{\mathrm{SOC}}\ \mathrm{CF}_{K}\ , \tag{A.53}$$

$$I_{\mathrm{SOC,Ca}} = 20 P_{\mathrm{SOC}}\ p_{\mathrm{SOC}}\ \mathrm{CF}_{\mathrm{Ca}}\ . \tag{A.54}$$

The open probability of this current depends on the Ca^{2+} concentration in the ER:

$$p_{\mathrm{SOC}} = \frac{1}{1+\exp\left(\frac{c_{\mathrm{er}}-K_{0.5,\mathrm{er}}}{3\times10^{-3}}\right)}\ , \tag{A.55}$$

where $K_{0.5,\mathrm{er}}$ is the half-activation of the current. This current is the counterpart of the I_{CRAN} current presented in Fridlyand models (Eq. (A.7)).

The background nonselective cation current, I_{bNSC} in this model, can be interpreted as a K^+ leak current. Although its nature is still unknown, there are evidences of its role in establishing the resting potential. It is assumed to be depending only on Na^+ and K^+ concentrations and voltage gradients and is described by

$$I_{\mathrm{bNSC,Na}} + I_{\mathrm{bNSC,K}} \ , \tag{A.56}$$

with

$$I_{\mathrm{bNSC,Na}} = P_{\mathrm{bNSC}} \ \mathrm{CF}_{\mathrm{Na}} \ , \tag{A.57}$$

$$I_{\mathrm{bNSC,K}} = 2.525 P_{\mathrm{bNSC}} \ \mathrm{CF}_{\mathrm{K}} \ . \tag{A.58}$$

The delayed rectifier K^+ current, I_{KDr}, is given by

$$I_{\mathrm{KDr}} = P_{\mathrm{KDr}} \ p_{\mathrm{KDr}} \ \mathrm{CF}_K \ , \tag{A.59}$$

where p_{KDr} is the open probability of the current. It is described by

$$p_{\mathrm{KDr}} = r_{\mathrm{KDr}}^2 (0.6 q_{\mathrm{KDr}} + 0.4) \ , \tag{A.60}$$

where r_{KDr} and q_{KDr} are the voltage-dependent activation and voltage-dependent inactivation gates of I_{KDr}, respectively. These last two variables are described by

$$\frac{dr_{\mathrm{KDr}}}{dt} = \alpha_r (1 - r_{\mathrm{KDr}}) - \beta_r r_{\mathrm{KDr}} \ , \tag{A.61}$$

$$\frac{dq_{\mathrm{KDr}}}{dt} = \alpha_q (1 - q_{\mathrm{KDr}}) - \beta_q q_{\mathrm{KDr}} \ , \tag{A.62}$$

with α_i and β_i V-dependent rates

$$\alpha_r = \frac{1}{33.07 \exp\left(-\frac{V}{8}\right) + 0.937 \exp\left(-\frac{V}{100}\right)} \ , \quad \beta_r = \frac{1}{22.73 \exp\left(\frac{V}{10}\right)} \ ,$$

$$\alpha_q = \frac{1}{800} \ , \quad \beta_q = \frac{1}{10^4 \exp\left(\frac{V}{8}\right) + 10^3 \exp\left(\frac{V}{100}\right)} \ .$$

In the current model, both long- and small-conductance K(Ca) channels are presented. It is important to note that the long-conductance K(Ca) channel was introduce in this model for the first time in the history of the β-cell model. The K^+ flux through this first class of channel results in the V- and Ca^{2+}-dependent transient outward K^+ current $I_{\mathrm{K(Ca),BK}}$:

$$I_{\mathrm{K(Ca),BK}} = G_{\mathrm{K(Ca),BK}} \ p_{\mathrm{K(Ca),BK}} (V - E_K) \ , \tag{A.63}$$

where $G_{\mathrm{K(Ca),BK}}$ is the conductance of the current and $p_{\mathrm{K(Ca),BK}}$ is the open probability

$$p_{\mathrm{K(Ca),BK}} = m_{\mathrm{K(Ca),BK}}\, h_{\mathrm{K(Ca),BK}}, \tag{A.64}$$

Once again, $m_{\mathrm{K(Ca),BK}}$ and $h_{\mathrm{K(Ca),BK}}$ are the activation and inactivation gates, respectively

$$\frac{dm_{\mathrm{K(Ca),BK}}}{dt} = \alpha_m(1 - m_{\mathrm{K(Ca),BK}}) - \beta_m m_{\mathrm{K(Ca),BK}}\ , \tag{A.65}$$

$$\frac{dh_{\mathrm{K(Ca),BK}}}{dt} = \alpha_h(1 - h_{\mathrm{K(Ca),BK}}) - \beta_h h_{\mathrm{K(Ca),BK}}\ , \tag{A.66}$$

whose rates constants are

$$\alpha_m = \frac{1}{13.65\exp\left(-\frac{V}{20}\right)}\ , \qquad \beta_m = \frac{1}{6.2\exp\left(\frac{V}{60}\right)}\ ,$$

$$\alpha_h = \frac{1}{570\exp\left(\frac{V}{500}\right)}\ , \qquad \beta_h = \frac{1}{7.765\exp\left(-\frac{V}{9}\right) + 4.076\exp\left(-\frac{V}{1000}\right)}\ .$$

On the other hand, the current through the second class of K(Ca) channel, namely the small-conductance channel family, is given by the Ca^{2+}-activated K^+ current, $I_{\mathrm{K(Ca),SK}}$, is described by

$$I_{\mathrm{K(Ca),SK}} = P_{\mathrm{K(Ca),SK}}\, p_{\mathrm{K(Ca),SK}}\, \mathrm{CF}_K\ , \tag{A.67}$$

with the Ca^{2+}-dependent open probability, $p_{\mathrm{K(Ca),SK}}$, is

$$p_{\mathrm{K(Ca),SK}} = \frac{1}{1 + \left(\frac{7.4\times10^{-4}}{c}\right)^{2.2}}\ . \tag{A.68}$$

The ATP-sensitive K^+ current, $I_{\mathrm{K(ATP)}}$, is

$$I_{\mathrm{K(ATP)}} = G_{\mathrm{K(ATP)}}\, p_{\mathrm{K(ATP)}}(V - E_K)\ , \tag{A.69}$$

where $G_{\mathrm{K(ATP)}}$ is the conductance and $p_{\mathrm{K(ATP)}}$ the open probability:

$$p_{\mathrm{K(ATP)}} = \frac{0.08\left(1 + \frac{2\mathrm{MgADP}}{10^{-2}}\right) + 0.89\left(\frac{\mathrm{MgADP}}{10^{-2}}\right)^2}{\left(1 + \frac{\mathrm{MgADP}}{10^{-2}}\right)^2\left(1 + \frac{0.45\mathrm{MgADP}}{2.6\times10^{-2}} + \frac{\mathrm{ATP}}{5\times10^{-2}}\right)}\ . \tag{A.70}$$

In this equation, MgADP represents the magnesium-ADP concentration in the cytosol and it is assumed proportional to the free ADP concentration, ADP_f:

$$\mathrm{MgADP} = 0.55\mathrm{ADP}_f\ . \tag{A.71}$$

ADP_f, in turn, is computed by

$$\mathrm{ADP}_f = \mathrm{A_{tot}} - \mathrm{ATP} - \mathrm{ADP}_b \ , \tag{A.72}$$

where $\mathrm{A_{tot}}$ is the total amount of ATP species and ADP_b is the cytosolic concentration of bound ADP. In this model, $\mathrm{A_{tot}}$ is assumed to be constant, while ADP_b dynamics is described in Eq. (A.101).

The definition of the current through the Na^+/K^+ pump, I_{NaCa}, was adopted from [70] and it can be read as follows:

$$I_{\mathrm{NaK}} = P_{\mathrm{NaK}} v_{cyc} F_{\mathrm{Glc}} \ , \tag{A.73}$$

where F_{Glc} is the glucose-dependent inhibition factor

$$F_{\mathrm{Glc}} = 0.4 + 0.6 \exp\left(-\frac{G}{5.84}\right) \ , \tag{A.74}$$

P_{NaK} is the constant limiting amplitude factor, and v_{cyc} the turn over rate:

$$v_{cyc} = \frac{\alpha_1^+ \alpha_2^+ \alpha_3^+ \alpha_4^+ - \alpha_1^- \alpha_2^- \alpha_3^- \alpha_4^-}{\Sigma} \ , \tag{A.75}$$

with

$$\begin{aligned}\Sigma =& \alpha_1^- \alpha_2^- \alpha_3^- + \alpha_1^+ \alpha_2^- \alpha_3^- + \alpha_1^+ \alpha_2^+ \alpha_3^- + \alpha_1^+ \alpha_2^+ \alpha_3^+ \\ &+ \alpha_2^- \alpha_3^- \alpha_4^- + \alpha_2^+ \alpha_3^- \alpha_4^- + \alpha_2^+ \alpha_3^+ \alpha_4^- + \alpha_2^+ \alpha_3^+ \alpha_4^+ \\ &+ \alpha_3^- \alpha_4^- \alpha_1^- + \alpha_3^+ \alpha_4^- \alpha_1^- + \alpha_3^+ \alpha_4^+ \alpha_1^- + \alpha_3^+ \alpha_4^+ \alpha_1^+ \\ &+ \alpha_4^- \alpha_1^- \alpha_2^- + \alpha_4^+ \alpha_1^- \alpha_2^- + \alpha_4^+ \alpha_1^+ \alpha_2^- + \alpha_4^+ \alpha_1^+ \alpha_2^+ \ ,\end{aligned} \tag{A.76}$$

and

$$\begin{aligned}
\alpha_1^+ &= \frac{h_1^+ \left(\frac{Na_i}{K_{d,Na_i}}\right)^3}{\left[1+\left(\frac{Na_i}{K_{d,Na_i}}\right)\right]^3 + \left[1+\left(\frac{K}{K_{d,K_i}}\right)\right]^2 - 1} \ , & \alpha_2^+ &= h_2^+ \ , \\
\alpha_3^+ &= \frac{h_3^+ \left[\frac{K_o}{K_{d,K_o}}\right]^3}{\left[1+\left(\frac{Na_o}{K_{d,Na_o}}\right)\right]^3 + \left[1+\left(\frac{K_o}{K_{d,K_o}}\right)\right]^2 - 1} \ , & \alpha_4^+ &= \frac{h_4^+ \left(\frac{\mathrm{MgATP}}{K_{d,\mathrm{MgATP}}}\right)}{1+\left(\frac{\mathrm{MgATP}}{K_{d,\mathrm{MgATP}}}\right)} \ , \\
\alpha_1^- &= h_1^- \mathrm{MgADP} \ , & \alpha_2^- &= \frac{h_2^- \left(\frac{Na_o}{K_{d,Na_o}}\right)^3}{\left[1+\left(\frac{Na_o}{K_{d,Na_o}}\right)\right]^3 + \left[1+\left(\frac{K_o}{K_{d,K_o}}\right)\right]^2 - 1} \ , \\
\alpha_3^- &= \frac{h_3^- Pi\ H^+}{1+\left(\frac{\mathrm{MgATP}}{K_{d,\mathrm{MgATP}}}\right)} \ , & \alpha_4^- &= \frac{h_4^- \left(\frac{K}{K_{d,K_i}}\right)^2}{\left[1+\left(\frac{Na_i}{K_{d,Na_i}}\right)\right]^3 + \left[1+\left(\frac{K}{K_{d,K_i}}\right)\right]^2 - 1} \ ,
\end{aligned} \tag{A.77}$$

The terms $h^{\pm}$ are rate constants, while $K_{d,x}$ are the dissociation constant of the ion $x \in \{\text{Ca}^{2+}, \text{K}^{+}, \text{Na}^{+}\}$.

$$\begin{aligned} K_{d,Na_o} &= K^0_{d,Na_o} \exp\left(\Delta_{Na_o} \frac{VF}{RT}\right) , & K_{d,Na_i} &= K^0_{d,Na_i} \exp\left(\Delta_{Na_i} \frac{VF}{RT}\right) , \\ K_{d,K_o} &= K^0_{d,K_o} \exp\left(\Delta_{K_o} \frac{VF}{RT}\right) , & K_{d,K_i} &= K^0_{d,K_i} \exp\left(\Delta_{K_i} \frac{VF}{RT}\right) . \end{aligned} \tag{A.78}$$

While the $\text{Na}^{+}/\text{K}^{+}$ pump import Na^{+} from the extracellular space into the cytosol, the $\text{Na}^{+}/\text{Ca}^{2+}$ exchange plays the opposite role and expels Na^{+} ions from the cytosol toward the outside of the cell. The resulting current I_{NaCa} is given by

$$I_{\text{NaCa}} = P_{\text{NaCa}}(k_1 p_{E_i Na} E_{\text{tot},i} - k_2 p_{E_o Na} E_{\text{tot},o}) . \tag{A.79}$$

The variables $E_{\text{tot},i}$ and $E_{\text{tot},o}$ represent the probability of active states with an internal or external binding site, respectively. They are described by

$$\frac{dE_{\text{tot},i}}{dt} = k_f E_{\text{tot},o} + \beta_1 I_1 + \beta_2 I_2 - (k_b + \alpha_1 p_{E_{i,Na}} + \alpha_2) E_{\text{tot},i} , \tag{A.80}$$

$$E_{\text{tot},o} = 1 - (E_{\text{tot},i} + I_1 + I_2) . \tag{A.81}$$

The terms α_1, β_1, α_2, and β_2 are constant rates

$$\begin{aligned} \alpha_1 &= 2 \times 10^{-3} f_{Ca} + 1.5 \times 10^{-3}(1 - f_{Ca}) , & \beta_1 &= 1.2 \times 10^{-3} f_{Ca} + 5 \times 10^{-7}(1 - f_{Ca}) , \\ \alpha_2 &= 3 \times 10^{-5} f_{Ca} + \times 10^{-2}(1 - f_{Ca}) , & \beta_2 &= 9 \times 10^{-2} f_{Ca} + \times 10^{-4}(1 - f_{Ca}) , \end{aligned} \tag{A.82}$$

with f_{Ca} the parameter to define the Ca^{2+}-dependency of the inactivation gate

$$f_{Ca} = \frac{c}{c + 4 \times 10^{-3}} . \tag{A.83}$$

The variables I_1 and I_2 in (A.80) are the probability of inactive states

$$\frac{dI_1}{dt} = \alpha_1 p_{E_{i,Na}} E_{\text{tot},i} - \beta_1 I_1 , \tag{A.84}$$

$$\frac{dI_2}{dt} = \alpha_2 E_{\text{tot},i} - \beta_2 I_2 , \tag{A.85}$$

and the rate constant k_f and k_b are given by

$$k_b = k_1 p_{E_i Na} + k_3 p_{E_i Ca} , \qquad k_f = k_2 p_{E_o Na} + k_4 p_{E_o Ca} , \tag{A.86}$$

with

$$k_1 = \exp\left[0.32 \frac{VF}{RT}\right] , \qquad k_2 = \exp\left[(0.32 - 1) \frac{VF}{RT}\right] , \qquad k_3 = 1 , \qquad k_4 = 1 . \tag{A.87}$$

Finally, the factors p_{E_iNa} and p_{E_oNa} (and p_{E_iCa} and p_{E_oCa}) are

$$p_{E_iNa} = \frac{\left(\frac{Na_i}{K_{Na_i}}\right)^3}{1+\left(\frac{Na_i}{K_{Na_i}}\right)^3+\frac{c}{K_{Ca_i}}}\,, \qquad p_{E_oNa} = \frac{\left(\frac{Na_o}{K_{Na_o}}\right)^3}{1+\left(\frac{Na_o}{K_{Na_o}}\right)^3+\frac{c_o}{K_{Ca_o}}}\,,$$

$$p_{E_iCa} = \frac{\left(\frac{c}{K_{Ca_i}}\right)^3}{1+\left(\frac{Na_i}{K_{Na_i}}\right)^3+\frac{c}{K_{Ca_i}}}\,, \qquad p_{E_oCa} = \frac{\left(\frac{c_o}{K_{Ca_o}}\right)^3}{1+\left(\frac{Na_o}{K_{Na_o}}\right)^3+\frac{c_o}{K_{Ca_o}}}\,.$$

The current though the plasma membrane Ca^{2+} pump I_{PMCA} is

$$I_{\mathrm{PMCA}} = P_{\mathrm{PMCA}} p_{\mathrm{PMCA}}\,, \tag{A.88}$$

with the Ca^{2+}-dependent open probability p_{PMCA}:

$$p_{\mathrm{PMCA}} = \frac{1}{1+\left(\frac{1.4\times10^{-4}}{c}\right)^2}\,. \tag{A.89}$$

Thus the Ca^{2+} concentrations in the cytosol and in the endoplasmic reticulum can be described by

$$\frac{dc}{dt} = \frac{f_i}{V_i}\left[\frac{-I_{\mathrm{VCa,Ca}} - I_{\mathrm{SOC,Ca}} + 2I_{\mathrm{NaCa}} - 2I_{\mathrm{PMCA}}}{2\mathrm{F}} - J_{\mathrm{SERCA}} + J_{\mathrm{rel}}\right]\,, \tag{A.90}$$

$$\frac{dc_{\mathrm{er}}}{dt} = \frac{f_{\mathrm{er}}}{V_{\mathrm{er}}}\left(J_{\mathrm{SERCA}} - J_{\mathrm{rel}}\right)\,. \tag{A.91}$$

The constant f_i and f_{er} represent the cytosolic and ER Ca^{2+} buffer strength, V_i and V_{er} the cytosolic and ER volumes, and F the Faraday constant. In the equation, J_{SERCA} and J_{rel} are the fluxes due to the Ca^{2+} uptake by SERCA or release from ER respectively

$$J_{\mathrm{SERCA}} = P_{\mathrm{SERCA}}\frac{1}{1+\left(\frac{5\times10^{-4}}{c}\right)^2}\,, \tag{A.92}$$

$$J_{\mathrm{rel}} = P_{\mathrm{rel}}(c_{\mathrm{er}} - c)\,. \tag{A.93}$$

The other ion concentrations are

$$\frac{dNa}{dt} = \frac{1}{V_i \mathrm{F}} [-I_{\mathrm{VCa,Na}} - I_{\mathrm{TRPM,Na}} - I_{\mathrm{SOC,Na}} - I_{\mathrm{bNSC,Na}} - 3I_{\mathrm{NaK}} + -3I_{\mathrm{NaCa}} + I_{\mathrm{PMCA}}] \ , \tag{A.94}$$

$$\frac{dK}{dt} = \frac{1}{V_i \mathrm{F}} \left[-I_{\mathrm{KDr}} - I_{\mathrm{K(Ca),BK}} - I_{\mathrm{K(Ca),SK}} - I_{\mathrm{K(ATP)}} - I_{\mathrm{VCa,K}} + -I_{\mathrm{TRPM,K}} - I_{\mathrm{SOC,K}} - I_{\mathrm{bNSC,K}} + 2I_{\mathrm{NaK}} - I_{\mathrm{inject}}\right] \ . \tag{A.95}$$

Finally, the metabolic compartment of the model can be described. The glucose enters into the cytosol and it is broken during the glycolysis and the β-oxidation to create intermediate metabolites and, eventually, pyruvate. In this model, these intermediate metabolites are represented by variable Re, i.e. reduced metabolic compounds, and it essentially represents the $\mathrm{NADH_m}$ concentration:

$$\frac{d\mathrm{Re}}{dt} = J_{\mathrm{Glc}} + J_{\beta,ox} - \frac{\mathrm{R}_{vol}}{N} J_{\mathrm{OP}} \ , \tag{A.96}$$

where R_{vol} is the volume ratio between cytosolic and mitochondria volumes, N is the stoichiometry of conversion from NADH and ATP. NADH production occurs through glycolysis and β-oxidation, J_{Glc} and $J_{\beta,ox}$:

$$J_{\mathrm{Glc}} = k_{\mathrm{Glc}} f_{\mathrm{Glc}} (\mathrm{Re_{tot}} - \mathrm{Re}) \ ,$$
$$J_{\beta,ox} = k_{\beta,ox} (\mathrm{Re_{tot}} - \mathrm{Re}) \ ,$$

with $\mathrm{Re_{tot}}$ the total amount of pyridine nucleotides and it is assumed constant. The factor f_{Glc} represents the ATP- and glucose-dependency of the glucose:

$$f_{\mathrm{Glc}} = \frac{1}{1 + \frac{0.5}{\mathrm{ATP}}} \frac{1}{1 + \left(\frac{K_{\mathrm{Glc}}}{G}\right)^{2.5}} \ . \tag{A.97}$$

On the other hand, NADH is consumed by oxidative phosphorylation to produce ATP. The flux of this reaction is J_{OP}:

$$J_{\mathrm{OP}} = P_{\mathrm{OP}} Re \frac{1}{1 + \left(\frac{2\times10^{-2}}{\mathrm{MgADP}}\right)} \ . \tag{A.98}$$

This chemical reaction is the source of ATP that in turn is used by the various pumps and extra factors summed up in the ATP consumption flux $J_{c,\mathrm{ATP}}$:

$$J_{c,\mathrm{ATP}} = (k_{\mathrm{ATP}} + k_{\mathrm{ATP},c} c)\mathrm{ATP} \ . \tag{A.99}$$

In this expression, k_{ATP} and $k_{\mathrm{ATP},c}$ represent the Ca^{2+}-independent and Ca^{2+}-independent ATP consumption rates, respectively.

Parameter	Value	Parameter	Value	Parameter	Value
I_{inject}	0	$G_{\text{K(ATP)}}$	2.31 pA mV^{-1}	P_{NaCa}	204 pA
C	6.158 pF	P_{NaK}	350 pA ms	K_{Na_o}	87.5 mM
$\frac{RT}{F}$	26.73 mV	Pi	1.9	K_{Ca_o}	1.38 mM
K_o	5.4 mM	H	0.0001	K_{Na_i}	20.75 mM
c_o	2.6 mM	Δ_{Na_o}	0.44	K_{Ca_i}	0.0184 mM
N_o	140 mM	Δ_{Na_i}	-0.14	P_{PMCA}	1.56 pA
V_i	764 fL	Δ_{K_o}	0.23	P_{SERCA}	0.096 amole ms^{-1}
V_{er}	280 fL	Δ_{K_i}	-0.14	P_{rel}	0.46 fL ms^{-1}
f_i	0.01	K^0_{d,Na_o}	26.8 mM	k_{Glc}	0.000126 ms^{-1}
f_{er}	0.025	K^0_{d,K_o}	0.8 mM	$k_{\beta,ox}$	0.0000063 ms^{-1}
z_{Na}	1	K^0_{d,Na_i}	5 mM	K_{Glc}	13 mM
z_K	1	K^0_{d,K_i}	18.8 mM	Re_{tot}	10 mM
z_{Ca}	2	$K_{d,\text{MgATP}}$	0.6 mM	P_{OP}	0.0005 ms^{-1}
P_{VCa}	48.9 pA mM^{-1}	h^+_1	1.2528 ms^{-1}	N	2.5
P_{TRPM}	0.0234 pA mM^{-1}	h^+_2	0.1392 ms^{-1}	R_{vol}	2.5
P_{SOC}	0.00764 pA mM^{-1}	h^+_3	6.96 ms^{-1}	ATP_{tot}	4 mM
$K_{0.5,\text{er}}$	0.003 mM	h^+_4	0.522 ms^{-1}	k_{ATP}	0.000062 ms^{-1}
P_{bNSC}	0.00396 pA mM^{-1}	h^-_1	0.139 mM^{-1} ms^{-1}	$k_{\text{ATP},c}$	0.187 mM^{-1} ms^{-1}
P_{KDr}	2.1 pA mM^{-1}	h^-_2	0.0139 ms^{-1}	$k_{\text{ADP},f}$	0.0002 ms^{-1}
$G_{\text{K(Ca),BK}}$	2.13 pA mV^{-1}	h^-_3	13900 mM^{-2} ms^{-1}	$k_{\text{ADP},b}$	0.00002 ms^{-1}
$P_{\text{K(Ca),SK}}$	0.2 pA mM^{-1}	h^-_4	0.348 ms^{-1}		

Table A.3.: Parameters for the Cha model 2011 [22].

Thus, ATP and ADP$_b$ dynamics are described by

$$\frac{d\text{ATP}}{dt} = J_{\text{OP}} - J_{c,\text{ATP}} - \left(\frac{I_{\text{NaK}} + I_{\text{PMCA}}}{F} + \frac{J_{\text{SERCA}}}{2}\right)\frac{1}{V_i}\,, \tag{A.100}$$

$$\frac{d\text{ADP}_b}{dt} = k_{\text{ADP},f}\text{ADP}_f - k_{\text{ADP},b}\text{ADP}_b\,, \tag{A.101}$$

where $k_{\text{ADP},f}$ is the rate constant from ADP$_f$ and ADP$_b$, and $k_{\text{ADP},b}$ from ADP$_b$ and ADP$_f$.

A.2.2 Silva Coupling 2014: Mathematical Model

The model published by Silva and collaborators in [85] was based on Cha's model [22]. For Silva's formulation, ATPase inhibition was made stronger by substituting (A.74) by

$$F_{\text{Glc}} = 0.3 + 0.7\exp\left(-\frac{G}{2}\right)\,, \tag{A.102}$$

that results in a more active Na^+/K^+ pump at low glucose concentrations. A second adjustment was made in the ATP sensitivity in the voltage-dependent Ca^{2+}

current. An ATP-interdependent term was introduced in I_{VCa} by substituting the ATP-dependent term in the open probability (A.43) by

$$k_{\mathrm{ATP}} = 0.5 + 0.5\frac{1}{1+\left(1+\frac{1.4}{\mathrm{ATP}}\right)^3}\,. \tag{A.103}$$

Two further minor changes were made in this formulation of Cha model. The first is the half-maximal activatory Ca^{2+} concentration of the plasma membrane Ca^{2+} pump (A.88), that was increased from 0.00014 up to 0.00018 mM. A second adapt was made in the background nonselective cation current I_{bNSC} (A.56) by reducing the mean permeability P_{bNSC} in the background Na^{+} current from 3.96 down to 3.00 pA/mM, and by increasing the mean permeability in background K^{+} current from 2.525 up to 6.

The cell-cell coupling was simulated by adding a gap junction current between each β-cell in the islet. Thus, the membrane potential of the i^{th} cell described in (A.36) is now replaced by

$$\begin{aligned}\frac{dV_i}{dt} = &-\frac{1}{C}\Big[I_{\mathrm{VCa}} + I_{\mathrm{TRPM}} + I_{\mathrm{SOC}} + I_{\mathrm{bNSC}} + I_{\mathrm{KDr}} + I_{\mathrm{K(Ca),BK}} + I_{\mathrm{K(Ca),SK}} + \\ &+ I_{\mathrm{K(ATP)}} + I_{\mathrm{NaK}} + I_{\mathrm{NaCa}} + I_{\mathrm{PMCA}} + I_{\mathrm{inject}}\Big] + \sum_{j\in\Omega_i}\left[g_{ij}(V_i - V_j)\right]\,,\end{aligned} \tag{A.104}$$

where Ω_i is the neighbourhood of the i^{th} cell, and g_{ij} are electrical coupling conductances. The values of the gap junction conductance follow a normal distribution of mean 215 pS and standard deviation 110 pS. The islet was assembled by linking several cells in a $4 \times 4 \times 4$ cube, initially, and then in a $10 \times 10 \times 10$ cube. Figure 3.8 illustrates a schematic of these islets. The β-cellsare assumed to be heterogeneous, so that the conductance of the major currents (I_{VCa}, I_{bNSC}, I_{KDr}, $I_{\mathrm{K(ATP)}}$, $I_{\mathrm{K(Ca),BK}}$, $I_{\mathrm{K(Ca),SK}}$) were allowed to vary with an standard deviation of 20% of the average.

B Stability of An Excitable System

In this chapter, we analyse the phase plane of a general excitable system with cubic nullcline. The model is given by an ODE for the variable, v, and an ODE for a activation variable, w:

$$\begin{aligned} \frac{dv}{dt} &= f(v,w) \ , \\ \frac{dw}{dt} &= g(v,w) \ , \end{aligned} \tag{B.1}$$

with $f(v,w)$ a cubic function in v. Figure B.1A, B, and C depict three possible interactions between v- and w-nullclines, given by $f(v,w) = 0$ and $g(v,w) = 0$, respectively. We observe that the v-nullcline can be split into three branches identified by the knee (here, maximum and minimum of the nullcline).

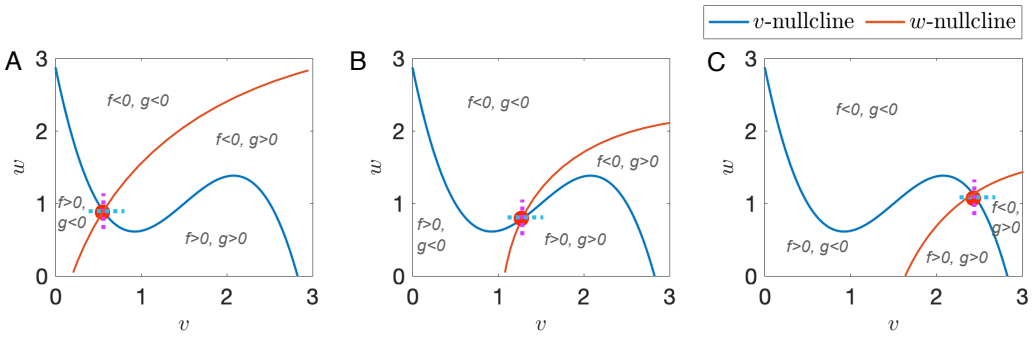

Figure B.1.: Phase plane analysis of the model in Eq. (B.1).

When there is an intersection on the left branch (panel A), $\frac{\partial f}{\partial v} < 0$ and $\frac{\partial f}{\partial w} < 0$. In fact, moving from left to right on the dashed blue line through the steady state, $f > 0 \rightarrow f < 0$, so $\frac{\partial f}{\partial v} < 0$. Moving from down to up on the dashed magenta line, $f > 0 \rightarrow f < 0$, so $\frac{\partial f}{\partial w} < 0$. Similarly, $\frac{\partial g}{\partial v} > 0$ and $\frac{\partial g}{\partial w} < 0$.

As we know, linear stability of the steady state depends on eigenvalues of the Jacobian matrix J, where

$$J = \begin{pmatrix} \frac{\partial f}{\partial v} & \frac{\partial f}{\partial w} \\ \frac{\partial g}{\partial v} & \frac{\partial g}{\partial w} \end{pmatrix} \ , \tag{B.2}$$

and the matrix trace is $\frac{\partial f}{\partial v} + \frac{\partial g}{\partial v}$ and $\frac{\partial f}{\partial v}\frac{\partial g}{\partial v} - \frac{\partial f}{\partial w}\frac{\partial g}{\partial w}$, respectively.

Evaluated at the steady state,

$$J = \begin{pmatrix} - & - \\ + & - \end{pmatrix} . \tag{B.3}$$

and the trace of the matrix is $(-)+(-) < 0$, so the sum of the eigenvalues is negative. In addition, the determinant is positive $((-)(-) - (-)(+) > 0)$, so the product of the eigenvalues is positive (they have the same sign). Thus, the eigenvalues are both negative and the steady state is stable.

When the intersection is on the middle branch (panel B), $\frac{\partial f}{\partial v} > 0$ and $\frac{\partial f}{\partial w} < 0$, while $\frac{\partial g}{\partial v} > 0$ and $\frac{\partial g}{\partial w} < 0$. Thus, the Jacobian evaluated at the steady state,

$$J = \begin{pmatrix} + & - \\ + & - \end{pmatrix} , \tag{B.4}$$

so the trace is $(+) + (-)$ which could be positive or negative. Thus, it is possible for the eigenvalues to have positive real part, and the steady state to become unstable.

Increasing the applied current even more can translate the v-nullcline high enough so that the intersection is on the right branch (panel C). In this case,

$$J = \begin{pmatrix} - & - \\ + & - \end{pmatrix} , \tag{B.5}$$

and the situation is similar to the left branch intersection, so the equilibrium is stable.

In Chapter 4, we use this result to discuss the stability of the glycolytic subsystem Eq. (4.14). In that case, the variable v and w play the role of the glycolytic variables FBP and F6P, respectively.

C The AUTO Software

In this dissertation, we often use the AUTO software to perform numerically the stability analysis. In this chapter, we give the most basic information about this software and we describe in detail how we obtain some of the results used in the thesis.

C.1 History of AUTO

AUTO is a software for continuation and bifurcation problems in ordinary differential equations (ODEs). The very first version of the software was developed by Eusebius Doedel in 1976, who was working at the California Institute of Technology (Pasadena, US) at that time. It was a very early program for boundary value problem in ODEs. A few years later Doedel moved to the Concordia University (Montreal, Canada) where he presented the first distributed version of AUTO in 1980. Later on, several people made significant contributions to AUTO, including Alan Champneys, Fabio Dercole, Thomas Fairgrieve, Yuri Kuznetsov, Bart Oldeman, Randy Paffenroth, Bjorn Sandstede, Xianjun Wang, and Chenghai Zhang. In Table C.1 we sum up the milestones in AUTO development.
In this dissertation, we use the latest version of the software, AUTO-07p.

C.2 What Can AUTO Do?

The AUTO software can be use to study:

- algebraic systems of the form

$$f(u, \boldsymbol{p}) = 0 \,, \qquad f(\cdot,\cdot), u \in \mathbb{R}^n \,; \tag{C.1}$$

- systems of ODEs of the form

$$u'(t) = f(u(t), \boldsymbol{p}) \,, \qquad f(\cdot,\cdot), u(\cdot) \in \mathbb{R}^n \tag{C.2}$$

Year	Version Specification
1976	Early program for BVP in ODEs
1980	First distributed version
1986	AUTO86
1994	X/Motif version : AUTO94
1994	Parallel version: AUTO94P
1997	AUTO97, with HOMCONT
2000	C Language Version
2007	AUTO-07p

Table C.1.: Historical evolution in AUTO development. The light blue steps were achieved at the California Institute of Technology (Pasadena, US) and the light green at the Concordia University (Montreal, Canada).

subject to boundary (including initial) conditions and integral constraints;

- partial differential equation (PDE) of the form

$$u_t = Du_{xx} + f(u, \boldsymbol{p}) \,, \qquad f(\cdot,\cdot), u(\cdot) \in \mathbb{R}^n \tag{C.3}$$

where D denotes a diagonal matrix of diffusion constants.

The term $\boldsymbol{p}$ in the equations denotes one or more free parameters.

More precisely, AUTO can be use to perform limited bifurcation analysis of algebraic systems (C.1), continuation of solutions of ODE system (C.2), and stationary solution and wave calculations for PDE (C.3).

C.2.1 Numerical Details

In Table C.2 we show the main numerical details that have to be communicated to AUTO in order to perform our analysis. This details are save in the file `c.constant`.

AUTO can detect various types of points that can be in solution and bifurcation diagram. The most interesting critical point to the purpose of this thesis are described in Table C.3.

Computation Constants	Meaning
e, s, dat, sv	Define file names: equation prefix (.f,.f90,.c), restart solution suffix (s.), user data prefix (.dat), output suffix (b.,s.,d.)
NDIM	Problem dimension
IPS	Problem type. 0=AE, 1=FP(ODEs), -1=FP(maps), 2=PO, -2=IVP, 4=BVP, 7=BVP with Floquet multipliers, 5=algebraic optimization problem, 15=optimization of periodic solutions
ILP	Fold detection; 1=on, 0=off
ICP	Continuation parameters
NTST	♯ mesh intervals
NCOL	♯ collocation points
IAD	Mesh adaption every IAD steps; 0=off
ISP	Bifurcation detection; 0=off, 1=BP(FP), 3=BP(PO,BVP), 2=all
NBC	Branch switching; 1=normal, -1=switch branch (BP, HB, PD), 2=switch to two-parameter continuation (LP, BP, HB, TR) 3=switch to three-parameter continuation (BP)
NINT	♯ integral conditions
NMX	Maximum number of steps
RL0, RL1	Parameter interval RL0 $\leq \lambda \leq$ RL1
NPR	Print and save restart data every NPR steps
ITMX	Maximum ♯ of iterations for locating special solutions/points
ITNW	Maximum ♯ of correction steps
NWTN	Corrector uses full newton for NWTN steps
JAC	User defines derivatives; 0=no, 1=yes
MXBF	Automatic branch switching for the first MXBF bifurcation points if IPS=0, 1
EPSL, EPSU, EPSS	Convergence criterion: parameters, solution components, special points
DS	Start step size
DSMIN, DSMAX	Step size interval DSMIN $\leq h \leq$ DSMAX
IADS	Step size adaption every IADS steps; 0=off
THL = 11:0.0	list of parameter
SP = ['BP0']	ist of bifurcations to check

Table C.2.: Legend for the computation constant.

Short name	Type
Fold	LP
Hopf bifurcation	HB
User requested point	UZ
Period doubling bifurcation	PD
Normal begin or end	EP

Table C.3.: Legend for the short names of the type of points.

C.3 Example: Supercritical Hopf Bifurcation

The first example we propose to show AUTO potentialities is the BioPhan model described in Chapter 3 and analysed in Chapter 7. In the latter chapter, we show that the fast subsystem is made up by the variables V, n, and c, while a and c_{er} are the slow variables. In particular, c_{er} is by far the slowest.

In this section, we describe the steps and numerical details that lead to the results shown in Figure 7.4. Therefore, we focus on the fast subsystem, treating a and c_{er} as parameters. In particular, a is used as bifurcation parameter.

C.3.1 Numerical Details

The numerical details of this numerical analysis have been saved in the `c.constant` file. The first two lines simply list the variables and parameters. Because of its key role in the dynamics, we also include $g_{\mathrm{K(Ca)}}$ in the list of parameters.

```
# AUTO constants file from which most calculations begin.
unames = {1:v,2:n,3:c}
parnames = {1:a, 2:cer, 3:gkca}
```

The next few lines are about the dynamical system and the bifurcation parameter. We are focusing on an ODE system (IPS=3) of dimension 3 (NDIM=3). The bifurcation parameter is a, the first parameter in our list (ICP=[1]). Finally, we look for all the critical points such as Hopf bifurcations and saddle-node bifurcations (ILP=1). Hence, we have:

```
NDIM = 3,
IPS = 1,
ILP = 1,
ICP = [1],
```

Now, we define the most important numerical details, such as the maximum number of steps, the parameter interval, the maximum number of iterations for locating special solutions/points or of correction steps, etc.

```
NTST = 1000,
NCOL = 4,
IAD = 3,
ISP = 2,
NBC = 0,
```

```
NINT = 0,

NMX = 10000000,
RL0=0,
RL1=3,

NPR = 50000,
ITMX = 8,
ITNW = 7,
NWTN = 3,
JAC = 1,
MXBF=5,

EPSL = 1e-9,
EPSU = 1e-9,
EPSS = 1e-7,

DS = 1e-2,
DSMIN = 1e-5,
DSMAX = 1e-2,
IADS = 1,

THL = {11:0.0}
SP = ['BP0']
```

C.3.2 Bifurcation Analysis

To perform the bifurcation analysis, we write a Python code, `BMB04_FSanalysis.py`. The first few lines of this code are to clear the directory and to remove files from previous runs.

```
# Clear directory
clean()
name = "BMB04_FSanalysis_avf"
delete(name)
```

The first step in our analysis is to locate the steady states and critical points using the chosen bifurcation parameter. To do so, we write the following commands into our Python file.

```
# Compute bifurcation diagram with DS>0 and save results
r1 = run(e=name, c="constants", ICP=[1], UZR={1:[0,3]},
    STOP=["UZ1"])
sv(name)

# Compute bifurcation diagram with DS<0 and append to saved file
r2 = run(e=name, c="constants", DS='-', UZR={1:[0,3]},
STOP=["UZ1"])
ap(name)
plot(name, stability=1, use_labels=1, use_symbols=0)
```

The command `e=name` reads the C++ file `BMB04_FSanalysis_avf.c` containing all the information about the system and the initial conditions for both variables and parameters.

Figure C.1 shows the bifurcation diagram obtained with AUTO.

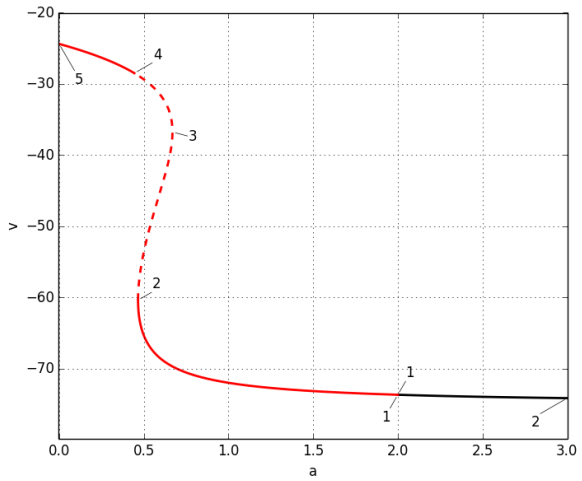

Figure C.1.: Location of the steady states for the BioPhan model obtained with AUTO and a as bifurcation parameter.

The black curve in Figure C.1 corresponds to the forward computation `r1` in the Python file, while the red to the backward computation `r2`. Also, AUTO uses the convention that solid line represents stable branch and dashed line unstable branch.

Thus, in our case, the bifurcation diagram is made up of three branches identified by the two saddle-node bifurcations (`LP`, label 2 and 3). We observe that the bottom branch is stable while the one in the middle is unstable. The top branch is unstable close to the saddle-node bifurcation, but it becomes stable when the equilibrium goes through a supercritical Hopf bifurcation (`HB`, label 4). A branch of stable periodic

solutions arises from the supercritical Hopf bifurcation. To compute these branches, we run the following code

```
# Grab the first HB and continue the periodic orbit
hr1 = run(r2('HB1'), IPS=2, ISW=-1,ICP=[1,11,12], STOP=["LP15"])
ap(name)
plot(name,stability=1, use_labels=1, use_symbols=0)
```

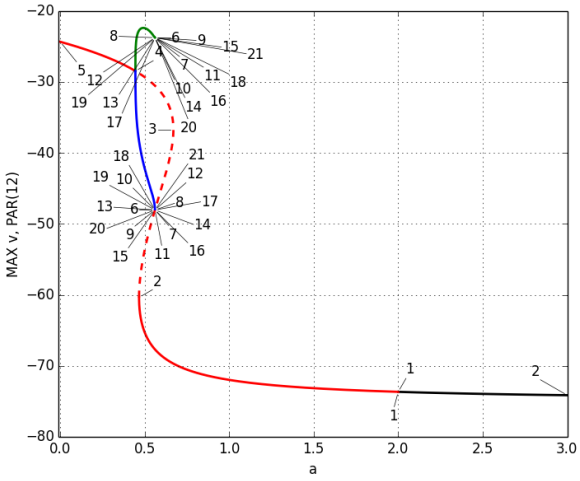

Figure C.2.: Bifurcation Diagram for the BioPhan model obtained with AUTO and a as bifurcation parameter. Branches of the periodic solutions arising from the Hopf bifurcation are shown in green and blue.

The green curve in Figure C.2 represents the maximum values of the periodic solution rising from the HB, whereas the blue curve the minimum.

The branch of periodic solutions disappears when it meets the middle branch of the z-curve in the homoclinic bifurcation. This bifurcation is not detected by AUTO. However, it is easy to locate it since the period rapidly increases after the period doubling bifurcation (PD, label 6).

C.4 Example: Subcritical Hopf Bifurcation

The second example we propose is the dynamics presented in Chapter 4 on the glycolytic subsystem of the IOM1.5:

$$\begin{aligned} \frac{d\mathrm{F6P}}{dt} &= 0.3\,(J_{\mathrm{GK}} - J_{\mathrm{PFK}}) \ , \\ \frac{d\mathrm{FBP}}{dt} &= J_{\mathrm{PFK}} - \frac{1}{2} J_{\mathrm{PDH}} \ . \end{aligned} \tag{C.4}$$

Our analysis aim is to investigate the nature of the solutions of the glycolytic subsystem with respect to the cytosolic Ca^{2+} concentration, c, and the parameter v_{PDH}. We assume ADP and mitochondrial Ca^{2+} at the equilibrium whose values can be explicitly computed as functions of c:

$$c_{\mathrm{m}} = \frac{(k_{\mathrm{uni}} + k_{\mathrm{NaCa}})\, c}{k_{\mathrm{NaCa}}}\,, \tag{C.5}$$

$$\mathrm{ADP} = \frac{4A_{\mathrm{tot}}\mathrm{K}}{3 + (2\mathrm{K}+1)^2}\,. \tag{C.6}$$

where $\mathrm{K} = \exp\left[\left(1 + 2.2\frac{J_{\mathrm{PDH}}}{0.05+J_{\mathrm{PDH}}}\right)\left(1 - \frac{c}{0.35}\right)\right]$.

C.4.1 Numerical Details

Once again, we save the numerical details in the file `c.constant`. We use the same computational details listed in the previous example, except for the description of the dynamical system. The variables we are now considering are F6P and FBP, and the set of parameters is given by c and v_{PDH}. Thus, the dimension of the ODE system is 2 and first use c as bifurcation parameter, that is reasonably assumed between 0 μM and 0.3 μM.

```
# AUTO constants file from which most calculations begin.
unames = {1:f6p, 2:fbp}
parnames = {1:c, 2: vpdh}
```

```
NDIM = 3,
IPS = 1,
ILP = 1,
ICP = [1]
```

```
RL0=0,
RL1=0.3
```

C.4.2 Bifurcation Analysis

The first step in our bifurcation analysis is to compute the bifurcation diagram. The code we use is, once again, similar to the previous example

```
# Clear directory
clean()
name = "IOM_GO_avf"
delete(name)
```

```
# Compute bifurcation diagram with DS>0 and save results
r1 = run(e=name,c="constants",ICP=[1],UZR={1:[0.0001, 0.03]},
STOP=["UZ1"])
sv(name)

# Compute bifurcation diagram with DS<0 and append to saved file
r2 = run(e=name,c="constants",DS='-',UZR={1:[0.0001, 0.03]},
STOP=["UZ1"])
ap(name)
plot(name,stability=1,use_labels=1,use_symbols=0)
```

Running these few lines gives us the bifurcation diagram shown in Figure C.3.

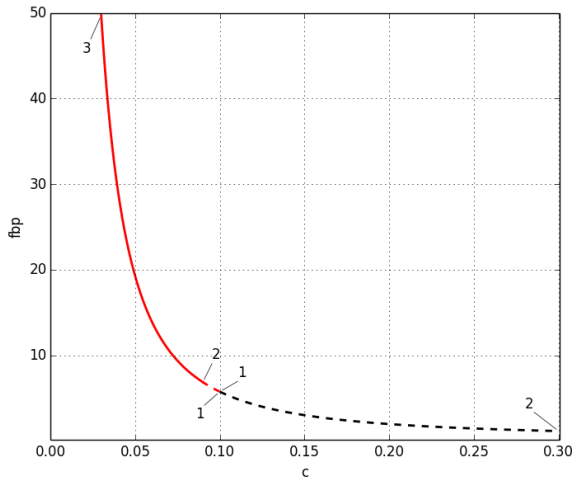

Figure C.3.: Location of the steady states for the glycolytic subsystem obtained with AUTO and c as bifurcation parameter.

We observe that for low values of c the steady state is stable (solid line) and FBP reaches very high values. The equilibrium goes through a Hopf bifurcation (HB, label 2) and it becomes unstable (dashed line). We now lunch the following lines of the Python code to compute the parameter continuation of the periodic orbit.

```
# Grab the first Hopf bifurcation and continue the PO
hr1 = run(r2('HB1'),IPS=2,ISW=-1,ICP=[1,11,12],
UZR={1:[0.0001, 0.03]}, STOP=["UZ1"])
ap(name)
plot(name,stability=1,use_labels=1,use_symbols=0)
```

The Hopf bifurcation is a subcritical Hopf bifurcation and a branch of unstable periodic solutions rises from the critical point. This brunch meets a branch of stable periodic solutions at a saddle-node of periodics bifurcation (LP, label 5). Hence, for c values to the right of the SNP point, the attractor of the glycolytic subsystem is a limit cycle. However, there is a region between the HB and the SNP of bistability we can have an oscillatory or silent glycolytic subsystem according to the initial conditions.

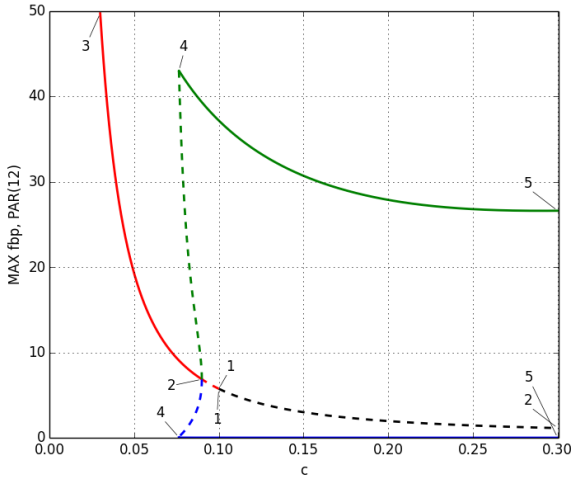

Figure C.4.: Bifurcation Diagram for the glycolytic subsystem obtained with AUTO and c as bifurcation parameter. Branches of the periodic solutions arising from the Hopf bifurcation are shown in green and blue.

So far, we have considered a 1D bifurcation diagram with only one bifurcation parameter. However, it is known the fundamental role of the parameter v_{PDH}. Thus, we investigate the location of both Hopf bifurcation and saddle-node of periodics with respect to the two parameters (c and v_{PDH}) simultaneously. We use AUTO to perform the two-parameter continuations of HB and SNP using c and v_{PDH} as bifurcation diagram. The correspondent code can be read as follows:

```
# Grab the first Hopf bifurcation and continue two parameter

hb1 = load(r2('HB1'), ISW=2)
hbr1 = run(hb1, ICP=[1,2], UZR={1:[0.0001, 0.03],
          2:[0.0001,0.01]}, STOP=["UZ1"])
ap(name)
hbr2= hbr1 + run(hb1, DS='-', ICP=[1,2], UZR={1:[0.0001, 0.03],
  2:[0.0001,0.01]}, STOP=["UZ1"])
sv(hbr2,'hbr')
ap(name)
plot(name, stability=1, use_labels=1, use_symbols=0)
```

```
# Grab the first LP bifurcation and two-parameter continuation
lp = load(hr1('LP2'), ISW=2,STOP=["UZ1"])
lpr = run(lp, ICP=[1, 2])
lpr1=run(lpr, UZR={1:[0.0001, 0.03], 2:[0.0001,0.01]},
STOP=["UZ1"])
ap(name)
lpr2=lpr1+run(lpr, DS='-', UZR={1:[0.0001, 0.03],
2:[0.0001,0.01]}, STOP=["UZ1"])
ap(name)
sv(lpr2,'lpr')
plot(name, stability=1, use_labels=1, use_symbols=0)
```

The output of the two-parameter continuations of HB and SNP is shown in Figure C.5.

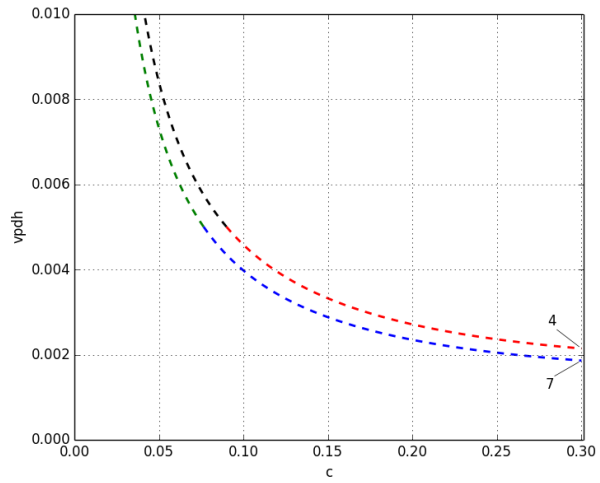

Figure C.5.: Two parameter continuation of the Hopf bifucation (black and red curves) and the saddle-node of periodics bifurcation (blue and red curves) on the (c, v_{PDH}) plane.

The red and black curves are the two-parameter continuations of HB, while the blue and green of the SNP. This plot shows that the parameter plane is split into three areas. The area in which the steady state is the only stable solution (above the HB curve), the one in which the limit cycle is the only stable attractor (below the SNP curve), and the third in which they are both attractors and the solution depends on the initial conditions (between the two curves). We widely discuss these results in Section 4.3.1.

Matlab Codes

D

The solutions to the mathematical models are obtained with the help of the computer program MATLAB (MathWorks Inc., Natick, MA). We use self-developed codes and the multistep ODE15s solver.

In this chapter, we present the computer codes for the most relevant models used in this dissertation, such as the IOM1.5 (Chapter 4), the IOM2.0 (Chapter 5), and the IOM2.2 (Chapter 8).

D.1 The IOM1.5

```
% Variables:
%    v -- cellular membrane potential (mV)
%    n -- activation of delayed rectifier
%    c -- free cytosolic calcium concentration (muM)
%    adp -- cytosolic ADP concentration (muM)
%    cer -- concentration of free calcium in the endoplasmic reticulum (muM)
%    cam -- mitocondrial calcium concentration (muM)
%    f6p -- fructose 6-phosphate concentration (muM)
%    fbp -- fructose 1,6-bisphosphate concentration (muM)

% Units:
% time: ms
% volume: l
% conductance: pS
% V: mV
% I: fA
% J: muM/ms
% alpha: mumol/fA/ms

function vf = IOM15_vf(t,x,param)

vf = zeros(8,1);


v=x(1);
n=x(2);
c=x(3);
cer=x(4);
cam=x(5);
adp=x(6);
f6p=x(7);
fbp=x(8);

%%%%%%%%%%%%%%%%%%%%%%%%%%%%%%%%
%% Electrical and Calcium Model %%
```

```
%%%%%%%%%%%%%%%%%%%%%%%%%%%%%%%%

%-------------------------------------
% Ca2+ current; ica
%-------------------------------------
gca = 1000; vca = 25;

nim = -20; sm = 12;
minf = 1/(1+exp((nim-v)/sm));

ica=gca*minf*(v-vca);


%-------------------------------------
% Delayed-rectifying K+ current; ik
%-------------------------------------
gk=2700; vk=-75;
taun=20;    nin=-16; sn=5;

ninf=1/(1+exp((nin-v)/sn));
ik=gk*n*(v-vk);

%-------------------------------------
%  Ca2+-activated K+ current; ikca
%-------------------------------------
kd=0.5;     gkca=param.gkca;

qinf=c^2/(kd^2+c^2);
ikca=-gkca*qinf*(vk-v);

%-------------------------------------
% K-ATP channel current; ikatp
%-------------------------------------
kdd=17; ktd=26; ktt=1;  atot=3000;
gkatpbar=25000;

rad=sqrt(-4*adp^2+(atot-adp)^2);
atp=(atot+rad-adp)/2;
mgadp=0.165*adp;
adp3m=0.135*adp;
atp4m=0.05*atp;
topo=0.08+0.89*mgadp^2/kdd^2+0.16*mgadp/kdd;
bottomo=(1+mgadp/kdd)^2*(1+atp4m/ktt +adp3m/ktd);
katpo=topo/bottomo;

ikatp=gkatpbar*katpo*(v-vk);


%-----------------------------------------------------------------------
% Ca2+ fluxes across the plasma membrane (L- and R-type)
%-----------------------------------------------------------------------
alpha=5.18E-18;  vcyt=1.15E-12;     kpmca=0.2;

Jmem = -(alpha/vcyt*ica+kpmca*c);

%-------------------------------------
% Ca2+ fluxes into ER
%-------------------------------------
kserca=0.4; pleak=2.0E-4;
```

```
Jer=kserca*c - pleak*(cer-c);

%-------------------------------------
% Ca2+ fluxes into the mitochondria
%-------------------------------------
kuni=0.4; knaca=0.001;

Jm= kuni*c - knaca*(cam-c);

%%%%%%%%%%%%%%%%%%%%%%%%%%%%%%%%%%
%%        Metabolic Model       %%
%%%%%%%%%%%%%%%%%%%%%%%%%%%%%%%%%%
%-------------------------------------
% Glucokinase reaction rate
%-------------------------------------
Jgk=0.001;

%-------------------------------------
% PFK reaction rate; Jpfk
%-------------------------------------

amp=adp^2/atp;

%  Parameters
%  k1--Kd for AMP binding
%  k2--Kd for FBP binding
%  k3--Kd for F6P binding
%  k4--Kd for ATP binding

% alpha=1 -- AMP bound
% beta=1 -- FBP bound
% gamma=1 -- F6P bound
% delta=1 -- ATP bound

k1=30; k2=1; k3=50000; k4=1000;
famp=0.02; fatp=20; ffbp=0.2; fbt=20; fmt=20;
kpfk =0.06; vpfk=0.01;

% (alpha,beta,gamma,delta)
% (0,0,0,0)
weight1=1;
topa1=0;
bottom1=1;

% (0,0,0,1)
weight2=atp^2/k4;
topa2=topa1;
bottom2=bottom1+weight2;

% (0,0,1,0)
weight3=f6p^2/k3;
topa3=topa2+weight3;
bottom3=bottom2+weight3;

% (0,0,1,1)
weight4=(f6p*atp)^2/(fatp*k3*k4);
topa4=topa3+weight4;
bottom4=bottom3+weight4;
```

```
% (0,1,0,0)
weight5=fbp/k2;
topa5=topa4;
bottom5=bottom4+weight5;

% (0,1,0,1)
weight6=(fbp*atp^2)/(k2*k4*fbt);
topa6=topa5;
bottom6=bottom5+weight6;

% (0,1,1,0)
weight7=(fbp*f6p^2)/(k2*k3*ffbp);
topa7=topa6+weight7;
bottom7=bottom6+weight7;

% (0,1,1,1)
weight8=(fbp*f6p^2*atp^2)/(k2*k3*k4*ffbp*fbt*fatp);
topa8=topa7+weight8;
bottom8=bottom7+weight8;

% (1,0,0,0)
weight9=amp/k1;
topa9=topa8;
bottom9=bottom8+weight9;

% (1,0,0,1)
weight10=(amp*atp^2)/(k1*k4*fmt);
topa10=topa9;
bottom10=bottom9+weight10;

% (1,0,1,0)
weight11=(amp*f6p^2)/(k1*k3*famp);
topa11=topa10+weight11;
bottom11=bottom10+weight11;

% (1,0,1,1)
weight12=(amp*f6p^2*atp^2)/(k1*k3*k4*famp*fmt*fatp);
topa12=topa11+weight12;
bottom12=bottom11+weight12;

% (1,1,0,0)
weight13=(amp*fbp)/(k1*k2);
topa13=topa12;
bottom13=bottom12+weight13;

% (1,1,0,1)
weight14=(amp*fbp*atp^2)/(k1*k2*k4*fbt*fmt);
topa14=topa13;
bottom14=bottom13+weight14;

% (1,1,1,0) -- the most active state of the enzyme
weight15=(amp*fbp*f6p^2)/(k1*k2*k3*ffbp*famp);
topa15=topa14;
topb=weight15;
bottom15=bottom14+weight15;

% (1,1,1,1)
weight16=(amp*fbp*f6p^2*atp^2)/(k1*k2*k3*k4*ffbp*famp*fbt*fmt*fatp);
```

```
topa16=topa15+weight16;
bottom16=bottom15+weight16;

Jpfk= vpfk*(topb + kpfk*topa16)/bottom16;


%-------------------------------------
% PDH reaction rate; Jpdh
%-------------------------------------
kCaPDH=200; vpdh=param.vpdh;

sinfty= cam/(cam+kCaPDH);
Jpdh=vpdh*sinfty*sqrt(fbp);




%%%%%%%%%%%%%%%%%%%%%%%%%%%%%%%%%
%%       The vector fields      %%
%%%%%%%%%%%%%%%%%%%%%%%%%%%%%%%%%

%-----------------------------------------------------------------------
% The vector field (Electrical and Calcium Model)
%-----------------------------------------------------------------------
Cm=5300 ;   fca=0.01;   sigmam=100; sigmaer=31;

vf(1)=-(ica + ik + ikca + ikatp)/Cm;                              % V
vf(2)=-(n-ninf)/taun;                                             % n
vf(3)= fca*(Jmem - Jm - Jer);                                     % c
vf(4)=fca*sigmaer*Jer;                                            % cer
vf(5)=fca*sigmam*Jm;                                              % cam


%-----------------------------------------------------------------------
% The vector field (Metabolic Model)
%-----------------------------------------------------------------------
taua= 300000;

vf(6)=(atp-exp((1+2.2*Jpdh/(Jpdh+0.05))*(1-c/0.35))*adp)/taua;   % adp
vf(7)=0.3*(Jgk-Jpfk);                                             % f6p
vf(8)=(Jpfk-Jpdh/2);                                              % fbp

end
```

D.2 The IOM2.0

```
% Variables:
%    v -- cellular membrane potential (mV)
%    n -- activation of delayed rectifier
%    c -- free cytosolic calcium concentration (muM)
%    adp -- cytosolic ADP concentration (muM)
%    cer -- concentration of free calcium in the endoplasmic reticulum (muM)
%    cam -- mitocondrial calcium concentration (muM)
%    f6p -- fructose 6-phosphate concentration (muM)
%    fbp -- fructose 1,6-bisphosphate concentration (muM)
%    adpm -- mitocondrial ADP concentration (muM)
%    nadhm -- mitocondrial NADH concentration (muM)
```

```
%    psim -- mitocondrial membrane potential (mV)


% Units:
% time: ms
% volume: l
% conductance: pS
% V: mV
% I: fA
% J: muM/ms
% alpha: mumol/fA/ms

function vf = IOM2_vf(t,x,param)

vf = zeros(11,1);

v = x(1);
n = x(2);
c = x(3);
cer = x(4);
cam = x(5);
adp = x(6);
f6p = x(7);
fbp = x(8);
adpm = x(9);
nadhm = x(10);
psim = x(11);

%%%%%%%%%%%%%%%%%%%%%%%%%%%%%%%%
%% Electrical and Calcium Model %%
%%%%%%%%%%%%%%%%%%%%%%%%%%%%%%%%

%-------------------------------------
% Ca2+ current; ica
%-------------------------------------
gca = 1000; vca = 25;
nim = -20; sm = 12;

minf = 1/(1+exp((nim-v)/sm));
ica=gca*minf*(v-vca);


%-------------------------------------
% Delayed-rectifying K+ current; ik
%-------------------------------------
gk=2700; vk=-75;
taun=20;    nin=-16; sn=5;

ninf=1/(1+exp((nin-v)/sn));
ik=gk*n*(v-vk);

%-------------------------------------
%  Ca2+-activated K+ current; ikca
%-------------------------------------
kd=0.5; gkca=param.gkca;

qinf=c^2/(kd^2+c^2);
ikca=-gkca*qinf*(vk-v);
```

```
%-------------------------------------
% K-atp channel current; ikatp
%-------------------------------------
kdd=17; ktd=26; ktt=1;  atot=3000;
gkatpbar=19700;

rad=sqrt(-4*adp^2+(atot-adp)^2);
atp=(atot+rad-adp)/2;
mgadp=0.165*adp;
adp3m=0.135*adp;
atp4m=0.05*atp;
topo=0.08+0.89*mgadp^2/kdd^2+0.16*mgadp/kdd;
bottomo=(1+mgadp/kdd)^2*(1+atp4m/ktt +adp3m/ktd);
katpo=topo/bottomo;

ikatp=gkatpbar*katpo*(v-vk);

%-------------------------------------------------------------------------
% Ca2+ fluxes across the plasma membrane
%-------------------------------------------------------------------------
alpha=5.18E-18;  vcyt=1.15E-12;    kpmca=0.2;

Jmem=-(alpha/vcyt*ica + kpmca*c);

%-------------------------------------
% Ca2+ fluxes into ER
%-------------------------------------
kserca=0.4; pleak=2.0E-4;

Jer=kserca*c - pleak*(cer-c);

%-------------------------------------
% Ca2+ fluxes into the mitochondria
%-------------------------------------
p21=0.013;  p22=1.6; p23=0.0015; p24=0.016;

Juni=(p21*psim-p22)*c^2;
JNaCa=p23*(cam-c)*exp(p24*psim);

Jm=Juni-JNaCa;

%%%%%%%%%%%%%%%%%%%%%%%%%%%%%%%%
%%        Metabolic Model       %%
%%%%%%%%%%%%%%%%%%%%%%%%%%%%%%%%

%-------------------------------------
% Glucokinase reaction rate
%-------------------------------------
Jgk=0.001;

%-------------------------------------
% PFK reaction rate; Jpfk
%-------------------------------------

amp=adp^2/atp;

%  Parameters
%  k1--Kd for AMP binding
%  k2--Kd for FBP binding
```

```
%  k3--Kd for F6P binding
%  k4--Kd for atp binding

% alpha=1 -- AMP bound
% beta=1 -- FBP bound
% gamma=1 -- F6P bound
% delta=1 -- atp bound

k1=30; k2=1; k3=50000; k4=1000;
famp=0.02; fatp=20; ffbp=0.2; fbt=20; fmt=20;
kpfk =0.06; vpfk=0.01;

% (alpha,beta,gamma,delta)
% (0,0,0,0)
weight1=1;
topa1=0;
bottom1=1;

% (0,0,0,1)
weight2=atp^2/k4;
topa2=topa1;
bottom2=bottom1+weight2;

% (0,0,1,0)
weight3=f6p^2/k3;
topa3=topa2+weight3;
bottom3=bottom2+weight3;

% (0,0,1,1)
weight4=(f6p*atp)^2/(fatp*k3*k4);
topa4=topa3+weight4;
bottom4=bottom3+weight4;

% (0,1,0,0)
weight5=fbp/k2;
topa5=topa4;
bottom5=bottom4+weight5;

% (0,1,0,1)
weight6=(fbp*atp^2)/(k2*k4*fbt);
topa6=topa5;
bottom6=bottom5+weight6;

% (0,1,1,0)
weight7=(fbp*f6p^2)/(k2*k3*ffbp);
topa7=topa6+weight7;
bottom7=bottom6+weight7;

% (0,1,1,1)
weight8=(fbp*f6p^2*atp^2)/(k2*k3*k4*ffbp*fbt*fatp);
topa8=topa7+weight8;
bottom8=bottom7+weight8;

% (1,0,0,0)
weight9=amp/k1;
topa9=topa8;
bottom9=bottom8+weight9;

% (1,0,0,1)
```

```
weight10=(amp*atp^2)/(k1*k4*fmt);
topa10=topa9;
bottom10=bottom9+weight10;

% (1,0,1,0)
weight11=(amp*f6p^2)/(k1*k3*famp);
topa11=topa10+weight11;
bottom11=bottom10+weight11;

% (1,0,1,1)
weight12=(amp*f6p^2*atp^2)/(k1*k3*k4*famp*fmt*fatp);
topa12=topa11+weight12;
bottom12=bottom11+weight12;

% (1,1,0,0)
weight13=(amp*fbp)/(k1*k2);
topa13=topa12;
bottom13=bottom12+weight13;

% (1,1,0,1)
weight14=(amp*fbp*atp^2)/(k1*k2*k4*fbt*fmt);
topa14=topa13;
bottom14=bottom13+weight14;

% (1,1,1,0) -- the most active state of the enzyme
weight15=(amp*fbp*f6p^2)/(k1*k2*k3*ffbp*famp);
topa15=topa14;
topb=weight15;
bottom15=bottom14+weight15;

% (1,1,1,1)
weight16=(amp*fbp*f6p^2*atp^2)/(k1*k2*k3*k4*ffbp*famp*fbt*fmt*fatp);
topa16=topa15+weight16;
bottom16=bottom15+weight16;

Jpfk= vpfk*(topb + kpfk*topa16)/bottom16;

%-------------------------------------
% PDH reaction rate; Jgpdh
%-------------------------------------
kCaPDH=1.5;

sinfty= cam/(cam+kCaPDH);
Jgpdh=sinfty*sqrt(fbp);


%-------------------------------------
% Adenine nucleotide translocator, Jant
%-------------------------------------
amtot=15000;  p19=0.6; p20=2;   FRT=.037;

atpm = amtot-adpm;
Jant = p19/(1+p20*adpm/atpm)*exp(FRT/2* psim);

%-------------------------------------
% Hydrolysis, Jhyd
%-------------------------------------
khyd=1.8640e-06; khydbas=6.4800e-07;
```

```
Jhyd = (khyd*c+khydbas)*atp;

%%%%%%%%%%%%%%%%%%%%%%%%%%%%%%%%%
%%      Mitochondria Model      %%
%%%%%%%%%%%%%%%%%%%%%%%%%%%%%%%%%
%-------------------------------------------------------------------------
% Phosphorylation. In uM/ms.
%-------------------------------------------------------------------------
p13=10000;  p14=190;    p15=8.5; p16=4;

b2=(p16*p13)/(p13+atpm);
JF1F0=b2/(1+exp((p14-psim)/p15));

%-------------------------------------------------------------------------
% Respiration (uM/ms)
%-------------------------------------------------------------------------
p4=5.28; p5=250; p6=165; p7=5;

JO=p4*nadhm/(p5+nadhm)/(1+exp((psim-p6)/p7));


%-------------------------------------------------------------------------
% Pyruvate dehydrogenase (PDH) (uM/ms)
%-------------------------------------------------------------------------
nadmtot=10000;
nadm=nadmtot-nadhm;

vpdh=param.vpdh;    KNADHmPDH=1.3;

Jpdh=vpdh*Jgpdh/(KNADHmPDH+nadhm/nadm);

%-------------------------------------------------------------------------
% Other dehydrogenase (DH) (uM/ms)
%-------------------------------------------------------------------------
vdh=1.1;   kCaDH=0.08;   KNADHmDH=1.3;

Jdh = vdh*cam/(cam+kCaDH)/(KNADHmDH+nadhm/nadm);

%-------------------------------------------------------------------------
% H+ leakage through mitochondrial inner membrane (uM/ms)
%-------------------------------------------------------------------------
p17=0.0014; p18=0.02;

JHleak=p17*psim-p18;

%-------------------------------------------------------------------------
% Proton pumping due to respiration  (uM/ms)
%-------------------------------------------------------------------------
p8=7.4; p9=100; p10=165; p11=5;

JHres=p8*nadhm/(p9+nadhm)/(1+exp((psim-p10)/p11));

%-------------------------------------------------------------------------
% Proton flux due to atpase (uM/ms)
%-------------------------------------------------------------------------
JHatp=3*JF1F0;


%%%%%%%%%%%%%%%%%%%%%%%%%%%%%%%%%
```

```
%%       The vector fields      %%
%%%%%%%%%%%%%%%%%%%%%%%%%%%%%%%%
%-----------------------------------------------------------------------
% The vector field (Electrical and Calcium Model)
%-----------------------------------------------------------------------
Cm=5300;   fca=0.01;    sigmam=290;     sigmaer=31;

vf(1)= -(ica + ik + ikca + ikatp)/Cm;                  % V
vf(2)= -(n-ninf)/taun;                                 % n
vf(3)= fca*(Jmem -  Jm/sigmam - Jer);                  % c
vf(4)= fca*sigmaer*Jer;                                % cer
vf(5)= fca*Jm;                                         % cam

%-----------------------------------------------------------------------
% The vector field (Metabolic Model)
%-----------------------------------------------------------------------

vf(6)=Jhyd - Jant/sigmam;                              % adp
vf(7)=0.3*(Jgk-Jpfk);                                  % f6p
vf(8)=(Jpfk-Jpdh/sigmam/2);                            % fbp

%-----------------------------------------------------------------------
% The vector field (Mitochondria Model)
%-----------------------------------------------------------------------
Cmito=180;

vf(9) = Jant-JF1F0;                                    %adpm
vf(10) = Jpdh + Jdh -J0;                               %nadhm
vf(11) = (JHres-JHatp-Jant-JHleak-JNaCa-2*Juni)/Cmito;  %psim

end
```

D.3 The IOM2.2

```
% Variables:
%    v -- cellular membrane potential (mV)
%    n -- activation of delayed rectifier
%    c -- free cytosolic calcium concentration (muM)
%    adp -- cytosolic ADP concentration (muM)
%    cmd -- concentration of free calcium in the micro-domain (muM)
%    cer -- concentration of free calcium in the endoplasmic reticulum (muM)
%    cam -- mitocondrial calcium concentration (muM)
%    f6p -- fructose 6-phosphate concentration (muM)
%    fbp -- fructose 1,6-bisphosphate concentration (muM)
%    adpm -- mitocondrial ADP concentration (muM)
%    nadhm -- mitocondrial NADH concentration (muM)
%    psim -- mitocondrial membrane potential (mV)
%    N1 -- number of primed granules bound to the micro-domain
%    N2 -- number of granules with 1 Ca2+ ion bounded
%    N3 -- number of granules with 3 Ca2+ ion bounded
%    N4 -- number of granules with 1 Ca2+ ion bounded
%    N5 -- number of primed granules outside the micro-domain
%    N6 -- number of docked insulin-containing granules not yet primed for the fusion
%    NF -- number of granules fused with the plasma membran
%    NR -- number of granules containing insulin in a "releasable" state
%    SE -- number of secreted insulin-containing granules per beta-cell
```

```
% Units:
% time: ms
% volume: l
% conductance: pS
% V: mV
% I: fA
% J: muM/ms
% alpha: mumol/fA/ms

function vf = IOM22_vf(t,x,param)

vf = zeros(21,1);

v = x(1);
n = x(2);
c = x(3);
cer = x(4);
cam = x(5);
cmd = x(6);
adp = x(7);
f6p = x(8);
fbp = x(9);
adpm = x(10);
nadhm = x(11);
psim = x(12);

N1 = x(13);
N2 = x(14);
N3 = x(15);
N4 = x(16);
N5 = x(17);
N6 = x(18);
NF = x(19);
NR = x(20);
SE = x(21);


%%%%%%%%%%%%%%%%%%%%%%%%%%%%%%%%
%% Electrical and Calcium Model %%
%%%%%%%%%%%%%%%%%%%%%%%%%%%%%%%%

%-------------------------------------
% Ca2+ current; ica
%-------------------------------------
gca = 1000; vca = 25;
nim = -20; sm = 12;

minf = 1/(1+exp((nim-v)/sm));
ica=gca*minf*(v-vca);

%-------------------------------------
% Delayed-rectifying K+ current; ik
%-------------------------------------
gk=2700; vk=-75;
taun=20; nin=-16; sn=5;

ninf=1/(1+exp((nin-v)/sn));
```

```
ik=gk*n*(v-vk);

%-------------------------------------
%  Ca2+-activated K+ current; ikca
%-------------------------------------
kd=0.5;     gkca=param.gkca;

qinf=c^2/(kd^2+c^2);
ikca=-gkca*qinf*(vk-v);

%-------------------------------------
% K-atp channel current; ikatp
%-------------------------------------
kdd=17; ktd=26; ktt=1;  atot=3000;
gkatpbar=19600;

rad=sqrt(-4*adp^2+(atot-adp)^2);
atp=(atot+rad-adp)/2;
mgadp=0.165*adp;
adp3m=0.135*adp;
atp4m=0.05*atp;
topo=0.08+0.89*mgadp^2/kdd^2+0.16*mgadp/kdd;
bottomo=(1+mgadp/kdd)^2*(1+atp4m/ktt +adp3m/ktd);
katpo=topo/bottomo;

ikatp=gkatpbar*katpo*(v-vk);

%-----------------------------------------------------------------------
% Ca2+ fluxes across the plasma membrane (L- and R-type)
%-----------------------------------------------------------------------
alpha=5.18E-18;  vcyt=1.15E-12; vmd=4.2E-15;
raL = 0.5;  kpmca=0.2; B=10;

icaL = raL*ica;
icaR = (1-raL)*ica;

JL = icaL*alpha/vmd;
JR = icaR*alpha/vcyt;

vmdcyt = vmd/vcyt;
Jmem = -(JR+vmdcyt*B*(c-cmd)+kpmca*c);

%-------------------------------------
% Ca2+ fluxes into ER
%-------------------------------------
kserca=0.4; pleak=2.0E-4;

Jer=kserca*c - pleak*(cer-c);

%-------------------------------------
% Ca2+ fluxes into the mitochondria
%-------------------------------------
p21=0.013;  p22=1.6; p23=0.0015; p24=0.016;

Juni=(p21*psim-p22)*c^2;
JNaCa=p23*(cam-c)*exp(p24*psim);
Jm=Juni-JNaCa;

%%%%%%%%%%%%%%%%%%%%%%%%%%%%%%%%%
```

```
%%        Metabolic Model       %%
%%%%%%%%%%%%%%%%%%%%%%%%%%%%%%%%%
Ge=11e3;

%-------------------------------------
% Glucokinase reaction rate
%-------------------------------------
Vgk=0.0037; Kgk=19e3;

Jgk=Vgk./(1.+(Kgk./Ge).^2);

%-------------------------------------
% PFK reaction rate; Jpfk
%-------------------------------------
amp=adp^2/atp;

%  Parameters
%  k1--Kd for AMP binding
%  k2--Kd for FBP binding
%  k3--Kd for F6P binding
%  k4--Kd for atp binding
% alpha=1 -- AMP bound
% beta=1 -- FBP bound
% gamma=1 -- F6P bound
% delta=1 -- atp bound

k1=30; k2=1; k3=50000; k4=1000;
famp=0.02; fatp=20; ffbp=0.2; fbt=20; fmt=20;
kpfk =0.06; vpfk=0.01;

% (alpha,beta,gamma,delta)
% (0,0,0,0)
weight1=1;
topa1=0;
bottom1=1;

% (0,0,0,1)
weight2=atp^2/k4;
topa2=topa1;
bottom2=bottom1+weight2;

% (0,0,1,0)
weight3=f6p^2/k3;
topa3=topa2+weight3;
bottom3=bottom2+weight3;

% (0,0,1,1)
weight4=(f6p*atp)^2/(fatp*k3*k4);
topa4=topa3+weight4;
bottom4=bottom3+weight4;

% (0,1,0,0)
weight5=fbp/k2;
topa5=topa4;
bottom5=bottom4+weight5;

% (0,1,0,1)
weight6=(fbp*atp^2)/(k2*k4*fbt);
topa6=topa5;
```

```
bottom6=bottom5+weight6;

% (0,1,1,0)
weight7=(fbp*f6p^2)/(k2*k3*ffbp);
topa7=topa6+weight7;
bottom7=bottom6+weight7;

% (0,1,1,1)
weight8=(fbp*f6p^2*atp^2)/(k2*k3*k4*ffbp*fbt*fatp);
topa8=topa7+weight8;
bottom8=bottom7+weight8;

% (1,0,0,0)
weight9=amp/k1;
topa9=topa8;
bottom9=bottom8+weight9;

% (1,0,0,1)
weight10=(amp*atp^2)/(k1*k4*fmt);
topa10=topa9;
bottom10=bottom9+weight10;

% (1,0,1,0)
weight11=(amp*f6p^2)/(k1*k3*famp);
topa11=topa10+weight11;
bottom11=bottom10+weight11;

% (1,0,1,1)
weight12=(amp*f6p^2*atp^2)/(k1*k3*k4*famp*fmt*fatp);
topa12=topa11+weight12;
bottom12=bottom11+weight12;

% (1,1,0,0)
weight13=(amp*fbp)/(k1*k2);
topa13=topa12;
bottom13=bottom12+weight13;

% (1,1,0,1)
weight14=(amp*fbp*atp^2)/(k1*k2*k4*fbt*fmt);
topa14=topa13;
bottom14=bottom13+weight14;

% (1,1,1,0) -- the most active state of the enzyme
weight15=(amp*fbp*f6p^2)/(k1*k2*k3*ffbp*famp);
topa15=topa14;
topb=weight15;
bottom15=bottom14+weight15;

% (1,1,1,1)
weight16=(amp*fbp*f6p^2*atp^2)/(k1*k2*k3*k4*ffbp*famp*fbt*fmt*fatp);
topa16=topa15+weight16;
bottom16=bottom15+weight16;

Jpfk= vpfk*(topb + kpfk*topa16)/bottom16;

%-----------------------------------
% PDH reaction rate; Jgpdh
%-----------------------------------
kCaPDH=1.5;
```

```
sinfty= cam/(cam+kCaPDH);
Jgpdh=sinfty*sqrt(fbp);

%-------------------------------------
% Adenine nucleotide translocator, Jant
%-------------------------------------
amtot=15000;  p19=0.6; p20=2;   FRT=.037;

atpm = amtot-adpm;
Jant = p19/(1+p20*adpm/atpm)*exp(FRT/2* psim);

%-------------------------------------
% Hydrolysis, Jhyd
%-------------------------------------
khyd=1.8640e-06; khydbas=6.4800e-07;

Jhyd = (khyd*c+khydbas)*atp;




%%%%%%%%%%%%%%%%%%%%%%%%%%%%%%%%%
%%      Mitochondria Model      %%
%%%%%%%%%%%%%%%%%%%%%%%%%%%%%%%%%

%----------------------------------------------------------------------
% Phosphorylation. In uM/ms.
%----------------------------------------------------------------------
p13=10000;  p14=190;    p15=8.5; p16=4;

b2=(p16*p13)/(p13+atpm);
JF1F0=b2/(1+exp((p14-psim)/p15));

%----------------------------------------------------------------------
% Respiration (uM/ms)
%----------------------------------------------------------------------
p4=5.28; p5=250; p6=165; p7=5;

J0=p4*nadhm/(p5+nadhm)/(1+exp((psim-p6)/p7));

%----------------------------------------------------------------------
% Pyruvate dehydrogenase (PDH) (uM/ms)
%----------------------------------------------------------------------
nadmtot=10000;
nadm=nadmtot-nadhm;

vpdh=param.vpdh;    KNADHmPDH=1.3;

Jpdh=vpdh*Jgpdh/(KNADHmPDH+nadhm/nadm);

%----------------------------------------------------------------------
% Other dehydrogenase (DH) (uM/ms)
%----------------------------------------------------------------------
vdh=1.1;   kCaDH=0.08;   KNADHmDH=1.3;

Jdh = vdh*cam/(cam+kCaDH)/(KNADHmDH+nadhm/nadm);

%----------------------------------------------------------------------
```

```
% H+ leakage through mitochondrial inner membrane (uM/ms)
%-------------------------------------------------------------------
p17=0.0014; p18=0.02;

JHleak=p17*psim-p18;

%-------------------------------------------------------------------
% Proton pumping due to respiration  (uM/ms)
%-------------------------------------------------------------------
p8=7.4; p9=100; p10=165; p11=5;

JHres=p8*nadhm/(p9+nadhm)/(1+exp((psim-p10)/p11));

%-------------------------------------------------------------------
% Proton flux due to atpase (uM/ms)
%-------------------------------------------------------------------
JHatp=3*JF1F0;


%%%%%%%%%%%%%%%%%%%%%%%%%%%%%%%%%
%%       Insulin Model           %%
%%%%%%%%%%%%%%%%%%%%%%%%%%%%%%%%%
%-------------------------------------
% Resupply and the priming steps
%-------------------------------------
Fct =10;    Kjo=0.15;
bas_r3=3.2e-05; r30=0.001205;
r20=6e-6; Kp=0.15;
cmdbas=0.001; cmdmax=0.1; kcmd=0.1;

r2 = r20*c/(c + Kp);
AmpFct=Fct*JO^2/(JO^2+Kjo^2);
r3 = bas_r3 + AmpFct*r30*c/(c + Kp);
mod_cmd= cmdbas + cmdmax*cmd^4/(cmd^4+kcmd^4);


%%%%%%%%%%%%%%%%%%%%%%%%%%%%%%%%%
%%       The vector fields      %%
%%%%%%%%%%%%%%%%%%%%%%%%%%%%%%%%%

%-------------------------------------------------------------------
% The vector field (Electrical and Calcium Model)
%-------------------------------------------------------------------
Cm=5300;   fca=0.01;    sigmam=290;    sigmaer=31;

vf(1)= -(ica + ik + ikca + ikatp)/Cm;                  % V
vf(2)= -(n-ninf)/taun;                                 % n
vf(3)= fca*(Jmem -  Jm/sigmam - Jer);                  % c
vf(4)= fca*sigmaer*Jer;                                % cer
vf(5)= fca*Jm;                                         % cam
vf(6)= fca*(-JL+B*(c-cmd));                            % cmd


%-------------------------------------------------------------------
% The vector field (Metabolic Model)
%-------------------------------------------------------------------
vf(7)=Jhyd - Jant/sigmam;                               % adp
vf(8)=0.3*(Jgk-Jpfk);                                   % f6p
vf(9)=(Jpfk-Jpdh/sigmam/2);                             % fbp
```

```
%-----------------------------------------------------------------------
% The vector field (Mitochondria Model)
%-----------------------------------------------------------------------
Cmito=180;

vf(10) = Jant-JF1F0;                                    %adpm
vf(11) = Jpdh + Jdh -JO;                                %nadhm
vf(12) = (JHres-JHatp-Jant-JHleak-JNaCa-2*Juni)/Cmito;  %psim


%-----------------------------------------------------------------------
% The vector field (Insulin Model)
%-----------------------------------------------------------------------
h1=0.02; hm1=0.1; r1=0.0006; rm1=0.001;
u1=2; rm2=1e-6; rm3=1e-7;
u2=0.003; u3=2e-5;

vf(13) = -(3*h1*mod_cmd + rm1)*N1 + hm1*N2 + r1*N5;               % N1
vf(14) = 3*h1*mod_cmd*N1 -(2*h1*mod_cmd + hm1)*N2 + 2*hm1*N3;     % N2
vf(15) = 2*h1*mod_cmd*N2 -(h1*mod_cmd + 2*hm1)*N3 + 3*hm1*N4;     % N3
vf(16) = h1*mod_cmd*N3 - (3*hm1 + u1)*N4;                         % N4
vf(17) = rm1*N1 - (r1 + rm2)*N5 + r2*N6;                          % N5
vf(18) = r3 + rm2*N5 - (rm3 + r2)*N6 ;                            % N6
vf(19) = u1*N4 - u2*NF;                                           % NF
vf(20) = u2*NF - u3*NR;                                           % NR
vf(21) = u3*NR;                                                   % SE

end
```

Bibliography

[1] F. M. Ashcroft, D .E. Harrison, and S. J. Ashcroft. “Glucose induces closure of single potassium channels in isolated rat pancreatic β-cells”. In: *Nature* 312.5993 (1984), pp. 446–8 (cit. on p. 15).

[2] K. Ashizawa, M. C. Willingham, C. M. Liang, and S. Y. Cheng. “In vivo regulation of monomer-tetramer conversion of pyruvate kinase subtype M2 by glucose is mediated via fructose 1,6-bisphosphate”. In: *Journal of Biological Chemistry* 266.25 (1991), pp. 16842–6 (cit. on p. 35).

[3] American Diabetes Association. “Standards of Medical Care in Diabetes—2019 Abridged for Primary Care Providers”. In: *Clinical Diabetes* 37.1 (2019), pp. 11–34 (cit. on p. 10).

[4] I. Atwater, C. M. Dawson, A. Scott, G. Eddlestone, and E. Rojas. “The nature of the oscillatory behaviour in electrical activity from pancreatic β-cell”. In: *Hormone and Metabolic Research* Suppl 10 (1980), pp. 100–7 (cit. on p. 14).

[5] S. Barg, L. Eliasson, E. Renström, and P. Rorsman. “A subset of 50 secretory granules in close contact with L-type Ca^{2+} channels accounts for first-phase insulin secretion in mouse β-cells”. In: *Diabetes* 51 Suppl 1 (2002), S74–82 (cit. on p. 112).

[6] R. K. P. Benninger, W. S. Head, M. Zhang, L. S. Satin, and D. W. Piston. “Gap junctions and other mechanisms of cell-cell communication regulate basal insulin secretion in the pancreatic islet”. In: *Journal of Physiology* 589.22 (2011), pp. 5453–5466 (cit. on p. 121).

[7] J. Berg, Y. P. Hung, and G. Yellen. “A genetically encoded fluorescent reporter of ATP:ADP ratio”. In: *Nature Methods* 6.2 (2009), pp. 161–166 (cit. on p. 35).

[8] P. Bergsten. “Glucose-induced pulsatile insulin release from single islets at stable and oscillatory cytoplasmic Ca^{2+}”. In: *American Journal of Physiology* 274.5 (1998), E796–E800 (cit. on pp. 118, 119).

[9] R. Bertram and J. E. Rubin. “Multi-timescale systems and fast-slow analysis”. In: *Mathematical Biosciences* 287 (2017), pp. 105–121 (cit. on p. 105).

[10] R. Bertram and A. Sherman. “A calcium-based phantom bursting model for pancreatic islets”. In: *Bulletin of Mathematical Biology* 66.5 (2004), pp. 1313–1344 (cit. on pp. xvi, 2, 16, 22–24, 26, 39, 47, 109).

[11] R. Bertram and A. Sherman. “Filtering of calcium transients by the endoplasmic reticulum in pancreatic β-cells”. In: *Biophysical Journal* 87.6 (2004), pp. 3775–85 (cit. on p. 22).

[12] R. Bertram, J. Rhoads, and W. P. Cimbora. “A phantom bursting mechanism for episodic bursting”. In: *Bulletin of Mathematical Biology* 70.7 (2008), pp. 1979–1993 (cit. on p. 55).

[13] R. Bertram, P. Smolen, A. Sherman, et al. “A role for calcium release-activated current (CRAC) in cholinergic modulation of electrical activity in pancreatic β-cells”. In: *Biophysical Journal* 68.6 (1995), pp. 2323–32 (cit. on p. 22).

[14] R. Bertram, M. Gram Pedersen, D. S. Luciani, and A. Sherman. “A simplified model for mitochondrial ATP production”. In: *Journal of Theoretical Biology* 243.4 (2006), pp. 575–586 (cit. on p. 31).

[15] R. Bertram, L. Satin, M. Zhang, P. Smolen, and A. Sherman. “Calcium and glycolysis mediate multiple bursting modes in pancreatic islets”. In: *Biophysical Journal* 87.5 (2004), pp. 3074–3087 (cit. on pp. xvi, 2, 24, 26, 29, 31).

[16] R. Bertram, L. S. Satin, and A. S. Sherman. “Closing in on the mechanisms of pulsatile insulin secretion”. In: *Diabetes* 67.3 (2018), pp. 351–359 (cit. on pp. 9, 38, 46).

[17] R. Bertram, L. S. Satin, M. G. Pedersen, D. S. Luciani, and A. Sherman. “Interaction of glycolysis and mitochondrial respiration in metabolic oscillations of pancreatic islets”. In: *Biophysical Journal* 92.5 (2007), pp. 1544–1555 (cit. on pp. xvi, 2, 24, 31, 34, 39, 60, 74, 77).

[18] R Bertram, A Sherman, and L S Satin. “Metabolic and electrical oscillations: Partners in controlling pulsatile insulin secretion”. In: *American Journal of Physiology* 293.4 (2007), E890–E900 (cit. on p. 60).

[19] R. Bertram, J. Previte, A. Sherman, T. A. Kinard, and L. S. Satin. “The phantom burster model for pancreatic β-cells”. In: *Biophysical Journal* 79.5 (2000), pp. 2880–2892 (cit. on p. 22).

[20] L. Boscá, J. J. Aragón, and A. Sols. “Specific activation by fructose 2,6-bisphosphate and inhibition by P-enolpyruvate of ascites tumor phosphofructokinase.” In: *Biochemical and Biophysical Research Communications* 106.2 (1982), pp. 486–91 (cit. on p. 61).

[21] O. Cabrera, D. M. Berman, N. S. Kenyon, et al. “The unique cytoarchitecture of human pancreatic islets has implications for islet cell function”. In: *Proceedings of the National Academy of Sciences* 103.7 (2006), pp. 2334–2339 (cit. on p. 7).

[22] C. Y. Cha, Y. Nakamura, Y. Himeno, et al. “Ionic mechanisms and Ca^{2+} dynamics underlying the glucose response of pancreatic β cells: A simulation study”. In: *The Journal of General Physiology* 138.1 (2011), pp. 21–37 (cit. on pp. xvi, 2, 16, 19–21, 39, 107, 109, 147, 156).

[23] T. R. Chay. “Effects of extracellular calcium on electrical bursting and intracellular and luminal calcium oscillations in insulin secreting pancreatic β-cells”. In: *Biophysical Journal* 73.3 (1997), pp. 1673–1688 (cit. on pp. 15, 37).

[24] T. R. Chay. “Electrical bursting and luminal calcium oscillation in excitable cell models.” In: *Biological Cybernetics* 75.5 (1996), pp. 419–31 (cit. on pp. 15, 37).

[25] T. R. Chay and D. L. Cook. “Endogenous bursting patterns in excitable cells”. In: *Mathematical Biosciences* 90.1-2 (1988), pp. 139–153 (cit. on pp. 15, 37).

[26] T. R. Chay and J. Keizer. “Minimal model for membrane oscillations in the pancreatic β-cell”. In: *Biophysical Journal* 42.2 (1983), pp. 181–189 (cit. on pp. xvi, 2, 14, 23, 37, 39, 102).

[27] Y.-D. Chen, S. Wang, and A. Sherman. “Identifying the targets of the amplifying pathway for insulin secretion in pancreatic β-cells by kinetic modeling of granule exocytosis”. In: *Biophysical Journal* 95.5 (2008), pp. 2226–2241 (cit. on p. 114).

[28] D. L. Cook. “Isolated islets of Langerhans have slow oscillations of electrical activity”. In: *Metabolism* 32.7 (1983), pp. 681–685 (cit. on p. 15).

[29] G. Da Silva Xavier. “The Cells of the Islets of Langerhans”. In: *Journal of Clinical Medicine* 7.3 (2018), p. 54 (cit. on pp. 6, 7).

[30] G. M. Dahlgren, L. M. Kauri, and R. T. Kennedy. “Substrate effects on oscillations in metabolism, calcium and secretion in single mouse islets of Langerhans”. In: *Biochimica et Biophysica Acta* 1724.1-2 (2005), pp. 23–36 (cit. on pp. 86, 87).

[31] P. Detimary, P. Gilon, and J. C. Henquin. “Interplay between cytoplasmic Ca^{2+} and the ATP/ADP ratio: a feedback control mechanism in mouse pancreatic islets.” In: *The Biochemical Journal* 333 (1998), pp. 269–74 (cit. on pp. xvi, 2, 15, 37, 39, 86).

[32] F. Diederichs. “Mathematical simulation of membrane processes and metabolic fluxes of the pancreatic β-cell.” In: *Bulletin of Mathematical Biology* 68.7 (2006), pp. 1779–818 (cit. on pp. 2, 16, 39).

[33] M. Düfer, D. Haspel, P. Krippeit-Drews, et al. “Oscillations of membrane potential and cytosolic Ca2+ concentration in SUR1(-/-) beta cells”. In: *Diabetologia* 47.3 (2004), pp. 488–498 (cit. on p. 72).

[34] G. A. Dunaway, T. P. Kasten, T. Sebo, and R. Trapp. “Analysis of the phosphofructokinase subunits and isoenzymes in human tissues”. In: *The Biochemical Journal* 251.3 (1988), pp. 677–83 (cit. on p. 61).

[35] L. G. Foe and R. G. Kemp. “Isolation and characterization of phosphofructokinase C from rabbit brain”. In: *The Journal of Biological Chemistry* 260.2 (1985), pp. 726–30 (cit. on p. 61).

[36] L. E. Fridlyand, L. Ma, and L. H. Philipson. “Adenine nucleotide regulation in pancreatic β-cells: modeling of ATP/ADP-Ca^{2+} interactions.” In: *American Journal of Physiology* 289.5 (2005), E839–48 (cit. on pp. 16, 17, 19, 102, 107, 109, 145, 147).

[37] L. E. Fridlyand, N. Tamarina, and L. H Philipson. “Modeling of Ca^{2+} flux in pancreatic β-cells: Role of the plasma membrane and intracellular stores”. In: *American Journal of Physiology* 285.1 (2003), E138–E154 (cit. on pp. xvi, 2, 16, 17, 39, 102, 141, 145, 146).

[38] D. Gall and I. Susa. “Effect of Na/Ca exchange on plateau fraction and $[Ca]_i$ in models for bursting in pancreatic β-cells.” In: *Biophysical Journal* 77.1 (1999), pp. 45–53 (cit. on pp. xvi, 2, 15).

[39] E. Heart and P. J. S. Smith. “Rhythm of the β-cell oscillator is not governed by a single regulator: multiple systems contribute to oscillatory behavior”. In: *American Journal of Physiology* 292.5 (2007), E1295–E1300 (cit. on pp. 86, 87).

[40] J. C. Henquin, H. P. Meissner, and W. Schmeer. “Cyclic variations of glucose-induced electrical activity in pancreatic β cells”. In: *Pflügers Archiv European Journal of Physiology* 393.4 (1982), pp. 322–327 (cit. on p. 15).

[41] A. L. Hodgkin and A. F. Huxley. “A quantitative description of membrane current and its application to conduction and excitation in nerve”. In: *The Journal of Physiology* 117.4 (1952), pp. 500–44 (cit. on p. 14).

[42] A. L. Hodgkin and A. F. Huxley. “Propagation of electrical signals along giant nerve fibers”. In: *Proceedings of the Royal Society of London. Series B, Biological sciences* 140.899 (1952), pp. 177–83 (cit. on p. 14).

[43] C. Ionescu-Tirgoviste, P. A. Gagniuc, E. Gubceac, et al. “A 3D map of the islet routes throughout the healthy human pancreas”. In: *Scientific Reports* 5.1 (2015), p. 14634 (cit. on p. 6).

[44] X. Jing, D. Q. Li, C. S. Olofsson, et al. “Cav2.3 calcium channels control second-phase insulin release”. In: *Journal of Clinical Investigation* 115.1 (2005), pp. 146–154 (cit. on p. 112).

[45] J. Keizer and G. Magnus. “ATP-sensitive potassium channel and bursting in the pancreatic beta cell. A theoretical study”. In: *Biophysical Journal* 56.2 (1989), pp. 229–242 (cit. on pp. 15, 37, 39, 46).

[46] J. Keizer and P. Smolen. “Bursting electrical activity in pancreatic beta cells caused by Ca^{2+}- and voltage-inactivated Ca^{2+} channels.” In: *Proceedings of the National Academy of Sciences* 88.9 (1991), pp. 3897–3901 (cit. on pp. xvi, 2, 15, 37).

[47] R. T. Kennedy, L. M. Kauri, G. M. Dahlgren, and S. K. Jung. “Metabolic oscillations in β-cells”. In: *Diabetes*. Vol. 51. SUPPL. American Diabetes Association, 2002, S152–S161 (cit. on p. 81).

[48] P. Klee, S. Bavamian, A. Charollais, et al. “Gap junctions and insulin secretion”. In: *Pancreatic Beta Cell in Health and Disease*. Tokyo: Springer Japan, 2008, pp. 111–132 (cit. on p. 121).

[49] E. Kohen, C. Kohen, B. Thorell, D. H. Mintz, and A. Rabinovitch. “Intercellular communication in pancreatic islet monolayer cultures: a microfluorometric study”. In: *Science* 195.4275 (1979), pp. 294–296 (cit. on p. 121).

[50] P. Krippeit-Drews, M. Düfer, and G. Drews. “Parallel Oscillations of Intracellular Calcium Activity and Mitochondrial Membrane Potential in Mouse Pancreatic B-Cells”. In: *Biochemical and Biophysical Research Communications* 267.1 (2000), pp. 179–183 (cit. on p. 80).

[51] K. Laios, M. Karamanou, Z. Saridaki, and G. Androutsos. *Aretaeus of Cappadocia and the first description of diabetes*. 2012 (cit. on p. 10).

[52] A. R. Leite, C. P. F. Carvalho, A. G. Furtado, et al. “Co-expression and regulation of connexins 36 and 43 in cultured neonatal rat pancreatic islets”. In: *Canadian Journal of Physiology and Pharmacology* 83.2 (2005), pp. 142–151 (cit. on p. 121).

[53] S. Lenzen, M. Lerch, T. Peckmann, and M. Tiedge. “Differential regulation of $[Ca^{2+}]_i$ oscillations in mouse pancreatic islets by glucose, alpha-ketoisocaproic acid, glyceraldehyde and glycolytic intermediates.” In: *Biochimica et Biophysica Acta* 1523.1 (2000), pp. 65–72 (cit. on pp. 86, 87).

[54] M. Loeb and W. Nernst. “Zur Kinetik der in Lösung befindlichen Körper”. In: *Zeitschrift für Physikalische Chemie* 2U.1 (2017), pp. 613–637 (cit. on p. 148).

[55] M. J. MacDonald, H. Al-Masri, M. Jumelle-Laclau, and M. O. Cruz. “Oscillations in activities of enzymes in pancreatic islet subcellular fractions induced by physiological concentrations of effectors”. In: *Diabetes* 46.12 (1997), pp. 1996–2001 (cit. on p. 35).

[56] G. Magnus and J. Keizer. “Model of β-cell mitochondrial calcium handling and electrical activity. I. Cytoplasmic variables”. In: *American Journal of Physiology* 274.4 (1998), pp. C1158–C1173 (cit. on pp. 15, 31, 37, 144).

[57] G. Magnus and J. Keizer. “Model of β-cell mitochondrial calcium handling and electrical activity. II. Mitochondrial variables”. In: *American Journal of Physiology* 274.4 (1998), pp. C1174–1184 (cit. on p. 31).

[58] I. Marinelli, T. Vo, L. Gerardo-Giorda, and R. Bertram. “Transitions between bursting modes in the integrated oscillator model for pancreatic β-cells”. In: *Journal of Theoretical Biology* 454 (2018), pp. 310–319 (cit. on p. 41).

[59] F. Martin, J. V. Sanchez-Andres, and B. Soria. “Slow [Ca2+]i oscillations induced by ketoisocaproate in single mouse pancreatic islets.” In: *Diabetes* 44.3 (1995), pp. 300–5 (cit. on pp. 86, 87).

[60] I. Martín-Timón and F. J. Del Cañizo-Gómez. “Mechanisms of hypoglycemia unawareness and implications in diabetic patients”. In: *World Journal of Diabetes* 6.7 (2015), p. 912 (cit. on p. 10).

[61] J. P. McKenna and R. Bertram. “Fast-slow analysis of the Integrated Oscillator Model for pancreatic β-cells”. In: *Journal of Theoretical Biology* 457 (2018), pp. 152–162 (cit. on pp. 36, 47).

[62] J. P. McKenna, J. Ha, M. J. Merrins, et al. “Ca^{2+} effects on ATP production and consumption have regulatory roles on oscillatory islet activity”. In: *Biophysical Journal* 110.3 (2016), pp. 733–742 (cit. on pp. xvi, 2, 24, 35, 36, 39, 63).

[63] J. P. McKenna, R. Dhumpa, N. Mukhitov, M. G. Roper, and R. Bertram. “Glucose oscillations can activate an endogenous oscillator in pancreatic islets”. In: *PLoS Computational Biology* 12.10 (2016), pp. 1–19 (cit. on pp. 93, 98).

[64] M. J. Merrins, A. R. Van Dyke, A. K. Mapp, M. A. Rizzo, and L. S. Satin. “Direct measurements of oscillatory glycolysis in pancreatic islet β-cells using novel fluorescence resonance energy transfer (FRET) biosensors for pyruvate kinase M2 activity.” In: *The Journal of Biological Chemistry* 288.46 (2013), pp. 33312–22 (cit. on pp. 35, 48).

[65] M. J. Merrins, B. Fendler, M. Zhang, et al. “Metabolic oscillations in pancreatic islets depend on the intracellular Ca^{2+} level but not Ca^{2+} oscillations”. In: *Biophysical Journal* 99.1 (2010), pp. 76–84 (cit. on pp. 60, 80).

[66] M. J. Merrins, C. Poudel, J. P. McKenna, et al. “Phase analysis of metabolic oscillations and membrane potential in pancreatic islet β-cells”. In: *Biophysical Journal* 110.3 (2016), pp. 691–699 (cit. on pp. xvii, 35, 48, 60, 79, 130).

[67] Y. Miwa and Y. Imai. “Simulation of spike-burst generation and Ca^{2+} oscillation in pancreatic β-cells.” In: *The Japanese Journal of Physiology* 49.4 (1999), pp. 353–64 (cit. on pp. xvi, 2, 15, 16, 37).

[68] C. S. Nunemaker, R. Bertram, A. Sherman, et al. “Glucose modulates $[Ca^{2+}]_i$ oscillations in pancreatic islets via ionic and glycolytic mechanisms”. In: *Biophysical Journal* 91.6 (2006), pp. 2082–2096 (cit. on pp. 81, 103).

[69] C. S. Nunemaker, M. Zhang, D. H. Wasserman, et al. “Individual mice can be distinguished by the period of their islet calcium oscillations: Is there an intrinsic islet period that is imprinted in vivo?” In: *Diabetes* 54.12 (2005), pp. 3517–3522 (cit. on pp. xv, 2).

[70] C. Oka, C. Y. Cha, and A. Noma. “Characterization of the cardiac Na+/K+ pump by development of a comprehensive and mechanistic model”. In: *Journal of Theoretical Biology* 265.1 (2010), pp. 68–77 (cit. on p. 152).

[71] M. Pérez-Armendariz, C. Roy, D. C. Spray, and M. V. Bennett. “Biophysical properties of gap junctions between freshly dispersed pairs of mouse pancreatic beta cells”. In: *Biophysical Journal* 59.1 (1991), pp. 76–92 (cit. on pp. 122, 123).

[72] M. Planck. “Ueber die Erregung von Electricität und Wärme in Electrolyten”. In: *Annalen der Physik* 275.2 (1890), pp. 161–186 (cit. on p. 148).

[73] I. Quesada, E. Fuentes, E. Andreu, et al. “On-line analysis of gap junctions reveals more efficient electrical than dye coupling between islet cells”. In: *American Journal of Physiology* 284.5 (2003), E980–E987 (cit. on p. 121).

[74] J. Ren, A. Sherman, R. Bertram, et al. “Slow oscillations of K ATP conductance in mouse pancreatic islets provide support for electrical bursting driven by metabolic oscillations”. In: *American Journal of Physiology* 305.7 (2013), E805–E817 (cit. on p. 84).

[75] A.-M. T. Richard, D.-L. Webb, J. M. Goodman, et al. “Tissue-dependent loss of phosphofructokinase-M in mice with interrupted activity of the distal promoter: impairment in insulin secretion”. In: *American Journal of Physiology* 293.3 (2007), E794–E801 (cit. on pp. 63, 66, 72).

[76] M. W. Roe, J. F. Worley, F. Qian, et al. “Characterization of a Ca^{2+} release-activated nonselective cation current regulating membrane potential and $[Ca^{2+}]_i$ oscillations in transgenically derived β-cells”. In: *Journal of Biological Chemistry* 273.17 (1998), pp. 10402–10410 (cit. on pp. xvi, 2, 15).

[77] P. Rorsman and F. M. Ashcroft. “Pancreatic β-Cell Electrical Activity and Insulin Secretion: Of Mice and Men”. In: *Physiological Reviews* 98.1 (2017), pp. 117–214 (cit. on pp. 7, 103).

[78] P. Rorsman and M. Braun. “Regulation of Insulin Secretion in Human Pancreatic Islets”. In: *Annual Review of Physiology* 75.1 (2013), pp. 155–179 (cit. on p. 6).

[79] R. M. Santos, L. M. Rosario, A. Nadal, et al. “Widespread synchronous $[Ca^{2+}]_i$ oscillations due to bursting electrical activity in single pancreatic islets”. In: *Pflügers Archiv European Journal of Physiology* 418.4 (1991), pp. 417–422 (cit. on p. 15).

[80] L. S. Satin. “Localized calcium influx in pancreatic β-cells: Its significance for Ca^{2+}-dependent insulin secretion from the islets of Langerhans”. In: *Endocrine* 13.3 (2000), pp. 251–262 (cit. on p. 112).

[81] L. S. Satin, P. C. Butler, J. Ha, and A. S. Sherman. “Pulsatile insulin secretion, impaired glucose tolerance and type 2 diabetes”. In: *Molecular Aspects of Medicine* 42 (2015), pp. 61–77 (cit. on pp. xv, 2).

[82] V. Seghers, M. Nakazaki, F. DeMayo, L. Aguilar-Bryan, and J. Bryan. “Sur1 knockout mice. A model for K(ATP) channel-independent regulation of insulin secretion.” In: *The Journal of Biological Chemistry* 275.13 (2000), pp. 9270–7 (cit. on p. 72).

[83] V. Serre-Beinier, S. Le Gurun, N. Belluardo, et al. “Cx36 preferentially connects β-cells within pancreatic islets”. In: *Diabetes* 49.5 (2000), pp. 727–734 (cit. on pp. 121, 126).

[84] A. Sherman and J. Rinzel. “Model for synchronization of pancreatic β-cells by gap junction coupling”. In: *Biophysical Journal* 59.3 (1991), pp. 547–559 (cit. on p. 122).

[85] J. R. Silva, P. Cooper, and C. G. Nichols. “Modeling K,ATP-dependent excitability in pancreatic islets”. In: *Biophysical Journal* 107.9 (2014), pp. 2016–2026 (cit. on pp. 19, 21, 156).

[86] P. Smolen. “A model for glycolytic oscillations based on skeletal muscle phosphofructokinase kinetics”. In: *Journal of Theoretical Biology* 174.2 (1995), pp. 137–148 (cit. on pp. 27, 28, 45, 46, 61).

[87] P. Smolen and J. Keizer. “Slow voltage inactivation of Ca^{2+} currents and bursting mechanisms for the mouse pancreatic β-cell”. In: *The Journal of Membrane Biology* 127.1 (1992), pp. 9–19 (cit. on pp. 15, 37, 39, 47).

[88] P. Smolen, J. Rinzel, and A. Sherman. “Why pancreatic islets burst but β beta cells do not. The heterogeneity hypothesis”. In: *Biophysical Journal* 64.6 (1993), pp. 1668–1680 (cit. on pp. 121, 122).

[89] J. Sturis, E. Van Cauter, J. D. Blackman, and K. S. Polonsky. “Entrainment of pulsatile insulin secretion by oscillatory glucose infusion”. In: *Journal of Clinical Investigation* 87.2 (1991), pp. 439–445 (cit. on pp. xix, 132).

[90] M. Tantama, J. R. Martínez-François, R. Mongeon, and G. Yellen. “Imaging energy status in live cells with a fluorescent biosensor of the intracellular ATP-to-ADP ratio”. In: *Nature Communications* 4 (2013), p. 2550 (cit. on p. 35).

[91] A. I. Tarasov, F. Semplici, D. Li, et al. “Frequency-dependent mitochondrial Ca^{2+} accumulation regulates ATP synthesis in pancreatic cells”. In: *Pflugers Archiv European Journal of Physiology* 465.4 (2013), pp. 543–554 (cit. on p. 103).

[92] K. Tornheim. “Are metabolic oscillations responsible for normal oscillatory insulin secretion?” In: *Diabetes* 46.9 (1997), pp. 1375–80 (cit. on pp. 15, 37, 39, 48, 81).

[93] K. Tornheim and J. M. Lowenstein. “Control of phosphofructokinase from rat skeletal muscle. Effects of fructose diphosphate, AMP, ATP, and citrate.” In: *The Journal of Biological Chemistry* 251.23 (1976), pp. 7322–8 (cit. on p. 61).

[94] K. Tornheim and J. M. Lowenstein. “The purine nucleotide cycle. 3. Oscillations in metabolite concentrations during the operation of the cycle in muscle extracts.” In: *Journal of Biological Chemistry* 248.8 (1973), pp. 2670–2677 (cit. on pp. xvi, 2, 15, 60, 61).

[95] K. Tsaneva-Atanasova, C. L. Zimliki, R. Bertram, and A. Sherman. “Diffusion of calcium and metabolites in pancreatic islets: Killing oscillations with a pitchfork”. In: *Biophysical Journal* 90.10 (2006), pp. 3434–3446 (cit. on p. 121).

[96] M. Valdeolmillos, A. Gomis, and J. V. Sánchez-Andrés. “In vivo synchronous membrane potential oscillations in mouse pancreatic β-cells: lack of coordination between islets.” In: *The Journal of Physiology* 493 (1996), pp. 9–18 (cit. on p. 121).

[97] M. Watts, B. Fendler, M. Merrins, et al. “Calcium and Metabolic Oscillations in Pancreatic Islets: Who’s Driving the Bus?” In: *SIAM Journal of Applied Dynamic Systems* 13.2 (2014), pp. 683–703 (cit. on pp. 29, 31, 54).

[98] G. C. Yaney, V. Schultz, B. A. Cunningham, et al. “Phosphofructokinase isozymes in pancreatic islets and clonal beta-cells (INS-1).” In: *Diabetes* 44.11 (1995), pp. 1285–9 (cit. on pp. 15, 48, 60).

[99] M. Zhang, P. Goforth, R. Bertram, A. Sherman, and L. Satin. “The Ca^{2+} dynamics of isolated mouse β-cells and islets: Implications for mathematical models”. In: *Biophysical Journal* 84.5 (2003), pp. 2852–2870 (cit. on p. 47).

List of Figures

List of Tables

List of Abbreviations

α-KIC	α-ketoisocaproic acid
ADP	Adenosine diphosphate
AMP	Adenosine monophosphate
ANT	Adenine nucleotide transporter
ATP	Adenosine triphosphate
Ca(V)	Voltage-dependent calcium
DH	Dehydrogenase
DOM	Dual Oscillator Model
Dz	Diazoxide
ER	Endoplasmic reticulum
EO	Electrical oscillator
F6P	Fructose 6-phosphate
FBP	Fructose 1,6-bisphosphate
FRET	Förster Resonance Energy Transfer
GDM	Gestational diabetes mellitus
GK	Glucokinase
GO	Glycolytic oscillator

GPDH	Glycerol-3-phosphate dehydrogenase
HB	Hopf bifurcation
HM	Homoclinic bifurcation
IOM	Integrated Oscillator Model
IP_3	Inositol 1,4,5-trisphosphate
K(ATP)	ATP-sensitive potassium
K(Ca)	Calcium-sensitive potassium
KCl	Potassium chloride
M-D	Micro-domain
MODY	Maturity-onset diabetes of the young
NADH	Reduced nicotinamide adenine dinucleotide
NADPH	Reduced nicotinamide adenine dinucleotide phosphate
NDM	Neonatal diabetes mellitus
ODE	Ordinary differential equation
PDH	Pyruvate dehydrogenase
Perceval-HR	Perceval High Resolution
PFK	Phosphofructokinase
PKAR	Pyruvate kinase activity reporter
PNDM	Permanent neonatal diabetes mellitus
SNP	Saddle-node of periodics bifurcation
SNB	Saddle-node bifurcation
TCA	Tricarboxylic acid
TNDM	Transient neonatal diabetes mellitus